

<sup>1</sup> **Searches for Supersymmetric signatures in  
2 all hadronic final states with the  $\alpha_T$   
3 variable.**

<sup>4</sup> Darren Burton

<sup>5</sup> Imperial College London  
<sup>6</sup> Department of Physics

<sup>7</sup> A thesis submitted to Imperial College London  
<sup>8</sup> for the degree of Doctor of Philosophy

---

## Abstract

A search for supersymmetric particles with in events with a missing energy signature and high  $p_T$  jets, is conducted using data recorded by the Compact Muon Solenoid detector based at the Large Hadron Collider. The analysis is performed with  $11.7 \text{ fb}^{-1}$  of data, collected with a center-of-mass collision energy of 8 TeV during the 2012 run period. The dimensionless kinematic variable  $\alpha_T$  is used as a tool to select events with genuine missing energy signatures, whilst Standard Model backgrounds in the signal region are estimated using data driven control samples, which have similar kinematic to the signal region. No excess of over Standard Model expectations is found. Exclusion limits are set at the 95% confidence level in the parameter space of a range of supersymmetric simplified model topologies, with special emphasis on those with compressed spectra (small mass splittings) and natural SUSY scenarios (large number of b flavoured quarks). A complementary method to search for natural SUSY signatures with a high number of b-flavoured jets, through the use of a simple template fit is also presented. The event selections of the  $\alpha_T$  search are used as a vehicle to demonstrate proof of principle of the technique in both data and simulation. Estimated Standard Model backgrounds from the template fits are compared with those determined from the data driven background estimation method of the  $\alpha_T$  search within the signal search region, where good agreement between the individual predictions and that of data are observed. Additionally the efficiency of the hadronic Level-1 single jet triggers are measured throughout the 2012 run period, where a change to the jet seed algorithm was implemented during the data taking period. This change was introduced to negate an increase in rate which can be attributed to pileup jets, whilst maintaining similar performance in the triggering of physics events.

39

## Declaration

40 I, the author of this thesis, declare that the work presented within this  
41 document to be my own. The work presented in Chapters 4, 5, 6 and Section  
42 3.4, is a result of the author's own work or that of which I have been a major  
43 contributor unless explicitly stated otherwise, and is carried out within the  
44 context of the Imperial College London and CERN SUSY groups, itself a  
45 subsection of the greater CMS collaboration. All figures and studies taken  
46 from external sources are referenced appropriately throughout this document.

47

Darren Burton

48

## Acknowledgements

49 I would like to thank the many people whom I have had the pleasure of working with  
50 during the course of the last three and a half years. The opportunity to work as part one  
51 of the largest scientific collaborations during one of the most exciting times in particle  
52 physics for decades, has been a real privilege to be a part of. I could not have achieved  
53 the results presented in this thesis without the help of my colleagues who were part of the  
54 RA1 team, Edward Laird, Chris Lucas, Henning Flaecher, Yossof Eshaq, Bryn Mathais,  
55 Sam Rogerson, Zhaoxia Meng and Georgia Karapostoli whom I worked with on L1 jets. I  
56 also thank my supervisor Oliver Buchmuller for his guidance in getting me to this point.

57 I also feel it important to single out thanks to the postdocs that I have worked with during  
58 my PhD. Jad Marrouche from whom I have learnt a great deal and Robert Bainbridge  
59 who has been like a second supervisor to me, helping me during my time at Imperial and  
60 CERN, especially during those most stressful of times approaching conference deadlines!

61 My fellow PhD students who I live with and have seen on an almost daily basis for the  
62 last few years, Andrew Gilbert, Patrick Owen, Indrek Sepp, Matthew Kenzie and my  
63 girlfriend Hannah. Thanks for putting up with the whinging, complaining and clopping.

64 Finally my largest thanks go to my Mum and Dad whose patience, encouragement and  
65 considerable financial support have allowed me to take the many steps that lead me here  
66 today.

# 67 Contents

68	<b>List of Figures</b>	viii
69	<b>List of Tables</b>	xiv
70	<b>1. Introduction</b>	2
71	<b>2. A Theoretical Overview</b>	5
72	2.1. The Standard Model . . . . .	5
73	2.1.1. Gauge Symmetries of the SM . . . . .	7
74	2.1.2. The Electroweak Sector and Electroweak Symmetry Breaking . . . . .	9
75	2.2. Motivation for Physics Beyond the Standard Model . . . . .	13
76	2.3. Supersymmetry Overview . . . . .	14
77	2.3.1. R-Parity . . . . .	16
78	2.4. Experimental Signatures of SUSY at the LHC . . . . .	16
79	2.4.1. Simplified models . . . . .	18
80	<b>3. The LHC And The CMS Detector</b>	20
81	3.1. The LHC . . . . .	20
82	3.2. The CMS Detector . . . . .	23
83	3.2.1. Detector subsystems . . . . .	23
84	3.2.2. Tracker . . . . .	24
85	3.2.3. Electromagnetic calorimeter . . . . .	25
86	3.2.4. Hadronic calorimeter . . . . .	26
87	3.2.5. Muon systems . . . . .	28
88	3.3. Event Reconstruction and Object Definition . . . . .	28
89	3.3.1. Jets . . . . .	28
90	3.3.2. B-tagging . . . . .	30
91	3.4. Triggering System . . . . .	33
92	3.4.1. The Level-1 trigger . . . . .	34

93	3.4.2. The L1 trigger jet algorithm . . . . .	35
94	3.4.3. Measuring L1 jet trigger efficiencies . . . . .	37
95	3.4.4. Effects of the L1 jet seed . . . . .	38
96	3.4.5. Robustness of L1 jet performance against pile-up . . . . .	40
97	3.4.6. Summary . . . . .	43
98	<b>4. SUSY Searches In Hadronic Final States</b>	<b>45</b>
99	4.1. An Introduction to the $\alpha_T$ Search . . . . .	46
100	4.1.1. The $\alpha_T$ variable . . . . .	48
101	4.2. Search Strategy . . . . .	50
102	4.2.1. Physics objects . . . . .	53
103	4.2.2. Event selection . . . . .	57
104	4.2.3. Control sample definition and background estimation . . . . .	60
105	4.2.4. Estimating the QCD multi-jet background . . . . .	67
106	4.3. Trigger Strategy . . . . .	69
107	4.4. Measuring MC Normalisation Factors via $H_T$ Sidebands . . . . .	70
108	4.5. Determining MC Simulation Yields with Higher Statistical Precision . . . . .	71
109	4.5.1. The formula method . . . . .	72
110	4.5.2. Establishing proof of principle . . . . .	73
111	4.5.3. Correcting measured efficiencies in simulation to data . . . . .	74
112	4.6. Systematic Uncertainties on Transfer Factors . . . . .	76
113	4.6.1. Determining systematic uncertainties from closure tests . . . . .	80
114	4.7. Simplified Models, Efficiencies and Systematic Uncertainties . . . . .	83
115	4.7.1. Signal efficiency . . . . .	83
116	4.7.2. Applying b-tag scale factor corrections in signal samples . . . . .	84
117	4.7.3. Experimental uncertainties . . . . .	86
118	4.8. Statistical Interpretation . . . . .	88
119	4.8.1. Hadronic sample . . . . .	89
120	4.8.2. $H_T$ evolution model . . . . .	89
121	4.8.3. Electroweak Sector (EWK) control samples . . . . .	90
122	4.8.4. Contributions from signal . . . . .	93
123	4.8.5. Total likelihood . . . . .	93
124	<b>5. Results and Interpretation</b>	<b>95</b>
125	5.1. Standard Model . . . . .	95
126	5.2. SUSY . . . . .	104
127	5.2.1. The $CL_s$ method . . . . .	104

128	5.2.2. Interpretation in simplified signal models . . . . .	105
129	<b>6. Searches For Natural SUSY With B-tag Templates.</b>	109
130	6.1. Concept . . . . .	109
131	6.2. Application to the $\alpha_T$ Search . . . . .	111
132	6.2.1. Proof of principle in simulation . . . . .	112
133	6.2.2. Results in a data control sample . . . . .	115
134	6.2.3. Application to the $\alpha_T$ hadronic search region . . . . .	117
135	6.3. Summary . . . . .	119
136	<b>7. Conclusions</b>	120
137	<b>A. Miscellaneous</b>	122
138	A.1. Jet Identification Criteria . . . . .	122
139	A.2. Primary Vertices . . . . .	123
140	<b>B. L1 Jets</b>	124
141	B.1. Jet matching efficiencies . . . . .	124
142	B.2. Leading Jet Energy Resolution . . . . .	125
143	B.3. Resolution for Energy Sum Quantities . . . . .	128
144	<b>C. Additional material on background estimation methods</b>	133
145	C.1. Determination of $k_{QCD}$ . . . . .	133
146	C.2. Effect of varying background cross sections on closure tests . . . . .	134
147	<b>D. Additional Material For B-tag Template Method</b>	136
148	D.1. Templates Fits in Simulation . . . . .	136
149	D.2. Pull Distributions for Template Fits . . . . .	139
150	D.3. Templates Fits in Data Control Sample . . . . .	140
151	D.4. Templates Fits in Data Signal Region . . . . .	142
152	<b>Bibliography</b>	145

# <sup>153</sup> List of Figures

<sup>154</sup> 2.1.	One loop quantum corrections to the Higgs squared mass parameter $m_h^2$ due to a fermion. . . . .	14
<sup>156</sup> 2.2.	Two example simplified model decay chains. . . . .	19
<sup>157</sup> 3.1.	A top down layout of the LHC, with the position of the four main detectors labelled. . . . .	21
<sup>159</sup> 3.2.	The total integrated luminosity delivered to and collected by Compact Muon Solenoid (CMS) during the 2012 8 TeV $pp$ runs . . . . .	22
<sup>161</sup> 3.3.	A pictorial depiction of the CMS detector. . . . .	24
<sup>162</sup> 3.4.	Illustration of the CMS Electromagnetic CALorimeter (ECAL). . . . .	26
<sup>163</sup> 3.5.	Schematic of the CMS Hadronic CALorimeter (HCAL). . . . .	27
<sup>164</sup> 3.6.	Combined Secondary Vertex (CSV) algorithm discriminator values in enriched ttbar and inclusive multi jet samples . . . . .	31
<sup>166</sup> 3.7.	Data/MC b-tag scale factors derived using the Combined Secondary Vertex Medium Working Point (CSVM) tagger. . . . .	32
<sup>168</sup> 3.8.	Data/MC mis-tag scale factors derived using the CSVM tagger. . . . .	33
<sup>169</sup> 3.9.	The CMS Level 1 Trigger (L1) Trigger system. . . . .	34
<sup>170</sup> 3.10.	Illustration of the Level-1 jet finding algorithm. . . . .	36
<sup>171</sup> 3.11.	L1 jet efficiency turn-on curves as a function of the offline CaloJet and PFJet $E_T$ . . . . .	38
<sup>173</sup> 3.12.	L1 jet efficiency turn-on curves as a function of the offline CaloJet $E_T$ for the 2012 run period B and C. . . . .	39

---

175	3.13. Trigger cross section for the L1HTT150 trigger path. . . . .	40
176	3.14. L1 $H_T$ efficiency turn-on curves as a function of the offline CaloJet $H_T$ . . . . .	41
177	3.15. L1 jet efficiency turn-on curves as a function of the leading offline $E_T$ Calo	
178	(left) and PF (right) jet, for low, medium and high pile-up conditions. . . . .	42
179	3.16. Fit values from an Exponentially Modified Gaussian (EMG) function fitted	
180	to the resolution plots of leading Calo jet $E_T$ measured as a function of	
181	$\frac{(L1\ E_T - \text{Offline}\ E_T)}{\text{Offline}\ E_T}$ for low, medium and high pile-up conditions. . . . .	43
182	3.17. Fit values from an EMG function fitted to the resolution plots of leading	
183	PF jet $E_T$ measured as a function of $\frac{(L1\ E_T - \text{Offline}\ E_T)}{\text{Offline}\ E_T}$ for low, medium and	
184	high pile-up conditions. . . . .	44
185	4.1. Reconstructed offline $H_T$ distribution in the hadronic signal selection, from	
186	$11.7\text{fb}^{-1}$ of data, in which no $\alpha_T$ requirement is made. . . . .	48
187	4.2. The event topologies of background QCD dijet events (right) and a generic	
188	SUSY signature with genuine $Z_T$ (left). . . . .	48
189	4.3. The $\alpha_T$ distributions for the low 2-3 (left) and high $\geq 4$ (right) jet	
190	multiplicities after a full analysis selection and shown for $H_T > 375$ . . . . .	50
191	4.4. Pictorial depiction of the analysis strategy employed by the $\alpha_T$ search to	
192	increase sensitivity to a wide spectra of SUSY models. . . . .	53
193	4.5. Data/MC comparisons of key variables for the hadronic signal region. . . . .	60
194	4.6. Data/MC comparisons of key variables for the $\mu +$ jets selection. . . . .	63
195	4.7. Data/MC comparisons of key variables for the $\mu\mu +$ jets selection. . . . .	65
196	4.8. Data/MC comparisons of key variables for the $\gamma +$ jets selection. . . . .	66
197	4.9. QCD sideband regions, used for determination of $k_{\text{QCD}}$ . . . . .	68
198	4.10. Tagging efficiencies of (a) b-jets, (b) c-jets, and (c) light-jets determined	
199	from all jets within each individual analysis $H_T$ bin. . . . .	75
200	4.11. Sets of closure tests overlaid on top of the systematic uncertainty used for	
201	each of the five $H_T$ regions. . . . .	82

---

202	4.12. Signal efficiencies fo the Simplified Model Spectra (SMS) models (a) T1 203 and (b) T2. . . . .	84
204	5.1. Comparison of the observed yields and Standard Model (SM) expectations 205 given by the simultaneous fit in bins of $H_T$ for the (a) hadronic, (b) $\mu +$ 206 jets, (c) $\mu\mu +$ jets and (d) $\gamma +$ jets samples when requiring $n_b^{reco} = 0$ and 207 $n_{jet} \leq 3$ . . . . .	97
208	5.2. Comparison of the observed yields and SM expectations given by the 209 simultaneous fit in bins of $H_T$ for the (a) hadronic, (b) $\mu +$ jets, (c) $\mu\mu +$ 210 jets and (d) $\gamma +$ jets samples when requiring $n_b^{reco} = 1$ and $n_{jet} \leq 3$ . . . . .	98
211	5.3. Comparison of the observed yields and SM expectations given by the 212 simultaneous fit in bins of $H_T$ for the (a) hadronic, (b) $\mu +$ jets, (c) $\mu\mu +$ 213 jets and (d) $\gamma +$ jets samples when requiring $n_b^{reco} = 2$ and $n_{jet} \leq 3$ . . . . .	99
214	5.4. Comparison of the observed yields and SM expectations given by the 215 simultaneous fit in bins of $H_T$ for the (a) hadronic, (b) $\mu +$ jets, (c) $\mu\mu +$ 216 jets and (d) $\gamma +$ jets samples when requiring $n_b^{reco} = 0$ and $n_{jet} \geq 4$ . . . . .	100
217	5.5. Comparison of the observed yields and SM expectations given by the 218 simultaneous fit in bins of $H_T$ for the (a) hadronic, (b) $\mu +$ jets, (c) $\mu\mu +$ 219 jets and (d) $\gamma +$ jets samples when requiring $n_b^{reco} = 1$ and $n_{jet} \geq 4$ . . . . .	101
220	5.6. Comparison of the observed yields and SM expectations given by the 221 simultaneous fit in bins of $H_T$ for the (a) hadronic, (b) $\mu +$ jets, (c) $\mu\mu +$ 222 jets and (d) $\gamma +$ jets samples when requiring $n_b^{reco} = 2$ and $n_{jet} \geq 4$ . . . . .	102
223	5.7. Comparison of the observed yields and SM expectations given by the 224 simultaneous fit in bins of $H_T$ for the (a) hadronic, (b) $\mu +$ jets, (c) $\mu\mu +$ 225 jets and (d) $\gamma +$ jets samples when requiring $n_b^{reco} = 3$ and $n_{jet} \geq 4$ . . . . .	102
226	5.8. Comparison of the observed yields and SM expectations given by the 227 simultaneous fit in bins of $H_T$ for the (a) hadronic, (b) $\mu +$ jets, (c) $\mu\mu +$ 228 jets and (d) $\gamma +$ jets samples when requiring $n_b^{reco} \geq 4$ and $n_{jet} \geq 4$ . . . . .	103
229	5.9. Production and decay modes for the various SMS models interpreted 230 within the analysis. . . . .	107
231	5.10. Upper limit of cross section at 95% CL as a function of $m_{\tilde{q}/\tilde{g}}$ and $m_{LSP}$ 232 for various SMS models. . . . .	108

---

233	6.1. The b-tagging (a), c-quark mis-tagging (b), and light-quark mis-tagging rate (c) as measured in simulation after the $\alpha_T$ analysis, $\mu + \text{jets}$ control sample selection in the region $H_T > 375$ . . . . .	111
236	6.2. The results of fitting the $Z = 0$ and $Z = 2$ templates to the $n_b^{reco} = 0, 1, 2$ bins taken directly from simulation in the region $H_T > 375$ GeV, for the $n_{jet} \geq 5$ category. . . . .	114
239	6.3. The results of fitting the $Z = 0$ and $Z = 2$ templates to the $n_b^{reco} = 0, 1, 2$ bins taken from data, for the $n_{jet} \geq 5$ category and medium CSV working point. . . . .	116
242	6.4. The results of fitting the $Z = 0$ and $Z = 2$ templates to the $n_b^{reco} = 0, 1, 2$ bins taken from data, in the $n_{jet} \geq 5$ and $H_T > 375$ category for all CSV working points. . . . .	118
245	B.1. Leading jet matching efficiency as a function of the offline CaloJet $E_T$ . . . . .	124
246	B.2. Resolution plots of the leading offline Calo $E_T$ measured as a function of $\frac{(L1 E_T - \text{Offline } E_T)}{\text{Offline } E_T}$ for low (a), medium (b) and high (c) pile-up conditions. . . . .	126
248	B.3. Resolution plots of the leading off-line PF $E_T$ measured as a function of $\frac{(L1 E_T - \text{Offline } E_T)}{\text{Offline } E_T}$ for low (a), medium (b) and high (c) pile-up conditions. . . . .	128
250	B.4. $\sum E_T$ resolution parameters in bins of Calo $\sum E_T$ measured for the defined low, medium and high pile up conditions. . . . .	129
252	B.5. $\sum E_T$ resolution parameters in bins of PF $\sum E_T$ measured for the defined low, medium and high pile up conditions. . . . .	129
254	B.6. $\cancel{E}_T$ resolution parameters in bins of Calo $\cancel{E}_T$ measured for the defined low, medium and high pile up conditions. . . . .	130
256	B.7. $\cancel{E}_T$ resolution parameters in bins of PF $\cancel{E}_T$ measured for the defined low, medium and high pile up conditions. . . . .	130
258	B.8. $H_T$ resolution parameters in bins of Calo $H_T$ measured for the defined low, medium and high pile up conditions. . . . .	131
260	B.9. $H_T$ resolution parameters in bins of PF $H_T$ measured for the defined low, medium and high pile up conditions. . . . .	131

---

262	B.10. $\mathcal{H}_T$ resolution parameters in bins of $\mathcal{H}_T$ measured for the defined low,	
263	medium and high pile up conditions. . . . .	132
264	B.11. $\mathcal{H}_T$ resolution parameters in bins of PF $\mathcal{H}_T$ measured for the defined low,	
265	medium and high pile up conditions. . . . .	132
266	C.1. $R_{\alpha_T}(H_T)$ and exponential fits for each of the data sideband regions. Fit is	
267	conducted between the $H_T$ region $275 < H_T < 575$ . . . . .	133
268	C.2. Sets of closure tests overlaid on top of the systematic uncertainty used for	
269	each of the five $H_T$ regions. . . . .	134
270	C.3. Sets of closure tests overlaid on top of the systematic uncertainty used for	
271	each of the five $H_T$ regions. . . . .	134
272	D.1. The results of fitting the $Z = 0$ and $Z = 2$ templates to the $n_b^{reco} = 0, 1, 2$	
273	bins taken directly from simulation in the region $H_T > 375$ GeV, for the	
274	$n_{jet} = 3$ category. . . . .	137
275	D.2. The results of fitting the $Z = 0$ and $Z = 2$ templates to the $n_b^{reco} = 0, 1, 2$	
276	bins taken directly from simulation in the region $H_T > 375$ GeV, for the	
277	$n_{jet} = 4$ category. . . . .	138
278	D.3. Pull distributions of $\frac{(\theta - \hat{\theta})}{\sigma}$ for $10^4$ pseudo-experiments generated from a	
279	gaussian distribution centred on the $n_b^{reco}$ template values from simulation	
280	with width $\sigma$ . . . . .	139
281	D.4. The results of fitting the $Z = 0$ and $Z = 2$ templates to the $n_b^{reco} = 0, 1, 2$	
282	bins taken directly from data, for the $n_{jet} = 3$ category and medium CSV	
283	working point. . . . .	140
284	D.5. The results of fitting the $Z = 0$ and $Z = 2$ templates to the $n_b^{reco} = 0, 1, 2$	
285	bins taken directly from data, for the $n_{jet} = 4$ category and medium CSV	
286	working point. . . . .	141
287	D.6. The results of fitting the $Z = 0$ and $Z = 2$ templates to the $n_b^{reco} = 0, 1, 2$	
288	bins taken from data, in the $n_{jet} = 3$ and $H_T > 375$ category for all CSV	
289	working points. . . . .	142

290	D.7. The results of fitting the $Z = 0$ and $Z = 2$ templates to the $n_b^{reco} = 0, 1, 2$	
291	bins taken from data, in the $n_{jet} = 4$ and $H_T > 375$ category for all CSV	
292	working points. . . . .	143

# **List of Tables**

294	2.1. The fundamental particles of the SM, with spin, charge and mass displayed.	6
295	3.1. Results of a cumulative EMG function fit to the turn-on curves for L1	
296	single jet triggers in 2012 Run Period C. . . . .	38
297	3.2. Results of a cumulative EMG function fit to the turn-on curves for L1	
298	single jet triggers in the 2012 run period B and C. . . . .	40
299	3.3. Results of a cumulative EMG function fit to the turn-on curves for $H_T$ in	
300	2012 run period B and C. . . . .	41
301	3.4. Results of a cumulative EMG function fit to the efficiency turn-on curves	
302	for L1 single jet triggers in the 2012 run period C, for low,medium and	
303	high pile-up conditions. . . . .	41
304	3.5. Results of a cumulative EMG function fit to the efficiency turn-on curves	
305	for Level-1 single jet triggers in the 2012 run period C, for low,medium	
306	and high pile-up conditions. . . . .	42
307	4.1. A summary of the SMS models interpreted in this analysis, involving both	
308	direct (D) and gluino-induced (G) production of squarks and their decays.	46
309	4.2. Muon Identification criteria used within the analysis for selection/veto	
310	purposes in the muon control/signal selections. . . . .	54
311	4.3. Photon Identification criteria used within the analysis for selection/veto	
312	purposes in the $\gamma +$ jets control/signal selections. . . . .	55
313	4.4. Electron Identification criteria used within the analysis for veto purposes.	56
314	4.5. Noise filters that are applied to remove spurious and non-physical $\cancel{E}_T$	
315	signatures within the CMS detector. . . . .	57

316	4.6. Jet thresholds used in the three $H_T$ regions of the analysis. . . . .	58
317	4.7. Best fit values for the parameters $k_{\text{QCD}}$ obtained from sideband regions	
318	B,C <sub>1</sub> ,C <sub>2</sub> ,C <sub>3</sub> . . . . .	69
319	4.8. Measured efficiencies of the $H_T$ and $\alpha_T$ legs of the HT and HT_alphaT	
320	triggers in independent analysis bins. . . . .	70
321	4.9. k-factors calculated for different EWK processes. . . . .	71
322	4.10. Comparing yields in simulation within the $\mu + \text{jets}$ selection determined	
323	from the formula method described in Equation (4.11), and that taken	
324	directly from simulation . . . . .	74
325	4.11. The absolute change in the Transfer Factor (TF)'s used to predict the	
326	entire signal region SM background, using the $\mu + \text{jets}$ control sample	
327	when the systematic uncertainties of the data to simulation scale factors	
328	are varied by $\pm 1\sigma$ . . . . .	76
329	4.12. A summary of the results obtained from zeroeth order polynomial (i.e.	
330	a constant) and linear fits to five sets of closure tests performed in the	
331	$2 \geq n_{\text{jet}} \geq 3$ category. . . . .	79
332	4.13. A summary of the results obtained from zeroeth order polynomial (i.e.	
333	a constant) and linear fits to five sets of closure tests performed in the	
334	$n_{\text{jet}} \geq 4$ category. . . . .	79
335	4.14. A summary of the results obtained from zeroeth order polynomial (i.e. a	
336	constant) and linear fits to five sets of closure tests performed between	
337	the $2 \leq n_{\text{jet}} \leq 3$ and $n_{\text{jet}} \geq 4$ categories. . . . .	79
338	4.15. Calculated systematic uncertainties for the five $H_T$ regions, determined	
339	from the closure tests. . . . .	81
340	4.16. Estimates of systematic uncertainties on the signal efficiency (%) for	
341	various SMS models when considering points in the region near to the	
342	diagonal . . . . .	88
343	4.17. Estimates of systematic uncertainties on the signal efficiency (%) for	
344	various SMS models when considering points in the region near to the	
345	diagonal . . . . .	88

---

346	4.18. The systematic parameters used in $H_T$ bins. . . . .	92
347	4.19. Nuisance parameters used within the different hadronic signal bins of the	
348	analysis . . . . .	94
349	5.1. Summary of control samples used by each fit results, and the Figures in	
350	which they are displayed. . . . .	96
351	5.2. Comparison of the measured yields in the each $H_T$ , $n_{jet}$ and $n_b^{reco}$ jet	
352	multiplicity bins for the hadronic sample with the SM expectations and	
353	combined statistical and systematic uncertainties given by the simultaneous	
354	fit. . . . .	96
355	5.3. A table representing the SMS models interpreted within the analysis. . .	105
356	6.1. Typical underlying b-quark content of different SM processes which are	
357	common to many SUSY searches. . . . .	110
358	6.2. Summary of the fit predictions in the $n_b^{reco}$ signal region for $n_{jet} = 3, =$	
359	$4, \geq 5$ . The fit region is $n_b^{reco} = 0, 1, 2$ and simulation yields are normalised	
360	to an integrated luminosity of $10 \text{ fb}^{-1}$ . . . . .	113
361	6.3. Summary of the fit predictions in the $n_b^{reco}$ signal region of the $\mu + \text{jets}$	
362	control sample, for $n_{jet} = 3, = 4, \geq 5$ . The fit region is $n_b^{reco} = 0, 1, 2$	
363	using $11.5 \text{ fb}^{-1}$ of data at $\sqrt{s} = 8\text{TeV}$ . . . . .	115
364	6.4. Summary of the fit predictions in the $n_b^{reco}$ signal region of the $\mu + \text{jets}$	
365	control sample, for $n_{jet} = 3, = 4, \geq 5$ . The fit region is $n_b^{reco} = 0, 1, 2$	
366	using $11.5 \text{ fb}^{-1}$ of data at $\sqrt{s} = 8\text{TeV}$ . . . . .	117
367	A.1. Criteria for a reconstructed jet to pass the loose calorimeter jet id. . . . .	122
368	A.2. Criteria for a reconstructed jet to pass the loose PF jet id. . . . .	123
369	A.3. Criteria for a vertex in an event to be classified as a 'good' reconstructed	
370	primary vertex. . . . .	123
371	B.1. Results of a cumulative EMG function fit to the turn-on curves for the	
372	matching efficiency of the leading jet in an event to a Level-1 jet in run	
373	2012C and 2012B data. . . . .	125

374	C.1. Translation factors constructed from the $\mu +$ jets control sample and signal selection MC, to predict yields for the $W +$ jets and $t\bar{t}$ back-grounds in the signal region. . . . .	135
375		
376		

*“The Universe is about 1,000,000 years old.”*

— Matthew Kenzie, 1987-present : Discoverer of the Higgs Boson.

# Chapter 1.

## <sup>379</sup> Introduction

<sup>380</sup> During the 20th century, great advances have been made in the human understanding  
<sup>381</sup> of the universe, it's origins, it's future and its composition. The Standard Model (**SM**)  
<sup>382</sup> first formulated in the 1960's is one of the crowning achievements in science's quest to  
<sup>383</sup> explain the most fundamental processes and interactions that make up our universe. It  
<sup>384</sup> has provided a highly successful explanation of a wide range of phenomena in Particle  
<sup>385</sup> Physics and has stood up to extensive experimental scrutiny [1].

<sup>386</sup> Despite it's successes it is not a complete theory, with significant questions remaining  
<sup>387</sup> unanswered. It describes only three of the four known forces with gravity not incorporated  
<sup>388</sup> within the framework of the **SM**. Cosmological experiments infer that just  $\sim 4\%$  of the  
<sup>389</sup> observable universe exists as matter, with elusive "Dark Matter" accounting for a further  
<sup>390</sup>  $\sim 23\%$  [2]. However no particle predicted by the **SM** is able to account for it. At higher  
<sup>391</sup> energy scales and small distances, the (non-)unification of the fundamental forces point  
<sup>392</sup> to problems with the **SM** at least at higher energies not yet probed experimentally.

<sup>393</sup> Many theories exist as extensions to the **SM**, predicting a range of observables that can  
<sup>394</sup> be detected at the Large Hadron Collider (**LHC**) of which SUperSYmmetry (**SUSY**) is  
<sup>395</sup> one such example. It predicts a new symmetry of nature in which all current particles  
<sup>396</sup> in the **SM** would have a corresponding supersymmetric partner. Common to most  
<sup>397</sup> Supersymmetric theories is a stable, weakly interacting Lightest Supersymmetric Partner  
<sup>398</sup> (**LSP**), which has the properties of a possible dark matter candidate. The **SM** and the  
<sup>399</sup> main principles of Supersymmetric theories are outlined in Chapter 2, with emphasis  
<sup>400</sup> placed on how experimental signatures of **SUSY** may reveal themselves in proton collisions  
<sup>401</sup> at the **LHC**.

402 The experimental goal of the LHC is to further test the framework of the SM, exploring the  
403 TeV mass scale for the first time, and to seek a connection between the particles produced  
404 in proton collisions and dark matter. The first new discovery by this extraordinary  
405 machine was announced on the 4th of July 2012. The long-awaited discovery was the  
406 culmination of decades of experimental endeavours in the search for the Higgs boson,  
407 providing an answer to the mechanism of electroweak symmetry breaking within the SM  
408 [3][4].

409 This discovery was made possible through data taken by the two multi purpose detectors  
410 (Compact Muon Solenoid (CMS) and A Toroidal LHC ApparatuS (ATLAS)) located  
411 on the LHC ring. An experimental description of the CMS detector and the LHC is  
412 described in Chapter 3, including some of the object reconstruction used by CMS in  
413 searches for SUSY signatures.

414 The performance of the CMS Level-1 single jet trigger, measured over the course of  
415 the year is also included within this chapter. The Level-1 triggers are of paramount  
416 importance to the recording of physics events at CMS, and to which a change in the jet  
417 seed algorithm was introduced approximately half way through the data taking period.  
418 The aim of this change, was to facilitate a reduction in the rate at which data from  
419 events not of interest to physics analyses were recorded, whilst avoiding impact on those  
420 which were.

421 Chapter 4, contains a description of the search for evidence of the production of Su-  
422 persymmetric particles at the LHC. The main basis of the search centres around the  
423 kinematic dimensionless  $\alpha_T$  variable, which provides strong rejection of backgrounds with  
424 fake missing energy signatures whilst maintaining good sensitivity to a variety of SUSY  
425 topologies. The author's work (as an integral part of the analysis group) is documented  
426 in detail, which has culminated in numerous publications over the past two years, the  
427 latest of which was published in the European Physical Journal C (EPJC) [5]. The results  
428 and interpretations within the framework of a variety of Simplified Model Spectra (SMS),  
429 which describe an array of possible SUSY event topologies is documented in Chapter 5.

430 The author in particular has played a major role in the extension of the  $\alpha_T$  analysis into  
431 the additional b-tagged and jet multiplicity dimensions increasing the sensitivity of the  
432 analysis to a range of SUSY topologies. Additionally the author has worked extensively  
433 in both increasing the statistical precision of electroweak predictions measured from  
434 simulation through analytical techniques, and the derivation of a data driven systematic

- 435 uncertainty through the establishment of closure tests within the control samples of the  
436 analysis.
- 437 Finally a method to search for **SUSY** signatures rich in top and bottom flavoured jet final  
438 states, is introduced in Chapter 6. These particular **SUSY** topologies are increasingly of  
439 interest to physicists in light of the discovery of the Higgs boson, and is discussed within  
440 the chapter. A parametrisation of the b-tagging distribution for different Electroweak  
441 processes is used to establish template shapes, which are then fitted at low b-tagged jet  
442 multiplicity (0-2), to estimate the expected number of 3 and 4 b-tagged jet events from  
443 **SM** processes. The  $\alpha_T$  event selections are used to test the functionality of this template  
444 method in both data and simulation, with background predictions from the signal region  
445 selection compared to those presented in Chapter 5.
- 446 Natural units are used throughout this thesis in which  $\hbar = c = 1$ .

# Chapter 2.

## <sup>447</sup> A Theoretical Overview

<sup>448</sup> Within this chapter, a brief introduction and background to the **SM** is given. Its success  
<sup>449</sup> as a rigorously tested and widely accepted theory is discussed as are its deficiencies,  
<sup>450</sup> leading to the argument that this theory is not a complete description of our universe.  
<sup>451</sup> The motivations for new physics at the TeV scale and in particular Supersymmetric  
<sup>452</sup> theories are outlined within Section (2.3), with the chapter concluding with how an  
<sup>453</sup> experimental signature of such theories can be produced and observed at the **LHC**,  
<sup>454</sup> Section (2.4).

### <sup>455</sup> 2.1. The Standard Model

<sup>456</sup> The **SM** is the name given to the relativistic Quantum Field Theory (**QFT**), where  
<sup>457</sup> particles are represented as excitations of fields, which describe the interactions and  
<sup>458</sup> properties of all the known elementary particles [6][7][8][9]. It is a renormalisable field  
<sup>459</sup> theory which contains three symmetries:  $SU(3)$  for colour charge,  $SU(2)$  for weak isospin  
<sup>460</sup> and  $U(1)$  relating to weak hyper charge, which require its Lagrangian  $\mathcal{L}_{SM}$  to be invariant  
<sup>461</sup> under local gauge transformation.

<sup>462</sup> Within the **SM** theory, matter is composed of spin  $\frac{1}{2}$  fermions, which interact with each  
<sup>463</sup> other via the exchange of spin-1 gauge bosons. A summary of the known fundamental  
<sup>464</sup> fermions and bosons is given in Table 2.1.

<sup>465</sup> Fermions are separated into quarks and leptons of which only quarks interact with the  
<sup>466</sup> strong nuclear force. Quarks unlike leptons are not seen as free particles in nature, but  
<sup>467</sup> rather exist only within baryons, composed of three quarks with an overall integer charge,  
<sup>468</sup> and quark-anti-quark pairs called mesons. Both leptons and quarks are grouped into

Particle	Symbol	Spin	Charge	Mass (GeV)
<b>First Generation Fermions</b>				
Electron Neutrino	$\nu_e$	$\frac{1}{2}$	0	$< 2.2 \times 10^{-6}$
Electron	e	$\frac{1}{2}$	-1	$0.51 \times 10^{-3}$
Up Quark	u	$\frac{1}{2}$	$\frac{2}{3}$	$2.3^{+0.7}_{-0.5} \times 10^{-3}$
Down Quark	d	$\frac{1}{2}$	$-\frac{1}{3}$	$4.8^{+0.7}_{-0.3} \times 10^{-3}$
<b>Second Generation Fermions</b>				
Muon Neutrino	$\nu_\mu$	$\frac{1}{2}$	0	-
Muon	$\mu$	$\frac{1}{2}$	-1	$1.05 \times 10^{-3}$
Charm Quark	c	$\frac{1}{2}$	$\frac{2}{3}$	$1.275 \pm 0.025$
Strange Quark	s	$\frac{1}{2}$	$-\frac{1}{3}$	$95 \pm 5 \times 10^{-3}$
<b>Third Generation Fermions</b>				
Tau Neutrino	$\nu_\tau$	$\frac{1}{2}$	0	-
Tau	$\tau$	$\frac{1}{2}$	-1	1.77
Top Quark	t	$\frac{1}{2}$	$\frac{2}{3}$	$173.5 \pm 0.8$
Bottom Quark	b	$\frac{1}{2}$	$-\frac{1}{3}$	$4.65 \pm 0.03$
<b>Gauge Bosons</b>				
Photon	$\gamma$	1	0	0
W Boson	$W^\pm$	1	$\pm 1$	$80.385 \pm 0.015$
Z Boson	Z	1	0	$91.187 \pm 0.002$
Gluons	g	1	0	0
Higgs Boson	H	0	0	$125.3 \pm 0.5$ [4]

**Table 2.1.:** The fundamental particles of the SM, with spin, charge and mass displayed. Latest mass measurements taken from [1].

<sup>469</sup> three generations which have the same properties, but with ascending mass in each  
<sup>470</sup> subsequent generation.

<sup>471</sup> The gauge bosons mediate the interactions between fermions. The field theories of  
<sup>472</sup> Quantum Electro-Dynamics (QED) and Quantum Chromo-Dynamics (QCD), yield  
<sup>473</sup> massless mediator bosons, the photon and eight coloured gluons which are consequences  
<sup>474</sup> of the gauge invariance of those theories, detailed in Section (2.1.1).

<sup>475</sup> The unification of the electromagnetic and weak-nuclear forces into the current Elec-  
<sup>476</sup> troweak theory yield the weak gauge bosons,  $W^\pm$  and Z through the mixing of the  
<sup>477</sup> associated gauge fields. The force carriers of this theory were experimentally detected by  
<sup>478</sup> the observation of weak neutral current, discovered in 1973 in the Gargamelle bubble  
<sup>479</sup> chamber located at European Organization for Nuclear Research (CERN) [10], with the  
<sup>480</sup> masses of the weak gauge bosons measured by the UA1 and U2 experiments at the Super  
<sup>481</sup> Proton Synchrotron (SPS) collider in 1983 [11][12].

### <sup>482</sup> 2.1.1. Gauge Symmetries of the SM

<sup>483</sup> Symmetries are of fundamental importance in the description of physical phenomena.  
<sup>484</sup> Noether's theorem states that for a dynamical system, the consequence of any symmetry  
<sup>485</sup> is an associated conserved quantity [13]. Invariance under translations, rotations, and  
<sup>486</sup> Lorentz transformations in physical systems lead to conservation of momentum, energy  
<sup>487</sup> and angular momentum.

<sup>488</sup> In the **SM**, a quantum theory described by Lagrangian formalism, the weak, strong and  
<sup>489</sup> electromagnetic interactions are described in terms of “gauge theories”. A gauge theory  
<sup>490</sup> possesses invariance under a set of “local transformations”, which are transformations  
<sup>491</sup> whose parameters are space-time dependent. The requirement of gauge invariance within  
<sup>492</sup> the **SM** necessitates the introduction of force-mediating gauge bosons and interactions  
<sup>493</sup> between fermions and the bosons themselves. Given the nature of the topics covered by  
<sup>494</sup> this thesis, the formulation of **EWK** within the **SM** Lagrangian is reviewed within this  
<sup>495</sup> section.

<sup>496</sup> The simplest example of the application of the principle of local gauge invariance within  
<sup>497</sup> the **SM** is in Quantum Electro-Dynamics (**QED**), the consequences of which require a  
<sup>498</sup> massless photon field [14][15].

<sup>499</sup> Starting from the free Dirac Lagrangian written as

$$\mathcal{L} = \bar{\psi}(i\gamma^\mu \partial_\mu - m)\psi, \quad (2.1)$$

<sup>500</sup> where  $\psi$  represents a free non interacting fermionic field, with the matrices  $\gamma^\mu$ ,  $\mu \in 0, 1, 2, 3$   
<sup>501</sup> defined by the anti commutator relationship  $\gamma^\mu \gamma^\nu + \gamma^\nu \gamma^\mu = 2\eta^{\mu\nu} I_4$ , with  $\eta^{\mu\nu}$  being the  
<sup>502</sup> flat space-time metric  $(+, -, -, -)$ , and  $I_4$  the  $4 \times 4$  identity matrix.

<sup>503</sup> Under a local U(1) abelian gauge transformation in which  $\psi$  transforms as:

$$\psi(x) \rightarrow \psi'(x) = e^{i\theta(x)}\psi(x) \quad \bar{\psi}(x) \rightarrow \bar{\psi}'(x) = e^{i\theta(x)}\bar{\psi}(x) \quad (2.2)$$

<sup>504</sup> the kinetic term of the Lagrangian will not remain invariant, due to the partial derivative  
<sup>505</sup> interposed between the  $\bar{\psi}$  and  $\psi$  yielding,

$$\partial_\mu \psi \rightarrow e^{i\theta(x)} \partial_\mu \psi + ie^{i\theta(x)} \psi \partial_\mu \theta. \quad (2.3)$$

To ensure that  $\mathcal{L}$  remains invariant, a modified derivative,  $D_\mu$ , that transforms covariantly under phase transformations is introduced. In doing this a vector field  $A_\mu$  with transformation properties that cancel out the unwanted term in (2.3) must also be included,

$$D_\mu \equiv \partial_\mu - ieA_\mu, \quad A_\mu \rightarrow A_\mu + \frac{1}{e} \partial_\mu \theta. \quad (2.4)$$

Invariance of the Lagrangian is then achieved by replacing  $\partial_\mu$  by  $D_\mu$ :

$$\begin{aligned} \mathcal{L} &= i\bar{\psi}\gamma^\mu D_\mu \psi - m\bar{\psi}\psi \\ &= \bar{\psi}(i\gamma^\mu \partial_\mu - m)\psi + e\bar{\psi}\gamma^\mu \psi A_\mu \end{aligned} \quad (2.5)$$

An additional interaction term is now present in the Lagrangian, coupling the Dirac particle to this vector field, which is interpreted as the photon in QED. To regard this new field as the physical photon field, a term corresponding to its kinetic energy must be added to the Lagrangian from Equation (2.5). Since this term must also be invariant under the conditions of Equation (2.4), it is defined in the form  $F_{\mu\nu} = \partial^\mu A^\nu - \partial^\nu A^\mu$ .

This then leads to the Lagrangian of QED:

$$\mathcal{L}_{QED} = \underbrace{i\bar{\psi}\gamma^\mu \partial_\mu \psi - \frac{1}{4}F_{\mu\nu}F^{\mu\nu}}_{\text{kinetic term}} + \underbrace{m\bar{\psi}\psi}_{\text{mass term}} + \underbrace{e\bar{\psi}\gamma^\mu \psi A_\mu}_{\text{interaction term}} \quad (2.6)$$

Within the Lagrangian there remains no mass term of the form  $m^2 A_\mu A^\mu$ , which is prohibited by gauge invariance. This implies that the gauge particle, the photon, must be massless.

## 520 2.1.2. The Electroweak Sector and Electroweak Symmetry 521 Breaking

- 522 The same application of gauge symmetry and the requirement of local gauge invariance  
523 can be used to unify QED and the Weak force in the Electroweak Sector (EWK).  
524 The nature of EWK interactions is encompassed within a Lagrangian invariant under  
525 transformations of the group  $SU(2)_L \times U(1)_Y$ .  
526 The weak interactions from experimental observation [16], are known to violate parity  
527 and are therefore not symmetric under interchange of left and right helicity fermions.  
528 Thus within the SM the left and right handed parts of these fermion fields are treated  
529 separately. A fermion field is then split into two left and right handed chiral components,  
530  $\psi = \psi_L + \psi_R$ , where  $\psi_{L/R} = (1 \pm \gamma^5)\psi$ .  
531 The  $SU(2)_L$  group is the special unitary group of  $2 \times 2$  matrices  $U$  satisfying  $UU^\dagger = I$   
532 and  $\det(U) = 1$ . It may be written in the form  $U = e^{-i\omega_i T_i}$ , with the generators of the  
533 group  $T_i = \frac{1}{2}\tau_i$  where  $\tau_i$ ,  $i \in 1,2,3$  being the  $2 \times 2$  Pauli matrices

$$\tau_1 = \begin{pmatrix} 0 & 1 \\ 1 & 0 \end{pmatrix} \quad \tau_2 = \begin{pmatrix} 0 & -i \\ i & 0 \end{pmatrix} \quad \tau_3 = \begin{pmatrix} 1 & 0 \\ 0 & -1 \end{pmatrix}, \quad (2.7)$$

- 534 which form a non Abelian group obeying the commutation relation  $[T^a, T^b] \equiv if^{abc}T^c \neq 0$ .  
535 The gauge fields that accompany this group are represented by  $\hat{W}_\mu = (\hat{W}_\mu^1, \hat{W}_\mu^2, \hat{W}_\mu^3)$   
536 and act only on the left handed component of the fermion field  $\psi_L$ .  
537 One additional generator  $Y$  which represents the hypercharge of the particle under  
538 consideration is introduced through the  $U(1)_Y$  group acting on both components of the  
539 fermion field, with an associated vector boson field  $\hat{B}_\mu$ .  
540 The  $SU(2)_L \times U(1)_Y$  transformations of the left and right handed components of  $\psi$  are  
541 summarised by,

$$\begin{aligned} \chi_L &\rightarrow \chi'_L = e^{i\theta(x) \cdot T + i\theta(x)Y} \chi_L, \\ \psi_R &\rightarrow \psi'_R = e^{i\theta(x)Y} \psi_R, \end{aligned} \quad (2.8)$$

<sup>542</sup> where the left handed fermions form isospin doubles  $\chi_L$  and the right handed fermions  
<sup>543</sup> are isosinglets  $\psi_R$ . For the first generation of leptons and quarks this represents

$$\chi_L = \begin{pmatrix} \nu_e \\ e \end{pmatrix}_L, \quad \begin{pmatrix} u \\ d \end{pmatrix}_L, \\ \psi_R = e_R, \quad u_R, d_R. \quad (2.9)$$

<sup>544</sup> Imposing local gauge invariance within  $\mathcal{L}_{EWK}$  is once again achieved by modifying the  
<sup>545</sup> covariant derivative

$$D_\mu = \partial_\mu - \frac{ig}{2}\tau^i W_\mu^i - \frac{ig'}{2}YB_\mu, \quad (2.10)$$

<sup>546</sup> where  $g$  and  $g'$  are the coupling constant of the  $SU(2)_L$  and  $U(1)_Y$  groups respectively.  
<sup>547</sup> Taking the example of the first generation of fermions defined in Equation.(2.9), with input  
<sup>548</sup> hypercharge values of -1 and -2 for  $\chi_L$  and  $e_R$  respectively, would lead to a Lagrangian  
<sup>549</sup>  $\mathcal{L}_1$  of the form,

$$\mathcal{L}_1 = \bar{\chi}_L \gamma^\mu [i\partial_\mu - g \frac{1}{2} \tau \cdot W_\mu - g' (-\frac{1}{2}) B_\mu] \chi_L \\ + \bar{e}_R \gamma^\mu [i\partial_\mu - g' (-1) B_\mu] e_R - \frac{1}{4} W_{\mu\nu} \cdot W^{\mu\nu} - \frac{1}{4} B_{\mu\nu} B^{\mu\nu}. \quad (2.11)$$

<sup>550</sup> As in QED, these additional gauge fields introduce field strength tensors  $B_{\mu\nu}$  and  $W_{\mu\nu}$ ,

$$\hat{B}_{\mu\nu} = \partial_\mu \hat{B}_\nu - \partial_\nu \hat{B}_\mu \quad (2.12)$$

$$\hat{W}_{\mu\nu} = \partial_\mu \hat{W}_\nu - \partial_\nu \hat{W}_\mu - g \hat{W}_\mu \times \hat{W}_\mu \quad (2.13)$$

<sup>551</sup> corresponding to the kinetic energy and self coupling of the  $W_\mu$  fields and the kinetic  
<sup>552</sup> energy term of the  $B_\mu$  field.

- 553 None of these gauge bosons are physical particles, and instead linear combinations of  
 554 these gauge bosons make up  $\gamma$  and the W and Z bosons, defined as

$$W^\pm = \frac{1}{\sqrt{2}} (W_\mu^1 \mp iW_\mu^2), \quad \begin{pmatrix} Z_\mu \\ A_\mu \end{pmatrix} = \begin{pmatrix} \cos\theta_W & -\sin\theta_W \\ \sin\theta_W & \cos\theta_W \end{pmatrix} \begin{pmatrix} W_\mu^3 \\ B_\mu \end{pmatrix}, \quad (2.14)$$

- 555 where the mixing angle,  $\theta_w = \tan^{-1} \frac{g'}{g}$ , relates the coupling of the neutral weak and  
 556 electromagnetic interactions.

557 As in the case of the formulation of the QED Lagrangian there remains no mass term for  
 558 the photon. However this is also the case for the W, Z and fermions in the Lagrangian,  
 559 contrary to experimental measurement. Any explicit introduction of mass terms would  
 560 break the symmetry of the Lagrangian and instead mass terms can be introduced through  
 561 spontaneous breaking of the EWK symmetry via the Higgs mechanism.

562 The Higgs mechanism induces spontaneous symmetry breaking through the introduction  
 563 of a complex scalar SU(2) doublet field  $\phi$  which attains a non-zero Vacuum Expectation  
 564 Value (VEV) [17][18][19][20].

$$\phi = \begin{pmatrix} \phi^+ \\ \phi^0 \end{pmatrix} \quad \text{with} \quad \begin{aligned} \phi^+ &\equiv (\phi_1 + i\phi_2)/\sqrt{2} \\ \phi^0 &\equiv (\phi_3 + i\phi_4)/\sqrt{2} \end{aligned} \quad (2.15)$$

- 565 The Lagrangian defined in Equation (2.11) attains an additional term  $\mathcal{L}_{Higgs}$  of the form

$$\mathcal{L}_{Higgs} = \overbrace{(D_\mu\phi)^\dagger(D^\mu\phi)}^{\text{kinetic}} - \overbrace{\mu^2\phi^\dagger\phi - \lambda(\phi^\dagger\phi)^2}^{\text{potential } V(\phi)} \quad (\mu^2, \lambda) > 0 \in \mathbb{R},$$

$$\mathcal{L}_{SM} = \mathcal{L}_{EWK} + \mathcal{L}_{Higgs}, \quad (2.16)$$

- 566 where the covariant derivative  $D_\mu$  is that defined in Equation (2.10). The last two terms  
 567 of  $\mathcal{L}_{Higgs}$  correspond to the Higgs potential, in which real positive values of  $\mu^2$  and  $\lambda$  are  
 568 required to ensure the generation of masses for the bosons and leptons. The minimum of

569 this potential is found at  $\phi^\dagger \phi = \frac{1}{2}(\phi_1^2 + \phi_2^2 + \phi_3^2 + \phi_4^2) = \mu^2/\lambda = v^2$ , where  $v$  represents  
570 the **VEV**.

571 Defining the ground state of the  $\phi$  field to be consistent with the  $V(\phi)$  minimum, and  
572 then expanding around a ground state chosen to maintain an unbroken electromagnetic  
573 symmetry thus preserving a zero photon mass [21] leads to

$$\phi_0 = \sqrt{\frac{1}{2}} \begin{pmatrix} 0 \\ v \end{pmatrix}, \quad \phi(x) = e^{i\tau \cdot \theta(x)/v} \sqrt{\frac{1}{2}} \begin{pmatrix} 0 \\ v + h(x) \end{pmatrix}, \quad (2.17)$$

574 where the fluctuations from the vacuum  $\phi_0$  are parametrized in terms of four real fields,  
575  $\theta_1, \theta_2, \theta_3$  and  $h(x)$ .

576 Choosing to gauge away the three massless Goldstone boson fields by setting  $\theta(x)$  to  
577 zero and substituting  $\phi(x)$  back into kinetic term of  $\mathcal{L}_{Higgs}$  from Equation (2.16) leads  
578 to mass terms for the  $W^\pm$  and Z bosons

$$(D_\mu \phi)^\dagger (D^\mu \phi) = \frac{1}{2} (\partial_\mu h)^2 + \frac{g^2 v^2}{2} W_\mu^+ W^{-\mu} + \frac{v^2 g^2}{8 \cos^2 \theta_w} Z_\mu Z^\mu + 0 A_\mu A^\mu, \quad (2.18)$$

579 where the relations between the physical and electroweak gauge fields from Equation  
580 (2.14) are used. The  $W^\pm$  and Z boson masses can then be determined to be

$$M_W = \frac{1}{2} g v \quad M_Z = \frac{1}{2} \frac{g v}{\cos \theta_w}. \quad (2.19)$$

581 This mechanism is also used to generate fermion masses by introducing a Yukawa coupling  
582 between the fermions and the  $\phi$  field [22], with the coupling strength of a particle to  
583 the  $\phi$  field governing its mass. Additionally a scalar boson  $h$  with mass  $m_h = v \sqrt{\frac{\lambda}{2}}$ , is  
584 also predicted as a result of this spontaneous symmetry breaking and became known as  
585 the Higgs boson. Its discovery by the CMS and ATLAS experiments in 2012 is the first  
586 direct evidence to support this method of mass generation within the SM.

## 587 2.2. Motivation for Physics Beyond the Standard 588 Model

589 As has been described, the **SM** has proven to be a very successful theory, predicting the  
590 existence of the  $W^\pm$  and  $Z$  bosons and the top quark long before they were experimentally  
591 observed. However the theory does not accurately describe all observed phenomena and  
592 has some fundamental theoretical flaws that hint at the need for additional extensions to  
593 the current theory.

594 On a theoretical level, the **SM** is unable to incorporate the gravitational interactions of  
595 fundamental particles within the theory. Whilst at the electroweak energy scales the  
596 relative strength of gravity is negligible compared to the other three fundamental forces,  
597 at much higher energy scales,  $M_{\text{planck}} \sim 10^{18} \text{GeV}$ , quantum gravitational effects become  
598 increasingly dominant. The failure to reconcile gravity within the **SM**, demonstrates that  
599 the **SM** must become invalid at some higher energy scale.

600 Other deficiencies with the **SM** include the fact that the predicted rate of Charge-Parity  
601 violation does not account for the matter dominated universe which we inhabit, and  
602 that the **SM** prediction of a massless neutrino conflicts with the observation of neutrino  
603 flavour mixing, attributed to mixing between neutrino mass eigenstates [23][24].

604 Perhaps one of the most glaring gaps in the predictive power of the **SM** is that there  
605 exists no candidate to explain the cosmic dark matter observed in galactic structures  
606 through indirect techniques including gravitational lensing and measurement of the  
607 orbital velocity of stars at galactic edges. Any such candidate must be very weakly  
608 interacting but must also be stable, owing to the lack of direct detection of the decay  
609 products of such a process. Therefore a stable dark matter candidate, is one of the  
610 main obstacles to address for any Beyond Standard Model (**BSM**) physics model.

611 The recent discovery of the Higgs boson whilst a significant victory for the predictive  
612 power of the **SM**, brings with it still unresolved questions. This issue is commonly  
613 described as the “hierarchy problem”.

614 In the absence of new physics between the TeV and Planck scale, calculating beyond  
615 tree-level contributions to the Higgs mass term given by its self interaction, result in  
616 divergent terms that push the Higgs mass up to the planck mass  $M_{\text{planck}}$ .

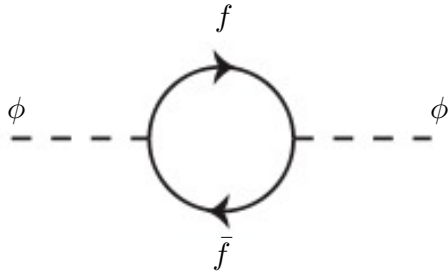


**Figure 2.1.:** One loop quantum corrections to the Higgs squared mass parameter  $m_h^2$  due to a fermion.

617 This can be demonstrated by considering the one loop quantum correction to the Higgs  
 618 mass with a fermion  $f$ , shown in Figure 2.1 with mass  $m_f$ . The Higgs field couples to  $f$   
 619 with a term in the Lagrangian  $-\lambda_f h \bar{f} f$ , yielding a correction of the form [25],

$$\delta m_h^2 = -\frac{|\lambda_f|^2}{8\pi^2} \Lambda^2 + \dots, \quad (2.20)$$

620 where  $\lambda_f$  represents the coupling strength for each type of fermion  $\propto m_f$ , and  $\Lambda$  the  
 621 cutoff energy scale at which the **SM** ceases to be a valid theory.

622 To recover the mass of the now discovered Higgs boson would require a fine-tuning of  
 623 the parameters to cancel out these mass corrections of the Higgs mass to the scale of  
 624 30 orders of magnitude. This appears as an unnatural solution to physicists and it is  
 625 this hierarchy problem that provides one of the strongest motivations for the theory of  
 626 SUperSYmmetry (**SUSY**).

### 627 2.3. Supersymmetry Overview

628 Supersymmetry provides potential solutions to many of the issues raised in the previous  
 629 section. It provides a dark matter candidate, can explain baryogenesis in the early  
 630 universe and also provides an elegant solution to the hierarchy problem [26][27][28][29].  
 631 At its heart it represents a new space-time symmetry that relates fermions and bosons.  
 632 This symmetry converts bosonic states into fermionic states, and vice versa, see Equation  
 633 (2.21) ,

$$Q|\text{Boson}\rangle = |\text{Fermion}\rangle \quad Q|\text{Fermion}\rangle = |\text{Boson}\rangle, \quad (2.21)$$

634 where the operator  $Q$  is the generator of these transformations. Quantum field theories  
 635 which are invariant under such transformations are called supersymmetric.

636 This symmetry operator therefore acts upon a particles spin altering it by a half integer  
 637 value. The consequences of the application of this additional space-time symmetry  
 638 introduce a new rich phenomenology. For example in supersymmetric theories, both  
 639 the left handed  $SU(2)$  doublet and right handed singlet of fermions will have a spin-0  
 640 superpartner, containing the same electric charge, weak isospin, and colour as its **SM**  
 641 partner. In the case of leptons  $(\nu_l, l)_L$ , they will have two superpartners, a sneutrino  $\tilde{\nu}_l{}_L$   
 642 and a slepton  $\tilde{l}_L$ , whilst the singlet  $l_R$  also has a superpartner slepton  $\tilde{l}_R$ .

643 Each particle in a supersymmetric theory is paired together with their superpartners as  
 644 a result of these supersymmetric transformations in a so called supermultiplet. These  
 645 superpartners will then consequently also contribute to the corrections to the Higgs mass.  
 646 Bosonic and fermionic loops contributing to the correction appear with opposite signs,  
 647 and therefore cancellation of these divergent terms will stabilise the Higgs mass, solving  
 648 the hierarchy problem [30][31].

649 One of the simplest forms of **SUSY**, is to simply have a set of **SM** supersymmetric  
 650 partners with the same mass and interactions as their counterparts. However the current  
 651 lack of any experimental evidence for that predicted sparticle spectrum implies **SUSY**  
 652 must be a broken symmetry in which any sparticle masses must be greater than their  
 653 **SM** counterparts.

654 There exist many techniques which can induce supersymmetric breaking [32][33][34]. Of  
 655 particular interest to experimental physicists are those at which the breaking scale is  
 656 of an order that is experimentally accessible to the **LHC** i.e.  $\sim$  TeV scale. Whilst  
 657 there is no requirement for supersymmetric breaking to occur at this energy scale, for  
 658 supersymmetry to provide a solution to the hierarchy problem, it is necessary for this  
 659 scale to not differ too drastically from the **EWK** scale [35][36].

### 660 2.3.1. R-Parity

661 Some supersymmetric theories also present a solution to the dark matter problem. These  
 662 theories contain a Lightest Supersymmetric Partner (**LSP**), which matches the criteria  
 663 of a Weakly Interacting Massive Particle (**WIMP**) required by cosmological observation  
 664 when R-parity is conserved.

665 Baryon (B) and Lepton (L) number conservation is forbidden in the **SM** by renormal-  
 666 isability requirements. The violation of Baryon or Lepton number results in a proton  
 667 lifetime much shorter than those set by experimental limits [37]. Another symmetry  
 668 called R-parity is then often introduced to **SUSY** theories to maintain baryon and lepton  
 669 conservation.

670 R-parity is described by the equation

$$R_P = (-1)^{3(B-L)+2s}, \quad (2.22)$$

671 where s represents the spin of the particles.  $B = \pm \frac{1}{3}$  for quarks/antiquarks and  $B = 0$   
 672 for all others,  $L = \pm 1$  for leptons/antileptons,  $L = 0$  for all others.

673 R-parity ensures the stability of the proton in **SUSY** models, and also has other conse-  
 674 quences for the production and decay of supersymmetric particles. In particle colliders  
 675 supersymmetric particles can only be pair produced, and similarly the decay of any pro-  
 676 duced supersymmetric particle is restricted to a **SM** particle and a lighter supersymmetric  
 677 particle as allowed by conservation laws. A further implication of R-parity is that once a  
 678 supersymmetric particle has decayed to the **LSP** it remains stable, unable to decay into  
 679 a **SM** particle.

680 A **LSP** will not interact in a detector at a particle collider, leaving behind a missing  
 681 energy  $\cancel{E}_T$  signature. The assumption of R-parity and its consequences are used to  
 682 determine the physical motivation and search strategies for **SUSY** models at the **LHC**.

### 683 2.4. Experimental Signatures of **SUSY** at the **LHC**

684 Should strongly interacting sparticles be within the experimental reach of the **LHC**, then  
 685 it is expected that they can be produced in a variety of ways :

- 686     • squark/anti-squark and gluino pairs can be produced via both gluon fusion and  
687        quark/anti-quark scattering,
- 688     • a gluino and squark produced together via quark-gluon scattering,
- 689     • squark pairs produced via quark-quark scattering.

690 Whilst most **SUSY** searches invoke the requirement of R-parity to explore parameter  
691 phase space, there still exist a whole plethora of possible **SUSY** model topologies which  
692 could be waiting to be discovered at the **LHC**.

693 During the 2011 run period at  $\sqrt{s} = 7$  TeV, particular models were used to benchmark  
694 performance and experimental reach of both **CMS** searches and previous experiments.  
695 The Compressed Minimal SuperSymmetric Model (**CMSSM**) was initially chosen for  
696 a number of reasons [38], one of the most compelling being the reduction of the up to  
697 105 new parameters that can be introduced by **SUSY** (in addition to the existing 19 of  
698 the **SM**), to just 5 free extra free parameters. It was this simplicity, combined with the  
699 theory not requiring any fine tuning of particle masses to produce experimentally verified  
700 **SM** observables that made it an attractive model to interpret physics results.

701 However recent results from the **LHC** now strongly disfavour large swathes of **CMSSM**  
702 parameter space [39][40][41]. In the face of such results a more pragmatic model indepen-  
703 dent search strategy is now applied across most **SUSY** searches at the **LHC**, see Section  
704 (2.4.1).

705 As previously stated, a stable **LSP** that exhibits the properties of a dark matter candidate  
706 would be weakly interacting and therefore will not be directly detected in a detector  
707 environment. Additionally the cascade decays of supersymmetric particles to this **LSP**  
708 state would also result in significant hadronic activity. These signatures will then be  
709 characterised through large amounts of hadronic jets (see Section (3.3.1)), leptons and  
710 a significant amount of missing energy dependent upon the size of the mass splitting  
711 between the **LSP** and the supersymmetric particle it has decayed from.

712 The **SM** contains processes which can exhibit a similar event topology to that described  
713 above. The largest contribution coming from the general QCD environment of a hadron  
714 collider. A multitude of different analytical techniques are used by experimental physicists  
715 to reduce or estimate any reducible or irreducible backgrounds, allowing a possible **SUSY**  
716 signature to be extracted. The techniques employed within this thesis are described in  
717 great detail within Section (4.1).

### 718 2.4.1. Simplified models

719 With such a variety of different ways for a **SUSY** signal to manifest itself, it is necessary  
720 to be able to interpret experimental reach through the masses of gluinos and squarks  
721 which can be excluded by experimental searches rather than on a model specific basis.

722 This is accomplished through **SMS** models, which are defined by a set of hypothetical  
723 particles and a sequence of their production and decay modes [42][43]. In the **SMS** models  
724 considered within this thesis, only the production process for the two primary particles  
725 are considered. Each primary particle can undergo a direct or a cascade decay through  
726 an intermediate new particle. At the end of each decay chain there remains a neutral,  
727 undetected **LSP** particle, denoted  $\tilde{\chi}_{LSP}$  which can represent a neutralino or gravitino.  
728 Essentially it is easier to consider each **SMS** with branching ratios set to 100%. The  
729 masses of the primary particle and the **LSP** remain as free parameters, in which the  
730 absolute value and relative difference between the primary and **LSP** particle alter the  
731 kinematics of the event.

732 Different **SMS** models are denoted with a T-prefix, with a summary of the types interpreted  
733 within this thesis listed below [44].

- 734 • **T1,T1xxxx**, models represent a simplified version of gluino pair production with  
735 each gluino (superpartner to the gluon) undergoing a three-body decay to a quark-  
736 antiquark pair and the **LSP** (i.e.  $\tilde{g} \rightarrow q\bar{q}\tilde{\chi}_{LSP}$ ). The resultant final state from this  
737 decay is typically 4 jets +  $\cancel{E}_T$  in the absence of initial/final state radiation and  
738 detector effects. xxxx denotes models in which the quarks are of a specific flavour,  
739 typically t or b quark-antiquarks.
- 740 • **T2,T2xx**, models represent a simplified version of squark anti-squark production  
741 with each squark undergoing a two-body decay into a light-flavour quark and **LSP**  
742 (i.e.  $\tilde{q} \rightarrow q\tilde{\chi}_{LSP}$ ). This results in final states with less jets than gluino mediated  
743 production, typically 2 jets +  $\cancel{E}_T$  when again ignoring the effect of initial/final state  
744 radiation and detector effects. xx models represent decays in which both the quark  
745 and the squark within the decay is of a specific flavour, which in this thesis are  
746 again  $\tilde{t}/t$  or  $\tilde{b}/b$ .

747 Models rich in b and t quarks are interpreted within this thesis as they remain of  
748 particular interest within “Natural **SUSY**” scenarios [45][46]. The largest contribution  
749 to the quadratic divergence in the Higgs mass parameter comes from a loop of top  
750 quarks via the Yukawa coupling. Cancellation of these divergences can be achieved in

<sup>751</sup> supersymmetric theories by requiring a light right handed top squark,  $\tilde{t}_R$ , and left-handed  
<sup>752</sup> double  $SU(2)_L$  doublet containing top and bottom squarks,  $(\tilde{\tilde{t}}_b)_L$  [47].

<sup>753</sup> These theories therefore solve the hierarchy problem by predicting light  $\sim$  EWK scale  
<sup>754</sup> third generation sleptons, to be accessible at the LHC. Search strategies involving the  
<sup>755</sup> requirement of b-tagging (see Section (3.3.2)) are used to give sensitivity to these type of  
<sup>756</sup> SUSY scenarios and are discussed in greater detail within Chapter 4.

<sup>757</sup> Two example decay chains are shown in Figure 2.2; the pair production of gluinos (T1)  
<sup>758</sup> and the pair production of squarks (T2) decaying into SM particles and LSP's.

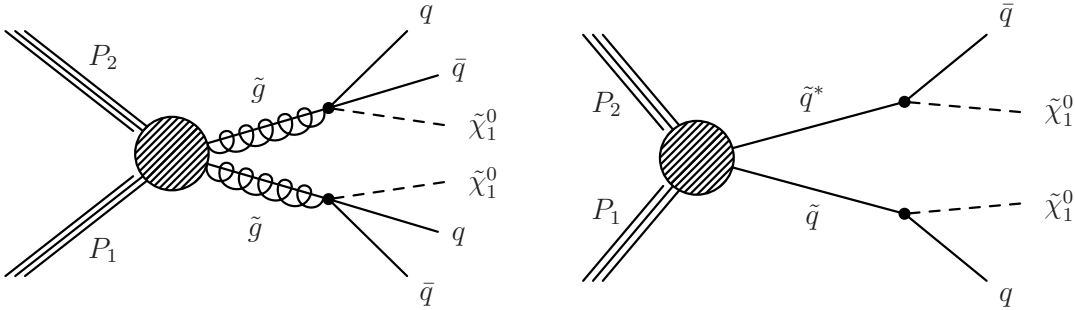


**Figure 2.2.:** Two example SMS model decays (T1 (left), T2 (right)), which are used in interpretations of physics reach by CMS.

# Chapter 3.

## <sup>759</sup> The LHC And The CMS Detector

<sup>760</sup> Probing the SM for signs of new physics would not be possible without the immensely  
<sup>761</sup> complex electronics and machinery that makes the TeV energy scale accessible to physi-  
<sup>762</sup> cists for the first time. This chapter will introduce both the LHC based at European  
<sup>763</sup> Organization for Nuclear Research (CERN) and the Compact Muon Solenoid (CMS)  
<sup>764</sup> detector (of which the author is a member). Section (3.2) serves to present an overview of  
<sup>765</sup> the different components of the CMS detector, with specific components relevant to the  
<sup>766</sup> search for supersymmetric particles described in greater detail. Section (3.3) will focus on  
<sup>767</sup> event and object reconstruction again with more emphasis on jet level quantities which  
<sup>768</sup> are most relevant to the author’s analysis research. Finally Section (3.4) will describe and  
<sup>769</sup> detail the service work for the CMS Collaboration performed by the author, in measuring  
<sup>770</sup> the performance of L1 single jet triggers in the Global Calorimeter Trigger (GCT) during  
<sup>771</sup> the 2012-2013 run period.

### <sup>772</sup> 3.1. The LHC

<sup>773</sup> The LHC is a storage ring, accelerator, and collider of circulating beams of protons or ions.  
<sup>774</sup> Housed in the tunnel dug for Large Electron-Positron Collidor (LEP), it is approximately  
<sup>775</sup> 27 km in circumference, 100 m underground, and straddles the border between France  
<sup>776</sup> and Switzerland outside of Geneva. It is currently the only collider in operation that  
<sup>777</sup> is able to study physics at the TeV scale. A double-ring circular synchrotron, it was  
<sup>778</sup> designed to collide both proton-proton (pp) and heavy ion (PbPb) with a centre of mass  
<sup>779</sup> energy  $\sqrt{s} = 14$  TeV at a final design luminosity of  $10^{34}\text{cm}^{-2}\text{s}^{-1}$ .

<sup>780</sup>

These counter-circulating beams of protons or Pb ions are merged in four sections around the ring to enable collisions of the beams, with each interaction point being home to one of the four major experiments; A Large Ion Collider Experiment (**ALICE**) [48] , A Toroidal LHC ApparatuS (**ATLAS**) [49], Compact Muon Solenoid (**CMS**) [50] and Large Hadron Collider Beauty (**LHCb**) [51] which record the resultant collisions. The layout of the **LHC** ring is shown in Figure 3.1. The remaining four sections contain acceleration, collimation and beam dump systems. In the eight arc sections, the beams are steered by magnetic fields of up to 8 T provided by super conduction dipole magnets, which are maintained at temperatures of 2 K using superfluid helium. Additional magnets for focusing and corrections are also present in straight sections within the arcs and near the interaction regions where the detectors are situated.

792

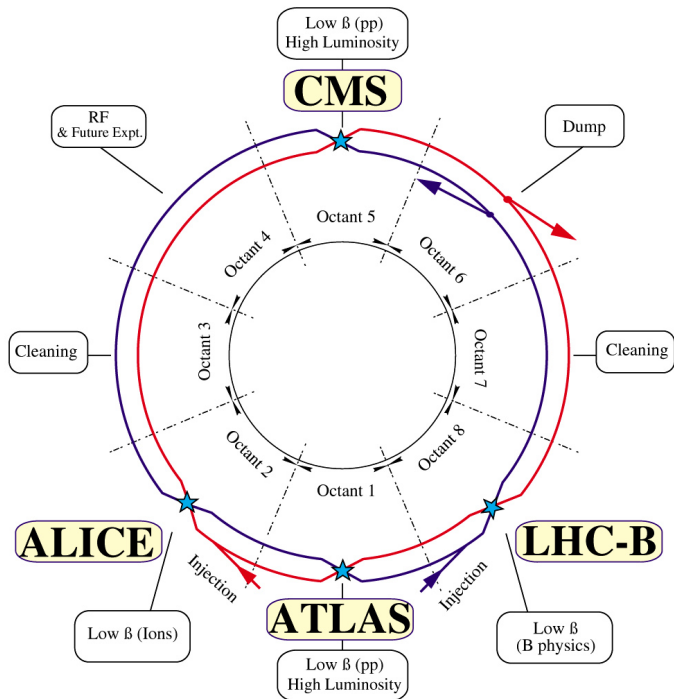


**Figure 3.1.:** A top down layout of the LHC. [52], with the position of the four main detectors labelled.

Proton beams are formed inside the Proton Synchrotron (**PS**) from bunches of protons 50 ns apart with an energy of 26 GeV. The protons are then accelerated in the Super Proton Synchrotron (**SPS**) to 450 GeV before being injected into the **LHC**. These **LHC** proton beams consists of many “bunches” (i.e. approximately  $1.1 \times 10^{11}$  protons localised into less than 1 ns in the direction of motion). Before collision, the beams are ramped to

798 4 TeV (2012) per beam in a process involving increasing the current passing through the  
 799 dipole magnets. Once the desired  $\sqrt{s}$  energy is reached then the beams are allowed to  
 800 collide at the interaction points. The luminosity falls regularly as the run progresses as  
 801 protons are lost in collisions, and eventually the beam is dumped before repeating the  
 802 process again.

803

804 Colliding the beams produced an instantaneous luminosity of approximately  $5 \times 10^{33}$   
 805  $\text{cm}^{-2}\text{s}^{-1}$  during the 2012 run. The high number of protons in each bunch increases  
 806 the likelihood of multiple interactions with each crossing of the counter-circulating  
 807 beams. This leads to isotropic energy depositions within the detectors positioned at these  
 808 interaction points, increasing the energy scale of the underlying event. This is known as  
 809 pile-up and the counteracting of it's effects are important to the many measurements  
 810 performed at the **LHC**.

811 In the early phase of prolonged operation after the initial shutdown the machine operated  
 812 in 2010-2011 at 3.5 TeV per beam,  $\sqrt{s} = 7$  TeV, delivering  $6.13 \text{ fb}^{-1}$  of data [53]. During  
 813 the 2012-2013 run period, data was collected at an increased  $\sqrt{s} = 8$  TeV improving the  
 814 sensitivity of searches for new physics. Over the whole run period  $23.3 \text{ fb}^{-1}$  of data was  
 815 delivered, of which  $21.8 \text{ fb}^{-1}$  was recorded by the **CMS** detector as shown in Figure 3.2  
 816 [53]. A total of  $12 \text{ fb}^{-1}$  of 8 TeV certified data was collected by October 2012, and it is  
 817 this data which forms the basis of the results presented within this thesis.

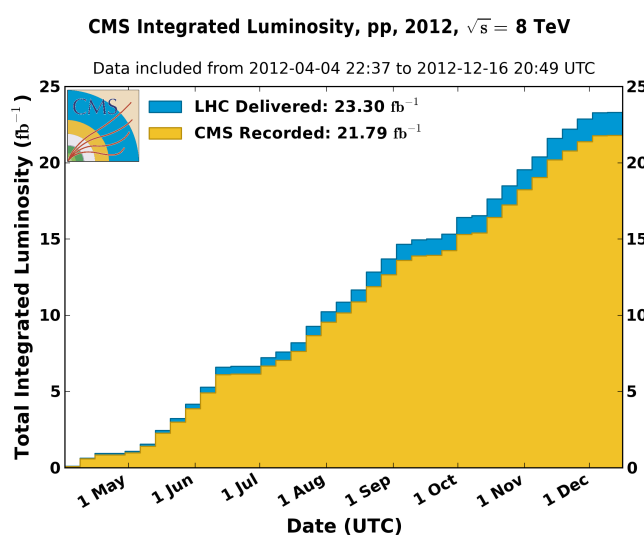


**Figure 3.2.:** The total integrated luminosity delivered to and collected by **CMS** during the 2012 8 TeV  $pp$  runs.

## 818 3.2. The CMS Detector

819 The Compact Muon Solenoid (**CMS**) detector is one of two general purpose detectors  
 820 at the **LHC** designed to search for new physics. The detector is designed to provide  
 821 efficient identification and measurement of many physics objects including photons,  
 822 electrons, muons, taus, and hadronic showers over wide ranges of transverse momentum  
 823 and direction. It's nearly  $4\pi$  coverage in solid angle allows for accurate measurement of  
 824 global transverse momentum imbalance. These design factors give **CMS** the ability to  
 825 search for direct production of **SUSY** particles at the TeV scale, making the search for  
 826 Supersymmetric particles one of the highest priorities among the wide range of physics  
 827 programmes at **CMS**.

828

829 **CMS** uses a right-handed Cartesian coordinate system with the origin at the interaction  
 830 point and the z-axis pointing along the beam axis, the x-axis points radially inwards to  
 831 the centre of the collider ring, with the y-axis points vertically upward. The azimuthal  
 832 angle,  $\phi$  ranging between  $[-\pi, \pi]$  is defined in the x-y plane starting from the x-axis. The  
 833 polar angle  $\theta$  is measured from the z axis. The common convention in particle physics is  
 834 to express an out going particle in terms of  $\phi$  and its pseudorapidity defined as

$$\eta = -\log \tan\left(\frac{\theta}{2}\right). \quad (3.1)$$

835 The variable  $\Delta R = \sqrt{\Delta\phi^2 + \Delta\eta^2}$  is commonly used to define angular distance between  
 836 objects within the detector and additionally energy and momentum is typically measured  
 837 in the transverse plane perpendicular to the beam line. These values are calculated  
 838 from the x and y components of the object and are denoted as  $E_T = E \sin \theta$  and  
 839  $p_T = \sqrt{p_x^2 + p_y^2}$ .

### 840 3.2.1. Detector subsystems

841 As the range of particles produced from  $pp$  collisions interact in different ways with  
 842 matter, **CMS** is divided into sub-detector systems, which perform complementary roles  
 843 to identify the identity, mass, and momentum of the different physics objects present in  
 844 each event. These detector sub-systems contained within **CMS** are wrapped in layers

845 around a central 13 m long 4 T super conducting solenoid as shown in Figure 3.3. With  
 846 the endcaps closed, CMS is a cylinder of length 22 m, diameter 15 m, and mass 12.5  
 847 kilotons. A more detailed complete description of the detector can be found elsewhere [50].  
 848

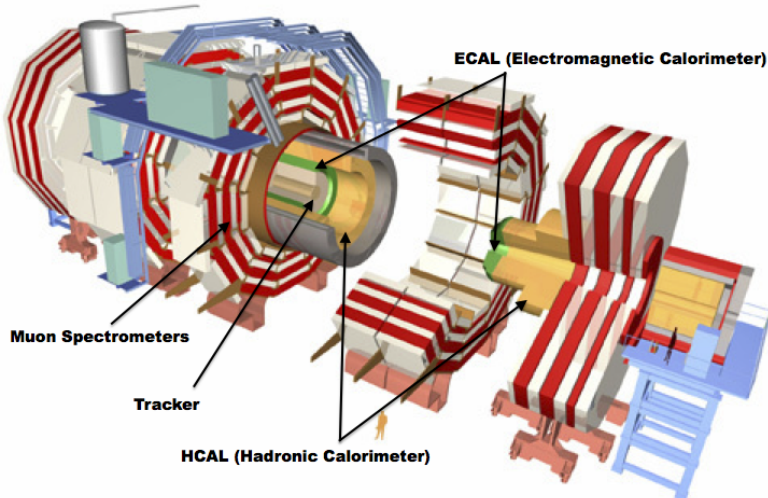


**Figure 3.3.:** A pictorial depiction of the CMS detector with the main detector subsystems labelled. [54]

### 849 3.2.2. Tracker

850 The inner-most sub-detector of the barrel is the multi-layer silicon tracker, formed of a  
 851 pixel detector component encased by layers of silicon strip detectors. The pixel detector  
 852 consists of three layers of silicon pixel sensors providing measurements of the momentum,  
 853 position coordinates of the charged particles as they pass, and the location of primary  
 854 and secondary vertices between 4 cm and 10 cm transverse to the beam. Outside the  
 855 pixel detector, ten cylindrical layers of silicon strip detectors extend the tracking system  
 856 out to a radius of 1.20 m from the beam line. The tracking system provides efficient  
 857 and precise determination of the charges, momenta, and impact parameters of charged  
 858 particles with the geometry of the tracker extending to cover a rapidity range up to  $|\eta| <$   
 859 2.5.

860

861 The tracking system also plays a crucial part in the identification of jets that originate  
 862 from b-quarks through the measurement of displaced secondary vertices. The methods  
 863 in which these b-flavoured jets are identified are discussed within Section (3.3.2). The

identification of b-jets is important in many searches for natural SUSY models and forms an important part of the inclusive search strategy described within Section (4.2).

### 3.2.3. Electromagnetic calorimeter

Immediately outside of the tracker, but still within the magnet core, sits the Electromagnetic CALorimeter (**ECAL**). Covering a pseudorapidity up to  $|\eta| < 3$  and comprising of over  $75 \times 10^3$  PbWO<sub>4</sub> (lead tungstate) crystals that scintillate as particles deposit energy, the **ECAL** provides high resolution measurements of the electromagnetic showers from photons and electrons in the detector.

872

Lead tungstate is used because of its short radiation length ( $X_0 \sim 0.9$  cm) and small Molieré radius ( $\sim 2.1$  cm) leading to high granularity and resolution. It's fast scintillation time ( $\sim 25$  ns) reduces the effects of pile-up, which occurs when energy from previous collisions are still being read out, and its radiation hardness gives it longevity. The crystals are arranged in modules which surround the beam line in a non-projective geometry, angled at  $3^\circ$  with respect to the interaction point to minimise the risk of particles escaping down the cracks between the crystals.

880

The **ECAL** is primarily composed of two sections, the Electromagnetic CALorimeter Barrel (**EB**) which extends in pseudo-rapidity to  $|\eta| < 1.479$  with a crystal front cross section of  $22 \times 22$  mm and a length of 230 mm corresponding to 25.8 radiation lengths, and the Electromagnetic CALorimeter Endcap (**EE**) covering a rapidity range of  $1.479 < |\eta| < 3.0$ , which consists of two identical detectors on either side of the **EB**. A lead-silicon sampling ‘pre-shower’ detector Electromagnetic CALorimeter pre-Shower (**ES**) is placed before the endcaps to aid in the identification of neutral pions. Their arrangement is shown in Figure 3.4.

889

Scintillation photons from the lead tungstate crystals are instrumented with Avalanche Photo-Diodes (**APD**) and Vacuum Photo-Triodes (**VPT**) located in the **EB** and **EE** respectively, converting the scintillating light into an electric signal which is consequently used to determine the amount of energy deposited within the crystal . These instruments are chosen for their resistance under operation to the strong magnetic field of **CMS**. The scintillation of the **ECAL** crystals as well as the response of the **APDs** varies as a function

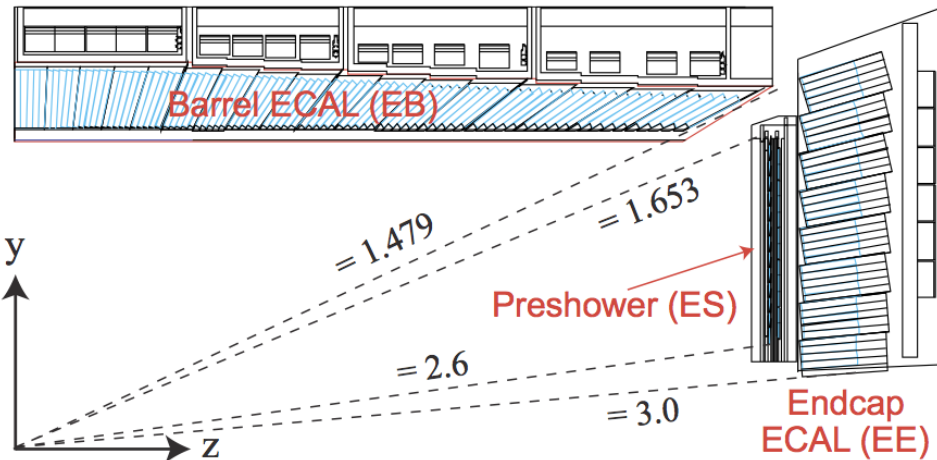


**Figure 3.4.:** Illustration of the **ECAL** showing the arrangement of the lead tungstate crystals in the **EB** and **EE**. The **ES** is also shown and is located in front of the **EE** [55].

896 of temperature and so cooling systems continually maintain an overall constant **ECAL**  
 897 temperature  $\pm 0.05^\circ\text{C}$ .

### 898 3.2.4. Hadronic calorimeter

899 Beyond the **ECAL** lies the Hadronic CALorimeter (**HCAL**) which is responsible for  
 900 the accurate measurement of hadronic showers, crucial for analyses involving jets or  
 901 missing energy signatures. The **HCAL** is a sampling calorimeter which consists of al-  
 902 ternating layers of brass absorber and plastic scintillator, except in the hadron forward  
 903 ( $3.0 < |\eta| < 5.0$ ) region in which steel absorbers and quartz fibre scintillators are used  
 904 because of their increased radiation tolerance. Hadron showers are initiated in the  
 905 absorber layers inducing scintillation in the plastic scintillator tiles. These scintillation  
 906 photons are converted by wavelength shifting fibres for read-out by hybrid photodiodes.  
 907

908 The **HCAL**'s size is constrained to a compact size by the presence of the solenoid, re-  
 909 quiring the placement of an additional outer calorimeter on the outside of the solenoid  
 910 to increase the sampling depth of the **HCAL**. A schematic of the **HCAL** can be seen in  
 911 Figure 3.5.

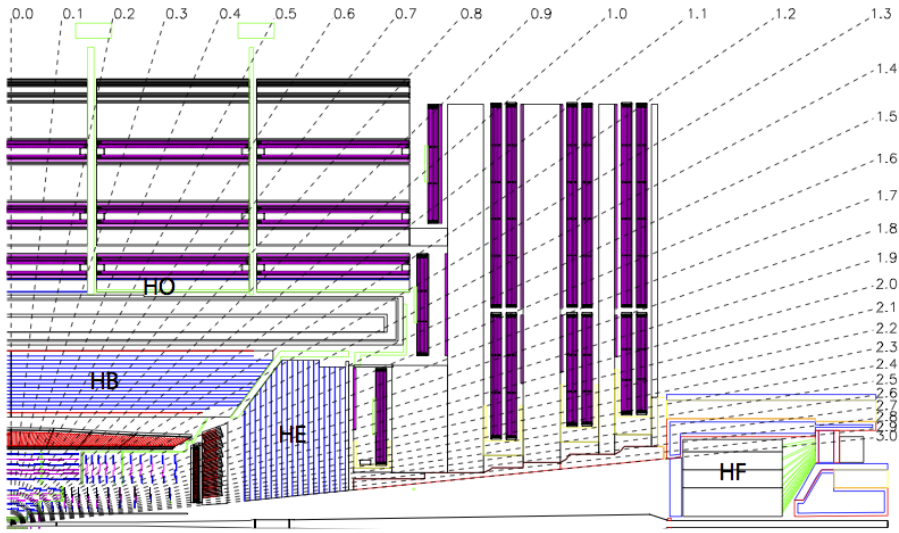


**Figure 3.5.:** Schematic of the hadron calorimeters in the r-z plane, showing the locations of the **HCAL** components and the **HF**. [50].

913 The **HCAL** covers the range  $|\eta| < 5$  and consists of four sub-detectors: the Hadron  
 914 Barrel (**HB**)  $|\eta| < 1.3$ , the Hadron Outer (**HO**), the Hadron Endcaps (**HE**)  $1.3 < |\eta| < 3.0$   
 915 and the Hadron Forward (**HF**). The **HB**, contained between the outer edge of the **ECAL**  
 916 and the inner edge of the solenoid is formed of 36 azimuthal wedges which are split  
 917 between two half-barrel segments. Each wedge is segmented into four azimuthal angle  
 918 ( $\phi$ ) sectors, and each half-barrel is further segmented into 16  $\eta$  towers. The electronic  
 919 readout chain, channels the light from the active scintillator layers from one  $\phi$ -segment  
 920 and all  $\eta$ -towers of a half-barrel to a Hybrid Photo Diode (**HPD**).

921 The relatively short number of interaction lengths ( $\lambda_l$ , the distance a hadron will travel  
 922 through the absorber material before it has lost  $\frac{1}{e}$  of its energy) within the **HB**, the lowest  
 923 being  $\lambda_l = 5.82$  at  $|\eta| = 0$ , facilitates the need for the ‘tail catching’ **HO** to increase the  
 924 sampling depth in the central barrel rapidity region  $|\eta| < 1.3$  to 11 interaction lengths .  
 925 Significant fractions of the hadrons energy will be deposited in the **ECAL** as it passed  
 926 through the detector. Therefore measurements of hadron energies in the central regions  
 927  $|\eta| < 3.0$  use both the **ECAL** and **HCAL** to reconstruct the true energy from showering  
 928 hadrons.

929 **3.2.5. Muon systems**

930 Muons being too massive to radiate away energy via Bremsstrahlung, interact little in  
931 the calorimeters and mostly pass through the detector until they reach the system of  
932 muon detectors which forms the outer most part of the CMS detector.

933 Outside of the superconducting solenoid are four muon detection layers interleaved with  
934 the iron return yokes which measure the muons energy via ionisation of gas within  
935 detector elements. Three types of gaseous chamber are used. The Drift Tube (DT),  
936 Cathode Stripe Chamber (CSC), and Resistive Plate Chamber (RPC) systems provide  
937 efficient detection of muons with pseudo-rapidity  $|\eta| < 2.4$ . The best reconstruction  
938 performance is obtained when the muon chamber is combined with the inner tracking  
939 information to determine muon trajectories and their momenta [56].

940

941 **3.3. Event Reconstruction and Object Definition**

942 The goal of event reconstruction is to take the raw information recorded by the detector  
943 and to compute from it higher-level quantities which can be used at an analysis level.  
944 These typically correspond to an individual particle’s energy and momenta, or groups of  
945 particles which shower in a narrow cone and the overall global energy and momentum  
946 balance of the event. The reconstruction of these objects are described in great detail in  
947 [57], however covered below are brief descriptions of those which are most relevant to the  
948 analysis detailed in Chapter 4.

949 **3.3.1. Jets**

950 Quarks and gluons are produced copiously at the LHC in the hard scattering of partons.  
951 As these quarks and gluons fragment, they hadronize and decay into a group of strongly  
952 interactive particles and their decay products. These streams of particles travel in the  
953 same direction, as they have been “boosted” by the momentum of the primary hadron.  
954 These collections of decay products are reconstructed and identified together as a “jet”.

955 At CMS jets are reconstructed from energy deposits in the detector using the anti-kt  
956 algorithm [58] with size parameter  $\Delta R = 0.5$ . The anti-kt jet algorithm clusters jets by  
957 defining a distance between hard (high  $p_T$ ) and soft (low  $p_T$ ) particles such that soft

958 particles are preferentially clustered with hard particles before being clustered between  
959 themselves. This produces jets which are robust to soft particle radiation from the pile-up  
960 conditions produced by the **LHC**.

961

962 There are two main type of jet reconstruction used at **CMS**, Calorimeter (Calo) and  
963 Particle Flow (PF) jets [59]. Calorimeter jets are reconstructed using both the **ECAL**  
964 and **HCAL** cells, combined into calorimeter towers . These calorimeter towers consist of  
965 geometrically matched **HCAL** cells and **ECAL** crystals. Electronics noise is suppressed by  
966 applying a threshold to the calorimeter cells, with pile-up effects reduced by a requirement  
967 placed on the tower energy [60]. Calorimeter jets are the jets used within the analysis  
968 presented in this thesis.

969 PF jets are formed from combining information from all of the **CMS** sub-detectors systems  
970 to determine which final state particles are present in the event. Generally, any particle  
971 is expected to produce some combination of a track in the silicon tracker, a deposit in  
972 the calorimeters, or a track in the muon system. The PF jet momentum and spatial  
973 resolutions are greatly improved with respect to calorimeter jets, as the use of the tracking  
974 detectors and of the high granularity of **ECAL** allows resolution and measurement of  
975 charged hadrons and photons inside a jet, which together constitute  $\sim 85\%$  of the jet  
976 energy [61].

977 The jets reconstructed by the clustering algorithm in **CMS** typically have an energy  
978 that differs to the ‘true’ energy measured by a perfect detector. This stems from the  
979 non-linear and nonuniform response of the calorimeters as well as other residual effects  
980 including pile-up and underlying events, and therefore additional corrections are applied  
981 to recover a uniform relative response as a function of pseudo-rapidity. These are applied  
982 as separate sub corrections [62].

- 983     • A pile-up correction is first applied to the jet. It subtracts the average extra energy  
984         deposited in the jet that comes from other vertices present in the event and is  
985         therefore not part of the hard jet itself.
- 986     •  $p_T$  and  $\eta$  dependant corrections derived from Monte Carlo simulations are used to  
987         account for the non-uniform response of the detector.
- 988     •  $p_T$  and  $\eta$  residual corrections are applied to data only to correct for difference  
989         between data and Monte Carlo. The residual is derived from QCD di-jet samples  
990         and the  $p_T$  residual from  $\gamma+$  jet and  $Z+$  jets samples in data.

---

### <sup>991</sup> 3.3.2. B-tagging

<sup>992</sup> The decays of b quarks are suppressed by small CKM matrix elements. As a result, the  
<sup>993</sup> lifetimes of b-flavoured hadrons, produced in the fragmentation of b quarks, are relatively  
<sup>994</sup> long;  $\mathcal{O}$  1ps. The identification of jets originating from b quarks is very important for  
<sup>995</sup> searches for new physics and for measurements of SM processes.

<sup>996</sup>

<sup>997</sup> Many different algorithms developed by CMS select b-quark jets based on variables such  
<sup>998</sup> as the impact parameters of the charged-particle tracks, the properties of reconstructed  
<sup>999</sup> decay vertices, and the presence or absence of a lepton, or combinations thereof [63]. One  
<sup>1000</sup> of the most efficient of which is the Combined Secondary Vertex (CSV) which operates  
<sup>1001</sup> based on secondary vertex and track-based lifetime information, benchmarked in ‘Loose’,  
<sup>1002</sup> ‘Medium’ and ‘Tight’ working points, of which the medium point is the tagger used  
<sup>1003</sup> within the  $\alpha_T$  search detailed in Section (4.1).

<sup>1004</sup> Using the CSV tagger, a likelihood-based discriminator distinguishes between jets from  
<sup>1005</sup> b-quarks, and those from charm or light quarks and gluons, which is shown in Figure 3.6.  
<sup>1006</sup> The minimum thresholds on the discriminator for each working point correspond to the  
<sup>1007</sup> mis-identification probability for light-parton jets of 10%, 1%, and 0.1%, respectively, in  
<sup>1008</sup> jets with an average  $p_T$  of about 80 GeV.

<sup>1009</sup> The b-tagging performance is evaluated to measure the b-jet tagging efficiency  $\epsilon_b$ , and the  
<sup>1010</sup> misidentification probability of charm  $\epsilon_c$  and light-parton jets  $\epsilon_s$ . The tagging efficiencies  
<sup>1011</sup> for each of these three jet flavours are compared between data and MC simulation, from  
<sup>1012</sup> which a series of  $p_T$  and  $|\eta|$  binned jet corrections are determined,

$$SF_{b,c,s} = \frac{\epsilon_{b,c,s}^{data}}{\epsilon_{b,c,s}^{MC}}. \quad (3.2)$$

<sup>1013</sup> These are collectively named ‘Btag Scale Factors’ and allow MC simulation to accu-  
<sup>1014</sup> rately reflect the running conditions and performance of the tagging algorithm in data.  
<sup>1015</sup> Understanding of the b-tagging efficiency is essential in order to minimise systematic  
<sup>1016</sup> uncertainties in physics analyses that employ b-tagging.

<sup>1017</sup>

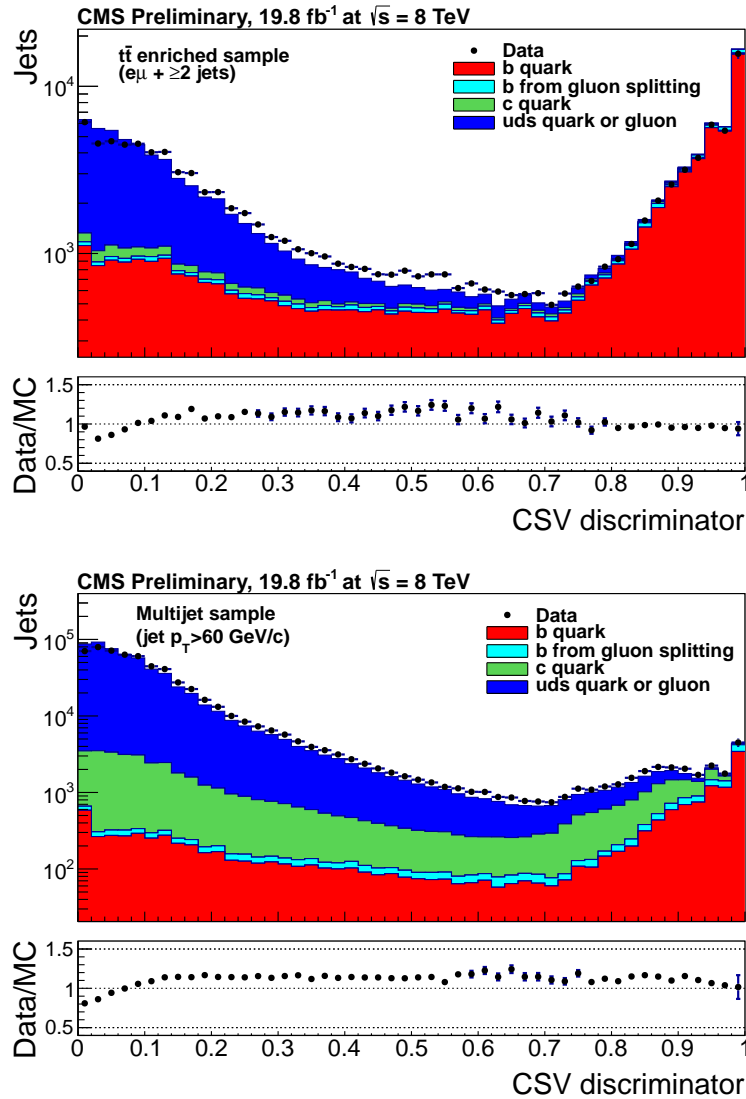


**Figure 3.6.:** CSV algorithm discriminator values in enriched  $t\bar{t}$  (top) and inclusive multi jet samples (bottom) for b,c and light flavoured jets [64]. The discriminator value used for each working points are determined from the misidentification probability for light-parton jets to be tagged as a b-jet, which are given as 0.244 (10%), 0.679 (1%) and 0.898 (0.1%) for the L, M and T working points respectively.

1018 The b-tagging efficiency is measured in data using several methods applied to multi  
 1019 jet events, primarily based on a sample of jets enriched in heavy flavour content. One  
 1020 method requires the collection of events with a soft muon within a cone  $\Delta R < 0.4$  around  
 1021 the jet axis. Because the semi-leptonic branching fraction of b hadrons is significantly  
 1022 larger than that for other hadrons, these jets are more likely to arise from b quarks than  
 1023 from another flavour, with the resultant momentum component of the muon transverse  
 1024 to the jet axis larger for muons from b-hadron decays than from light or charm jets.

1025 Additionally the performance of the tagger can also be benchmarked in  $t\bar{t}$  events where  
 1026 in the SM, the top quark is expected to decay to a W boson and a b quark about 99.8%  
 1027 of the time [1]. Further selection criteria is applied to these events to further enrich the  
 1028 b quark content of these events. The methods to identify b-jets in data are discussed  
 1029 in great detail at [65]. The jet flavours are determined in simulation using truth level  
 1030 information and are compared to data to determine the correction scale factors ( $SF_b$ ),  
 1031 which are displayed for the CSVM tagger in Figure 3.7.

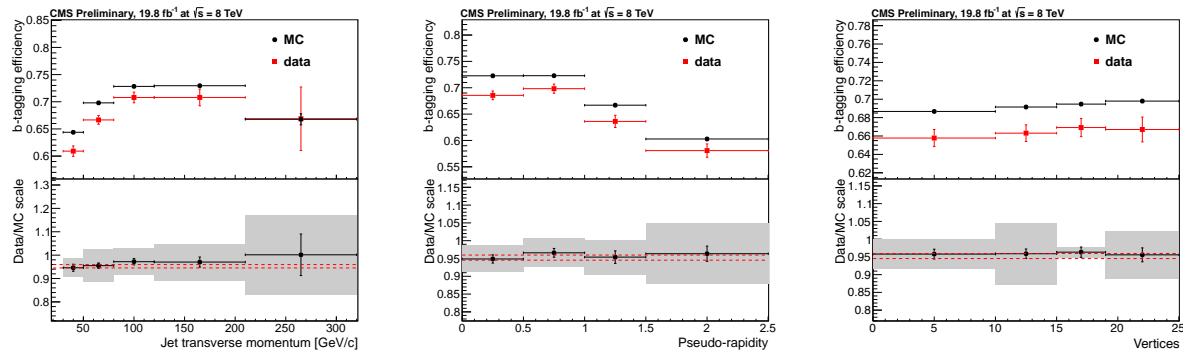


**Figure 3.7.:** Measured in  $t\bar{t} \rightarrow$  di-lepton events using the CSVM tagger: (upper panels) b-tagging efficiencies and (lower panels) data/MC scale factor  $SF_b$  as a function of (left) jet  $p_T$ , (middle) jet  $|\eta|$  and (right) number of primary vertices. In the lower panels, the grey filled areas represent the total statistical and systematic uncertainties, whereas the dotted lines are the average  $SF_b$  values within statistical uncertainties.

1032 The measurement of the misidentification probability for light-parton jets relies on the  
 1033 inversion of tagging algorithms, selecting non-b jets using the same variables and tech-  
 1034 niques used in benchmarking the b-tagging efficiency. The scale factors ( $SF_s$ ) to be  
 1035 applied to MC are shown in Figure 3.8 for the CSVM tagger.

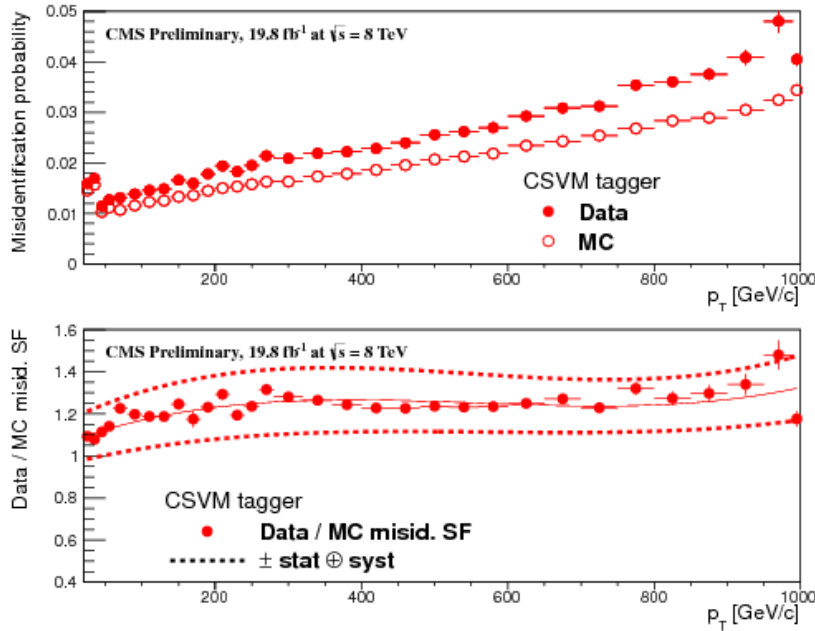


**Figure 3.8.:** For the **CSVM** tagging criterion: (top) misidentification probability in data (filled circles) and simulation (open circles); (bottom) scale factor for the misidentification probability. The last  $p_T$  bin in each plot includes all jets with  $p_T > 1000$  GeV. The solid curve is the result of a polynomial fit to the data points. The dashed curves represent the overall statistical and systematic uncertainties on the measurements.

## 1036 3.4. Triggering System

1037 With bunch crossings separated by just 25 ns, the rate at which data from all collisions  
 1038 would have to be written out and processed would be unfeasible. A two-tiered triggering  
 1039 system is applied at **CMS** in order to cope with the high collision rate of protons. The  
 1040 **CMS** trigger is designed to use limited information from each event to determine whether  
 1041 to record the event, reducing the rate of data taking to manageable levels whilst ensuring  
 1042 a high efficiency of interesting physics object events are selected.

1043 The **L1** is a pipelined, dead-timeless system based on custom-built electronics [66], and is  
 1044 a combination of several sub systems which is shown pictorially in Figure 3.9. The L1  
 1045 system is covered in more detail within the following section along with a description  
 1046 of the service work undertaken by the author to benchmark the performance of the L1  
 1047 calorimeter trigger during the 2012 8 TeV run period.

1048 The Higher Level Trigger (**HLT**) is a large farm of commercial computers [67]. The **HLT**  
 1049 processes events with software reconstruction algorithms that are more detailed, giving  
 1050 performance more similar to the reconstruction used offline. The **HLT** reduces the event

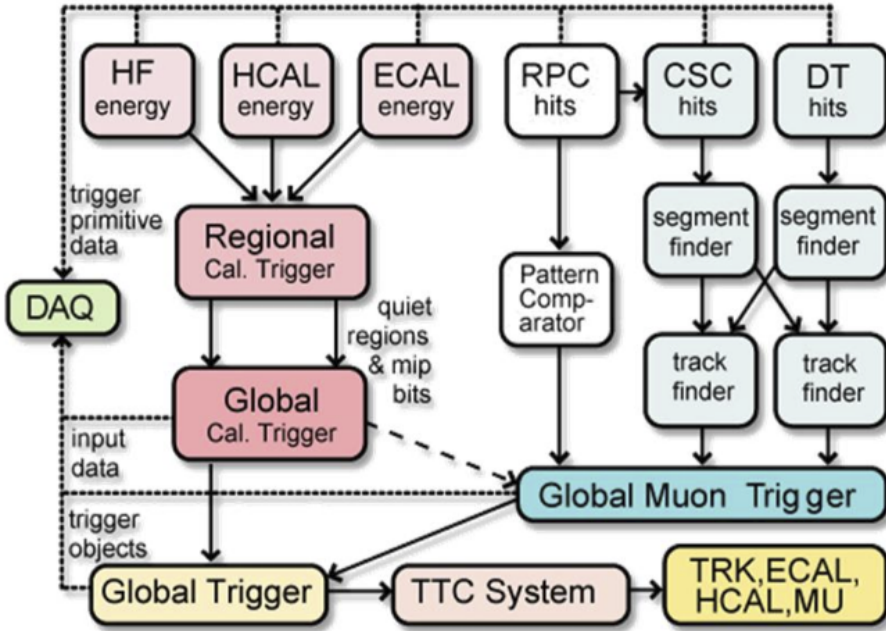


**Figure 3.9.:** The CMS L1 Trigger system.

1051 rate written to disk by a factor of  $\sim 500$  ( $\sim 200\text{Hz}$ ). The recorded events are transferred  
 1052 from CMS to the CERN computing centre, where event reconstruction is performed, and  
 1053 then distributed to CMS computing sites around the globe for storage and analysis.

### 1054 3.4.1. The Level-1 trigger

1055 The L1 trigger reduces the rate of events collected from 40 MHz to  $\sim 100\text{ kHz}$  using  
 1056 information from the calorimeters and muon chambers, but not the tracker. A tree  
 1057 system of triggers is used to decide whether to pass on an event to the HLT for further  
 1058 reconstruction. Firstly the calorimeter and muon event information is kept separate, with  
 1059 local reconstruction of objects ( $\mu$ ,  $e$ ,  $\gamma$ , and jets) performed by the Regional Calorimeter  
 1060 Trigger (RCT) and Regional Muon Trigger (RMT) respectively. The RCT generates up to  
 1061 72 isolated and non-isolated electromagnetic objects. These are sorted by rank, which is  
 1062 equivalent to transverse energy  $E_T$ , with the four highest ranked electromagnetic objects  
 1063 being passed via the Global Calorimeter Trigger (GCT) and Global MuonTrigger (GMT)  
 1064 to the Global Trigger (GT).

1065 In the L1 **GCT**, coarse measurements of the energy deposited in the electromagnetic and  
1066 hadronic calorimeters are combined, and by using sophisticated algorithms the following  
1067 physics objects are formed:

- 1068 • isolated and non-isolated electromagnetic objects ( $e$  and  $\gamma$ );
- 1069 • hadronic jets in the central and forward sections of the hadronic calorimeters;
- 1070 • hadronically decaying tau leptons;
- 1071 • total transverse energy ( $E_T$ ), the scalar sum of the energy measured at L1, and  
1072 missing transverse energy ( $\cancel{E}_T$ ), defined as the vector sum of the energy of L1  
1073 objects;
- 1074 • total transverse jet energy ( $H_T$ ), the scalar sum of the energy of all L1 jet objects,  
1075 and missing transverse jet energy ( $\cancel{H}_T$ ), defined as the vector sum of the energy of  
1076 L1 jets, are calculated from uncorrected L1 jets.

1077 In addition quantities suitable for triggering minimum bias events, forward physics and  
1078 beam background events are calculated. Additionally relevant muon isolation information  
1079 is also passed on to the **GMT** for decisions involving the muon triggers where it is  
1080 combined with information from across the three muon sub-systems. The resultant final  
1081 accept/reject decision at **L1** is then performed by the **GT** based on the objects received  
1082 from the **GCT** and **GMT** ( $e/\gamma$ ,  $\mu$ , jets,  $E_T$ ,  $\cancel{E}_T$ ,  $H_T$ ).

1083 The L1 trigger is therefore of upmost importance to the functioning of the detector.  
1084 Without a high-performing trigger and a good understanding of its performance, there  
1085 would be no data to analyse. Observations of how the L1 trigger performance is affected  
1086 by changing **LHC** running conditions over the 2012 run period and also the introduction  
1087 of a jet seed threshold to the L1 jet trigger algorithm is presented in the following Sections  
1088 (3.4.2 - 3.4.6).

### 1089 3.4.2. The L1 trigger jet algorithm

1090 The L1 jet trigger uses the transverse energy sums computed in the calorimeter (both  
1091 hadronic and electromagnetic) trigger regions. Each region consists of  $4 \times 4$  trigger tower  
1092 windows, spanning a region of  $\Delta\eta \times \Delta\phi = 0.087 \times 0.087$  in pseudorapidity-azimuth. The  
1093 jet trigger uses a  $3 \times 3$  calorimeter region (112 trigger towers) sliding window technique  
1094 which spans the full  $(\eta, \phi)$  coverage of the **CMS** calorimeter as shown in Figure 3.10.

1095 In forming a L1 jet is it required that the central region to be higher than the eight  
1096 neighbouring regions  $E_T$  central >  $E_T$  surround. Additionally a minimum threshold of 5 GeV  
1097 on  $E_T$  central was introduced during the 2012 run period to suppress noise from pile-up.  
1098 A comparison between these two configurations is shown in Section (3.4.4).

1099 The L1 jets are characterised by the  $E_T$ , summed over the  $3 \times 3$  calorimeter regions,  
1100 which corresponds to  $12 \times 12$  trigger towers in barrel and endcap or  $3 \times 3$  larger **HF**  
1101 towers in the **HF**. The  $\phi$  size of the jet window is the same everywhere, whilst the  $\eta$   
1102 binning gets somewhat larger at high  $\eta$  due to calorimeter and trigger tower segmentation.  
1103 The jets are labelled by the  $(\eta, \phi)$  indices of the central calorimeter region.

1104 Jets with  $|\eta| > 3.0$  are classified as forward jets, whereas those with  $|\eta| < 3.0$  are classified  
1105 as central. The four highest energy central, forward and  $\tau$  jets in the calorimeter are  
1106 passed through Look Up Table (**LUT**)’s, which apply a programmable  $\eta$ –dependent jet  
1107 energy scale correction. These are then used to make L1 trigger decisions.

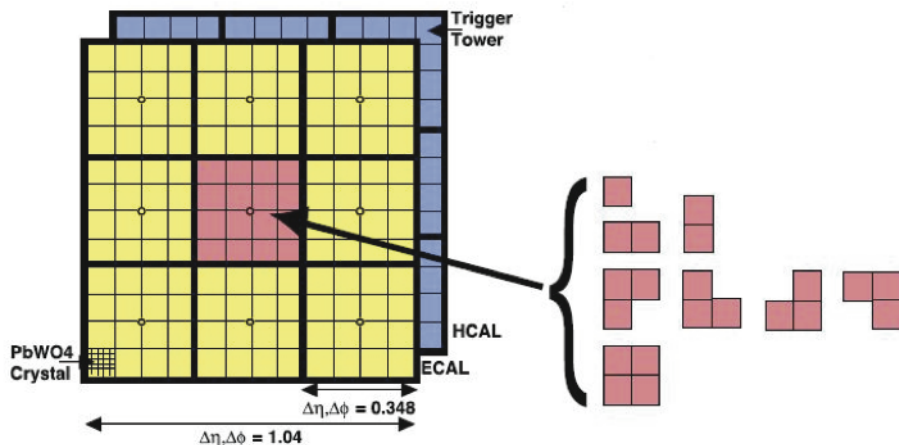


**Figure 3.10.:** Illustration of the Level-1 jet finding algorithm.

1108 The performance of the L1 jets is evaluated with respect to offline jets, which are taken  
1109 from the standard Calo jet and the PF jet reconstruction algorithms of **CMS**. Jets are  
1110 corrected for pile-up and detector effects as described in 3.3.1. A moderate level of noise  
1111 rejection is applied to the offline jets by selecting jets passing the “loose” identification  
1112 criteria for both Calo and PF. These jet criteria are listed in Appendix (A.1).

---

### <sup>1113</sup> 3.4.3. Measuring L1 jet trigger efficiencies

<sup>1114</sup> The L1 jet efficiency is defined as the fraction of leading offline jets which were matched  
<sup>1115</sup> with a L1 tau or central jet above a certain trigger threshold, divided by all the leading  
<sup>1116</sup> offline jets in the event. This quantity is then plotted as a function of the offline jet  $E_T$ ,  
<sup>1117</sup>  $\eta$  and  $\phi$ .

<sup>1118</sup> The efficiency is determined by matching the L1 and reconstructed offline jets spatially  
<sup>1119</sup> in  $\eta - \phi$  space. This is done by calculating the minimum separation in  $\Delta R$  between the  
<sup>1120</sup> highest offline reconstructed jet in  $E_T$  ( $E_T > 10$  GeV,  $|\eta| < 3$ ) and any L1 jet. A jet will  
<sup>1121</sup> be matched if this value is found to be  $< 0.5$ . Should more than one jet satisfy this, the  
<sup>1122</sup> jet closest in  $\Delta R$  is taken as the matched jet. The matching efficiency is close to 100%,  
<sup>1123</sup> above 30(45) GeV for run 2012B(C) data (see Appendix B.1).

<sup>1124</sup> Each efficiency curve is fitted with a function which is the cumulative distribution function  
<sup>1125</sup> of an Exponentially Modified Gaussian (EMG) distribution:

$$\text{<sup>1126</sup> } f(x; \mu, \sigma, \lambda) = \frac{\lambda}{2} \cdot e^{\frac{\lambda}{2}(2\mu + \lambda\sigma^2 - 2x)} \cdot \text{erfc} \left( \frac{\mu + \lambda\sigma^2 - x}{\sqrt{2}\sigma} \right) \quad (3.3)$$

where erfc is the complementary error function defined as:

$$\text{erfc}(x) = 1 - \text{erf}(x) = \frac{2}{\sqrt{\pi}} \int_x^\infty e^{-t^2} dt.$$

<sup>1127</sup> In this functional form, the parameter  $\mu$  determines the point of 50% of the plateau  
<sup>1128</sup> efficiency and the  $\sigma$  gives the resolution. This parametrisation is used to benchmark  
<sup>1129</sup> the efficiency at the plateau, the turn-on points and resolution for each L1 Jet trigger.  
<sup>1130</sup> The choice of function is purely empirical. Previous studies used the error function  
<sup>1131</sup> alone, which described the data well at high threshold values but could not describe the  
<sup>1132</sup> efficiencies well at lower thresholds [68].

<sup>1133</sup> The efficiency turn-on curves for various L1 jet thresholds are evaluated as a function of  
<sup>1134</sup> the offline reconstructed jet  $E_T$  for central jets with  $|\eta| < 3$ . These are measured using  
<sup>1135</sup> single isolated  $\mu$  triggers which have high statistics, and are orthogonal and therefore  
<sup>1136</sup> unbiased to the hadronic triggers under study. The efficiency is calculated with respect to  
<sup>1137</sup> offline Calo and PF Jets in Figure 3.11. Table 3.1 shows the values of these parameters,  
<sup>1138</sup> calculated for three example L1 single jet triggers taken from 2012 8 TeV data.

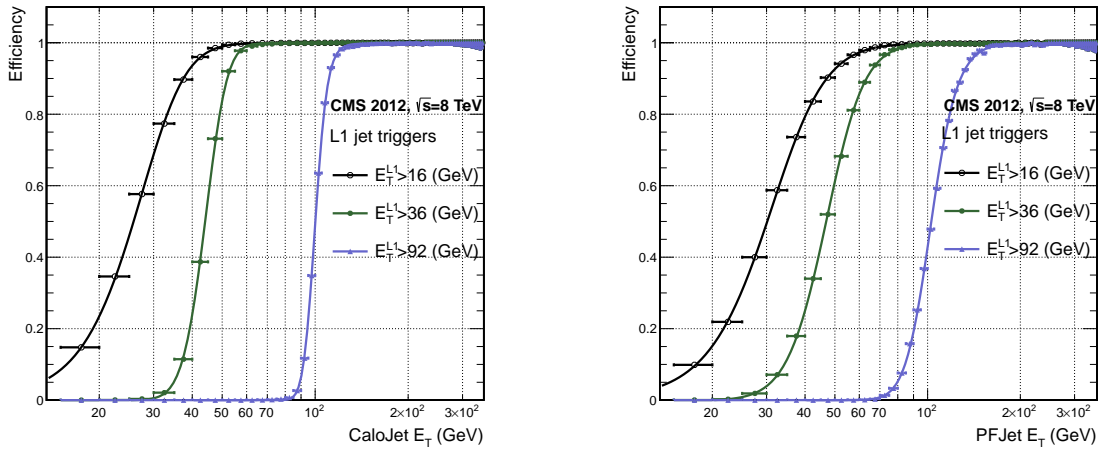


**Figure 3.11.:** L1 jet efficiency turn-on curves as a function of the offline CaloJet  $E_T$  (left) and PFJet  $E_T$  (right), measured in 2012 Run Period C data and collected with an isolated single  $\mu$  data sample.

Trigger	Calo		PF	
	$\mu$	$\sigma$	$\mu$	$\sigma$
L1_SingleJet16	$21.09 \pm 0.03$	$7.01 \pm 0.02$	$22.17 \pm 0.04$	$7.83 \pm 0.03$
L1_SingleJet36	$41.15 \pm 0.05$	$5.11 \pm 0.02$	$39.16 \pm 0.06$	$8.04 \pm 0.03$
L1_SingleJet92	$95.36 \pm 0.13$	$5.62 \pm 0.03$	$90.85 \pm 0.19$	$11.30 \pm 0.10$

**Table 3.1.:** Results of a cumulative EMG function fit to the turn-on curves for L1 single jet triggers in run 2012 Run Period C, measured in an isolated  $\mu$  data sample. The turn-on point,  $\mu$ , and resolution,  $\sigma$ , of the L1 jet triggers are measured with respect to offline Calo Jets (left) and PF Jets (right).

The results from the L1 single jet triggers shows good performance for both Calo and PF jets. A better resolution for Calo jets with respect to L1 jets quantities is observed. This effect is due to Calo jet reconstruction using the same detector systems as in L1 jets, whereas with PF jet construction using tracker and muon information, a more smeared resolution when compared to L1 is expected.

#### 3.4.4. Effects of the L1 jet seed

Between run period B and C of the 2012 data taking period, a jet seed threshold was introduced into the L1 trigger jet algorithm. There was previously no direct requirement made on the energy deposited in the central region. The introduction of a jet seed threshold required that the central region have  $E_T \geq 5\text{GeV}$ , and was introduced to

1149 counteract the effects of high pile up running conditions which create a large number of  
1150 soft non-collimated jets, that are then added to the jets from the primary interaction or  
1151 other soft jets from other secondary interactions [69]. This in turn causes a large increase  
1152 in trigger rate due to the increase in the likelihood that the event causes the L1 trigger to  
1153 fire. This was implemented to maintain trigger thresholds by cutting the rate of events  
1154 recorded without significant reduction in the efficiency of physics events of interest.

1155 The effect of the introduction of this jet seed threshold between these two run periods is  
1156 benchmarked through a comparison of the efficiency of the L1 jet triggers with respect  
1157 to offline Calo jets shown in Figure 3.12, and the L1  $H_T$  trigger efficiency in Figure 3.14  
1158 which is compared to offline  $H_T$  constructed from Calo jets with  $E_T \geq 40\text{GeV}$ .

1159 To negate any effects from different pile-up conditions in the run periods, the efficiencies  
1160 are measured in events which contain between 15 and 20 primary vertices as defined in  
1161 Appendix (A.2).

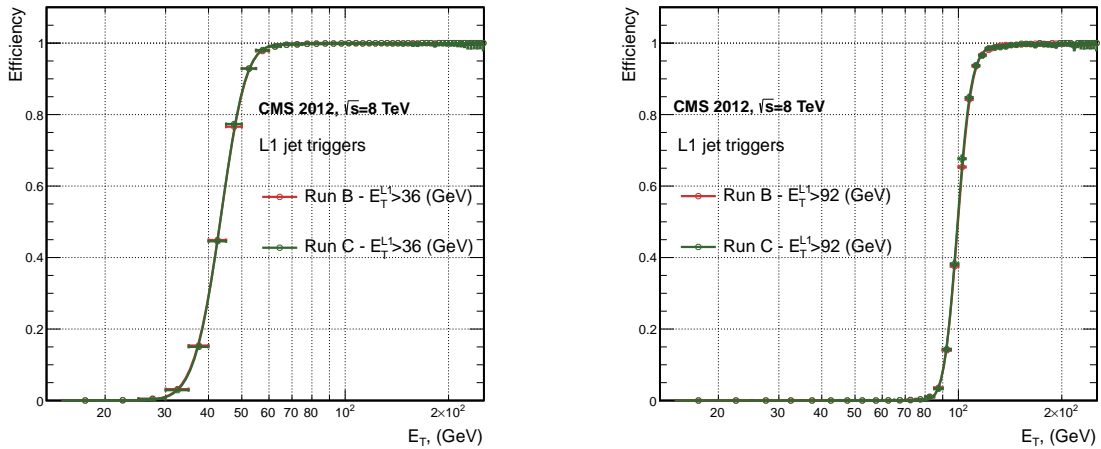


**Figure 3.12.:** L1 jet efficiency turn-on curves as a function of the offline CaloJet  $E_T$ , measured for the L1 SingleJet 36 and 92 trigger in 2012 run period B and C collected with an isolated single  $\mu'$  sample.

1162 It can be seen that the performance of the  $E_T > 36, 92$  single jet are almost identical,  
1163 with the jet seed having no measurable effect on these triggers as shown in Table 3.2 .

1164 For the  $H_T$  triggers, a large increase in rate during high pile-up conditions is expected.  
1165 This is due to the low energy threshold required for a jet to be added to the L1  $H_T$  sum,  
1166 which is compiled from all uncorrected L1 jets formed in the RCT. The introduction  
1167 of the jet seed threshold removes the creation of many of these soft low  $E_T$  jets, thus

Trigger	2012B		2012C	
	$\mu$	$\sigma$	$\mu$	$\sigma$
L1_SingleJet36	$40.29 \pm 0.04$	$5.34 \pm 0.02$	$40.29 \pm 0.11$	$5.21 \pm 0.05$
L1_SingleJet92	$94.99 \pm 0.09$	$5.93 \pm 0.06$	$94.82 \pm 0.29$	$5.74 \pm 0.18$

**Table 3.2.:** Results of a cumulative EMG function fit to the turn-on curves for L1 single jet triggers in the 2012 run period B and C, preselected on an isolated muon trigger. The turn-on point  $\mu$  and resolution  $\sigma$  of the L1 jet triggers are measured with respect to offline Calo Jets in run B (left) and run C (right).

lowering the  $H_T$  calculation at L1. The effect on the trigger cross section for L1  $H_T$  150 trigger can be seen in Figure 3.13.

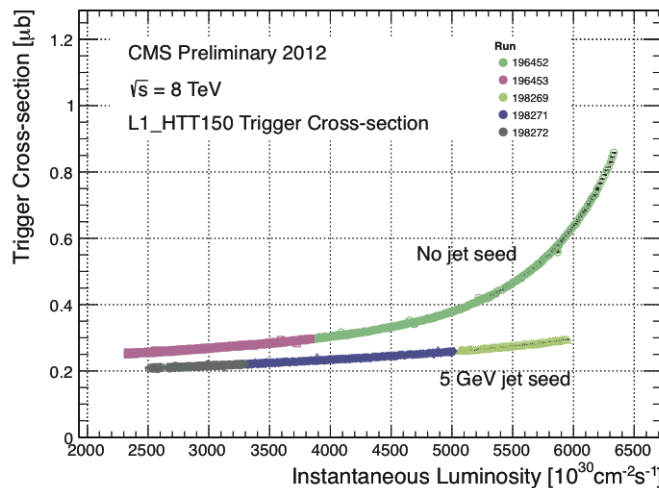


**Figure 3.13.:** Trigger cross section for the L1HTT150 trigger path. Showing that a 5 GeV jet seed threshold dramatically reduces the dependance of cross section on the instantaneous luminosity for L1  $H_T$  triggers [70].

Different behaviours for the trigger turn ons between these run periods are therefore expected. The turn on point is observed to shift to higher  $H_T$  values after the introduction of the jet seed threshold, whilst having a sharper resolution due to less pile-up jets being included the  $H_T$  sum. This effect is demonstrated in Table 3.3.

### 3.4.5. Robustness of L1 jet performance against pile-up

The performance of the L1 single jet triggers is evaluated in different pile-up conditions to benchmark any dependence on pile-up. Three different pile-up bins of 0-10, 10-20 and  $>20$  vertices are defined, reflecting the low, medium and high pile-up running conditions

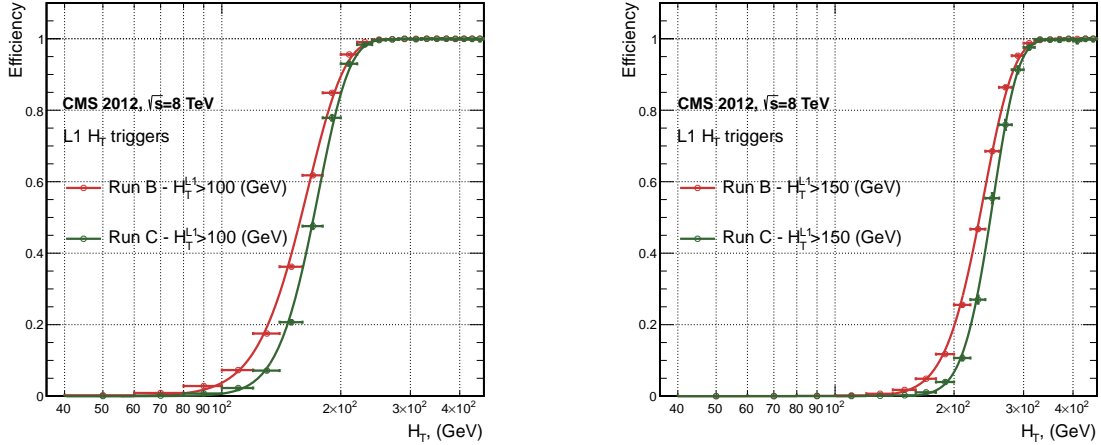


**Figure 3.14.:** L1  $H_T$  efficiency turn-on curves as a function of the offline CaloJet  $H_T$ , measured for the L1  $H_T$  100 and 150 trigger during the run 2012 B and C collected using an isolated single  $\mu$  triggered sample.

2012B			2012C		
Trigger	$\mu$	$\sigma$	$\mu$	$\sigma$	
L1 HT-100	$157.5 \pm 0.08$	$32.9 \pm 0.08$	$169.8 \pm 0.08$	$28.7 \pm 0.03$	
L1 H1-150	$230.9 \pm 0.02$	$37.3 \pm 0.01$	$246.4 \pm 0.16$	$31.8 \pm 0.05$	

**Table 3.3.:** Results of a cumulative EMG function fit to the turn-on curves for  $H_T$  in run 2012 B and C, preselected on an isolated single  $\mu$  trigger. The turn-on point  $\mu$ , resolution  $\sigma$  of the L1  $H_T$  triggers are measured with respect to offline  $H_T$  formed from CaloJets with a  $E_T \geq 40$  in run period B (left) and C (right).

at CMS in 2012. This is benchmarked relative to Calo and PF jets for the run 2012 C period where the jet seed threshold is applied, with L1 single jet thresholds of 16, 36 and 92 GeV, shown in Figure 3.15. The results of fits to these efficiency turn-on curves are given in Table 3.4 and Table 3.5 for Calo and PF jets respectively.

Vertices	0-10		11-20		> 20	
	$\mu$	$\sigma$	$\mu$	$\sigma$	$\mu$	$\sigma$
L1_SingleJet16	$19.9 \pm 0.1$	$6.1 \pm 0.3$	$20.8 \pm 0.1$	$6.5 \pm 0.1$	$22.3 \pm 0.2$	$7.5 \pm 0.1$
L1_SingleJet36	$41.8 \pm 0.1$	$4.6 \pm 0.1$	$40.9 \pm 0.1$	$5.1 \pm 0.1$	$40.6 \pm 0.6$	$5.9 \pm 0.2$
L1_SingleJet92	$95.9 \pm 0.2$	$5.4 \pm 0.1$	$95.2 \pm 0.2$	$5.6 \pm 0.1$	$94.5 \pm 0.6$	$6.2 \pm 0.3$

**Table 3.4.:** Results of a cumulative EMG function fit to the efficiency turn-on curves for L1 single jet triggers in the 2012 run period C, measured from isolated  $\mu$  triggered data. The turn-on point,  $\mu$ , and resolution,  $\sigma$ , of the L1 jet triggers are measured with respect to offline Calo jets in low (left), medium (middle) and high (right) pile-up conditions.

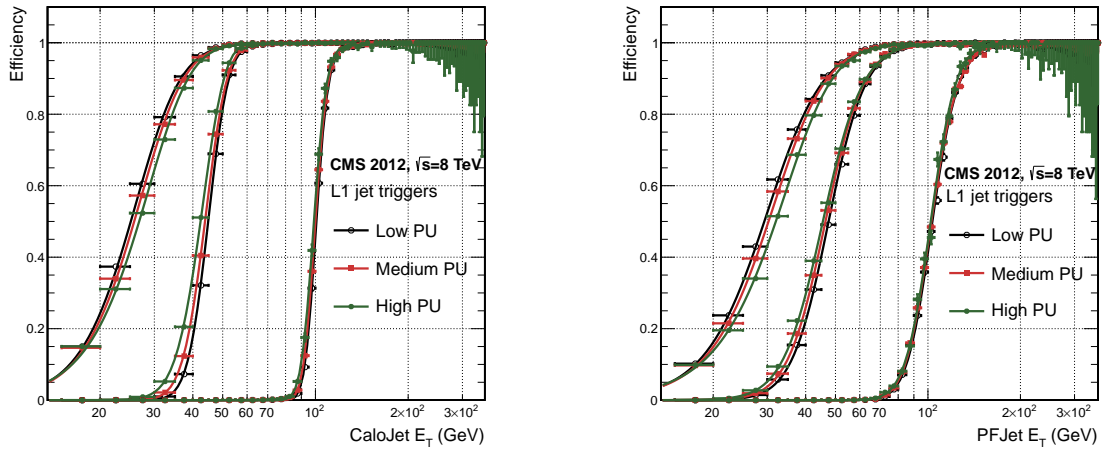


**Figure 3.15.:** L1 jet efficiency turn-on curves as a function of the leading offline  $E_T$ Calo (left) and PF (right) jet, for low, medium and high pile-up conditions.

Vertices	0-10		11-20		> 20	
	$\mu$	$\sigma$	$\mu$	$\sigma$	$\mu$	$\sigma$
L1_SingleJet16	21.1 $\pm$ 0.1	7.16 $\pm$ 0.05	22.34 $\pm$ 0.1	7.9 $\pm$ 0.1	24.6 $\pm$ 0.2	9.5 $\pm$ 0.1
L1_SingleJet36	39.6 $\pm$ 0.1	7.4 $\pm$ 0.1	38.4 $\pm$ 0.1	7.4 $\pm$ 0.1	37.1 $\pm$ 0.2	7.5 $\pm$ 0.1
L1_SingleJet92	91.6 $\pm$ 0.3	11.3 $\pm$ 0.2	90.4 $\pm$ 0.3	11.2 $\pm$ 0.1	92.0 $\pm$ 0.9	12.1 $\pm$ 0.4

**Table 3.5.:** Results of a cumulative EMG function fit to the efficiency turn-on curves for Level-1 single jet triggers in the 2012 run period C, measured from isolated  $\mu$  triggered data. The turn-on point,  $\mu$ , and resolution,  $\sigma$ , of the L1 jet triggers are measured with respect to offline PF jets in low (left), medium (middle) and high (right) pile-up conditions.

1182 No significant drop in efficiency is observed in the presence of a high number of primary  
 1183 vertices. The increase in hadronic activity in higher pile-up conditions, combined with  
 1184 the absence of pile-up subtraction for L1 jets, results in the expected observation of  
 1185 a decrease in the  $\mu$  value of the efficiency turn-ons as a function of pile-up, while the  
 1186 resolution,  $\sigma$  of the turn-ons are found to gradually worsen as expected with increasing  
 1187 pile-up.

1188 These features are further emphasised when shown as a function of

$$\frac{(L1 E_T - \text{Offline } E_T)}{\text{Offline } E_T} \quad (3.4)$$

1189 in bins of matched leading offline jet  $E_T$ , of which the individual fits can be found in  
1190 Appendix (B.2). Each of these distributions are fitted with an EMG function as defined  
1191 in Equation (3.3).

1192 The  $\mu$ ,  $\sigma$  and  $\lambda$  values extracted for the low, medium and high pile-up conditions are  
1193 shown for Calo and PF jets in Figure 3.16 and Figure 3.17 respectively. The central value  
1194 of  $\frac{(L1 E_T - \text{Offline } E_T)}{\text{Offline } E_T}$  is observed to increases as a function of jet  $E_T$ , whilst the resolution  
1195 is also observed to improve at higher offline jet  $E_T$ .

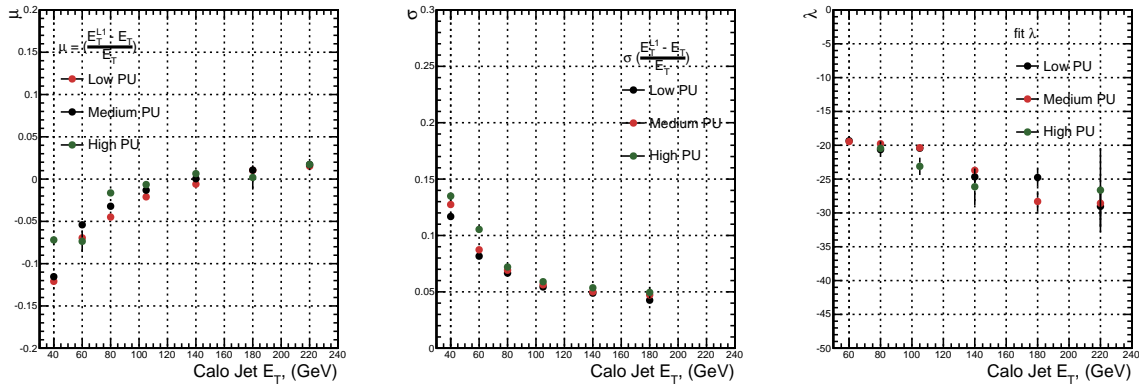


**Figure 3.16.:** Fit values from an EMG function fitted to the resolution plots of leading Calo jet  $E_T$  measured as a function of  $\frac{(L1 E_T - \text{Offline } E_T)}{\text{Offline } E_T}$  for low, medium and high pile-up conditions. The plots show the mean  $\mu$  (left), resolution  $\sigma$  (middle) of the Gaussian as well as the decay term  $\lambda$  (right) of the exponential.

1196 The resolution of other L1 energy sum quantities,  $H_T$ ,  $\not{E}_T$  and  $\sum E_T$  parameterised as  
1197 in Equation (3.4), can be found in Appendix (B.3). The same behaviour observed for  
1198 the single jet triggers is also found for these quantities, where in the presence of higher  
1199 pile-up the  $\mu$  values are shifted to higher values, with a worsening resolution,  $\sigma$  again  
1200 due to the increase in soft pile-up jets and the absence of pile-up subtraction at L1.

### 1201 3.4.6. Summary

1202 The performance of the CMS Level-1 Trigger has been studied and evaluated for jets and  
1203 energy sum quantities using data collected during the 2012 LHC 8 TeV run. These studies  
1204 include the effect of introduction of a 5 GeV jet seed threshold into the jet algorithm  
1205 configuration, the purpose of which is to mitigate the effects of pile-up on the rate of  
1206 L1 triggers whilst not adversely affecting the efficiency of these triggers. No significant

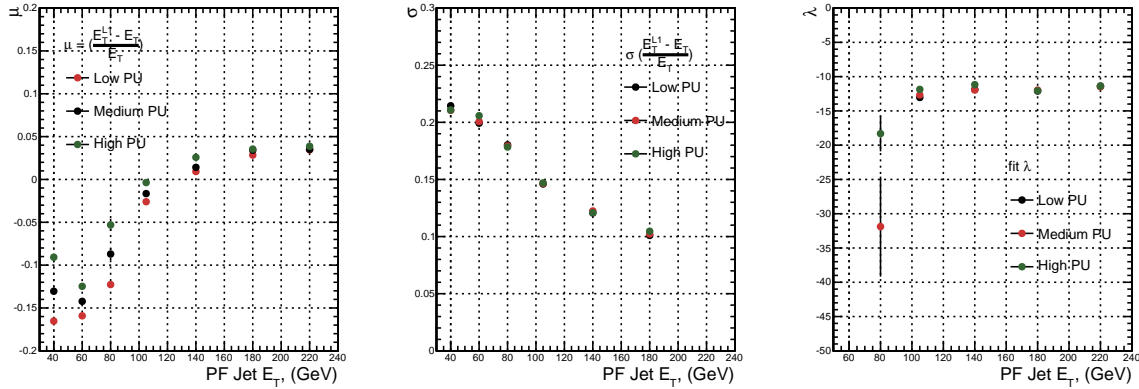


**Figure 3.17.:** Fit values from an **EMG** function fitted to the resolution plots of leading PF jet  $E_T$  measured as a function of  $\frac{(L1 E_T - \text{Offline } E_T)}{\text{Offline } E_T}$  for low and medium pile-up conditions. The plots show the mean  $\mu$  (left), resolution  $\sigma$  (middle) of the Gaussian as well as the decay term  $\lambda$  (right) of the exponential.

1207 change in performance is observed with this change and good performance is observed  
 1208 for a range of L1 quantities.

# Chapter 4.

## <sub>1209</sub> SUSY Searches In Hadronic Final <sub>1210</sub> States

<sub>1211</sub> In this chapter a model independent search for **SUSY** in hadronic final states with  
<sub>1212</sub>  $\cancel{E}_T$  using the  $\alpha_T$  variable at different b-quark and jet multiplicities is introduced and  
<sub>1213</sub> described in detail. The results presented are based on a data sample of pp collisions  
<sub>1214</sub> collected in 2012 at  $\sqrt{s} = 8$  TeV, corresponding to an integrated luminosity of  $11.7 \pm 0.5$   
<sub>1215</sub>  $\text{fb}^{-1}$  [5].

<sub>1216</sub> The kinematic variable  $\alpha_T$  is motivated as a variable to provide strong rejection of the  
<sub>1217</sub> overwhelming QCD background, prevalent to jets + $\cancel{E}_T$  final states at the **LHC**. This  
<sub>1218</sub> is achieved whilst maintaining sensitivity to a possible **SUSY** signal and described in  
<sub>1219</sub> Section (4.1). The search and trigger strategy in addition to the event reconstruction  
<sub>1220</sub> and selection are outlined within Sections (4.2 - 4.3).

<sub>1221</sub> The method in which the **SM** background is estimated using an analytical technique to  
<sub>1222</sub> improve statistical precision at higher b-tag multiplicities is detailed within Section (4.5).  
<sub>1223</sub> Included in this section is a discussion on the impact of b-tagging and mis-tagging scale  
<sub>1224</sub> factors between data and simulation on any background predictions. Improved precision  
<sub>1225</sub> in estimating background yields at large number of b-tagged jets, is important in the  
<sub>1226</sub> context of interpreting natural **SUSY** models, first outlined in Section (2.4.1).

<sub>1227</sub> A description of the formulation of appropriate systematic uncertainties applied to the  
<sub>1228</sub> background predictions to account for theoretical uncertainties and limitations in the  
<sub>1229</sub> simulation modelling of event kinematics and instrumental effects is covered in Section  
<sub>1230</sub> (4.6).

Finally the statistical likelihood model to interpret the observations in the signal and control samples is described in Section (4.8). The experimental reach of the analysis discussed within this thesis is interpreted in two classes of **SMS** models, both first introduced in Section (2.4.1). The **SMS** models considered in this analysis are summarised in Table 4.1. For each model, the **LSP** is assumed to be the lightest neutralino.

Within the table are also defined reference points, parameterised in terms of parent gluino/squark and **LSP** sparticle masses,  $m_{\text{parent}}$  and  $m_{\text{LSP}}$ , respectively, which are used within the following two chapters to demonstrate potential yields within the signal region of the search.

The masses are chosen to reflect parameter space which is within the expected sensitivity reach of the search, and also in the case of T1tttt and T1bbbb, reflect examples of potential natural **SUSY** topologies.

Model	Production/decay mode	Reference model	
		$m_{\text{parent}}$	$m_{\text{LSP}}$
G1 (T1)	$pp \rightarrow \tilde{g}\tilde{g}^* \rightarrow q\bar{q}\tilde{\chi}_1^0 q\bar{q}\tilde{\chi}_1^0$	700	300
G2 (T1bbbb)	$pp \rightarrow \tilde{g}\tilde{g}^* \rightarrow b\bar{b}\tilde{\chi}_1^0 b\bar{b}\tilde{\chi}_1^0$	900	500
G3 (T1tttt)	$pp \rightarrow \tilde{g}\tilde{g}^* \rightarrow t\bar{t}\tilde{\chi}_1^0 t\bar{t}\tilde{\chi}_1^0$	850	250
D1 (T2)	$pp \rightarrow \tilde{q}\tilde{q}^* \rightarrow q\tilde{\chi}_1^0 q\tilde{\chi}_1^0$	600	250
D2 (T2bb)	$pp \rightarrow \tilde{b}\tilde{b}^* \rightarrow b\tilde{\chi}_1^0 b\tilde{\chi}_1^0$	500	150
D3 (T2tt)	$pp \rightarrow \tilde{t}\tilde{t}^* \rightarrow t\tilde{\chi}_1^0 t\tilde{\chi}_1^0$	400	0

**Table 4.1.:** A summary of the **SMS** models interpreted in this analysis, involving both direct (D) and gluino-induced (G) production of squarks and their decays. Reference models are also defined in terms of parent and **LSP** sparticle mass

## 4.1. An Introduction to the $\alpha_T$ Search

A proton-proton collision resulting in the production and decay of supersymmetric particles, would manifest as a final state containing energetic jets and  $\cancel{E}_T$  in the hadronic channel. The search focuses on topologies where new heavy supersymmetric, R-parity conserving particles are pair-produced in pp collisions. These particles decaying to a **LSP** escape the detector undetected, leading to significant missing energy and missing hadronic transverse energy,

$$\mathcal{H}_T = \left| \sum_{i=1}^n \vec{p_T}^{jet_i} \right|, \quad (4.1)$$

1250 defined as the vector sum of the transverse energies of jets selected in an event. Energetic  
1251 jets produced in the decay of these supersymmetric particles also can produce significant  
1252 visible transverse energy,

$$H_T = \sum_{i=1}^n E_T^{jet_i}, \quad (4.2)$$

1253 defined as the scalar sum of the transverse energies of jets selected in an event.

1254 A search within this channel is greatly complicated in a hadron collider environment,  
1255 where the overwhelming background comes from inherently balanced multi-jet (“QCD”)  
1256 events which are produced with an extremely large cross section as demonstrated within  
1257 Figure 4.1.  $\cancel{E}_T$  can appear in such events with a substantial mis-measurement or  
1258 stochastic fluctuations of jet energy or missed objects due to detector mis-calibration or  
1259 noise effects.

1260 Additional SM background from EWK processes with genuine  $\cancel{E}_T$  from escaping neutrinos  
1261 comprise the irreducible background within this search and come mainly from:

- 1262 •  $Z \rightarrow \nu\bar{\nu}$  + jets,
- 1263 •  $W \rightarrow l\nu$  + jets in which a lepton falls outside of detector acceptance, is not  
1264 reconstructed, is mis-identified, or the lepton decays hadronically  $\tau \rightarrow$  had ,
- 1265 •  $t\bar{t}$  with at least one leptonically decaying W, which is missed in the detector as  
1266 detailed above,
- 1267 • small background contributions from DY, single top and Diboson (WW,ZZ,WZ)  
1268 processes.

1269 The search is designed to have a strong separation between events with genuine and  
1270 “fake”  $\cancel{E}_T$  which is achieved primarily through the dimensionless kinematic variable,  $\alpha_T$   
1271 [71][72].

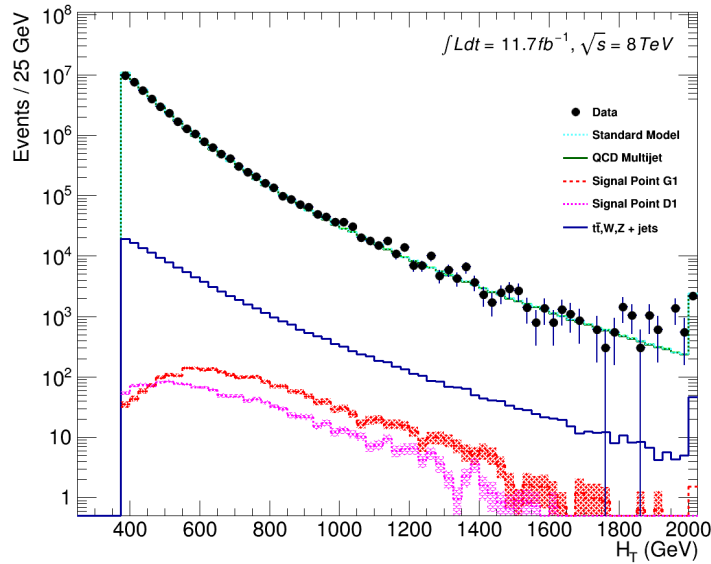


**Figure 4.1.:** Reconstructed offline  $H_T$  distribution in the hadronic signal selection, from  $11.7\text{fb}^{-1}$  of data, in which no  $\alpha_T$  requirement is made. Sample is collected from prescaled  $H_T$  triggers. Overlaid are expectations from MC simulation of EWK processes as well as a reference signal models (labelled G1 and D1 from Table 4.1).

### 1272 4.1.1. The $\alpha_T$ variable

1273 For a perfectly measured di-jet QCD event, conservation laws dictate that both jets must  
 1274 be of equal magnitude and produced in opposite directions. However in the case of di-jet  
 1275 events with genuine  $\cancel{E}_T$  (as detailed above), no such requirement is made of the two jets,  
 as depicted in Figure 4.2.

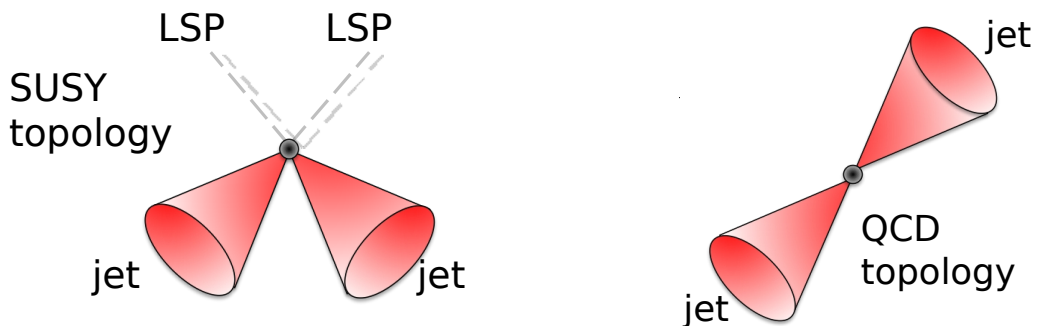


**Figure 4.2.:** The event topologies of background QCD dijet events (right) and a generic SUSY signature with genuine  $\cancel{E}_T$  (left).

1277 Exploiting this feature leads to the formulation of  $\alpha_T$  (first inspired by [73]) in di-jet  
1278 systems defined as,

$$\alpha_T = \frac{E_T^{j_2}}{M_T}, \quad (4.3)$$

1279 where  $E_T^{j_2}$  is the transverse energy of the least energetic of the two jets and  $M_T$  defined  
1280 as:

$$M_T = \sqrt{\left(\sum_{i=1}^2 E_T^{j_i}\right)^2 - \left(\sum_{i=1}^2 p_x^{j_i}\right)^2 - \left(\sum_{i=1}^2 p_y^{j_i}\right)^2} \equiv \sqrt{H_T^2 - \cancel{H}_T^2}. \quad (4.4)$$

1281 A perfectly balanced di-jet event i.e.  $E_T^{j_1} = E_T^{j_2}$  would yield an  $\alpha_T$  value of 0.5, where  
1282 as events with jets which are not back-to-back, for example in events in which a W or  
1283 Z recoils off a system of jets,  $\alpha_T$  can achieve values in excess of 0.5. Most importantly  
1284 balanced QCD events in which jets are mis-measured, will generally result in an  $\alpha_T$  of  
1285 less than 0.5, thus giving the  $\alpha_T$  variable discriminating power between these processes.

1286  $\alpha_T$  can be extended to apply to any arbitrary number of jets, undertaken by modelling  
1287 a system of  $n$  jets as a di-jet system, through the formation of two pseudo-jets [74].  
1288 The two pseudo-jets are built by merging the jets present in the event such that the  
1289 2 pseudo-jets are chosen to be as balanced as possible, i.e the  $\Delta H_T \equiv |E_T^{pj_1} - E_T^{pj_2}|$  is  
1290 minimised between the two pseudo jets. Using Equation (4.4),  $\alpha_T$  can be rewritten as,

$$\alpha_T = \frac{1}{2} \frac{H_T - \Delta H_T}{\sqrt{H_T^2 - \cancel{H}_T^2}} = \frac{1}{2} \frac{1 - \Delta H_T/H_T}{\sqrt{1 - (\cancel{H}_T/H_T)^2}}. \quad (4.5)$$

1291 The distribution of  $\alpha_T$  for the two jet categories used within this analysis,  $2 \leq n_{jet} \leq 3$   
1292 and  $n_{jet} \geq 4$  jets, is shown in the Figure 4.3. It can be seen that the distributions peak  
1293 at an  $\alpha_T$  of 0.5, before falling away sharply and being free of multi-jet background at  
1294 larger  $\alpha_T$  values. These distributions serve to demonstrate the ability of the  $\alpha_T$  variable  
1295 to discriminate between multi-jet events and EWK processes with genuine  $\cancel{E}_T$  in the  
1296 final state.

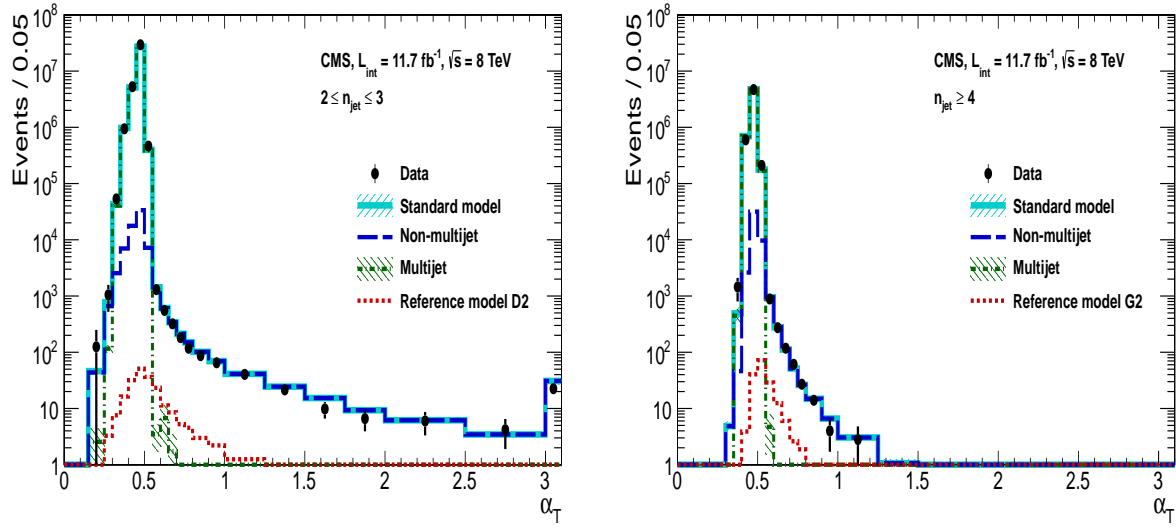


**Figure 4.3.:** The  $\alpha_T$  distributions for the low 2-3 (left) and high  $\geq 4$  (right) jet multiplicities after a full analysis selection and shown for  $H_T > 375$ . Data is collected using both prescaled  $H_T$  triggers and dedicated  $\alpha_T$  triggers for below and above  $\alpha_T = 0.55$  respectively. . Expected yields as given by simulation are also shown for multi-jet events (green dash-dotted line), EWK backgrounds with genuine  $E_T$  (blue long-dashed line), the sum of all SM processes (cyan solid line) and the reference signal model D2 (left, red dotted line) or G2 (right, red dotted line).

1297 The  $\alpha_T$  requirement used within the search is chosen to be  $\alpha_T > 0.55$  to ensure that  
 1298 the QCD multi-jet background is negligible even in the presence of moderate jet mis-  
 1299 measurement. There still remains other effects which can cause multi-jet events to  
 1300 artificially have a large  $\alpha_T$  value, which are discussed in detail in Section (4.2.2).

## 1301 4.2. Search Strategy

1302 The aim of the analysis presented in this thesis is to identify an excess of events in data  
 1303 over the SM background expectation in multi-jet final states and significant  $E_T$ . The  
 1304 essential suppression of the dominant QCD background for such a search is addressed by  
 1305 the  $\alpha_T$  variable described in the previous section. For estimation of the remaining EWK  
 1306 backgrounds, three independent data control samples are used to predict the different  
 1307 processes that compose the background :

- 1308 •  $\mu +$  jets control sample to determine  $W +$  jets,  $t\bar{t}$  and single top backgrounds,  
 1309 •  $\gamma +$  jets control sample to determine the irreducible  $Z \rightarrow \nu\bar{\nu} +$  jets background,

1310 •  $\mu\mu + \text{jets}$  control sample to also determine the irreducible  $Z \rightarrow \nu\bar{\nu} + \text{jets}$  background.

1311 These control samples are chosen to both be rich in specific **EWK** processes, be free of  
1312 QCD multi-jet events and to also be kinematically similar to the hadronic signal region  
1313 that they are estimating the backgrounds of, see Section (4.2.3). The redundancy of  
1314 using the  $\gamma + \text{jets}$  and  $\mu\mu + \text{jets}$  sample to predict the same background within the  
1315 signal region, brings an opportunity to reliably cross check and validate the background  
1316 estimation method and is utilised in both the determination of background estimation  
1317 systematics (Section(4.6)), and in the maximum likelihood fit (Section(4.8)).

1318 To remain inclusive to a large range of possible **SUSY** models, the signal region is split  
1319 into the following categories to allow for increased sensitivity in the interpretation of  
1320 results for different **SUSY** topologies:

1321 **Sensitivity to a range of SUSY mass splittings**

1322 The hadronic signal region is defined by  $H_T > 275$ , divided into eight bins in  $H_T$ .  
1323 – Two bins of width 50 GeV in the range  $275 < H_T < 375$  GeV,  
1324 – five bins of width 100 GeV in the range  $375 < H_T < 875$  GeV,  
1325 – and a final open bin,  $H_T > 875$  GeV.

1326 The choice of the lowest  $H_T$  bin in the analysis is driven primarily by trigger  
1327 constraints. The mass difference between the **LSP** and the particle that it decays  
1328 from is an important factor in the amount of hadronic activity in the event.

1329 A large mass splitting will lead to hard high  $p_T$  jets which contribute to the  $H_T$  sum.  
1330 From Figure 4.1 it can be seen that the **SM** background falls sharply at high  $H_T$   
1331 values, therefore binning in  $H_T$  will lead to easier of identification of such signals.  
1332 Conversely smaller mass splittings lead to softer jet  $p_T$ 's which will subsequently  
1333 fall into the lower  $H_T$  range.

1334 **Sensitivity to production method of SUSY particles**

1335 The production mechanism of any potential **SUSY** signal can lead to different event  
1336 topologies. One such way to discriminate between gluino ( $g\tilde{g}$  - “high multiplicity”),  
1337 and direct squark ( $q\tilde{q}$  - “low multiplicity”) induced production of **SUSY** particles is  
1338 realised through the number of reconstructed jets in the final state.

1339 The analysis is thus split into two jet categories : 2-3 jets ,  $\geq 4$  jets to give sensitivity  
1340 to both of these mechanisms.

1341 **Sensitivity to “Natural SUSY” via tagging jets from b-quarks**

1342 Jets originating from bottom quarks (b-jets) are identified through vertices that  
1343 are displaced with respect to the primary interaction. The algorithm used to tag  
1344 b-jets is the Combined Secondary Vertex Medium Working Point (**CSVM**) tagger,  
1345 described within Section (3.3.2). A cut is placed on the discriminator variable of  
1346  $> 0.679$ , leading to a gluon/light-quark mis-tag rate of approximately 1% and a jet  
1347  $p_T$  dependant b-tagging efficiency of 60-70% [64].

1348 Natural **SUSY** models would be characterised through final-state signatures rich  
1349 in bottom quarks. A search relying on methods to identify jets originating from  
1350 bottom quarks through b-tagging, will significantly improve the sensitivity to this  
1351 class of signature. This gain in sensitivity stems from a vast reduction in the vector  
1352 boson + jet backgrounds (W,Z) at higher b-tag jet multiplicities, which typically  
1353 have no b-flavoured quarks in their decays.

1354 Therefore events are categorised according to the number of b-tagged jets recon-  
1355 structed in each event, in the following: 0,1,2,3, $\geq 4$  b-tag categories . In the highest  
1356  $\geq 4$  b-tag category due to a limited number of expected signal and background, just  
1357 three  $H_T$  bins are employed: 275-325 GeV, 325-375 GeV,  $\geq 375$  GeV.

1358 This characterisation is identically mirrored in all control samples, with the infor-  
1359 mation from all samples and b-tag categories used simultaneously in the likelihood  
1360 model, see Section (4.8).

1361 The combination of the  $H_T$ , jet multiplicity and b-tag categorisation of the signal region as  
1362 described above, resultantly leads to 67 different bins in which the analysis is interpreted  
1363 in, and is depicted in Figure 4.4.

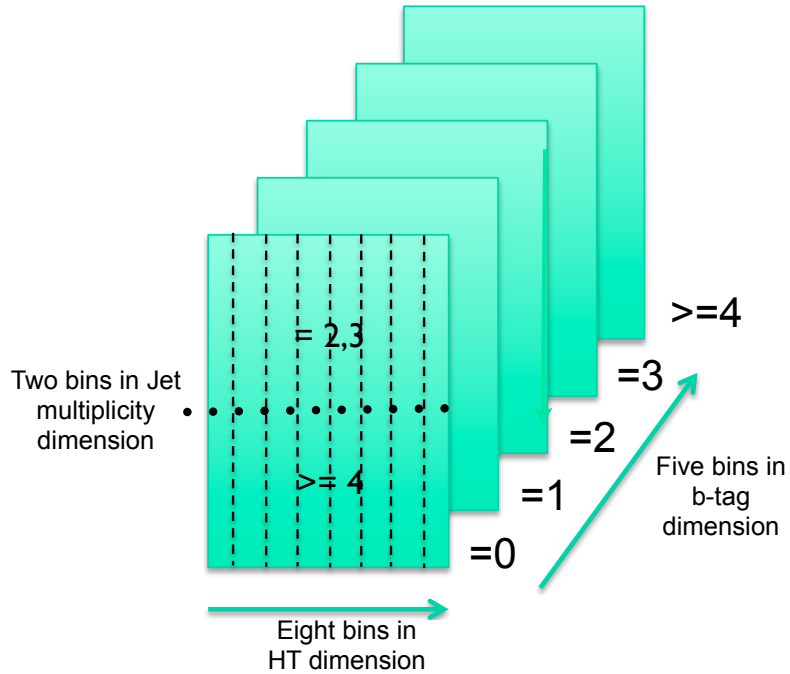


**Figure 4.4.:** Pictorial depiction of the analysis strategy employed by the  $\alpha_T$  search to increase sensitivity to a wide spectra of **SUSY** models.

### <sup>1364</sup> 4.2.1. Physics objects

<sup>1365</sup> The physics objects used in the analysis defined below, follow the recommendation of  
<sup>1366</sup> the various **CMS** Physics Object Groups (**POGs**).

#### <sup>1367</sup> • Jets

<sup>1368</sup> The jets used in this analysis are CaloJets, reconstructed as described in Section  
<sup>1369</sup> (3.3.1) using the anti- $k_T$  jet clustering algorithm.

<sup>1370</sup> To ensure the jet object falls within the calorimeter systems a pseudo-rapidity  
<sup>1371</sup> requirement of  $|\eta| < 3$  is applied. Each jet must pass a “loose” identification criteria  
<sup>1372</sup> to reject jets resulting from unphysical energy, the criteria of which are detailed in  
<sup>1373</sup> Table A.1 [75].

#### <sup>1374</sup> • Muons

<sup>1375</sup> Muons are selected in the  $\mu + \text{jets}$  and  $\mu\mu + \text{jets}$  control samples, and vetoed in  
<sup>1376</sup> the signal region. The same cut based identification criteria is applied to muons in  
<sup>1377</sup> both search regions and is summarised in Table 4.2 [76].

Variable	Definition
Is Global Muon	Muon contains both a hit in the muon chamber and a matched track in the inner tracking system [77].
$\chi^2 < 10$	$\chi^2$ of global muon track fit. Used to suppress hadronic punch-through and muons from decays in flight.
Muon chamber hits > 0	At least one muon chamber hit included in global muon track fit.
Muon station hits > 1	Muon segment hits in at least two muon stations, which suppresses hadronic punch-through and accidental track-to-segment matches.
$d_{xy} < 0.2\text{mm}$	The tracker track transverse impact parameter w.r.t the primary vertex. Suppresses cosmic muons and muons from decays in flight.
$d_z < 0.5\text{mm}$	The longitudinal distance of the tracker track w.r.t the primary vertex. Loose cut to further suppress cosmic muons, muons from decays in flight and tracks from pileup.
Pixel hits > 0	Suppresses muons from decays in flight by requiring at least one pixel hit in the tracker.
Track layer hits > 5	Number of tracker layers with hits, to guarantee a good $p_T$ measurement. Also suppresses muons from decays in flight.
PF Iso < 0.12	Isolation based upon the sum of the charged and neutral hadrons and photon objects within a $\Delta R$ 0.4 cone of the muon object, corrected for pile up effects on the isolation sum.

**Table 4.2.:** Muon Identification criteria used within the analysis for selection/veto purposes in the muon control/signal selections.

1378        Additionally muons are required to be within the acceptance of the muon tracking  
 1379        systems. For the muon control samples, trigger requirements necessitate a  $|\eta| <$   
 1380        2.1 for the selection of muons. In the signal region where muons are vetoed these  
 1381        conditions are relaxed to  $|\eta| < 2.5$  and a minimum threshold of  $p_T > 10 \text{ GeV}$  is  
 1382        required of muon objects.

1383        **• Photons**

1384        Photons are selected within the  $\gamma + \text{jets}$  control sample and vetoed in all other  
 1385        selections. Photons are identified in both cases according to the cut based criteria  
 1386        listed in Table 4.3 [78].

Variable	Definition
H/E < 0.05	The ratio of hadronic energy in the <b>HCAL</b> tower directly behind the <b>ECAL</b> super-cluster and the <b>ECAL</b> super-cluster itself.
$\sigma_{i\eta i\eta} < 0.011$	The log energy weighted width ( $\sigma$ ), of the extent of the shower in the $\eta$ dimension.
R9 < 1.0	The ratio of the energy of the $3 \times 3$ crystal core of the super-cluster compared to the total energy stored in the $5 \times 5$ super-cluster.
Combined Isolation < 6 GeV	The photons are required to be isolated with no electromagnetic or hadronic activity within a radius $\Delta R = 0.3$ of the photon object. A combination of the pileup subtracted [79], <b>ECAL</b> , <b>HCAL</b> and tracking isolation sums are used to determine the combined total isolation value.

**Table 4.3.:** Photon Identification criteria used within the analysis for selection/veto purposes in the  $\gamma +$  jets control/signal selections.

1387 Photon objects are also required to have a minimum momentum of  $p_T > 25$  GeV.

1388 **• Electrons**

1389 Electron identification is defined for veto purposes. They are selected according to  
1390 the following cut-based criteria listed in Table 4.4, utilising PF-based isolation.

1391 Electrons are required to be identified at  $|\eta| < 2.5$ , with a minimum  $p_T > 10$  GeV  
1392 threshold to ensure that the electron falls within the tracking system of the detector.

Variable	Barrel	EndCap	Definition
$\Delta\eta_{In}$	<0.007	<0.009	$\Delta\eta$ between SuperCluster position and the coordinate of the associated track at the interaction vertex, assuming no radiation.
$\Delta\phi_{In}$	<0.15	<0.10	$\Delta\phi$ between SuperCluster position and track direction at interaction vertex extrapolated to ECAL assuming no radiation.
$\sigma_{in\eta\eta}$	<0.01	<0.03	Cluster shape covariance, measure the $\eta$ dispersion of the electrons electromagnetic shower over the ECAL supercluster.
H/E	<0.12	<0.10	The ratio of hadronic energy in the HCAL tower directly behind the ECAL super-cluster and the ECAL super-cluster itself.
d0 (vtx)	<0.02	<0.02	The tracker track transverse impact parameter w.r.t the primary vertex.
dZ (vtx)	<0.20	<0.20	The longitudinal distance of the tracker track w.r.t the primary vertex.
$ (\frac{1}{E_{ECAL}} - \frac{1}{p_{track}}) $	<0.05	<0.05	Comparison of energy at supercluster $1/E_{ECAL}$ and that of the track momentum at the vertex $1/p_{track}$ . Causes suppression of fake electrons at low $p_T$ .
PF Iso	<0.15	<0.15	Combined PF isolation of charged hadrons, photons, neutral hadrons within a $\Delta R < 0.3$ cone size. Isolation sum is corrected for pileup using effective area corrections for neutral particles.

**Table 4.4.:** Electron Identification criteria used within the analysis for veto purposes.

**• Noise and  $E_T$  Filters**

A series of Noise filters are applied to veto events which contain spurious non-physical jets that are not picked up by the jet id, and events which give large unphysical  $E_T$  values. These filters are listed within Table 4.5.

1393

1394

1395

1396

Noise Filters	Variable	Definition
CSC tight beam halo filter		As proton beams circle the <b>LHC</b> , proton interactions with the residual gas particles or the beam collimators can occur, producing showers of secondary particles which can interact with the <b>CMS</b> detector.
HBHE noise filter with isolated noise rejection		Anomalous noise in the <b>HCAL</b> not due to electronics noise, but rather due to instrumentation issues associated with the <b>HPD</b> 's and Readout Boxes ( <b>RBXs</b> ).
HCAL laser filter		The <b>HCAL</b> uses laser pulses for monitoring the detector response. Some laser pulses have accidentally been fired in the physics orbit, and ended up polluting events recorded for physics analysis.
ECAL dead cell trigger primitive (TP) filter		<b>EB</b> and <b>EE</b> have single noisy crystals which are masked in reconstruction. Use the Trigger Primitive ( <b>TP</b> ) information to assess how much energy was lost in masked cells.
Bad EE Supercrystal filter		Two supercrystals in <b>EE</b> are found to occasionally produce high amplitude anomalous pulses in several channels at once, causing a large $E_T$ spike.
ECAL Laser correction filter		A laser calibration multiplicative factor is applied to correct for transparency loss in each crystal during irradiation. A small number of crystals receive unphysically large values of this correction and become very energetic, resulting in $E'_T$ .

**Table 4.5.:** Noise filters that are applied to remove spurious and non-physical  $\cancel{E}_T$  signatures within the **CMS** detector.

### **4.2.2. Event selection**

- <sup>1397</sup> The selection criteria for events within the analysis are detailed below. A set of common cuts are applied to both signal (maximise acceptance to a range of **SUSY** signatures), and control samples (retain similar jet kinematics for background predictions), with additional selection cuts applied to each control sample to enrich the sample in a particular **EWK** processes, see Section (4.2.3).
- <sup>1403</sup> The jets considered in the analysis are required to have a transverse momentum  $p_T > 50$  GeV, with a minimum of two jets required in the event. The highest  $E_T$  jet is required to lie within the central tracker acceptance  $|\eta| < 2.5$ , and the two leading  $p_T$  jets must each have  $p_T > 100$  GeV. Any event which has a jet with  $p_T > 50$  GeV that either fails the “loose” identification criteria described in Section(4.2.1) or has  $|\eta| > 3.0$ , is rejected.
- <sup>1408</sup> Similarly events in which an electron, muon or photon fails object identification but pass  $\eta$  and  $p_T$  restrictions, are identified as an “odd” lepton/photon and the event is vetoed.
- <sup>1410</sup> At low  $H_T$ , the jet threshold requirements applied to be considered as part of the analysis and enter the  $H_T$  sum are scaled downwards. These are scaled down in order to extend

<sup>1412</sup> phase space at low  $H_T$ , preserving similar jet multiplicities and background admixture  
<sup>1413</sup> seen at higher  $H_T$ , as listed in Table 4.6.

$H_T$ bin	minimum jet $p_T$	second leading jet $p_T$
$275 < H_T < 325$	36.7	73.3
$325 < H_T < 375$	43.3	86.6
$375 < H_T$	50.0	100.0

**Table 4.6.:** Jet thresholds used in the three  $H_T$  regions of the analysis.

<sup>1414</sup> Within the signal region to suppress **SM** processes with genuine  $\cancel{E}_T$  from neutrinos,  
<sup>1415</sup> events containing isolated electrons or muons are vetoed. Furthermore to ensure a pure  
<sup>1416</sup> multi-jet topology, events are vetoed if an isolated photon is found with  $p_T > 25$  GeV.  
<sup>1417</sup> An  $\alpha_T$  requirement of  $> 0.55$  is required to reduce the QCD multi-jet background  
<sup>1418</sup> to a negligible amount. Finally additional cleaning cuts are applied to protect against  
<sup>1419</sup> pathological deficiencies such as reconstruction failures or severe energy mis-measurements  
<sup>1420</sup> due to detector inefficiencies:

- Significant  $\cancel{H}_T$  can arise in events with no real  $\cancel{E}_T$  due to multiple jets falling below the  $p_T$  threshold for selecting jets. This in turn leads to events which can then incorrectly pass the  $\alpha_T$  requirements of the analysis. This effect can be negated by requiring that the missing transverse momentum reconstructed from jets alone does not greatly exceed the missing transverse momentum reconstructed from all of the detector's calorimeter towers,

$$R_{miss} = \cancel{H}_T / \cancel{E}_T < 1.25.$$

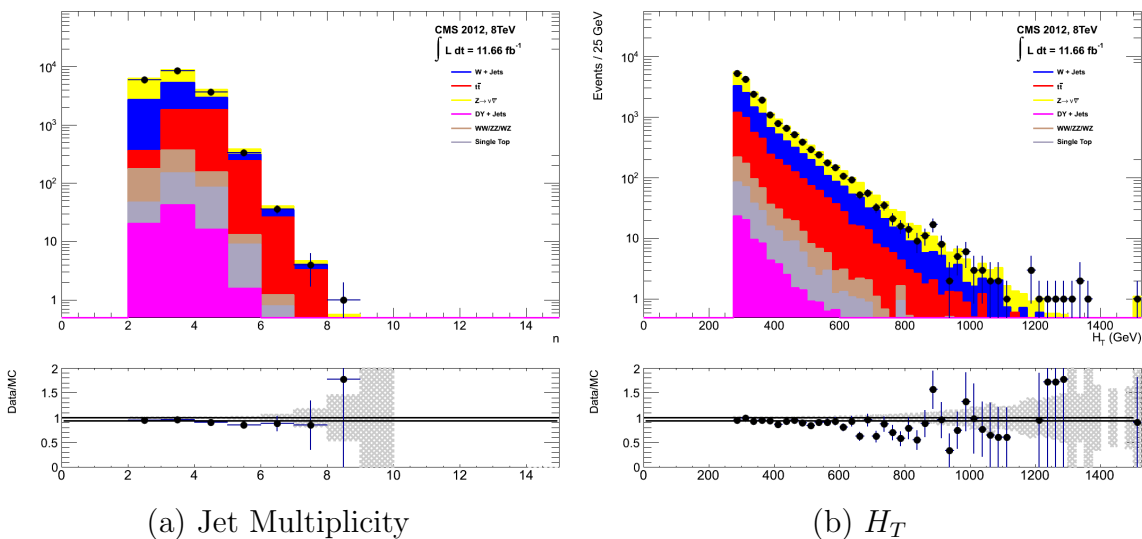
<sup>1421</sup> • Fake  $\cancel{E}_T$  and  $\cancel{H}_T$  can arise due to significant jet mis-measurements caused by a small  
<sup>1422</sup> number of non-functioning **ECAL** regions. These regions absorb electromagnetic  
<sup>1423</sup> showers which are subsequently not added to the jet energy sum. To circumvent  
<sup>1424</sup> this problem the following procedure is employed : For each jet in the event, the  
<sup>1425</sup> angular separation

$$\Delta\phi_j^* \equiv \Delta\phi(\vec{p_j} - \sum_{i \neq j} \vec{p_i}), \quad (4.6)$$

is calculated where that jet is itself removed from the event. Here  $\Delta\phi^*$  is a measure of how aligned the  $H_T$  of an event is with a jet. A small value (i.e. the  $H_T$  vector lies along the jet axis) is indicative of an inherently balanced event in which a jet has been mis-measured. For every jet in a event with  $\Delta\phi^* < 0.5$ , if the  $\Delta R$  distance between the selected jet and the closest dead **ECAL** region is also  $< 0.3$ , then the event is rejected. Similarly events are rejected if the jet points within  $\Delta R < 0.3$  of the **ECAL** barrel-endcap gap at  $|\eta| = 1.5$ .

Some of the key distributions of the data used in this analysis compared to MC simulation are shown in Figure 4.5. The MC samples are normalised to a luminosity of  $11.7 \text{ fb}^{-1}$ , with no requirement placed upon the number of b-tagged jets or number of jets in the events. In the case of this inclusive selection the dominant backgrounds in the signal regions are,  $Z \rightarrow \nu\bar{\nu}$  and  $W + \text{jets}$  processes, with a smaller  $t\bar{t}$  background accompanied by other residual backgrounds.

The distributions shown are presented for purely illustrative purposes, with the MC simulation itself not used in absolute term to estimate the yields from background processes, see Sections (4.2.3, 4.5). However it is nevertheless important to demonstrate that good agreement exists between simulation and observation in data.



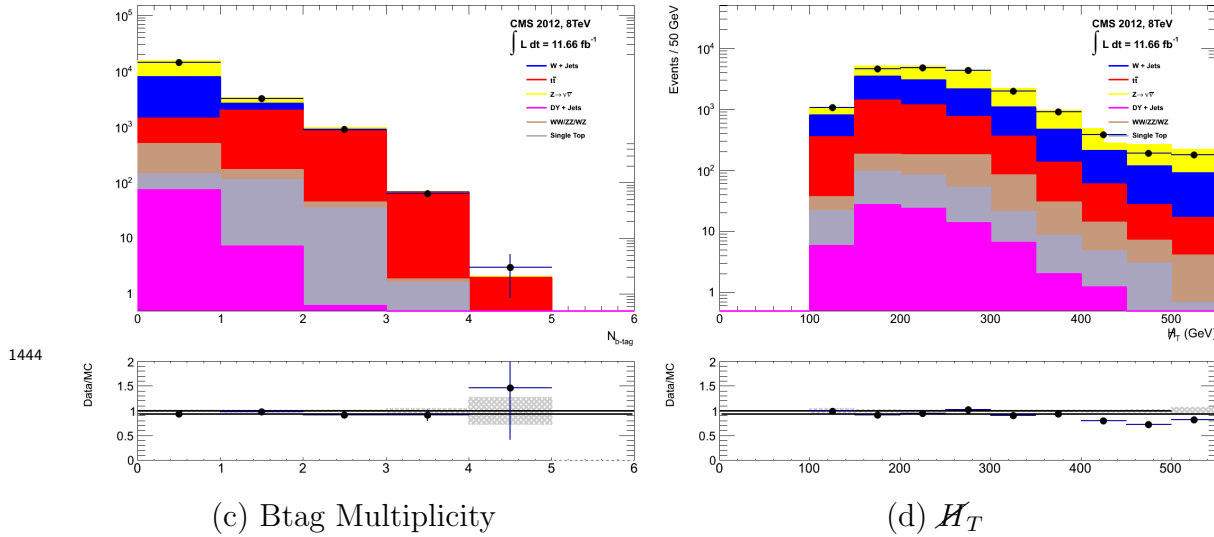


**Figure 4.5.:** Data/MC comparisons of key variables for the hadronic signal region, following the application of the hadronic selection criteria and the requirements of  $H_T > 275$  GeV and  $\alpha_T > 0.55$ . Bands represent the uncertainties due to the statistical size of the MC samples. No requirement is made upon the number of b-tagged jets or jet multiplicity in these distributions.

### 1445 4.2.3. Control sample definition and background estimation

1446 The method used to estimate the background contributions in the hadronic signal region  
 1447 relies on the use of a Transfer Factor (**TF**). This is determined from MC simulation  
 1448 in both the control,  $N_{MC}^{\text{control}}$ , and signal,  $N_{MC}^{\text{signal}}$ , region to transform the observed yield  
 1449 measured in data for a control sample,  $N_{\text{obs}}^{\text{control}}$ , into a background prediction,  $N_{\text{pred}}^{\text{signal}}$ , via  
 1450 Equation (4.7),

$$N_{\text{pred}}^{\text{signal}} = \frac{N_{MC}^{\text{signal}}}{N_{MC}^{\text{control}}} \times N_{\text{obs}}^{\text{control}}. \quad (4.7)$$

1451 All MC samples are normalised to the luminosity of the data samples,  $11.7 \text{ fb}^{-1}$ . Through  
 1452 this method, “vanilla” predictions for the **SM** background in the signal region can be  
 1453 made by considering separately the sum of the prediction from either the  $\mu + \text{jets}$  and  $\gamma$   
 1454 + jets, or  $\mu + \text{jets}$  and  $\mu\mu + \text{jets}$  samples. However the final background estimation from  
 1455 which results are interpreted, is calculated via a fitting procedure defined formally by  
 1456 the likelihood model described in Section (4.8).

<sup>1457</sup> The sum of the expected yields from all MC processes, in each control sample enter the  
<sup>1458</sup> denominator,  $N_{MC}^{\text{control}}$ , of the **TF** defined in Eq (4.7). However for the numerator ,  $N_{MC}^{\text{signal}}$ ,  
<sup>1459</sup> only the relevant processes that are being estimated, enter into the **TF**.

<sup>1460</sup> For the  $\mu + \text{jets}$  sample the simulated MC processes which enter the numerator of the  
<sup>1461</sup> **TF** are,

$$N_{MC}^{\text{signal}}(H_T, n_{\text{jet}}) = N_W + N_{t\bar{t}} + N_{DY} + N_t + N_{di-boson}, \quad (4.8)$$

<sup>1462</sup> whilst for both the  $\mu\mu + \text{jets}$  and  $\gamma + \text{jets}$  samples the only MC process used in the  
<sup>1463</sup> numerator is,

$$N_{MC}^{\text{signal}}(H_T, n_{\text{jet}}) = N_{Z \rightarrow \nu\bar{\nu}}. \quad (4.9)$$

<sup>1464</sup> The control samples and the **EWK** processes they are specifically tuned to select are  
<sup>1465</sup> defined below, with distributions of key variables for each of the control samples shown  
<sup>1466</sup> for illustrative purposes in Figures 4.6, 4.7 and 4.8. No requirement is placed upon  
<sup>1467</sup> the number of b-tagged jets or jet multiplicity in the distributions shown. The MC  
<sup>1468</sup> distributions highlight the background compositions of each control sample, where in  
<sup>1469</sup> general, good agreement is observed between data and simulation, giving confidence  
<sup>1470</sup> that the samples are well understood. The contribution from QCD multi-jet events is  
<sup>1471</sup> expected to be negligible :

### <sup>1472</sup> The $\mu + \text{jets}$ control sample

<sup>1473</sup> Events from  $W + \text{jets}$  and  $t\bar{t}$  processes enter into the hadronic signal sample due  
<sup>1474</sup> to unidentified leptons from acceptance effects or reconstruction inefficiencies and  
<sup>1475</sup> hadronic tau decays. These leptons originate from the decay of high  $p_T$   $W$  bosons.

<sup>1476</sup> The control samples specifically identifies  $W \rightarrow \mu\bar{\nu}$  decays within a similar phase-  
<sup>1477</sup> space of the signal region, where the muon is subsequently ignored in the calculation  
<sup>1478</sup> of event level variables, i.e.  $H_T$ ,  $\cancel{H}_T$ ,  $\alpha_T$ . All kinematic jet-based cuts are identical  
<sup>1479</sup> to those applied in the hadronic search region (with the exception of  $\alpha_T$ , discussed  
<sup>1480</sup> below) detailed in Section (4.2.2), with the same  $H_T$ , jet multiplicity and b-jet  
<sup>1481</sup> multiplicity binning described above.

- Muons originating from W boson decays are selected by requiring one tightly isolated muon defined in Table 4.2, with a  $p_T > 30$  GeV and  $|\eta| < 2.1$ . Both of these threshold arise from trigger restrictions.
- The transverse mass of the W candidate must satisfy  $M_T(\mu, \cancel{E}_T) > 30$  GeV (to suppress QCD multi-jet events).
- Events which contain a jet overlapping with a muon  $\Delta R(\mu, \text{jet}) < 0.5$  are vetoed to remove events from muons produced as part of a jet’s hadronisation process.
- Events containing a second muon candidate which has failed id, but passing  $p_T$  and  $|\eta|$  requirements, are checked to have an invariant mass that satisfies  $|M_{\mu\mu} - m_Z| > 25$ , thus removing  $Z \rightarrow \mu\mu$  contamination.

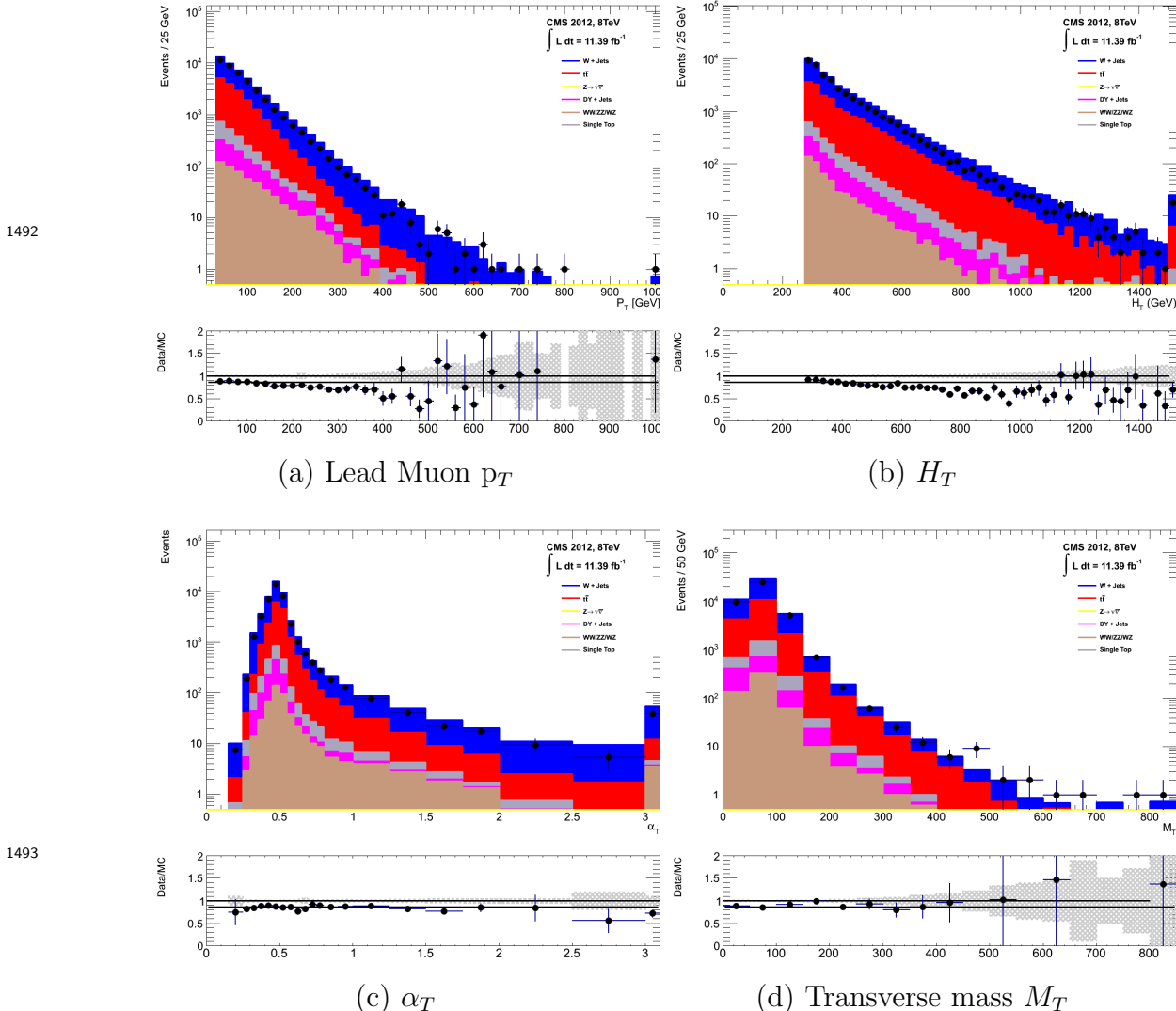


**Figure 4.6.:** Data/MC comparisons of key variables for the  $\mu + \text{jets}$  selection, following the application of selection criteria and the requirements that  $H_T > 275$  GeV. Bands represent the uncertainties due to the statistical size of the MC samples. No requirement is made upon the number of b-tagged jets or jet multiplicity in these distributions.

### The $\mu\mu + \text{jets}$ control sample

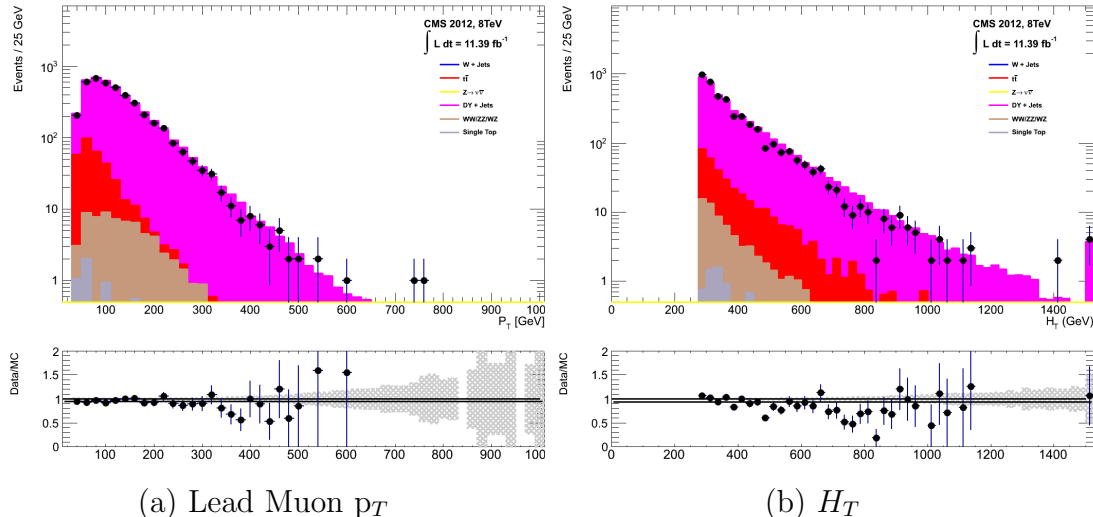
The  $Z \rightarrow \nu\bar{\nu} + \text{jets}$  background enters into the signal region from genuine  $E_T$  from the escaping neutrinos. This background is estimated using two control samples, the first of which is the  $Z \rightarrow \mu\bar{\mu} + \text{jets}$  process, which posses identical kinematic properties, but with different acceptance and branching ratio [1].

The same acceptance requirements as the  $\mu + \text{jets}$  selection for muons is applied, as defined in Table 4.2. Muons in the event are ignored for the purpose of the

calculation of event level variables. Kinematic jet-based cuts and phase space binning identical to the hadronic search region are also applied.

- Muons origination from a Z boson decay are selected requiring exactly two tightly isolated muons. Due to trigger requirements the leading muon is required to have  $p_T > 30$  GeV and  $|\eta| < 2.1$ . The requirement of the  $p_T$  on the second muon is relaxed to 10 GeV.
- Events are vetoed if containing a jet overlapping with a muon  $\Delta R(\mu, \text{jet}) < 0.5$ .
- In order to specifically select two muons both originating from a single Z boson decay, the invariant mass of the two muons must satisfy  $|M_{\mu\mu} - m_Z| < 25$ .

The  $\mu\mu + \text{jets}$  sample is used to make predictions in the signal region in the two lowest  $H_T$  bins, providing coverage where the  $\gamma + \text{jets}$  sample is unable to, due to trigger requirements. In higher  $H_T$  bins, the higher statistics of the  $\gamma + \text{jets}$  sample is also used in determining the  $Z \rightarrow \nu\bar{\nu}$  estimation.



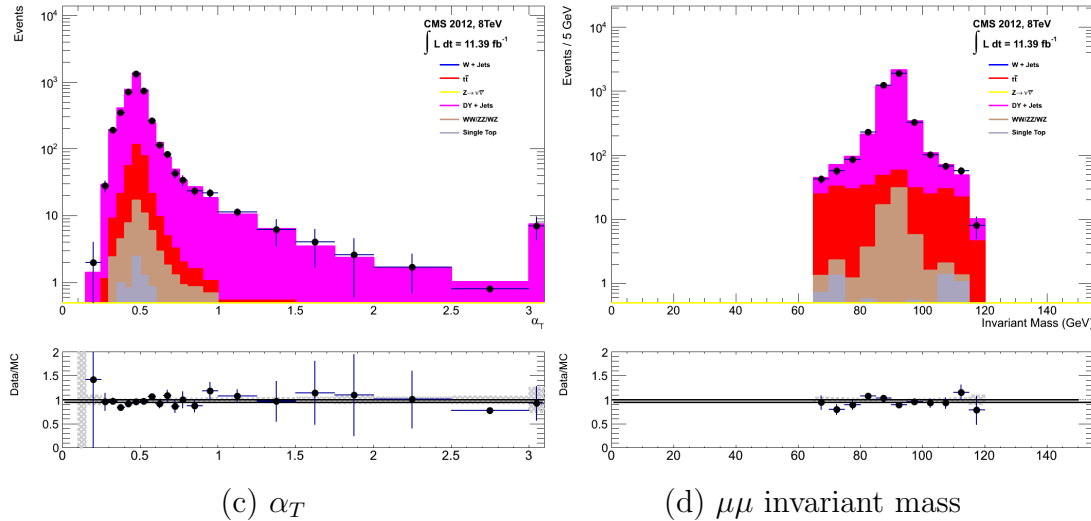


**Figure 4.7.:** Data/MC comparisons of key variables for the  $\mu\mu + \text{jets}$  selection, following the application of selection criteria and the requirements that  $H_T > 275$  GeV. Bands represent the uncertainties due to the statistical size of the MC samples. No requirement is made upon the number of b-tagged jets or jet multiplicity in these distributions.

## The $\gamma$ + jets control sample

The  $Z \rightarrow \nu\bar{\nu} + \text{jets}$  background is also estimated from a  $\gamma + \text{jets}$  control sample. When the  $E_T$  of the photon is greater than the mass of the  $Z$ , it possesses a larger cross section and kinematic properties similar to those of  $Z \rightarrow \mu\bar{\mu}$  events where the photon is ignored [80]. The photon is ignored for the purpose of the calculation of event level variables, and identical selection cuts to the hadronic signal region are applied.

- Exactly one photon is selected, satisfying identification criteria as detailed in Table 4.3, with a minimum  $p_T > 165$  GeV to satisfy trigger thresholds and  $|\eta| < 1.45$  to ensure the photon remains in the barrel of the detector.
  - A selection criteria of  $\Delta R(\gamma, jet) < 1.0$ , between the photon and all jets is applied to ensure the acceptance of only well isolated  $\gamma + \text{jets}$  events.
  - Given that the photon is ignored, this control sample can only be applied in the  $H_T$  region  $> 375$  GeV, due to the trigger thresholds on the minimum  $p_T$  of the photon, and the  $H_T$  requirement of an  $\alpha_T > 0.55$  cut from Equation (4.5), which is maintained in this control sample due to contamination from QCD in the absence of an  $\alpha_T$  cut.

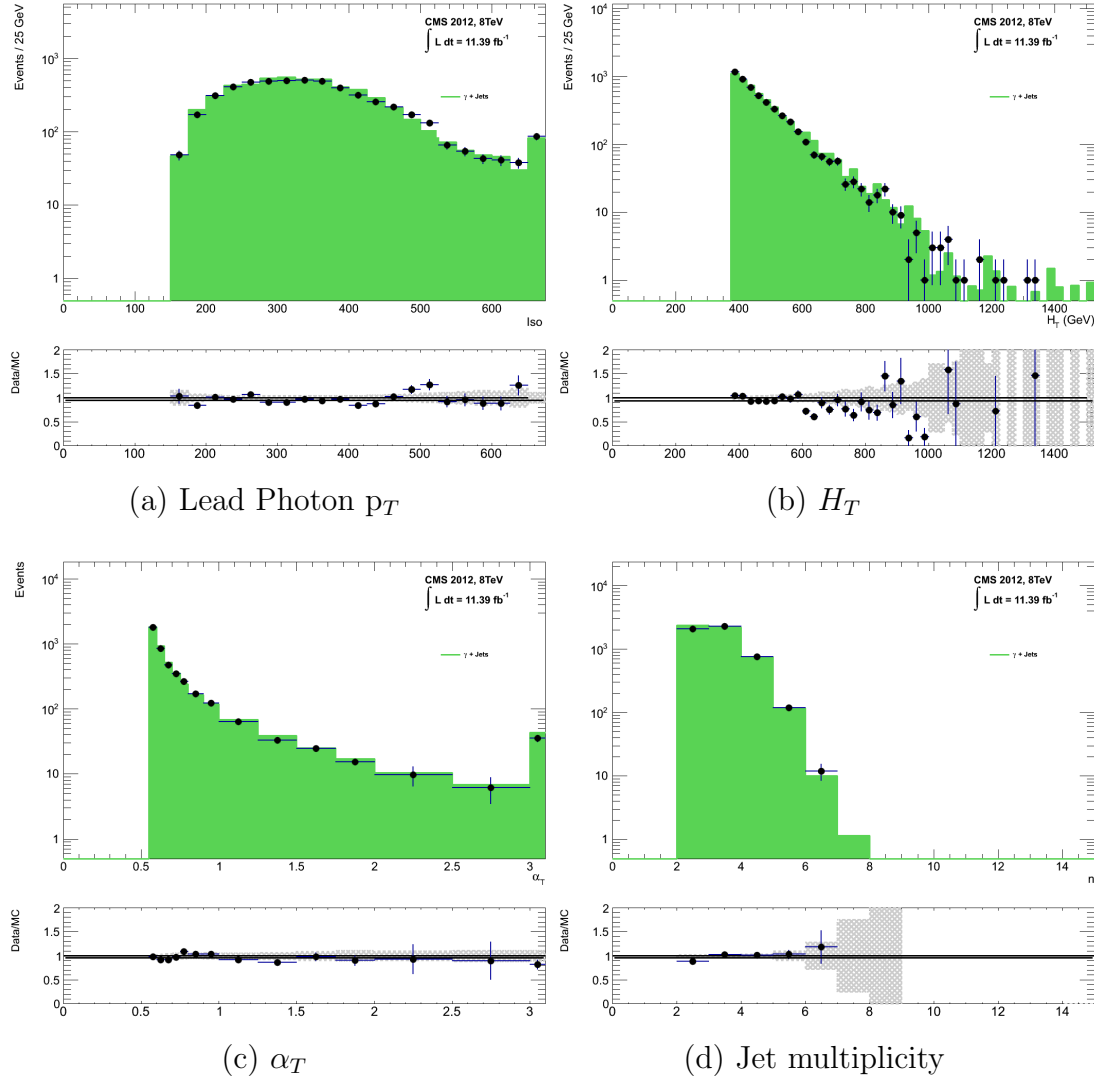


**Figure 4.8.:** Data/MC comparisons of key variables for the  $\gamma + \text{jets}$  selection, following the application of selection criteria and the requirements that  $H_T > 375 \text{ GeV}$  and  $\alpha_T > 0.55$ . Bands represent the uncertainties due to the statistical size of the MC samples. No requirement is made upon the number of b-tagged jets or jet multiplicity in these distributions.

1534 The selection criteria of the three control samples are defined to ensure background  
 1535 composition and event kinematics mirror closely the signal region. This is done in order  
 1536 to minimise the reliance on MC simulation to model correctly the backgrounds and event  
 1537 kinematics in the control and signal samples.

1538 However in the case of the  $\mu + \text{jets}$  and  $\mu\mu + \text{jets}$  samples, the  $\alpha_T$  requirement is relaxed  
 1539 in the selection criteria of these samples. This is made possible as contamination from  
 1540 QCD multi-jet events is suppressed to a negligible level by the other kinematic selection  
 1541 criteria within the two control samples, to select pure EWK processes. Thus in this way,

1542 the acceptance of the two muon control samples can be significantly increased, which  
1543 simultaneously improves their predictive power and further reduces the effect of any  
1544 potential signal contamination.

1545 The modelling of the  $\alpha_T$  variable is probed through a dedicated set of closure tests,  
1546 described in Section (4.6), which demonstrate that the different  $\alpha_T$  acceptances for the  
1547 control and signal samples have no significant systematic bias on the prediction.

#### 1548 4.2.4. Estimating the QCD multi-jet background

1549 A negligible background from QCD multi-jet events within the hadronic signal region  
1550 is expected due to the selection requirement, and additional cleaning filters applied.  
1551 However a conservative approach is still adopted and the likelihood model, see Section  
1552 (4.8.2), is given the freedom to accommodate any potential QCD multi-jet contamination.

1553 Any potential contamination can be identified through the variable  $R_{\alpha_T}$ , defined as the  
1554 ratio of events above and below the  $\alpha_T$  threshold value used in the analysis. This is  
1555 modelled by a  $H_T$  dependant falling exponential function which takes the form,

$$R_{\alpha_T}(H_T) = A_{\text{QCD}} \exp^{-k_{\text{QCD}} H_T}, \quad (4.10)$$

1556 where the parameters  $A_{\text{QCD}}$  and  $k_{\text{QCD}}$  are the normalisation and exponential decay  
1557 constants respectively.

1558 For QCD event topologies this exponential behaviour is expected as a function of  $H_T$  for  
1559 several reasons. The improvement of jet energy resolution at higher  $H_T$  due to higher  $p_T$   
1560 jets leads to a narrower peaked distribution, causing  $R_{\alpha_T}$  to fall. Similarly at higher  $H_T$   
1561 values  $> 375$  GeV, the jet multiplicity rises slowly with  $H_T$ . As shown in Figure 4.3, at  
1562 higher jet multiplicities, the result of the combinatorics used in the determination of  $\alpha_T$ ,  
1563 then leads to a narrower distribution.

1564 The value of the decay constant  $k_{\text{QCD}}$  is constrained via measurements within data  
1565 sidebands to the signal region. This is also done to validate the falling exponential  
1566 assumption for QCD multi-jet topologies. The sidebands are enriched in QCD multi-jet  
1567 background and defined as regions where  $\alpha_T$  is relaxed or that the  $R_{\text{miss}}$  cut is inverted.

1568 Figure 4.9 depicts the definition of these data sidebands used to constrain the value of  
1569  $k_{\text{QCD}}$ .

1570

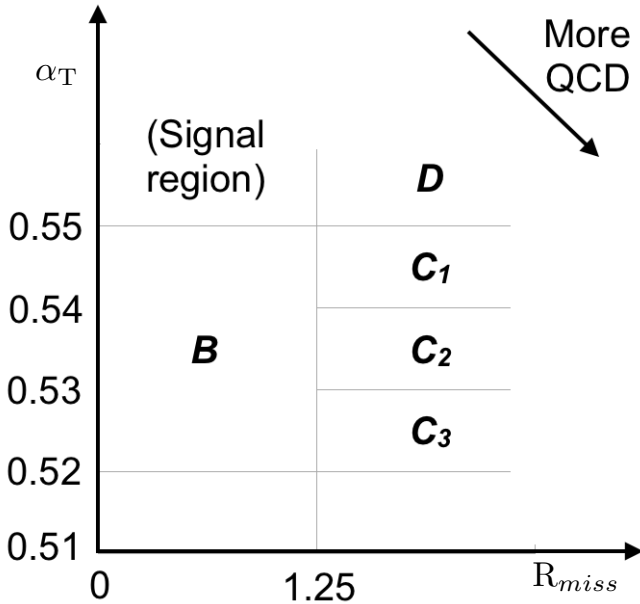


**Figure 4.9.:** QCD sideband regions, used for determination of  $k_{\text{QCD}}$ .

1571 The fits to determine the value of  $k_{\text{QCD}}$  are shown in Appendix (C.1), for which the best  
1572 fit value obtained from sideband region B is determined to be  $k_{\text{QCD}} = 2.96 \pm 0.64 \times 10^{-2}$   
1573  $\text{GeV}^{-1}$ .

1574 The best fit values of the remaining three C sideband regions are used to estimate  
1575 the systematic uncertainty on the central value obtained from sideband region B. The  
1576 variation of these measured values is used to determine the error on the determined  
1577 central value, and is calculated to be  $1.31 \pm 0.26 \times 10^{-2} \text{ GeV}^{-1}$ . This relative error of  $\sim$   
1578 20% gives an estimate of the systematic uncertainty of the measurement to be applied to  
1579  $k_{\text{QCD}}$ .

1580 Finally the same procedure is performed for sideband region D as an independent cross  
1581 check, to establish that the value of  $k_{\text{QCD}}$  extracted from a lower  $\alpha_T$  slice, can be applied  
1582 to the signal region  $\alpha_T > 0.55$ . The likelihood fit is performed across all  $H_T$  bins within  
1583 the QCD enriched region with no constraint applied to  $k_{\text{QCD}}$ . The resulting best fit  
1584 value for  $k_{\text{QCD}}$  shows good agreement between that and the weighted mean determined  
1585 from the three C sidebands regions. This demonstrates that the assumption of using the  
1586 central value determined from sideband region B, to provide an unbiased estimator for  
1587  $k_{\text{QCD}}$  in the signal region ( $\alpha_T > 0.55$ ) is valid.

1588 Table 4.7, summarises the best fit  $k_{\text{QCD}}$  values determined for each of the sideband  
1589 regions to the signal region.

Sideband region	$k_{\text{QCD}} (\times 10^{-2} \text{GeV}^{-1})$	$p$ -value
B	$2.96 \pm 0.64$	0.24
C <sub>1</sub>	$1.19 \pm 0.45$	0.93
C <sub>2</sub>	$1.47 \pm 0.37$	0.42
C <sub>3</sub>	$1.17 \pm 0.55$	0.98
C(weighted mean)	$1.31 \pm 0.26$	-
D(likelihood fit)	$1.31 \pm 0.09$	0.57

**Table 4.7.:** Best fit values for the parameters  $k_{\text{QCD}}$  obtained from sideband regions B,C<sub>1</sub>,C<sub>2</sub>,C<sub>3</sub>. The weighted mean is determined from the three measurements made within sideband region C. The maximum likelihood value of  $k_{\text{QCD}}$  given by the simultaneous fit using sideband region D. Quotes errors are statistical only.

### 1590 4.3. Trigger Strategy

1591 A cross trigger based on the  $H_T$  and  $\alpha_T$  values of an event, is used with varying thresholds  
1592 across  $H_T$  bins to record the events used in the hadronic signal region. The  $\alpha_T$  legs of  
1593 the HT\_alphaT triggers used in the analysis are chosen to suppress QCD multi-jet events  
1594 and control trigger rate, whilst maintaining signal acceptance. To further maintain an  
1595 acceptable rate for these analysis specific triggers, only calorimeter information is used  
1596 in the reconstruction of the  $H_T$  sum, leading to the necessity for Calo jets to be used  
1597 within the analysis.

1598 A single object prescaled HT trigger is used to collect events for the hadronic control  
1599 region described above in Section (4.2.4).

1600 The performance of the  $\alpha_T$  and  $H_T$  triggers used to collect data for the signal and  
1601 hadronic control region is measured with respect to a reference sample collected using the  
1602 muon system. This allows measurement of both the Level 1 seed and higher level triggers  
1603 simultaneously, as the reference sample is collected independent of any jet requirements.

1604 The selection for the trigger efficiency measurement is identical to that described in  
1605 Section (4.2.2), with the requirement of exactly one well identified muon with  $p_T > 30$   
1606 GeV which is subsequently ignored.

1607 The efficiencies measured for the HT\_alphaT triggers in bins individual  $H_T$  and  $\alpha_T$  legs,  
1608 is summarised in Table 4.8.

$H_T$ range (GeV)	$\epsilon$ on $H_T$ leg (%)	$\epsilon$ on $\alpha_T$ leg (%)
275-325	$87.7^{+1.9}_{-1.9}$	$82.8^{+1.0}_{-1.1}$
325-375	$90.6^{+2.9}_{-2.9}$	$95.9^{+0.7}_{-0.9}$
375-475	$95.7^{+0.1}_{-0.1}$	$98.5^{+0.5}_{-0.9}$
475- $\infty$	$100.0^{+0.0}_{-0.0}$	$100.0^{+0.0}_{-4.8}$

**Table 4.8.:** Measured efficiencies of the  $H_T$  and  $\alpha_T$  legs of the HT and HT\_alphaT triggers in independent analysis bins. The product of the two legs gives the total efficiency of the trigger in a given offline  $H_T$  bin.

1609 Data for the control samples of the analysis, detailed in Section (4.2.3), are collected  
1610 using single object photon trigger for the  $\gamma +$  jets sample, and a single object muon  
1611 trigger for both the  $\mu +$  jets and  $\mu\mu +$  jets control samples.

1612 The photon trigger is measured to be full efficient for the threshold  $p_T^{\text{photon}} > 150$  GeV,  
1613 whilst the single muon efficiency satisfying  $p_T^{\text{muon}} > 30$  GeV is measured to have an  
1614 efficiency of  $(88 \pm 2)\%$  that is independent of  $H_T$ . In the case of the  $\mu\mu +$  jets control  
1615 sample, the efficiency is measured to be  $(95 \pm 2)\%$  for the lowest  $H_T$  bin, rising (due to  
1616 the average  $p_T$  of the second muon in the event increasing at larger  $H_T$ ) to  $(98 \pm 2)\%$  for  
1617 the highest  $H_T$  bin.

## 1618 4.4. Measuring MC Normalisation Factors via $H_T$ 1619 Sidebands

1620 The theoretical cross sections of different **SM** processes at Next to Next Leading Order  
1621 (**NNLO**) and the number of MC simulated events generated for that particular process,  
1622 is typically used to determine the appropriate normalisation for a MC sample. However  
1623 within the particular high- $H_T$  and high- $\cancel{E}_T$  corners of kinematic phase space probed  
1624 within this search, the theoretical cross sections for various processes are far less well  
1625 understood.

1626 To mitigate the problem of theoretical uncertainties and arbitrary choices of cross sections,  
1627 the normalisation of MC samples used in the analysis are determined through the use  
1628 data sidebands. The sidebands are used to calculate sample specific correction factors  
1629 (k-factors) that are appropriate for the  $H_T$ - $\cancel{E}_T$  phase space covered by this analysis.

1630 They are defined within the  $\mu +$  jets and  $\mu\mu +$  jets control sample, by the region  $200 <$   
1631  $H_T < 275$ , using the same jet  $p_T$  thresholds as the adjacent first analysis bin. Individual

1632 EWK processes are isolated within each of these control samples via requirements on  
1633 jet multiplicity and the requirement on b-tags, summarised in Table 4.9. The purity of  
1634 the samples are typically  $> 90\%$  with any residual contamination corrected for. The  
1635 resultant k-factor for each process is determined by then taking ratio of the data yield  
1636 over the MC expectation in the sideband. Subsequently these k-factors are then applied  
1637 to the processes within the phase space of the analysis.

Process	Selection	Observation	MC expectation	k-factor
W + jets	$\mu + \text{jets}, n_b=0, n_{jet} = 2,3$	26950	$29993.2 \pm 650.1$	$0.90 \pm 0.02$
$Z \rightarrow \mu\mu + \text{jets}$	$\mu\mu + \text{jets}, n_b=0, n_{jet} = 2,3$	3141	$3402.0 \pm 43.9$	$0.92 \pm 0.02$
$t\bar{t}$	$\mu + \text{jets}, n_b=2, n_{jet} = \geq 4$	2190	$1967.8 \pm 25.1$	$1.11 \pm 0.02$

**Table 4.9.:** k-factors calculated for different EWK processes. All k-factors are derived relative to theoretical cross sections calculated in NNLO. The k-factors measured for the  $Z \rightarrow \mu\mu + \text{jets}$  processes, are also applied to the  $Z \rightarrow \nu\bar{\nu} + \text{jets}$  and  $\gamma + \text{jets}$  MC samples.

1638 It is worth pointing out that these correction factors have a negligible effect when  
1639 providing a background estimation for the signal region. The TF's used in the analysis  
1640 are found to be unaffected by application of these k-factors due to the similarity in the  
1641 background composition of the control and signal regions. However when systematic  
1642 uncertainties are determined in Section (4.6), the closure tests performed are sensitive  
1643 to these corrections when extrapolations between different  $n_b^{reco}$  and  $n_{jet}$  categories are  
1644 performed.

## 1645 4.5. Determining MC Simulation Yields with 1646 Higher Statistical Precision

1647 Reconstructing events from EWK processes with many b-tagged jets ( $\geq 3$ ),  $n_b^{reco}$ , is largely  
1648 driven by the mis-tagging of light jets within the event. This is clear when considering  
1649 the main EWK backgrounds in the analysis, such as  $t\bar{t} + \text{jets}$  events, which typically  
1650 contain two b-flavoured jets from the decay of the top quarks, whilst W + jets and  
1651 Z  $\rightarrow \mu\mu + \text{jets}$  events will typically contain no b-flavoured jets.

1652 When the expectation for the number of  $n_b^{reco}$  is taken directly from simulation, the  
1653 statistical uncertainty at large b-tag multiplicities becomes relatively large. In order to  
1654 reduce this uncertainty one approach is to use the information encoded throughout all  
1655 events in the simulation sample, to measure each of the four ingredients:

- 
- 1656     1. the b-tagging efficiency in the event selection,  
1657     2. the charm-tagging efficiency in the event selection  
1658     3. the mis-tagging rate in the event selection,  
1659     4. the underlying flavour distribution of the jets in the events,

1660   that determine the  $n_b^{reco}$  distribution of the process being measured. This method allows  
1661   the determination of higher b-tag multiplicities to a higher degree of accuracy reducing  
1662   the statistical uncertainties of the MC which enter into the TF's. For the discussion that  
1663   follows, these predictions are determined on average (i.e not on an event-by-event basis),  
1664   and is known as the formula method.

#### 1665   **4.5.1. The formula method**

1666   The assigning of jet flavours to reconstruction level jets in simulation is achieved via an  
1667   algorithmic method defined as:

- 1668   • Try to find the parton that most likely determines the properties of the jet and  
1669    assign that flavour as true flavour,  
1670   • “final state” partons (after showering, radiation) are analysed (also within  $\Delta R <$   
1671    0.3 of reconstructed jet cone),  
1672   • If there is a b/c flavoured parton within the jet cone: label as b/c flavoured jet,  
1673   • Otherwise: assign flavour of the hardest parton.

1674   This process is employed within each individual MC process and independently for each  
1675    $H_T$ -  $n_{jet}$  bin in the analysis, the  $n_b^{reco}$  distribution is then constructed in the following  
1676   way:

1677   Let  $N(n_b^{gen}, n_c^{gen}, n_q^{gen})$  represent the yield in simulation of events with  $b$  underlying  
1678   b-quarks,  $c$  underlying c-quarks and  $q$  underlying light quarks which are matched to  
1679   reconstructed jets as detailed above. Light quarks defined as those which originate from  
1680   a  $u$ ,  $d$ ,  $s$ ,  $g$  and  $\tau$  jets, which having similar mis-tagging rates are grouped together.  
1681   Similarly  $\epsilon$ ,  $\beta$  and  $m$  represent the measured b-tagging, c-tagging and mis-tagging  
1682   efficiency averaged over all the jets within that particular analysis bin.

1683 Using this information the expected  $n_b^{reco}$  distribution can be analytically calculated  
1684 using the formula :

$$N(n_b) = \sum_{n_b^{gen} + n_c^{gen} + n_q^{gen} = n_{jet}} \sum_{n_b^{tag} + n_c^{tag} + n_q^{tag} = n_b} N(n_b^{gen}, n_c^{gen}, n_q^{gen}) \times P(n_b^{tag}, n_b^{gen}, \epsilon) \times \\ P(n_c^{tag}, n_c^{gen}, \beta) \times P(n_q^{tag}, n_q^{gen}, m), \quad (4.11)$$

1685 with  $N(n_b)$  representing the yield where  $n_b$  jets have been b-tagged. The variables  $n_b^{tag}$ ,  
1686  $n_c^{tag}$  and  $n_q^{tag}$  represent the number of times that a particular jet flavour results in a  
1687 b-tagged jet, and finally  $P(n_b^{tag}, n_b^{gen}, \epsilon)$ ,  $P(n_c^{tag}, n_c^{gen}, \beta)$  and  $P(n_q^{tag}, n_q^{gen}, m)$  represent  
1688 the binomial probabilities for that to happen.

1689 This approach ultimately results in a more precise  $n_b^{reco}$  distribution prediction, due to  
1690 the utilisation of the entire MC sample in extracting the estimated underlying  $n_b^{reco}$   
1691 distribution.

### 1692 4.5.2. Establishing proof of principle

1693 In order to validate the procedure, the predictions obtained from the formula method  
1694 summarised in Equation (4.11), are compared directly to those obtained directly from  
1695 simulation. Resultantly no simulation to data correction factors are applied when making  
1696 this comparison

1697 This sanity check for the  $\mu +$  jets control sample is presented in Table 4.10, for all  $n_b^{reco}$   
1698 and  $H_T$  bins with no requirement placed upon the jet multiplicity of the events.

1699 It can be seen as expected, that there is good consistency between the results determined  
1700 via the formula method and ‘raw’ simulation yields. Similarly the power of this approach  
1701 can be seen in the reduction of this statistical error in the prediction across all  $H_T$  and  
1702  $n_b^{reco}$  bins. In particular the statistical uncertainty is reduced by several factors in the  
1703 highest  $n_b^{reco} \geq 4$  category.

$H_T$ Bin (GeV)	275–325	325–375	375–475	475–575
Formula $n_b = 0$	12632.66 $\pm$ 195.48	6696.08 $\pm$ 82.59	6368.96 $\pm$ 75.34	2906.27 $\pm$ 39.65
Vanilla $n_b = 0$	12612.95 $\pm$ 198.68	6687.97 $\pm$ 83.78	6359.27 $\pm$ 76.50	2898.27 $\pm$ 36.89
Formula $n_b = 1$	4068.09 $\pm$ 45.71	2272.76 $\pm$ 26.14	2181.32 $\pm$ 25.07	1089.14 $\pm$ 13.82
Vanilla $n_b = 1$	4067.73 $\pm$ 60.30	2268.02 $\pm$ 30.20	2180.69 $\pm$ 28.73	1094.37 $\pm$ 24.14
Formula $n_b = 2$	1963.71 $\pm$ 22.44	1087.55 $\pm$ 13.57	1055.57 $\pm$ 13.25	554.96 $\pm$ 7.95
Vanilla $n_b = 2$	1984.53 $\pm$ 26.19	1094.43 $\pm$ 16.67	1068.96 $\pm$ 16.36	558.14 $\pm$ 10.51
Formula $n_b = 3$	146.94 $\pm$ 2.07	79.97 $\pm$ 1.37	78.05 $\pm$ 1.35	49.84 $\pm$ 1.03
Vanilla $n_b = 3$	149.52 $\pm$ 4.84	85.98 $\pm$ 3.64	74.45 $\pm$ 3.29	49.54 $\pm$ 2.68
Formula $n_b \geq 4$	2.26 $\pm$ 0.12	1.29 $\pm$ 0.10	5.32 $\pm$ 0.20	-
Vanilla $n_b \geq 4$	1.84 $\pm$ 0.50	1.02 $\pm$ 0.39	4.86 $\pm$ 0.83	-
$H_T$ Bin (GeV)	575–675	675–775	775–875	>875
Formula $n_b = 0$	1315.68 $\pm$ 19.49	640.49 $\pm$ 11.90	327.81 $\pm$ 7.91	424.27 $\pm$ 9.27
Vanilla $n_b = 0$	1315.23 $\pm$ 20.20	641.96 $\pm$ 12.48	329.09 $\pm$ 8.36	424.02 $\pm$ 9.73
Formula $n_b = 1$	490.41 $\pm$ 7.45	226.95 $\pm$ 4.42	109.91 $\pm$ 2.84	129.97 $\pm$ 3.07
Vanilla $n_b = 1$	490.52 $\pm$ 9.92	222.22 $\pm$ 6.21	107.46 $\pm$ 4.15	129.64 $\pm$ 4.64
Formula $n_b = 2$	256.75 $\pm$ 4.58	113.45 $\pm$ 2.70	52.10 $\pm$ 1.69	59.29 $\pm$ 1.78
Vanilla $n_b = 2$	253.43 $\pm$ 6.52	117.17 $\pm$ 4.27	52.70 $\pm$ 2.80	59.45 $\pm$ 3.00
Formula $n_b = 3$	25.66 $\pm$ 0.69	12.48 $\pm$ 0.46	5.52 $\pm$ 0.31	6.83 $\pm$ 0.33
Vanilla $n_b = 3$	29.18 $\pm$ 2.06	11.77 $\pm$ 1.26	6.18 $\pm$ 0.95	7.53 $\pm$ 1.05

**Table 4.10.:** Comparing yields in simulation within the  $\mu +$  jets selection determined from the formula method described in Equation (4.11), and that taken directly from simulation . The numbers are normalised to  $11.4\text{fb}^{-1}$ . No simulation to data corrections are applied.

### 4.5.3. Correcting measured efficiencies in simulation to data

As detailed in Section (3.3.2), it is necessary for certain  $p_T$  and  $\eta$  dependant corrections, to be applied to both the b-tagging efficiency and mis-tagging rates in order correct the efficiencies from simulation to the distributions seen in data. These corrections factors are considered when determining the simulation yields for each selection, which are used to construct the TF's of the analysis.

Each of the corrections factors for the b, c and light flavoured jets come with an associated systematic uncertainty. The uncertainties across different jet  $p_T$  and  $\eta$  bins, are considered as fully correlated. When computing the magnitude of the effect of this systematic uncertainty on the TF's of the analysis, the scale factors are therefore scaled

1714 up/down simultaneously within each  $H_T$  bin of the analysis for all of the  $SF_{b,c,\text{light}}$  scale  
1715 factors. The magnitude of this correction is shown for each  $H_T$  bin within Figure 4.10.

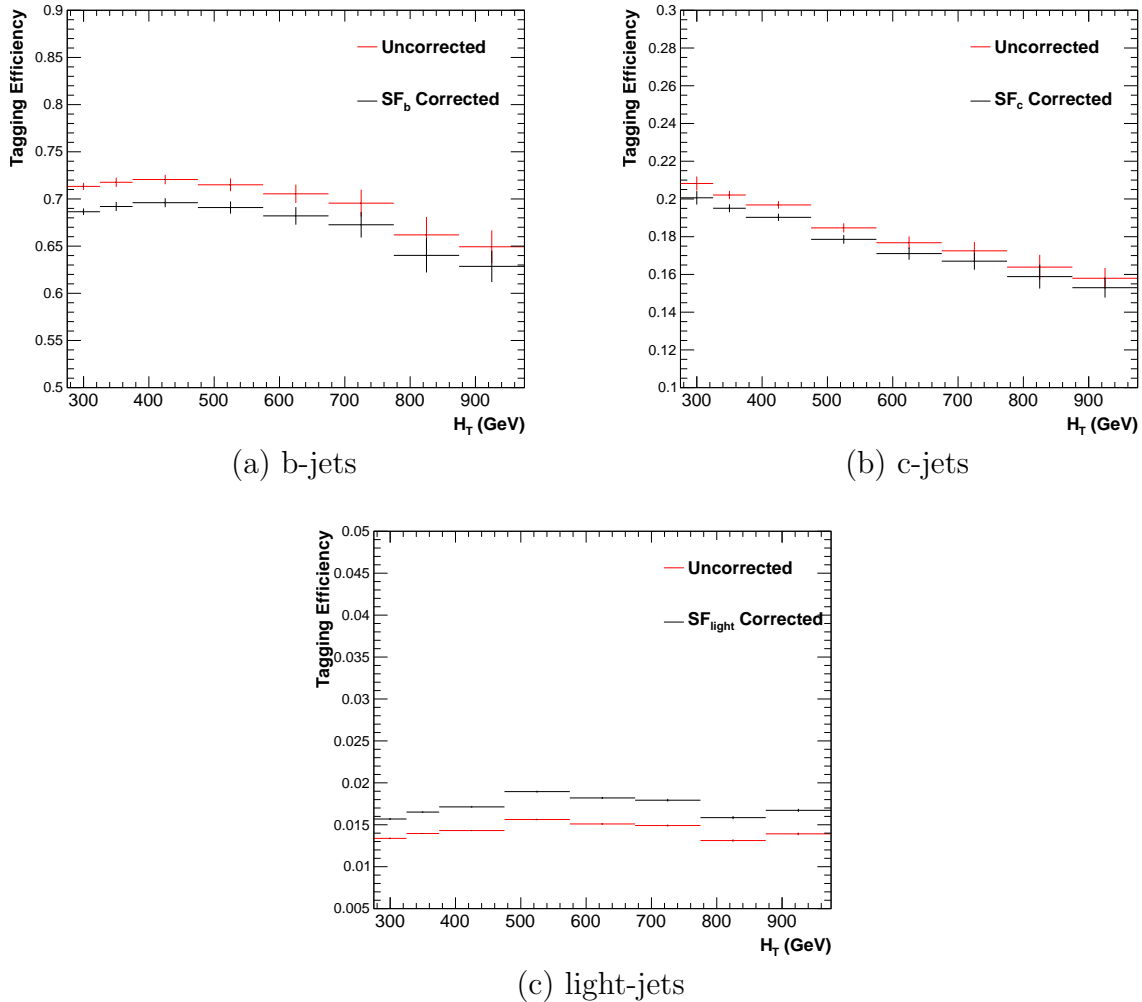


**Figure 4.10.:** Tagging efficiencies of (a) b-jets, (b) c-jets, and (c) light-jets as a function all jets within each individual analysis  $H_T$  bin. Efficiencies measured directly from simulation (black) and with data to simulation  $SF_{b,c,\text{light}}$  correction factors (red) are applied.

1716 Varying the scale factor corrections by their systematic uncertainty will change the  
1717 absolute yields within each  $n_b^{reco}$  bin of all selections. However, ultimately it is the change  
1718 in the TF's which influences the final background prediction from each of the control  
1719 samples. The magnitude of the absolute change in each TF, constructed from when the  
1720  $\mu + \text{jets}$  control sample is used to predict the entire hadronic signal region background,  
1721 is shown in Table 4.11.,

$n_b^{reco}$	275–325	325–375	375–475	475–575
= 0	0.557 $^{+0.001}_{-0.001}$ $\pm$ 0.012	0.495 $^{+0.001}_{-0.001}$ $\pm$ 0.009	0.383 $^{+0.001}_{-0.001}$ $\pm$ 0.005	0.307 $^{+0.001}_{-0.002}$ $\pm$ 0.006
= 1	0.374 $^{+0.006}_{-0.006}$ $\pm$ 0.006	0.320 $^{+0.006}_{-0.005}$ $\pm$ 0.005	0.251 $^{+0.005}_{-0.005}$ $\pm$ 0.004	0.185 $^{+0.003}_{-0.003}$ $\pm$ 0.004
= 2	0.226 $^{+0.002}_{-0.002}$ $\pm$ 0.004	0.201 $^{+0.001}_{-0.002}$ $\pm$ 0.004	0.159 $^{+0.001}_{-0.001}$ $\pm$ 0.004	0.134 $^{+0.000}_{-0.001}$ $\pm$ 0.004
= 3	0.221 $^{+0.002}_{-0.002}$ $\pm$ 0.005	0.208 $^{+0.002}_{-0.001}$ $\pm$ 0.007	0.164 $^{+0.001}_{-0.000}$ $\pm$ 0.006	0.144 $^{+0.001}_{-0.001}$ $\pm$ 0.007
$\geq 4$	0.222 $^{+0.004}_{-0.005}$ $\pm$ 0.015	0.248 $^{+0.003}_{-0.003}$ $\pm$ 0.035	0.123 $^{+0.002}_{-0.003}$ $\pm$ 0.009	-
	575–675	675–775	775–875	$\geq 875$
= 0	0.263 $^{+0.001}_{-0.002}$ $\pm$ 0.006	0.215 $^{+0.000}_{-0.001}$ $\pm$ 0.007	0.171 $^{+0.000}_{-0.001}$ $\pm$ 0.009	0.111 $^{+0.000}_{-0.001}$ $\pm$ 0.006
= 1	0.154 $^{+0.003}_{-0.003}$ $\pm$ 0.005	0.138 $^{+0.003}_{-0.004}$ $\pm$ 0.006	0.121 $^{+0.005}_{-0.005}$ $\pm$ 0.007	0.091 $^{+0.002}_{-0.002}$ $\pm$ 0.006
= 2	0.104 $^{+0.000}_{-0.001}$ $\pm$ 0.005	0.079 $^{+0.001}_{-0.001}$ $\pm$ 0.006	0.063 $^{+0.001}_{-0.002}$ $\pm$ 0.007	0.071 $^{+0.000}_{-0.000}$ $\pm$ 0.008
= 3	0.116 $^{+0.001}_{-0.001}$ $\pm$ 0.009	0.069 $^{+0.001}_{-0.001}$ $\pm$ 0.007	0.079 $^{+0.001}_{-0.001}$ $\pm$ 0.017	0.095 $^{+0.003}_{-0.002}$ $\pm$ 0.020

**Table 4.11.:** The absolute change in the **TF**'s used to predict the entire signal region **SM** background, using the  $\mu + \text{jets}$  control sample when the systematic uncertainties of the data to simulation scale factors are varied by  $\pm 1\sigma$ . The impact of the change is shown for each  $H_T$  and  $n_b^{reco}$  bin with no requirement made on the jet multiplicity of the events. (Also quoted are the statistical uncertainties)

1722 It can be seen that the **TF**'s are found to be relatively insensitive to the systematic  
 1723 uncertainty of the b-tag scale factors (showing typically less than  $\sim 2\%$  change). This can  
 1724 be accounted for by the similar composition of the signal and control sample backgrounds,  
 1725 such that any change in the underlying  $n_b^{reco}$  distribution will be reflected in both signal  
 1726 and control regions and cancel out in the **TF**.

1727 Any overall systematic effect on the overall background prediction of the analysis from  
 1728 these b-tag scale factor uncertainties is incorporated within the data driven systematics  
 1729 introduced in the following section.

## 1730 4.6. Systematic Uncertainties on Transfer Factors

1731 Since the **TF**'s used to establish the background prediction are obtained from simulation,  
 1732 an appropriate systematic uncertainty is assigned to each factor to account for theoretical  
 1733 uncertainties [81] and limitations in the simulation modelling of event kinematics and  
 1734 instrumental effects.

1735 The magnitudes of these systematic uncertainties are established through a set of data  
1736 driven method, in which the three independent control samples of the analysis ( $\mu + \text{jets}$ ,  
1737  $\mu\mu + \text{jets}$ ,  $\gamma + \text{jets}$ ) are used to in a series of closure tests. The yields from one of these  
1738 control samples, along with the corresponding TF obtained from simulation, are used to  
1739 predict the yields in another control sample, using the same method of establishing a  
1740 background prediction for the signal region as described in Section (4.2.3).

1741 The level of agreement between the predicted and observed yields is expressed as the  
1742 ratio

$$\frac{(N_{\text{obs}} - N_{\text{pred}})}{N_{\text{pred}}}, \quad (4.12)$$

1743 while considering only the statistical uncertainties on  $N_{\text{pred}}$ , the prediction, and  $N_{\text{obs}}$ , the  
1744 observation. No systematic uncertainty is assigned to the prediction, and resultantly the  
1745 level of closure is defined by the statistical significance of a deviation from the ratio from  
1746 zero.

1747 This ratio is measured for each  $H_T$  bin in the analysis, allowing these closure tests to be  
1748 sensitive to both the presence of any significant biases or any possible  $H_T$  dependence on  
1749 the level of closure.

1750 Eight sets of closure tests are defined between the three data control samples, conducted  
1751 independently between the two jet multiplicity ( $2 \leq n_{\text{jet}} \leq 3$ ,  $n_{\text{jet}} \geq 4$ ) bins. Each of  
1752 these tests are specifically chosen to probe each of the different key ingredients of the  
1753 simulation modelling that can affect the background prediction.

1754 Each of the different modelling components and the relevant closure tests are described  
1755 below :

### 1756 $\alpha_T$ modelling

1757 The modelling of the  $\alpha_T$  distribution in genuine  $E_T$  events is probed with the  $\mu +$   
1758 jets control sample. This test is important to verify the approach of remove the  $\alpha_T$   
1759  $> 0.55$  requirement from the  $\mu + \text{jets}$  and  $\mu\mu + \text{jets}$  samples to increase the precision  
1760 of the background prediction. The test uses the  $\mu + \text{jets}$  sample without an  $\alpha_T$  cut  
1761 to make a prediction into the  $\mu + \text{jets}$  sample defined with the requirement  $\alpha_T >$   
1762 0.55.

**1763 Background admixture**

1764 The sensitivity of the translation factors to the relative admixture of events from  
1765  $W + \text{jets}$  and  $t\bar{t}$  processes is probed by two closure tests. These tests represent  
1766 an extremely conservative approach as the admixture of the background remains  
1767 similar between the  $\mu + \text{jets}$  sample and the signal region, contrary to the defined  
1768 closure tests which make predictions between two very different admixtures of  $W +$   
1769 jets and  $t\bar{t}$  events.

1770 Within the  $\mu + \text{jets}$  sample, a  $W$  boson enriched sub-sample ( $n_b = 0$ ) is used  
1771 to predict yields in a  $t\bar{t}$  enriched sub-sample ( $n_b = 1$ ). Similarly the  $t\bar{t}$  enriched  
1772 sub-sample ( $n_b = 1$ ) is also used to predict yields for a further enriched  $t\bar{t}$  sub-sample  
1773 ( $n_b = 2$ ), further probing the modelling of the  $n_b^{reco}$  distribution.

1774 Similarly a further closure test probes the relative contribution of  $Z + \text{jets}$  to  $W + \text{jets}$   
1775 and  $t\bar{t}$  events, through the use of the  $\mu + \text{jets}$  sample to predict yields for the  $\mu\mu +$   
1776  $\text{jets}$  control sample. This closure test, also at some level probes the muon trigger  
1777 and reconstruction efficiencies, given that exactly one or two muons are required by  
1778 the different selections.

**1779 Consistency check between  $Z \rightarrow \nu\bar{\nu}$  predictions**

1780 An important consistency check between the  $\mu\mu + \text{jets}$  and  $\gamma + \text{jets}$ , which are  
1781 both used in the prediction of the  $Z \rightarrow \nu\bar{\nu}$  in the signal region. This is conducted by  
1782 using the  $\gamma + \text{jets}$  sample to predict yields for the  $\mu\mu + \text{jets}$  control sample. Using  
1783  $\gamma + \text{jets}$  processes as a method to predict  $Z + \text{jet}$  processes is subject to theory  
1784 uncertainties [82], which can be probed by this data driven closure test within a  
1785  $Z \rightarrow \mu\mu$  control sample.

**1786 Modelling of jet multiplicity**

1787 The simulation modelling of the jet multiplicity within each control sample is  
1788 important due to the exclusive jet multiplicity binning within the analysis. This is  
1789 probed via the use of each of the three control samples to independently predict from  
1790 the lower jet multiplicity category  $2 \leq n_{\text{jet}} \leq 3$ , to the high jet category  $n_{\text{jet}} \geq 4$ .

1791 For the case of the  $\mu + \text{jets}$  and  $\mu\mu + \text{jets}$  control samples this test is also a  
1792 further probe of the admixture between  $W + \text{jets}/Z + \text{jets}$  and  $t\bar{t}$ .

1793 To test for the assumption that no  $H_T$  dependences exist within the background predic-  
1794 tions of the analysis, the first five closure tests defined above are used, with zeroeth and

1795 first order polynomial fits are applied to each test individually. This is summarised in  
1796 Table 4.12 and Table 4.13 which show the results for both the  $2 \leq n_{jet} \leq 3$  and  $\geq 4$  jet  
1797 multiplicity bins respectively.

Closure test	Symbol	Constant fit		Linear fit	
		Best fit value	p-value	Slope ( $10^{-4}$ )	p-value
$\alpha_T < 0.55 \rightarrow \alpha_T > 0.55 (\mu + \text{jets})$	Circle	$-0.06 \pm 0.02$	0.93	$-1.3 \pm 2.2$	0.91
$0 \text{ b-jets} \rightarrow 1 \text{ b-jet } (\mu + \text{jets})$	Square	$0.07 \pm 0.02$	0.98	$-1.6 \pm 1.6$	1.00
$1 \text{ b-jets} \rightarrow 2 \text{ b-jet } (\mu + \text{jets})$	Triangle	$-0.07 \pm 0.03$	0.76	$-2.7 \pm 3.0$	0.76
$\mu + \text{jets} \rightarrow \mu\mu + \text{jets}$	Cross	$0.10 \pm 0.03$	0.58	$-1.1 \pm 2.3$	0.49
$\mu\mu + \text{jets} \rightarrow \gamma + \text{jets}$	Star	$-0.06 \pm 0.04$	0.31	$4.2 \pm 4.3$	0.29

**Table 4.12.:** A summary of the results obtained from zeroeth order polynomial (i.e. a constant) and linear fits to five sets of closure tests performed in the  $2 \geq n_{jet} \geq 3$  category. The two columns show the best fit value for the slope obtained when performing a constant (left) and linear (right) fit and the p-value for that fit.

Closure test	Symbol	Constant fit		Linear fit	
		Best fit value	p-value	Slope ( $10^{-4}$ )	p-value
$\alpha_T < 0.55 \rightarrow \alpha_T > 0.55 (\mu + \text{jets})$	Circle	$-0.05 \pm 0.03$	0.21	$3.0 \pm 2.9$	0.21
$0 \text{ b-jets} \rightarrow 1 \text{ b-jet } (\mu + \text{jets})$	Square	$-0.03 \pm 0.03$	0.55	$-1.0 \pm 1.9$	0.47
$1 \text{ b-jets} \rightarrow 2 \text{ b-jet } (\mu + \text{jets})$	Triangle	$-0.02 \pm 0.03$	0.39	$1.1 \pm 2.2$	0.31
$\mu + \text{jets} \rightarrow \mu\mu + \text{jets}$	Cross	$0.08 \pm 0.07$	0.08	$4.8 \pm 4.3$	0.07
$\mu\mu + \text{jets} \rightarrow \gamma + \text{jets}$	Star	$-0.03 \pm 0.10$	0.72	$-4.0 \pm 7.0$	0.64

**Table 4.13.:** A summary of the results obtained from zeroeth order polynomial (i.e. a constant) and linear fits to five sets of closure tests performed in the  $n_{jet} \geq 4$  category. The two columns show the best fit value for the slope obtained when performing a constant (left) and linear (right) fit and the p-value for that fit.

1798 Table 4.14 shows the same fits applied to the three closure tests that probe the modelling  
1799 between the different  $n_{jet}$  bins. The best fit value and its uncertainty is listed for each  
1800 set of closure tests in all three tables, along with the p-value of the constant and linear  
1801 fits applied.

Closure test	Symbol	Constant fit		Linear fit	
		Best fit value	p-value	Slope ( $10^{-4}$ )	p-value
$\mu + \text{jets}$	Inverted triangle	$-0.03 \pm 0.02$	0.02	$0.0 \pm 1.0$	0.01
$\mu + \text{jets}$ (outlier removed)	Inverted triangle	$-0.04 \pm 0.01$	0.42	$-1.4 \pm 1.1$	0.49
$\gamma + \text{jets}$	Diamond	$0.12 \pm 0.05$	0.79	$6.0 \pm 4.7$	0.94
$\mu\mu + \text{jets}$	Asterisk	$-0.04 \pm 0.07$	0.20	$4.9 \pm 4.4$	0.20

**Table 4.14.:** A summary of the results obtained from zeroeth order polynomial (i.e. a constant) and linear fits to five sets of closure tests performed between the  $2 \leq n_{jet} \leq 3$  and  $n_{jet} \geq 4$  categories. The two columns show the best fit value for the slope obtained when performing a constant (left) and linear (right) fit and the p-value for that fit.

1802 The best fit value for the constant parameter is indicative of the level of closure, averaged  
1803 across the full range of  $H_T$  bins in the analysis, and the p-value an indicator of any  
1804 significant dependence on  $H_T$  within the closure tests. The best fit values of all the tests  
1805 are either statistically compatible with zero bias (i.e, less than  $2\sigma$  from zero) or at the  
1806 level of 10% or less, with the exception of one closure test discussed below.

1807 Within Table 4.14, there exists one test that does not satisfy the above statement, which  
1808 is the  $2 \leq n_{jet} \leq 3 \rightarrow n_{jet} \geq 4$  test using the  $\mu +$  jets control sample. The low p-value  
1809 can be largely attributed to an outlier in the  $675 < H_T < 775$  GeV bin, rather than any  
1810 significant trend in  $H_T$ . Removing this single outlier from the constant fit performed,  
1811 gives a best fit value of  $-0.04 \pm 0.01$ ,  $\chi^2/\text{d.o.f} = 6.07/6$ . and a p-value of 0.42. These  
1812 modified fit results are included within Table 4.14 .

1813 In addition the best fit values for the slope terms of the linear fits in all three tables are  
1814 of the order  $10^{-4}$ , which corresponds to a percent level change per 100 GeV. However in  
1815 all cases, the best fit values are fully compatible with zero (within  $1\sigma$ ) once again with  
1816 the exception detailed above, indicating that the level of closure is  $H_T$  independent.

#### 1817 4.6.1. Determining systematic uncertainties from closure tests

1818 Once it has been established that no significant bias or trend has been exist within  
1819 the closure tests, systematic uncertainties are determined. The statistical precision  
1820 of the closure tests is considered a suitable benchmark for determining the systematic  
1821 uncertainties that are assigned to the TF's, which are propagated through to the likelihood  
1822 fit.

1823 The systematic uncertainty band is split into five separate regions of  $H_T$ . Within each  
1824 region the square root of the sample variance,  $\sigma^2$ , is taken over the eight closure tests to  
1825 determine the systematic uncertainties to be applied within that region.

1826 Using this procedure the systematic uncertainties for each region are calculated and are  
1827 shown in Table 4.15, with the systematic uncertainty to be used in the likelihood model  
1828 conservatively rounded up to the nearest decile and applied across all  $n_b^{reco}$  categories.

1829 Figure 4.11 shows the sets of closure tests overlaid on top of grey bands that represent  
1830 the  $H_T$  dependent systematic uncertainties. These systematic uncertainties are assumed  
1831 to fully uncorrelated between the different  $n_b$  multiplicity categories and across the five

$H_T$ band (GeV)	$2 \leq n_{jet} \leq 3$	$n_{jet} \geq 4$
$275 < H_T < 325$	10%	10%
$325 < H_T < 375$	10%	10%
$375 < H_T < 575$	10%	10%
$575 < H_T < 775$	20%	20%
$H_T > 775$	20%	30%

**Table 4.15.:** Calculated systematic uncertainties for the five  $H_T$  regions, determined from the closure tests. Uncertainties shown for both jet multiplicity categories. Values used within the likelihood model are conservatively rounded up to the nearest decile and shown in brackets.

- 1832  $H_T$  regions. This can be considered a more conservative approach given that some  
 1833 correlations between adjacent  $H_T$  bins could be expected due to comparable kinematics.
- 1834 These closure tests represent a conservative estimate of the systematic uncertainty in  
 1835 making a background prediction for the signal region, which is due to significant differences  
 1836 in the background composition and event kinematics between the two sub-samples used  
 1837 in the closure tests. This is contrary to the signal region prediction where the two  
 1838 sub-samples are both have a comparable background admixture and similar kinematics  
 1839 owing to the fact that the predictions are always made using the same ( $n_{jet}$ ,  $n_b^{reco}$ ,  $H_T$ )  
 1840 bin.
- 1841 This point is emphasised when we examine the sensitivity of the TF's to a change in the  
 1842 admixture of  $W +$  jets and  $t\bar{t}$  with the control and signal samples. This is accomplished  
 1843 by varying the cross sections of the  $W +$  jets and  $t\bar{t}$  by +20% and -20%, respectively.  
 1844 Figures C.2 and C.3 within Appendix C, show the effect upon the closure tests for both  
 1845 jet multiplicity categories. Given these variations in cross sections, the level of closure is  
 1846 found to be significantly worse, with biases as large as  $\sim 30\%$ , most apparent in the  
 1847 lowest  $H_T$  bins. However the TF's used to extrapolate from control to signal are seen to  
 1848 change only at the percent level by this large change in cross section, shown in Table C.1.
- 1849 Given the robust behaviour of the translation factors with respect to large (and opposite)  
 1850 variations in the  $W +$  jets and  $t\bar{t}$  cross sections, one can assume with confidence that  
 1851 any bias in the translation factors is adequately (and conservatively) covered by the  
 1852 systematic uncertainties used in the analysis.

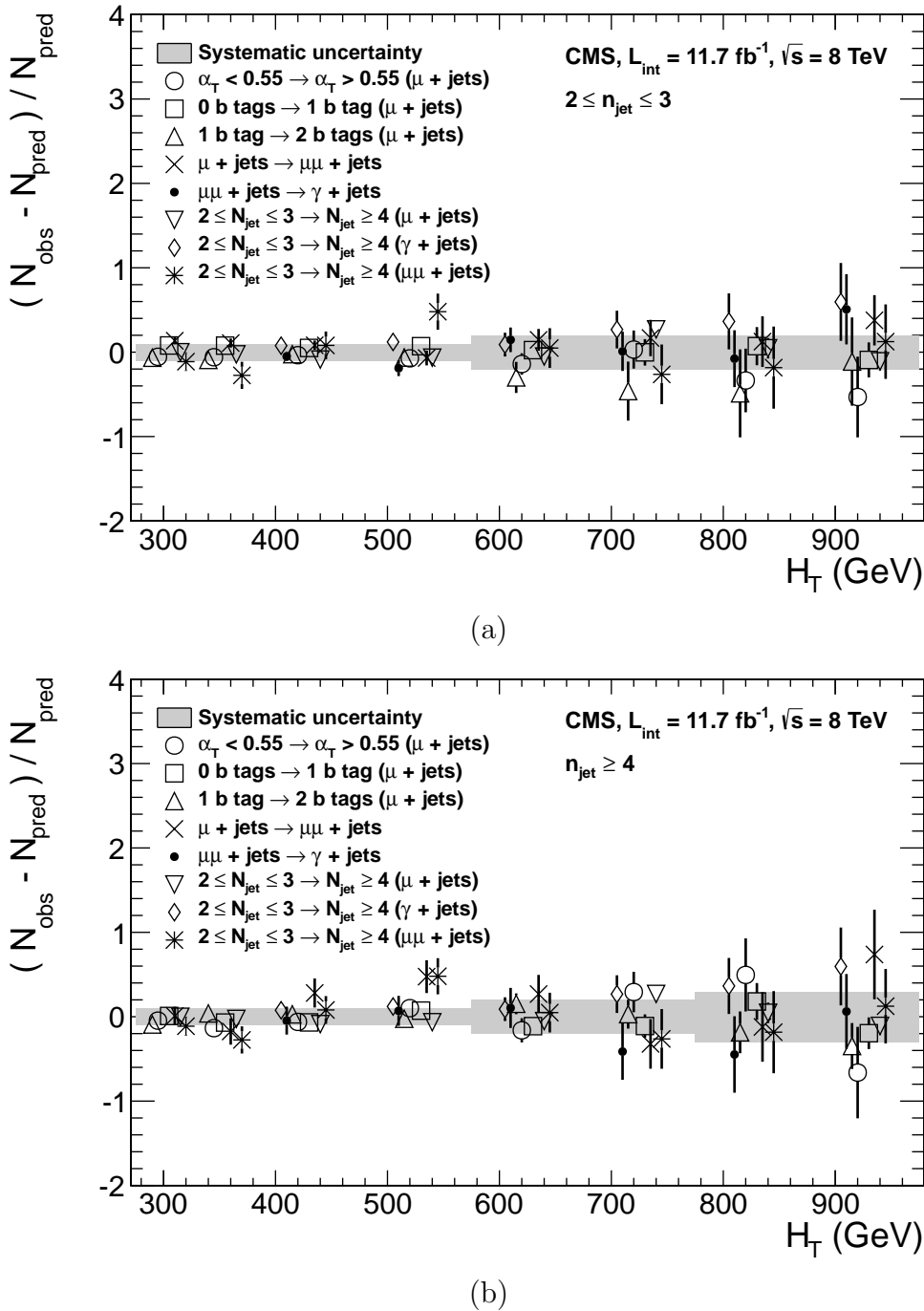


**Figure 4.11.:** Sets of closure tests (open symbols) overlaid on top of the systematic uncertainty used for each of the five  $H_T$  regions (shaded bands) and for the two different jet multiplicity bins: (a)  $2 \leq n_{\text{jet}} \leq 3$  and (b)  $n_{\text{jet}} \geq 4$ .

1853 **4.7. Simplified Models, Efficiencies and Systematic  
1854 Uncertainties**

1855 The results of the analysis are interpreted using various **SMS** signal models, which as  
1856 already introduced in Section (2.4.1) offer a natural starting point for quantifying and  
1857 characterising **SUSY** signals, and a means to identify the boundaries of search sensitivity  
1858 for different mass splittings, kinematic ranges, and final states.

1859 Each model is parameterised in a two dimensional parameter space, ( $m_{\tilde{q}/\tilde{g}}$ ,  $m_{\text{LSP}}$ ), from  
1860 which upper limits on the production cross sections of the various **SMS** models can be  
1861 set.

1862 Each signal sample is generated at Leading Order (**LO**) with Pythia [83], and cross  
1863 sections calculated for Next to Leading Order (**NLO**) and Next to Leading Logarithmic  
1864 Order (**NLL**) [84], with events simulated using the **Fastsim** framework. This framework  
1865 represents a simplified simulation of the **CMS** detector, but allows for faster production  
1866 of various signal topologies with different mass parameters. A series of correction factors  
1867 are applied to account for differences between **Fastsim** [85] and **Fullsim** [86] simulation,  
1868 which can affect the resultant  $n_b^{\text{reco}}$  distribution and which are detailed in Section (4.7.2).

1869 **4.7.1. Signal efficiency**

1870 The analysis selection efficiency,  $\epsilon$ , is measured for each mass point of the interpreted  
1871 model, this serves as a measure of the sensitivity of the signal selection for that particular  
1872 sparticle and **LSP** mass. The signal yield is then given by

$$Y(m_{\tilde{q}/\tilde{g}}, m_{\text{LSP}}) = \epsilon \times \sigma \times \mathcal{L}, \quad (4.13)$$

1873 where  $\sigma$  represents the model's cross section and  $\mathcal{L}$  the luminosity. An upper limit on  $\sigma$   
1874 taken from theory can then allow for the setting of limits in terms of the particle mass.

1875 Figure 4.12 shows the expected signal efficiency of the signal selection for the T1 and  
1876 T2 **SMS** models interpreted in this analysis. The efficiency maps are produced with the  
1877 requirement  $H_T > 275$  GeV (i.e., no binning in  $H_T$ ) and requirements on  $n_{\text{jet}}$  and  $n_b^{\text{reco}}$   
1878 that are appropriate for the model in question.

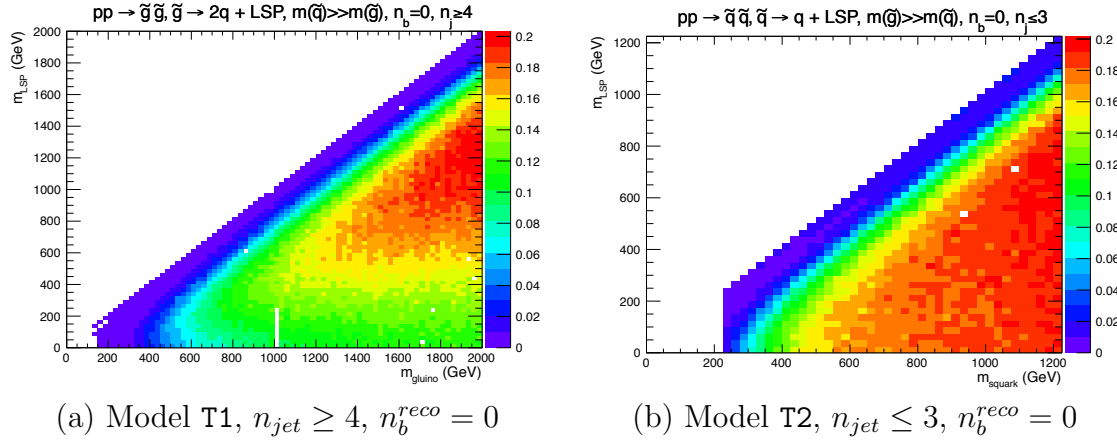


**Figure 4.12.:** Signal efficiencies for the **SMS** models (a) T1 ( $\tilde{g}\tilde{g}^* \rightarrow q\tilde{\chi}_1^0 q\bar{q}\tilde{\chi}_1^0$ ) and (b) T2 ( $\tilde{q}\tilde{q}^* \rightarrow q\tilde{\chi}_1^0 \bar{q}\tilde{\chi}_1^0$ ) when requiring  $n_{jet} \geq 4$  and  $\leq 3$  respectively, and  $n_b^{reco} = 0$ .

1879 The same procedure is conducted in the analysis control samples. It is found in the  $\mu$   
 1880 + jets control samples, that the S/B ratios for the expected signal yields in each of the  
 1881 **SMS** models are many time smaller than in the hadronic signal region. The relative  
 1882 contamination for the  $\mu\mu$  + jets sample is smaller still due to the requirement of a second  
 1883 muon. The relative contamination for the  $\gamma$  + jets sample is expected to be zero for the  
 1884 models under consideration. These small, relative levels of contamination are accounted  
 1885 for in the fitting procedure, as described in Section (4.8.4).

### 1886 4.7.2. Applying b-tag scale factor corrections in signal samples

1887 High-statistic **FastSim** signal simulation samples are unavailable for each signal signal  
 1888 point, which means that a different procedure to the formula method described in Section  
 1889 (4.5) is employed. Furthermore, the use of the **FastSim** framework in the reconstruction  
 1890 introduces an extra set of scale-factor corrections, to be applied simultaneously with  
 1891 those correcting the full-simulation to the data.

1892 For these signal models, an event-by-event re-weighting procedure is applied. This applied  
 1893 weight depends on both the flavour content and the b-tagging status of the reconstruction  
 1894 level jets in the event.

1895 The re-weighting procedure can be described by first considering a single jet in an signal  
 1896 sample event. The flavour of the jet is determined using the method described in Section  
 1897 (4.5.1).

- 1898 Taking the flavour,  $p_T$  and  $\eta$  values of the jet, the expected tagging efficiency,  $\epsilon_{MC}(p_T, \eta, f)$ ,  
 1899 in simulation is retrieved from a map of tagging efficiencies determined from the **FullSim**  
 1900 **SM** simulation samples, and binned as a function of jet  $p_T$ ,  $\eta$  and flavour after the  
 1901 application of the hadronic signal selection. The binning is chosen to reflect the set of  $p_T$   
 1902 and  $\eta$  dependant corrections of simulation to data defined by [87].  
 1903 The actual tagging efficiency of the **FastSim** jet,  $\epsilon_{\text{FastSim}}(p_T, \eta, f)$ , differs from that  
 1904 measured in **FullSim**,  $\epsilon_{MC}(p_T, \eta, f)$  and is related via an additional correction factor,

$$\epsilon_{\text{FastSim}}(p_T, \eta, f) = \frac{\epsilon_{MC}(p_T, \eta, f)}{SF_{\text{Fast} \rightarrow \text{Full}}(p_T, \eta, f)}, \quad (4.14)$$

- 1905 where  $SF_{\text{Fast} \rightarrow \text{Full}}(p_T, \eta, f)$  represents a set of  $p_T$  and  $\eta$  dependant corrections determined  
 1906 from the ratio between the efficiency and mis-tagging rates of a  $t\bar{t}$  **FullSim** and  $t\bar{t}$  **FastSim**  
 1907 sample. Similarly the tagging efficiencies measured in data [64],  $\epsilon_{Data}(p_T, \eta, f)$ , are further  
 1908 related to  $\epsilon_{\text{FastSim}}(p_T, \eta, f)$  by the equation,

$$\begin{aligned} \epsilon_{Data}(p_T, \eta, f) &= \epsilon_{MC}(p_T, \eta, f) \times SF_{MC \rightarrow Data}(p_T, \eta, f) \\ &= \epsilon_{\text{FastSim}}(p_T, \eta, f) \times \underbrace{SF_{\text{Fast} \rightarrow \text{Full}}(p_T, \eta, f) \times SF_{MC \rightarrow Data}(p_T, \eta, f)}_{\text{SF}_{\text{Fast} \rightarrow \text{Data}}} . \end{aligned} \quad (4.15)$$

- 1909 For each jet, the weight of the event is re-weighted according to whether the jet fires the  
 1910 b-tagger. In the instance that the jet *is* b-tagged the event weight is modified by,

$$\text{weight} = SF_{\text{Fast} \rightarrow \text{Data}} \times \text{weight}, \quad (4.16)$$

- 1911 and in the case that the jet is *not* tagged,

$$\text{weight} = \frac{1 - \epsilon_{Data}(p_T, \eta, f)}{1 - \epsilon_{\text{FastSim}}(p_T, \eta, f)} \times \text{weight}. \quad (4.17)$$

1912 Once all events have been reweighted this way, the yields in each  $n_b^{reco}$  bin represent the  
1913 corrected simulation yields.

### 1914 4.7.3. Experimental uncertainties

1915 The systematic uncertainty on the expected signal acceptance times analysis efficiency is  
1916 determined independently for the each **SMS** model considered. These systematics stem  
1917 from uncertainties on the parton distribution functions, the luminosity measurement,  
1918 jet energy scale, b-tag scale factor measurements and the efficiencies of various cuts used  
1919 in the signal selection, including the  $H_T / E_T$ , dead **ECAL** cleaning filter and lepton /  
1920 photon event vetoes.

1921 Rather than trying to estimate the level of systematic that is applicable point-by-point in  
1922 a model space, general behaviours are considered and constant systematics are estimated  
1923 in two regions of the **SMS** models parameter space.

1924 Within these two regions, the systematic uncertainties are found to be relatively flat  
1925 across the plane, and are defined as, near (small mass splittings) and far (large mass  
1926 splittings) from the diagonal, where far is realised by the condition

$$m_{\tilde{q}/\tilde{g}} - m_{LSP} > 350 \text{GeV} \quad m_{\tilde{q}/\tilde{g}} > 475 \text{GeV}.$$

1927 The total systematics in each region are evaluated in the following ways:

1928 **Jet energy scale** : The relative change in the signal efficiency is gauged by varying  
1929 the energy of all jets in an event up or down according to a  $p_T$  and  $\eta$  dependent jet  
1930 energy scale uncertainty. Within the two systematic regions, the resulting systematic  
1931 uncertainties for each **SMS** model are determined by taking the value of the 68<sup>th</sup>  
1932 percentile for the distributions of the relative change in the signal efficiency.

1933 **Luminosity measurement** : The measurement of luminosity taken propagates  
1934 through to an uncertainty on the signal event yield when considering any new  
1935 physics model, which is currently 4.4% [88].

1936 **Parton density function** : The effects of varying the set of parton distribution  
1937 functions used and changing the renormalization/factorisation scale used to compute

1938        the cross sections by a factor of two up or down have been found to affect the  
 1939        efficiency by up to 10%.

1940         **$H_T/E_T$  cleaning cut** : The ratio of the efficiencies of the cleaning cut are compared  
 1941        in simulation and data after application of the  $\mu +$  jets control sample selection.  
 1942        No  $\alpha_T$  cut or further event cleaning filters are applied. The ratio of the efficiencies  
 1943        observed in data and simulation for a cut value of  $H_T/E_T < 1.25$  and the two jet  
 1944        multiplicity bins,  $2 \leq n_{\text{jet}} \leq 3$  and  $n_{\text{jet}} \geq 4$  are  $1.028 \pm 0.007$  and  $1.038 \pm 0.015$   
 1945        respectively. These deviations are taken to represent the systematic uncertainty on  
 1946        the simulation modelling of this variable.

1947        **Deal ECAL cleaning filter** : The ratio of the efficiencies observed in data and  
 1948        simulation for this filter in the two jet multiplicity bins,  $2 \leq n_{\text{jet}} \leq 3$  and  $n_{\text{jet}} \geq 4$ ,  
 1949        are  $0.961 \pm 0.008$  and  $0.961 \pm 0.009$ , respectively. These deviations from unity  
 1950        are taken to represent the systematic uncertainties in the modelling in simulation of  
 1951        this filter.

1952        **Lepton and photon vetoes** : The uncertainty on the efficiency of the lepton and  
 1953        photon vetoes is determined by considering truth information. The efficiency of  
 1954        the vetoes is measured after applying relevant object filters with identical logic,  
 1955        but based on truth instead of reconstructed objects. Where the efficiency is found  
 1956        to not be 100%, it is taken to represent the fraction of signal events that are  
 1957        incorrectly vetoed. This deviation is taken directly as the systematic uncertainty on  
 1958        the efficiency. The systematic uncertainty is only non-zero for models which contain  
 1959        third-generation quarks in the final state, where the uncertainties are at the order  
 1960        of 1% level.

1961        **B-tag scale factor uncertainties** : The relative change in the signal efficiency is  
 1962        observed when relevant flavour,  $p_T$  and  $\eta$  dependant b-tag correction factors, are  
 1963        varied up or down by their uncertainty. Within the two systematic regions, the  
 1964        resulting systematic uncertainties for each **SMS** model are determined by taking  
 1965        the value of the 68<sup>th</sup> percentile for the distributions of the relative change in the  
 1966        signal efficiency, over all mass points.

1967        Tables 4.16 and 4.17 summarise all the aforementioned systematic uncertainties on the  
 1968        signal efficiencies for each individual **SMS** model interpreted in the analysis. In the case  
 1969        of the T1tttt model, in which pair produced gluinos decay to  $t\bar{t}$  pairs and the **LSP**,  
 1970        the near region of **SMS** space is not considered, and so no systematic uncertainties are  
 1971        included.

<sup>1972</sup> The systematic uncertainties used for the region near to the diagonal fall in the range  
<sup>1973</sup> 13-15%; similarly, for the region far from the diagonal, the uncertainties used fall in the  
<sup>1974</sup> range 12-23%. These uncertainties are all included in the limit calculation.

Model	Luminosity	p.d.f	JES	$\cancel{H}_T/\cancel{E}_T$	Dead ECAL	Lepton Veto	b-tagging	Total
T1	4.4	10.0	5.6	3.8	4.1	n/a	3.1	13.9
T2	4.4	10.0	4.1	2.8	4.1	n/a	2.4	12.9
T2tt	4.4	10.0	6.5	3.8	4.1	0.8	0.8	13.9
T2bb	4.4	10.0	4.8	2.8	4.1	0.3	2.2	13.1
T1tttt	n/a	n/a	n/a	n/a	n/a	n/a	n/a	n/a
T1bbbb	4.4	10.0	7.3	3.8	4.1	0.5	2.7	14.5

**Table 4.16.:** Estimates of systematic uncertainties on the signal efficiency (%) for various **SMS** models when considering points in the region near to the diagonal (i.e. small mass splitting and compressed spectra). The uncertainties are added in quadrature to obtain the total.

Model	Luminosity	p.d.f	JES	$\cancel{H}_T/\cancel{E}_T$	Dead ECAL	Lepton Veto	b-tagging	Total
T1	4.4	10.0	0.8	3.8	4.1	n/a	6.6	14.0
T2	4.4	10.0	1.1	2.8	4.1	n/a	5.8	13.4
T2tt	4.4	10.0	3.5	3.8	4.1	0.6	1.6	12.9
T2bb	4.4	10.0	0.9	2.8	4.1	0.3	2.7	12.3
T1tttt	4.4	10.0	0.5	3.8	4.1	1.4	19.4	23.0
T1bbbb	4.4	10.0	1.5	3.8	4.1	0.4	10.1	16.0

**Table 4.17.:** Estimates of systematic uncertainties on the signal efficiency (%) for various **SMS** models when considering points in the region far from the diagonal (i.e. large mass splitting). The uncertainties are added in quadrature to obtain the total.

## 4.8. Statistical Interpretation

<sup>1975</sup> For a given category of events satisfying requirements on both  $n_{jet}$  and  $n_b^{reco}$ , a likelihood model of the observations in multiple data samples is used to gauge agreement between the observed yields in the hadronic signal region, and the predicted yields obtained from the control samples. In addition to checking whether the predictions are compatible with a **SM** only hypothesis, the likelihood model is also used to test for the presence of a variety of signal models. The statistical framework outlined within this section is presented in greater detail within [89].

<sub>1983</sub> **4.8.1. Hadronic sample**

<sub>1984</sub> Let  $N$  be the number of bins on  $H_T$ , with  $n^i$  the number of events observed satisfying  
<sub>1985</sub> all selection requirements in each  $H_T$  bin  $i$ . The likelihood of the observations can then  
<sub>1986</sub> be written :

$$L_{had} = \prod_i \text{Pois}(n^i | b^i + s^i), \quad (4.18)$$

<sub>1987</sub> where  $b^i$  represents the expected SM background

$$b^i = EWK_i + QCD_i, \quad (4.19)$$

<sub>1988</sub> and  $s^i$  the expected number of signal events from the different SMS models interpreted.  
<sub>1989</sub> Pois refers to the Poisson distribution of these values and is defined as :

$$\text{Pois}(\chi|\lambda) = \frac{\lambda^\chi \exp^{-\lambda}}{k!}. \quad (4.20)$$

<sub>1990</sub> **4.8.2.  $H_T$  evolution model**

<sub>1991</sub> The hypothesis, that for a process the  $\alpha_T$  ratio falls exponentially see Section (4.2.4 )  
<sub>1992</sub> in  $H_T$  is defined by Equation (4.10), where  $k_{QCD}$  is constrained by measurements in a  
<sub>1993</sub> signal sideband region.

<sub>1994</sub> The expected QCD background,  $QCD^i$ , within a bin  $i$  is then modelled as,

$$QCD^i = m^i A_{QCD} e^{-k_{QCD} \langle H_T \rangle}, \quad (4.21)$$

<sub>1995</sub> where  $m_i$  represent the number of events observed with  $\alpha_T \leq 0.55$  in each  $H_T$  bin  $i$ , and  
<sub>1996</sub>  $\langle H_T \rangle$  represents the mean  $H_T$  of each bin. Expressed as functions of just the zeroth bin,  
<sub>1997</sub>  $QCD^0$ , and  $k_{QCD}$ , the QCD expectation is given by

$$QCD^i = QCD^0 \left( \frac{m^i}{m^0} \right) e^{-k_{QCD} (\langle H_T \rangle^i - \langle H_T \rangle^0)}. \quad (4.22)$$

<sub>1998</sub> **4.8.3. EWK control samples**

<sub>1999</sub> The **EWK** background estimation within each bin,  $i$ , is broken into two components, the  
<sub>2000</sub> expected yield from  $Z \rightarrow \nu\bar{\nu}$  and  $t\bar{t}$ -W (plus other residual backgrounds) events. This is  
<sub>2001</sub> written as,  $Z_{inv}^i$  and  $t\bar{t}W^i$ , and it follows that

$$EWK^i = Z_{inv}^i + t\bar{t}W^i. \quad (4.23)$$

<sub>2002</sub> This can be further expressed as

$$Z_{inv}^i \equiv f_{Zinv}^i \times EWK^i, \quad (4.24)$$

$$t\bar{t}W^i \equiv (1 - f_{Zinv}^i) \times EWK^i, \quad (4.25)$$

<sub>2003</sub> where  $f_{Zinv}^i$  represents the expected yield from  $Z \rightarrow \nu\bar{\nu}$  in bin  $i$  divided by the expected  
<sub>2004</sub> **EWK** background  $EWK^i$ . This fraction is modelled as a linear component

$$f_{Zinv}^i = f_{Zinv}^0 + \frac{\langle H_T \rangle^i - \langle H_T \rangle^0}{\langle H_T \rangle^{N-1} - \langle H_T \rangle^0} (f_{Zinv}^{N-1} - f_{Zinv}^i), \quad (4.26)$$

<sub>2005</sub> where  $N$  again represents the number of  $H_T$  bins, and  $f_{Zinv}^i$  and  $f_{Zinv}^{N-1}$  are float parameters  
<sub>2006</sub> whose final values are limited between zero and one.

<sub>2007</sub> Within each  $H_T$  bin there are three background measurements for the different control  
<sub>2008</sub> samples,  $n_\gamma^i$ ,  $n_\mu^i$  and  $n_{\mu\mu}^i$ , representing the event yields from the  $\gamma +$  jets,  $\mu +$  jets and  
<sub>2009</sub>  $\mu\mu +$  jets control samples respectively. Each of these have a corresponding yield in  
<sub>2010</sub> simulation,  $MC_\gamma^i$ ,  $MC_\mu^i$  and  $MC_{\mu\mu}^i$ . Within the hadronic signal region there are also  
<sub>2011</sub> corresponding simulated yields for  $Z \rightarrow \nu\bar{\nu}$  ( $MC_{Zinv}^i$ ) and  $t\bar{t} + W$  ( $MC_{t\bar{t}+W}^i$ ), which are  
<sub>2012</sub> used to define

$$r_\gamma^i = \frac{MC_\gamma^i}{MC_{Zinv}^i}; \quad r_{\mu\mu}^i = \frac{MC_{\mu\mu}^i}{MC_{Zinv}^i}; \quad r_\mu^i = \frac{MC_\mu^i}{MC_{t\bar{t}+W}^i}, \quad (4.27)$$

where  $r_p^i$  represents the inverse of the TF's used to extrapolate the yield of each background process.

The likelihoods regarding the three measured yields  $n_\gamma^i$ ,  $n_{\mu\mu}^i$ ,  $n_\mu^i$  can then be fully expressed as

$$L_\gamma = \prod_i \text{Pois}(n_\gamma^i | \rho_{\gamma Z}^j \cdot r_\gamma^i \cdot Z_{inv}^i), \quad (4.28)$$

$$L_{\mu\mu} = \prod_i \text{Pois}(n_{\mu\mu}^i | \rho_{\mu\mu Z}^j \cdot r_{\mu\mu}^i \cdot Z_{inv}^i), \quad (4.29)$$

$$L_\mu = \prod_i \text{Pois}(n_\mu^i | \rho_{\mu Y}^j \cdot r_\mu^i \cdot Y^i + s_\mu^i), \quad (4.30)$$

$$(4.31)$$

which contain an additional term  $s_\mu^i$ , which represents the signal contamination in the  $\mu + \text{jets}$  sample. The parameters  $\rho_{\gamma Z}^j$ ,  $\rho_{\mu\mu Z}^j$  and  $\rho_\mu^j$  represent “correction factors” that accommodate the data driven systematic uncertainties derived from the controls in Section (4.12).

Each of these equations are used to estimate the maximum likelihood value for relevant background in the signal region given the observations  $n_p^i$  in each of the control samples (see Section (4.2.3)).

The measurements in each of the control samples and the hadronic signal region, along with the ratios  $r_\gamma^i$ ,  $r_{\mu\mu}^i$ , and  $r_\mu^i$ , are all considered simultaneously through the relationships defined by Equations (4.19),(4.24) and (4.25).

In addition to the Poisson product, an additional log-normal term is introduced to accommodate the systematic uncertainties given by,

$$L_{EWK \ syst} = \prod_j \text{Logn}(1.0 | \rho_{\mu W}^j, \sigma_{\mu W}^j) \times \text{Logn}(1.0 | \rho_{\mu\mu Z}^j, \sigma_{\mu\mu Z}^j) \times \text{Logn}(1.0 | \rho_{\gamma Z}^j, \sigma_{\gamma Z}^j), \quad (4.32)$$

2029 where  $\sigma_{\gamma Z}^j$ ,  $\sigma_{\mu\mu Z}^j$  and  $\sigma_{\mu W}^j$  represent the relative systematic uncertainties for the control  
2030 sample constraints and Logn is the log-normal distribution [90],

$$\text{Logn}(x | \mu, \sigma_{rel}) = \frac{1}{x\sqrt{2\pi}\ln k} \exp\left(\frac{\ln^2(\frac{x}{\mu})}{2\ln^2 k}\right); \quad k = 1 + \sigma_{rel}. \quad (4.33)$$

2031 Five parameters per control sample are used to span the eight  $H_T$  bins, with just one  
2032 used for the three  $H_T$  bins in the  $n_b^{reco} \geq 4$  category. These parameters span the same  
2033  $H_T$  ranges described in Section (4.6) and is shown in Table 4.18.

$H_T$ bin (i)	0	1	2	3	4	5	6	7
syst. parameter (j)	0	1	2	2	3	3	4	4

$H_T$ bin (i)	0	1	2
syst. parameter (j)	0	0	0

**Table 4.18.:** The systematic parameters used in  $H_T$  bins. Left: categories with eight bins; right: category with three bins.

2034 Alternatively, in the higher  $n_b^{reco}$  categories ( $n_b^{reco} = 3$ ,  $n_b^{reco} \geq 4$ ), the single muon sample  
2035 is used to constrain the total EWK background. Therefore the likelihood function is  
2036 greatly simplified and is represented by

$$L'_\mu = \prod_i \text{Pois}(n_\mu^i | \rho_{\mu Y}^j \cdot r_\mu'^i \cdot EWK^i + s_\mu^i), \quad (4.34)$$

2037 where,

$$r_\mu'^i = \frac{MC_\mu^i}{MC_{tot}^i}. \quad (4.35)$$

---

2038 **4.8.4. Contributions from signal**

2039 The cross section for each model is represented by  $x$  and  $l$  represents the total recorded  
2040 luminosity considered by the analysis in the signal region. Let  $\epsilon_{had}^i$  and  $\epsilon_\mu^i$  represent the  
2041 analysis selection efficiency for that particular signal model in  $H_T$  bin  $i$  of the hadronic  
2042 and  $\mu + \text{jets}$  control sample respectively. Letting  $\delta$  represent the relative uncertainty on  
2043 the signal yield, assumed to be fully correlated across all bins, and  $\rho_{sig}$  the “correction  
2044 factor” to the signal yield which accommodates this uncertainty.  $f$  represents an unknown  
2045 multiplicative factor on the signal cross section, for which an allowed interval is computed.

2046 The expected signal yield  $s^i$  is thus given by

$$s^i \equiv f \rho_{sig} x l \epsilon_{had}^i \quad (4.36)$$

2047 and signal contamination with the  $\mu + \text{jets}$  control sample by

$$s_\mu^i \equiv f \rho_{sig} x l \epsilon_\mu^i \quad (4.37)$$

2048 The systematic uncertainty on the signal is additionally included by the term

$$L_{\text{sig}} = \text{Logn}(1.0 | \rho_{sig}, \delta). \quad (4.38)$$

2049 A discussion of the **SMS** signal models through which the analysis is interpreted can be  
2050 found in the following Chapter.

2051 **4.8.5. Total likelihood**

2052 The total likelihood function for a given signal bin  $k(n_b^{reco}, n_{jet})$  is given by the product  
2053 of the likelihood functions introduced within the previous sections:

$$L^k = L_{had}^k \times L_\mu^k \times L_\gamma^k \times L_{\mu\mu}^k \times L_{EWKsyst}^k \times L_{QCD}^k. \quad (4.39)$$

2054 In categories containing eight  $H_T$  bins and utilising the three control samples ( $\mu + \text{jets}, \mu\mu$   
 2055  $+ \text{jets}, \gamma + \text{jets}$ ), there are 25 nuisance parameters, whilst when just one control sample is  
 2056 used to estimate the EWK background, there are 15 nuisance parameters. Where three  
 2057  $H_T$  bins are used (the highest  $n_b^{reco}$  category), there are 6 nuisance parameters. This  
 2058 information is summarised within Table 4.19.

Nuisance parameter	Total
$(EWK^i)_{i:0-7(2)}$	8 (3)
$f_{Zinv}^0 *$	1
$f_{Zinv}^{\tau} *$	1
$QCD^0$	1
$k_{QCD}$	1
$(\rho_{\gamma Z}^j)_{j:2-4} *$	3
$(\rho_{\mu\mu Z}^j)_{j:0-4} *$	5
$(\rho_{\mu W}^j)_{j:0-4(0)}$	5 (1)

**Table 4.19.:** Nuisance parameters used within the different hadronic signal bins of the analysis. Parameters denoted by a \* are not considered in the case of a single control sample being used to predict the EWK background. Numbers within brackets highlight the number of nuisance parameters in the case of three  $H_T$  bins being used.

2059 When considering SUSY signal models within the likelihood, the additional  $L_{sig}$  term is  
 2060 included and therefore when multiple categories are fit simultaneously the total likelihood  
 2061 is then represented by

$$L = L_{sig} \times \prod_k L_{had}^k \times L_\mu^k \times L_\gamma^k \times L_{\mu\mu}^k \times L_{EWKsyst}^k \times L_{QCD}^k. \quad (4.40)$$

# Chapter 5.

## <sup>2062</sup> Results and Interpretation

<sup>2063</sup> Using the statistical framework outlined in the previous chapter, results are compared to  
<sup>2064</sup> a SM-only hypothesis (Section (5.1)) and interpreted using various SMS models (Section  
<sup>2065</sup> (5.2)).

### <sup>2066</sup> 5.1. Standard Model

<sup>2067</sup> The SM background only hypothesis is tested by removing any signal contributions  
<sup>2068</sup> within the signal and control samples, and the likelihood function is maximised over all  
<sup>2069</sup> parameters using Rootfit [91] and MINUIT [92]. The results of the search consist of the  
<sup>2070</sup> observed yields in the hadronic signal sample, and the  $\mu + \text{jets}$ ,  $\mu\mu + \text{jets}$  and  $\gamma + \text{jets}$   
<sup>2071</sup> control samples.

<sup>2072</sup> These observed yields along with the expectations and uncertainties given by the simulta-  
<sup>2073</sup> neous fit for the hadronic signal region are given in Table 5.2. The results obtained from  
<sup>2074</sup> the simultaneous fits, including that of the three control samples, are shown in Figure  
<sup>2075</sup> 5.1-5.8, as summarised in Table 5.1.

<sup>2076</sup> The figures show a comparison between the observed yields and the SM expectations  
<sup>2077</sup> across all  $H_T$  bins, for events in both  $n_{jet}$  and  $n_b^{reco}$  multiplicity categories. In all categories  
<sup>2078</sup> the samples are well described by the SM only hypothesis. In particular no significant  
<sup>2079</sup> excess is observed above SM expectation within the hadronic signal region.

$n_{jet}$	$n_b^{reco}$	Control samples fitted	Figure
2-3	0	$\mu + \text{jets}, \mu\mu + \text{jets}, \gamma + \text{jets}$	5.1
2-3	1	$\mu + \text{jets}, \mu\mu + \text{jets}, \gamma + \text{jets}$	5.2
2-3	1	$\mu + \text{jets}$	5.3
$\geq 4$	0	$\mu + \text{jets}, \mu\mu + \text{jets}, \gamma + \text{jets}$	5.4
$\geq 4$	1	$\mu + \text{jets}, \mu\mu + \text{jets}, \gamma + \text{jets}$	5.5
$\geq 4$	2	$\mu + \text{jets}$	5.6
$\geq 4$	3	$\mu + \text{jets}$	5.7
$\geq 4$	4	$\mu + \text{jets}$	5.8

**Table 5.1.:** Summary of control samples used by each fit results, and the Figures in which they are displayed.

Cat	$n_b^{reco}$	$n_{jet}$	$H_T$ bin (GeV)							
			275-325	325-375	375-475	474-575	575-675	675-775	775-875	875- $\infty$
SM Data	0	$\leq 3$	$6235^{+100}_{-67}$	$2900^{+60}_{-54}$	$1955^{+34}_{-39}$	$558^{+14}_{-15}$	$186^{+11}_{-10}$	$51.3^{+3.4}_{-3.8}$	$21.2^{+2.3}_{-2.2}$	$16.1^{+1.7}_{-1.7}$
			6232	2904	1965	552	177	58	16	25
SM Data	0	$\geq 4$	$1010^{+34}_{-24}$	$447^{+19}_{-16}$	$390^{+19}_{-15}$	$250^{+12}_{-11}$	$111^{+9}_{-7}$	$53.3^{+4.3}_{-4.3}$	$18.5^{+2.4}_{-2.4}$	$19.4^{+2.5}_{-2.7}$
			1009	452	375	274	113	56	16	27
SM Data	1	$\leq 3$	$1162^{+37}_{-29}$	$481^{+18}_{-19}$	$341^{+15}_{-16}$	$86.7^{+4.2}_{-5.6}$	$24.8^{+2.8}_{-2.7}$	$7.2^{+1.1}_{-1.0}$	$3.3^{+0.7}_{-0.7}$	$2.1^{+0.5}_{-0.5}$
			1164	473	329	95	23	8	4	1
SM Data	1	$\geq 4$	$521^{+25}_{-17}$	$232^{+15}_{-12}$	$188^{+12}_{-11}$	$106^{+6}_{-6}$	$42.1^{+4.1}_{-4.4}$	$17.9^{+2.2}_{-2.0}$	$9.8^{+1.5}_{-1.4}$	$6.8^{+1.2}_{-1.1}$
			515	236	204	92	51	13	13	6
SM Data	2	$\leq 3$	$224^{+15}_{-14}$	$98.2^{+8.4}_{-6.4}$	$59.0^{+5.2}_{-6.0}$	$12.8^{+1.6}_{-1.6}$	$3.0^{+0.9}_{-0.7}$	$0.5^{+0.2}_{-0.2}$	$0.1^{+0.1}_{-0.1}$	$0.1^{+0.1}_{-0.1}$
			222	107	58	12	5	1	0	0
SM Data	2	$\geq 4$	$208^{+17}_{-9}$	$103^{+9}_{-7}$	$85.9^{+7.2}_{-6.9}$	$51.7^{+4.6}_{-4.7}$	$19.9^{+3.4}_{-3.0}$	$6.8^{+1.2}_{-1.3}$	$1.7^{+0.7}_{-0.4}$	$1.3^{+0.4}_{-0.3}$
			204	107	84	59	24	5	1	2
SM Data	3	$\geq 4$	$25.3^{+5.0}_{-4.2}$	$11.7^{+1.7}_{-1.8}$	$6.7^{+1.4}_{-1.2}$	$3.9^{+0.8}_{-0.8}$	$2.3^{+0.6}_{-0.6}$	$1.2^{+0.3}_{-0.4}$	$0.3^{+0.2}_{-0.1}$	$0.1^{+0.1}_{-0.1}$
			25	13	4	2	2	3	0	0
SM Data	4	$\geq 4$	$0.9^{+0.4}_{-0.7}$	$0.3^{+0.2}_{-0.2}$				$0.6^{+0.3}_{-0.3}$		2
			1	0						

**Table 5.2.:** Comparison of the measured yields in the each  $H_T$ ,  $n_{jet}$  and  $n_b^{reco}$  jet multiplicity bins for the hadronic sample with the SM expectations and combined statistical and systematic uncertainties given by the simultaneous fit.

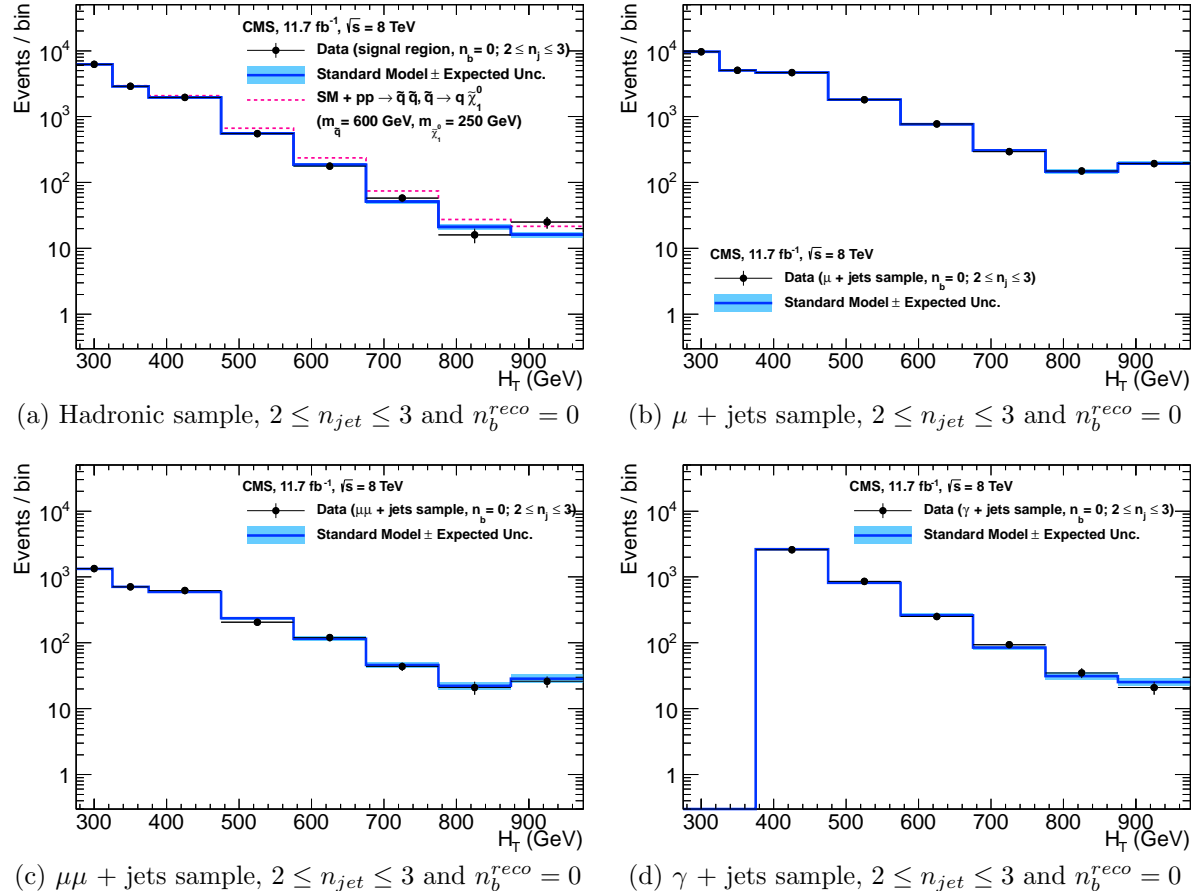


**Figure 5.1.:** Comparison of the observed yields and SM expectations given by the simultaneous fit in bins of  $H_T$  for the (a) hadronic, (b)  $\mu +$  jets, (c)  $\mu\mu +$  jets and (d)  $\gamma +$  jets samples when requiring  $n_b^{reco} = 0$  and  $n_{jet} \leq 3$ . The observed event yields in data (black dots) and the expectations and their uncertainties for all SM processes (blue line with light blue bands) are shown. An example signal expectation (red solid line) for the D1 SMS signal point from Table 4.1 is superimposed on the SM background expectation.

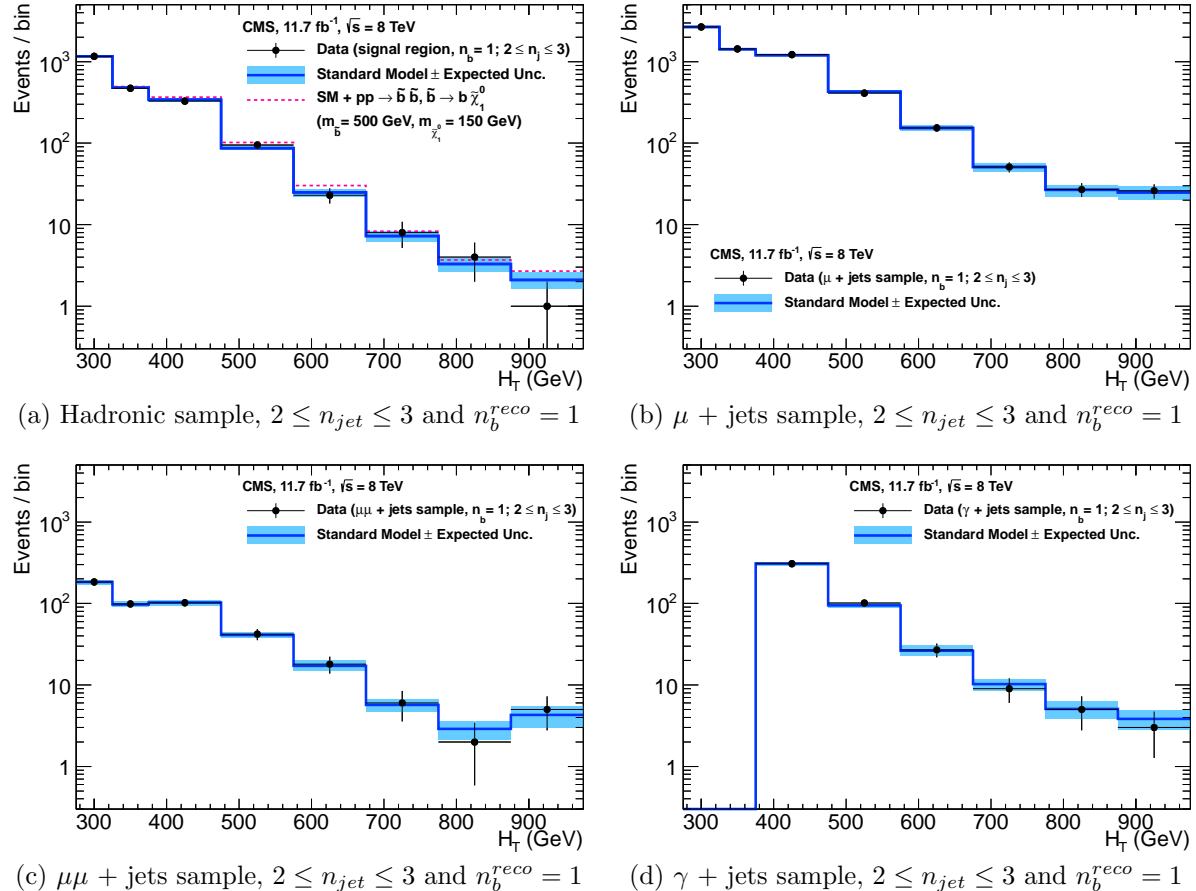


**Figure 5.2.:** Comparison of the observed yields and SM expectations given by the simultaneous fit in bins of  $H_T$  for the (a) hadronic, (b)  $\mu +$  jets, (c)  $\mu\mu +$  jets and (d)  $\gamma +$  jets samples when requiring  $n_b^{reco} = 1$  and  $n_{jet} \leq 3$ . The observed event yields in data (black dots) and the expectations and their uncertainties for all SM processes (blue line with light blue bands) are shown. An example signal expectation (red solid line) for the D2 SMS signal point from Table 4.1 is superimposed on the SM background expectation.

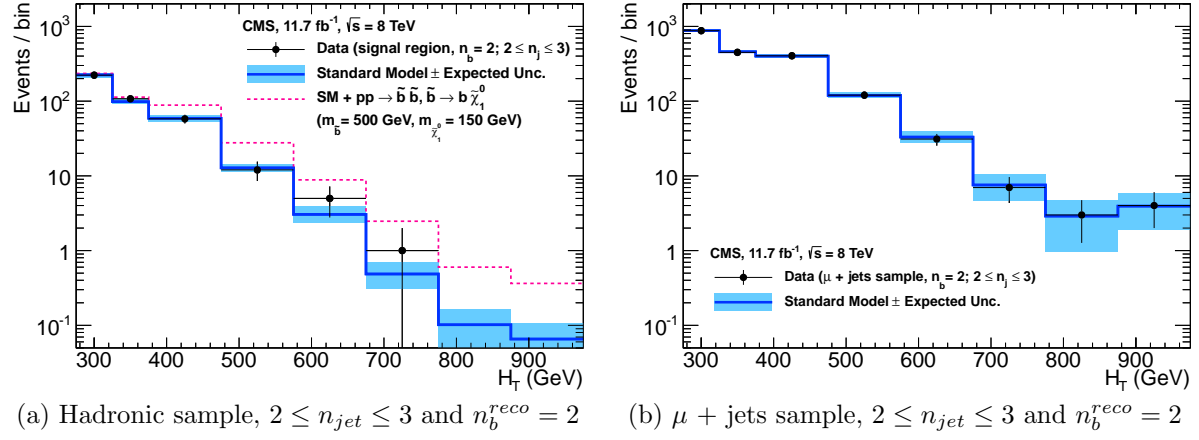


**Figure 5.3.:** Comparison of the observed yields and SM expectations given by the simultaneous fit in bins of  $H_T$  for the (a) hadronic, (b)  $\mu +$  jets, (c)  $\mu\mu +$  jets and (d)  $\gamma +$  jets samples when requiring  $n_b^{reco} = 2$  and  $n_{jet} \leq 3$ . The observed event yields in data (black dots) and the expectations and their uncertainties for all SM processes (blue line with light blue bands) are shown. An example signal expectation (red solid line) for the D2 SMS signal point from Table 4.1 is superimposed on the SM background expectation.

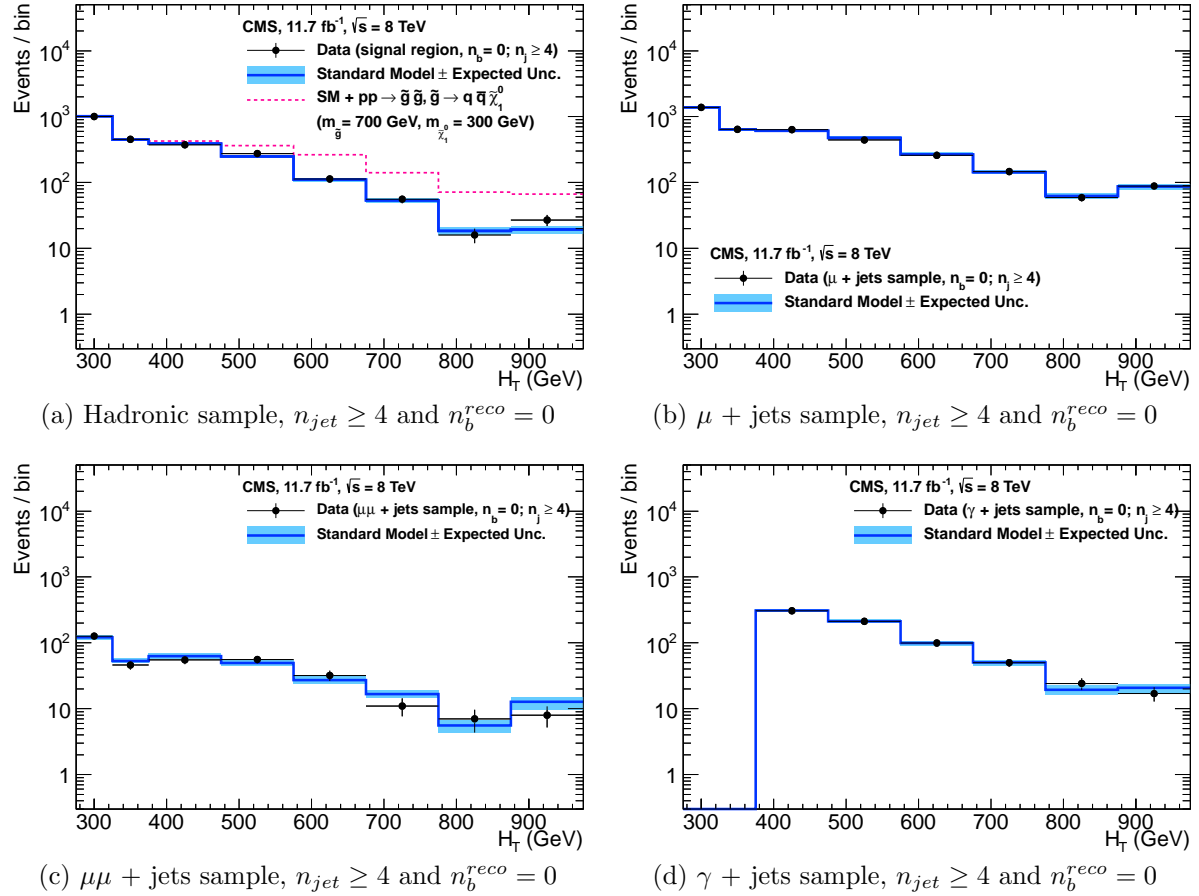


**Figure 5.4.:** Comparison of the observed yields and SM expectations given by the simultaneous fit in bins of  $H_T$  for the (a) hadronic, (b)  $\mu +$  jets, (c)  $\mu\mu +$  jets and (d)  $\gamma +$  jets samples when requiring  $n_b^{reco} = 0$  and  $n_{jet} \geq 4$ . The observed event yields in data (black dots) and the expectations and their uncertainties for all SM processes (blue line with light blue bands) are shown. An example signal expectation (red solid line) for the D2 SMS signal point from Table 4.1 is superimposed on the SM background expectation.

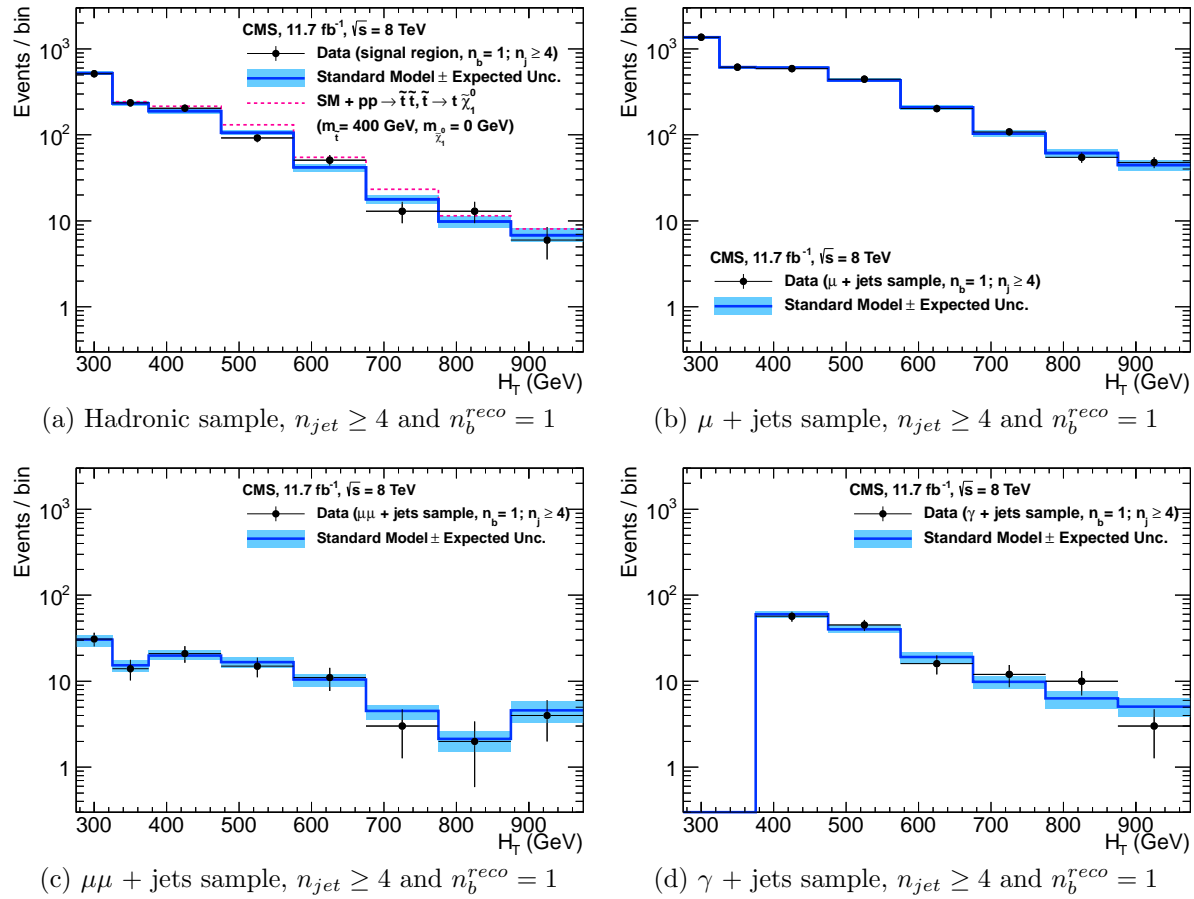


**Figure 5.5.:** Comparison of the observed yields and SM expectations given by the simultaneous fit in bins of  $H_T$  for the (a) hadronic, (b)  $\mu +$  jets, (c)  $\mu\mu +$  jets and (d)  $\gamma +$  jets samples when requiring  $n_b^{reco} = 1$  and  $n_{jet} \geq 4$ . The observed event yields in data (black dots) and the expectations and their uncertainties for all SM processes (blue line with light blue bands) are shown.

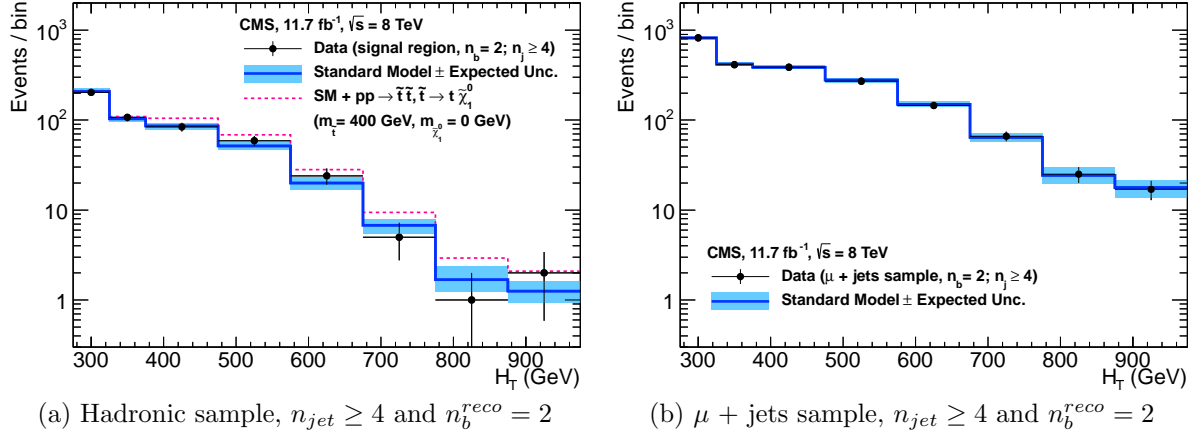


**Figure 5.6.:** Comparison of the observed yields and SM expectations given by the simultaneous fit in bins of  $H_T$  for the (a) hadronic, (b)  $\mu +$  jets, (c)  $\mu\mu +$  jets and (d)  $\gamma +$  jets samples when requiring  $n_b^{reco} = 2$  and  $n_{jet} \geq 4$ . The observed event yields in data (black dots) and the expectations and their uncertainties for all SM processes (blue line with light blue bands) are shown. An example signal expectation (red solid line) for the D3 SMS signal point from Table 4.1 is superimposed on the SM background expectation.

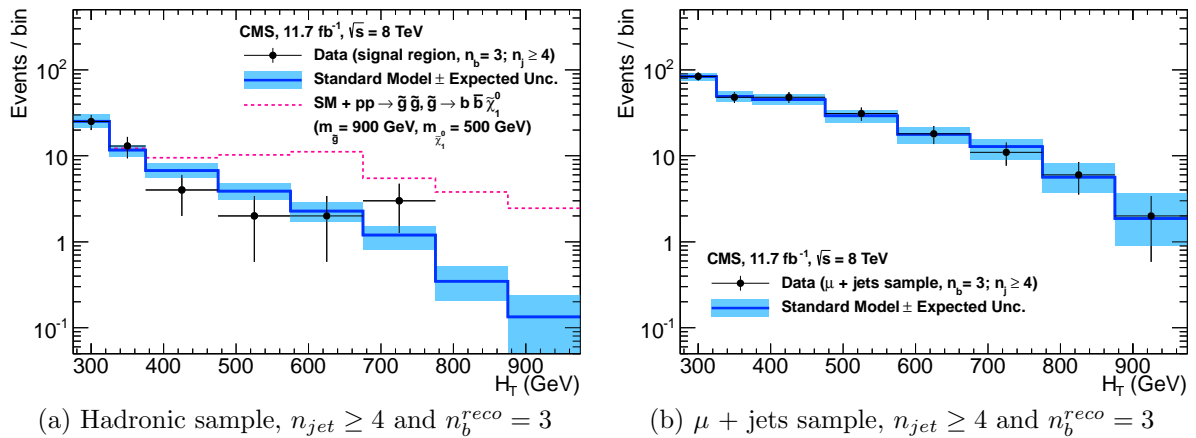


**Figure 5.7.:** Comparison of the observed yields and SM expectations given by the simultaneous fit in bins of  $H_T$  for the (a) hadronic, (b)  $\mu +$  jets, (c)  $\mu\mu +$  jets and (d)  $\gamma +$  jets samples when requiring  $n_b^{reco} = 3$  and  $n_{jet} \geq 4$ . The observed event yields in data (black dots) and the expectations and their uncertainties for all SM processes (blue line with light blue bands) are shown. An example signal expectation (red solid line) for the G2 SMS signal point from Table 4.1 is superimposed on the SM background expectation.

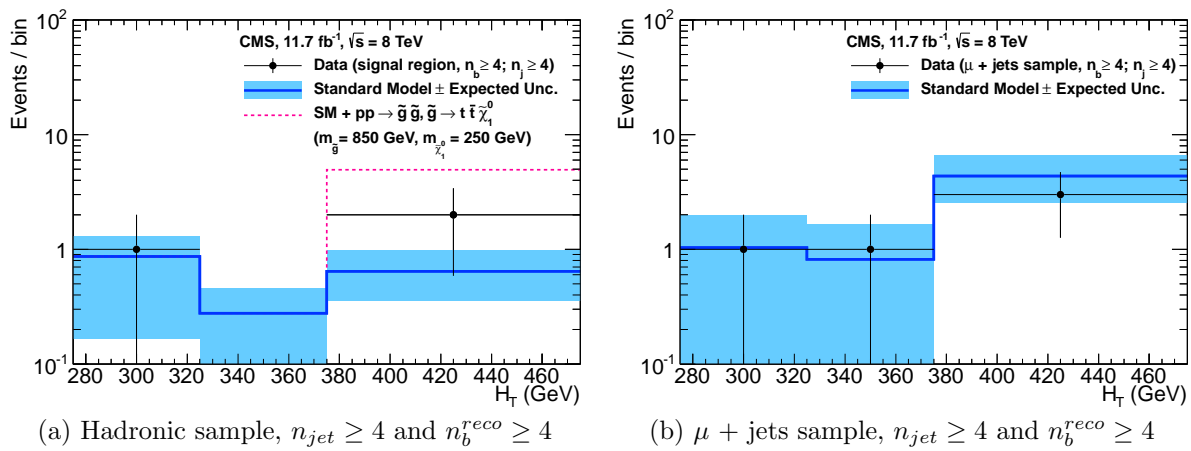


**Figure 5.8.: Comparison of the observed yields and SM expectations given by the simultaneous fit in bins of  $H_T$  for the (a) hadronic, (b)  $\mu +$  jets, (c)  $\mu\mu +$  jets and (d)  $\gamma +$  jets samples when requiring  $n_b^{reco} \geq 4$  and  $n_{jet} \geq 4$ . The observed event yields in data (black dots) and the expectations and their uncertainties for all SM processes (blue line with light blue bands) are shown. An example signal expectation (red solid line) for the G3 SMS signal point from Table 4.1 is superimposed on the SM background expectation.**

2080 **5.2. SUSY**

2081 Limits are set in the parameter space of a set of **SMS** models that characterise both  
2082 natural **SUSY** third generation squark production, and compressed spectra where the  
2083 mass splitting between the particle and **LSP** is small, leading to soft final state jets.  
2084 However as detailed in Section (2.4.1), the individual models are not representative of a  
2085 real physical **SUSY** model as only one decay process is considered. Instead these models  
2086 represent a way to test for signs of specific signatures indicating new physics.

2087 **5.2.1. The  $CL_s$  method**

2088 The  $CL_s$  method [93][94][95] is used to compute the limits for signal models, with the  
2089 one-sided profile likelihood ratio as the test statistic [96].

The test statistic is defined as

$$q(\mu) = \begin{cases} -2\log\lambda(\mu) & \text{when } \mu \geq \hat{\mu}, \\ 0 & \text{otherwise.} \end{cases} \quad (5.1)$$

2090 where

$$\lambda(\mu) = \frac{L(\mu, \theta_\mu)}{L(\hat{\mu}, \hat{\theta})} \quad (5.2)$$

2091 represents the profile likelihood ratio, in which  $\mu \equiv f$  from Section (4.8.4), is the  
2092 parameter characterising the signal strength.  $\hat{\mu}$  is defined at the maximum likelihood  
2093 value,  $\hat{\theta}$  the set of maximum likelihood values of the nuisance parameters and  $\theta_\mu$  the set  
2094 of maximum values of the nuisance parameters for a given value of  $\mu$ .

2095 When  $\mu \equiv f = 1$ , the signal model is considered at its nominal production cross section.  
2096 The distribution of  $q_\mu$  is built up via the generation of pseudo experiments in order to  
2097 obtain two distributions for the background (B) and signal plus background (S+B) cases.  
2098 The compatibility of a signal model with observations in data is determined by the  
2099 parameter  $CL_s$ ,

$$\text{CL}_S = \frac{\text{CL}_{S+B}}{\text{CL}_B}, \quad (5.3)$$

with  $\text{CL}_B$  and  $\text{CL}_{S+B}$  defined as one minus the quantiles of the observed value in the data of the two distributions. A model is considered to be excluded at 95% confidence level when  $\text{CL}_s \leq 0.05$  [97].

### 5.2.2. Interpretation in simplified signal models

Different  $n_{jet}$  and  $n_b^{reco}$  bins are used in the interpretation of different **SMS** models. The choice of the categories used are made to increase sensitivity to that particular type of final state signature. The production and decay modes of the **SMS** models under consideration are summarised in Table 5.3, with limit plots of the experimental reach in these models shown in Figure 5.10.

The models T1 and T2 are used to characterise the pair production of gluinos and first or second generation squarks, respectively, with parameters for the sparticle mass as well as on the **LSP** mass. The simplified models T2bb, T1tttt, and T1bbbb describe various production and decay mechanisms in the context of third-generation squarks.

Model	Production/decay	$n_{jet}$	$n_b^{reco}$	Process	Limit	$m_{\tilde{q}/\tilde{g}}^{\text{best}}$ (GeV)	$m_{\text{LSP}}^{\text{best}}$ (GeV)
T1	$pp \rightarrow \tilde{g}\tilde{g}^* \rightarrow q\bar{q}\tilde{\chi}_1^0 q\bar{q}\tilde{\chi}_1^0$	$\geq 4$	0	5.9(a)	5.10(a)	$\sim 950$	$\sim 450$
T2	$pp \rightarrow \tilde{q}\tilde{q}^* \rightarrow q\tilde{\chi}_1^0 \bar{q}\tilde{\chi}_1^0$	$\leq 3$	0	5.9(b)	5.10(b)	$\sim 775$	$\sim 325$
T2bb	$pp \rightarrow \tilde{b}\tilde{b}^* \rightarrow b\tilde{\chi}_1^0 \bar{b}\tilde{\chi}_1^0$	$\leq 3$	1,2	5.9(c)	5.10(c)	$\sim 600$	$\sim 200$
T1tttt	$pp \rightarrow \tilde{g}\tilde{g}^* \rightarrow t\bar{t}\tilde{\chi}_1^0 t\bar{t}\tilde{\chi}_1^0$	$\geq 4$	$2,3,\geq 4$	5.9(d)	5.10(d)	$\sim 975$	$\sim 325$
T1bbbb	$pp \rightarrow \tilde{b}\tilde{b}^* \rightarrow b\tilde{\chi}_1^0 b\bar{b}\tilde{\chi}_1^0$	$\geq 4$	$2,3,\geq 4$	5.9(e)	5.10(e)	$\sim 1125$	$\sim 650$

**Table 5.3.:** A table representing the **SMS** models interpreted within the analysis. The model name and production and decay chain is specified in the first two columns. Each **SMS** model is interpreted in specific  $n_{jet}$  and  $n_b^{reco}$  categories which are detailed in the third and fourth columns. The last two columns indicate the search sensitivity for each model, representing the largest  $m_{\tilde{q}/\tilde{g}}$  mass beyond which no limit can be set for this particular decay topology. The quotes values are conservatively determined from the observed exclusion based on the theoretical production cross section minus  $1\sigma$  uncertainty.

Experimental uncertainties on the **SM** background predictions (10 – 30%, Section (4.6.1)), the luminosity measurement (4.4%), and the total acceptance times efficiency of the selection for the considered signal model (12 – 18%, Section (4.7)) are included in the calculation of the limit.

2117 Signal efficiency in the kinematic region defined by  $0 < m_{\tilde{g}(\tilde{q})} < 175$  GeV or  $m_{\tilde{g}(\tilde{q})} < 300$   
2118 GeV is strongly affected by the presence of Initial State Radiation (**ISR**). This region in  
2119 which direct (i.e., non-**ISR** induced) production is kinematically forbidden due to the  $H_T$   
2120  $> 275$  GeV requirement, therefore a large percentage of signal acceptance is due to the  
2121 effect of **ISR** jets. Given the large associated uncertainties, no interpretation is provided  
2122 for this kinematic region.

2123 The estimates on mass limits shown in Table 5.3, are determined conservatively from  
2124 the observed exclusion based on the theoretical production cross section, minus  $1\sigma$   
2125 uncertainty. The most stringent mass limits on pair-produced sparticles are obtained at  
2126 low **LSP** masses, while the limits typically weaken for compressed spectra points close to  
2127 the diagonal. In particular, for all of the considered **SMS** models, there is an **LSP** mass  
2128 beyond which no limit can be set, which can be observed from the figures referenced in the  
2129 table.

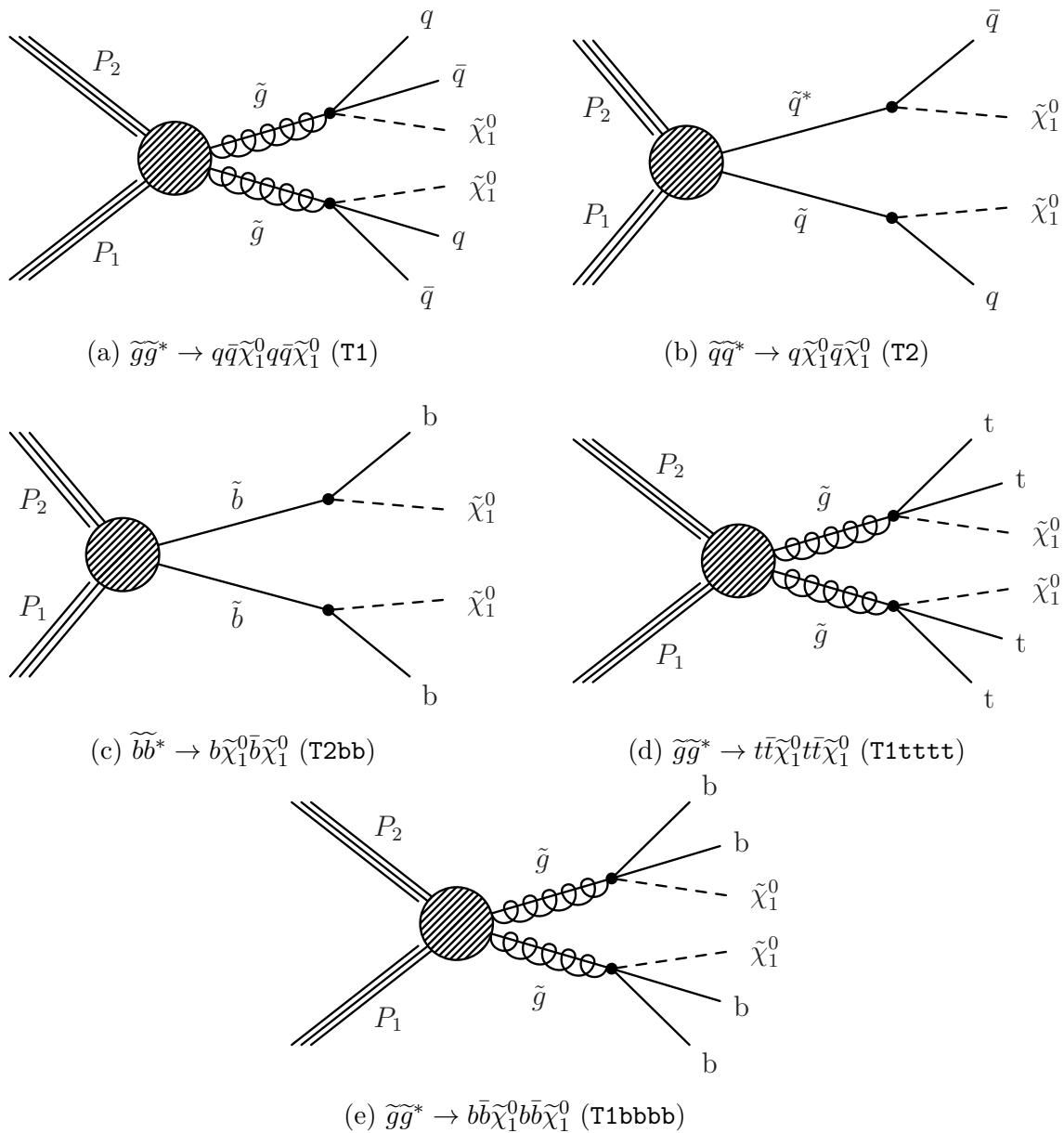


**Figure 5.9.:** Production and decay modes for the various **SMS** models interpreted within the analysis.

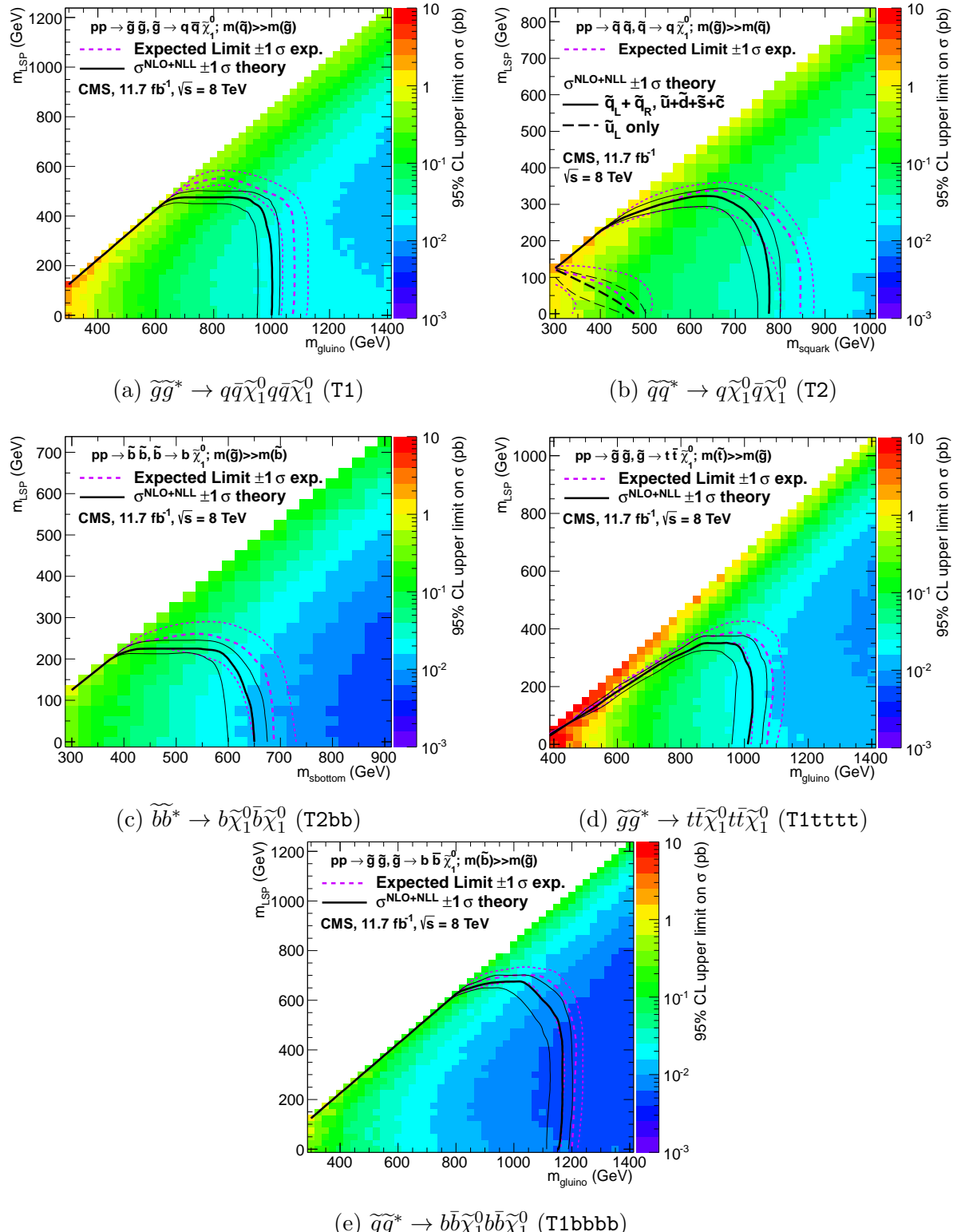


**Figure 5.10.:** Upper limit of cross section at 95% CL as a function of  $m_{\tilde{q}/\tilde{g}}$  and  $m_{LSP}$  for various **SMS** models. The solid thick black line indicates the observed exclusion region assuming **NLO** and **NLL** SUSY production cross section. The analysis selection efficiency is measured for each interpreted model, with the signal yield per point given by  $\epsilon \times \sigma$ . The thin black lines represent the observed excluded region when varying the cross section by its theoretical uncertainty. The dashed purple lines indicate the median (thick line)  $1\sigma$  (thin lines) expected exclusion regions.

# Chapter 6.

## 2130 Searches For Natural SUSY With 2131 B-tag Templates.

2132 Within this chapter a complimentary technique is discussed as a means to predict the  
2133 distribution of three and four reconstructed b-quark jets in an event. The recent discovery  
2134 of the Higgs boson has made third-generation “Natural SUSY” models attractive, given  
2135 that light top and bottom squarks are a candidate to stabilise divergent loop corrections  
2136 to the Higgs boson mass.

2137 Using the  $\alpha_T$  search as a base, a simple templated fit is employed to estimate the  
2138 SM background in higher b-tag multiplicities (3-4) from a region of a low number of  
2139 reconstructed b-jets (0-2). As a proof-of-concept, the procedure after being shown to  
2140 close in simulation, is applied to the SM enriched  $\mu + \text{jets}$  control sample of the  $\alpha_T$   
2141 all-hadronic search detailed in Chapter 4. To highlight the relative insensitivity of the  
2142 choice of the b-tagging algorithm working points in the effectiveness of the procedure,  
2143 results are presented using the CSV tagger (introduced in Section (3.3.2)) for the “Loose”,  
2144 “Medium” and “Tight” working points.

### 2145 6.1. Concept

2146 The dominant SM backgrounds most SUSY searches are typically  $t\bar{t} + \text{jets}$ ,  $W + \text{jets}$  and  
2147  $Z \rightarrow \nu\bar{\nu} + \text{jets}$ . These process are characterised by typically having zero or two underlying  
2148 b-quarks per event. The first step in this approach is to categorise two templates to be  
2149 fitted to the low  $n_b^{reco}$  multiplicity in terms of these underlying b-quark event topologies.

Typical underlying b-quark content	Process
= 0	$W \rightarrow l\nu + \text{jets}$ $Z \rightarrow \nu\bar{\nu} + \text{jets}$ $Z/\gamma^* \rightarrow \mu\mu + \text{jets}$
= 1	$t + \text{jets}$
= 2	$t\bar{t} + \text{jets}$

**Table 6.1.:** Typical underlying b-quark content of different SM processes which are common to many SUSY searches.

- 2150 Thus two templates are defined, Z0 and Z2 ( $t\bar{t}$  is combined with single top) which  
 2151 represent processes which have an underlying b-quark content of zero or two respectively.
- 2152 Both these templates can be generated through the application of the relevant event  
 2153 selection and taking the underlying  $n_b^{reco}$  distribution directly from simulation. However  
 2154 as discussed within Section (4.5), there are large uncertainties for high  $n_b^{reco}$  multiplicities  
 2155 due to limited MC statistics. This is particularly prominent for the Z0 templates, where  
 2156 the number of reconstructed b-tags is driven primarily by the light-quark mis-tagging  
 2157 rate. Therefore to improve the statistical precision of the predictions the formula method,  
 2158 introduced in Section (4.5.1) is used.
- 2159 The generation of these templates is then dependant upon the jet-flavour content and  
 2160 b-tagging rate within the phase space of interest, with the tagging probabilities of a jet  
 2161 being a function of the jet  $p_T$ , the pseudo-rapidity  $|\eta|$ , and the jet-flavour. This can be  
 2162 observed in Figure 6.1, where the b-tagging / c-quark mis-tagging / light mis-tagging  
 2163 efficiency for the three working points of the CSV tagger is shown as a function of jet  $p_T$ .
- 2164 Before the templates are generated, the relevant jet  $p_T$  and  $\eta$  corrections are applied to  
 2165 correct simulation to data, as specified in Section (4.5.3), to then determine the average  
 2166 tagging rates per analysis bin.
- 2167 These two templates are then fit to data in the low  $n_b^{reco}$  region (0-2). The fit result is  
 2168 used, along with the knowledge of the template shapes, to extrapolate an estimate to the  
 2169 high  $n_b^{reco}$  signal region (3,4), which is then compared to what is observed in data.
- 2170 This method can, in principle, be applied to any analysis where the signal hypothesis  
 2171 has a larger underlying b-quark spectra than the SM backgrounds, as it solely relies on  
 2172 fitting to the shape of the  $n_b^{reco}$  distribution.

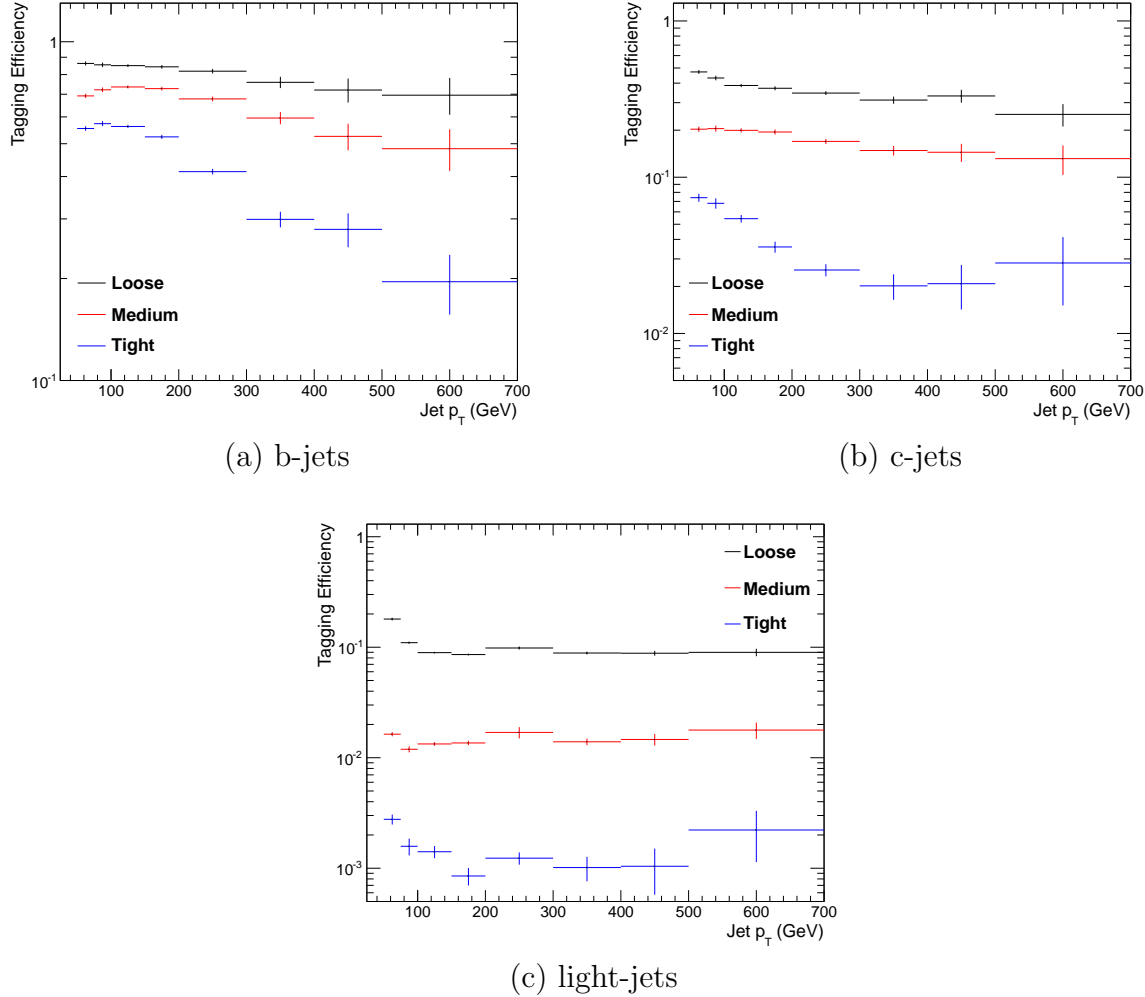


**Figure 6.1.:** The b-tagging (a), c-quark mis-tagging (b), and light-quark mis-tagging rate (c) as measured in simulation after the  $\alpha_T$  analysis,  $\mu + \text{jets}$  control sample selection in the region  $H_T > 375$ .

## 2173 6.2. Application to the $\alpha_T$ Search

2174 As detailed in the previous chapter, the  $\alpha_T$  analysis is a search for **SUSY** particles  
 2175 in all-hadronic final states, utilising the kinematic variable  $\alpha_T$  to suppress QCD to a  
 2176 negligible level. **SM** enriched control samples are used to estimate the background within  
 2177 an all-hadronic signal region.

2178 The selection for the  $\mu + \text{jets}$  control samples defined in Section (4.2.3) is used to  
 2179 demonstrate the template fitting procedure both conceptually in simulation, and also  
 2180 when applied in data. This is chosen, as such a selection is dominated by events stemming  
 2181 from the **SM** processes with little or no signal contamination from potential new physics..

2182 Neither are contributions from rate **SM** processes with a higher underlying b-quark  
2183 content (e.g.  $t\bar{t}b\bar{b}$ ) expected. For these reasons, there is a degree of confidence that the  
2184 procedure should close when applied to this phase space.

2185 The analysis presented here is binning in source jet multiplicity bins, of 3,4 and  $\geq 5$   
2186 reconstructed jets per event (di-jet events are not included as there is no contribution  
2187 to the high  $n_b^{reco}$  region (3,4)) , in order to reduce the kinematic jet  $p_T$  dependence.  
2188 Furthermore the analysis is split into three  $H_T$  regions,

2189 • 275-325 GeV

2190 • 325-375 GeV

2191 •  $> 375$  GeV

2192 contrary to the eight used within the  $\alpha_T$  analysis. Templates for both underlying b-quark  
2193 content hypotheses are then generated for the nine defined analysis bins.

### 2194 6.2.1. Proof of principle in simulation

2195 In order to demonstrate that the template procedure produces accurate predictions  
2196 within simulation, the simulation samples in the analysis are firstly split into two to allow  
2197 for statistically independent fits to be performed.

2198 By combining the relevant ingredients necessary to employ the formula method,  $n_b^{reco}$   
2199 templates for  $Z = 0$  and  $Z= 2$  are generated individually for each  $n_{jet}$  and  $H_T$  bin using  
2200 one half of each simulation sample. A fit of these two templates is then performed in the  
2201 low  $n_b^{reco}$  (0-2) region, back to the sum of the other halves of each simulation sample in  
2202 order to check that the relevant information can be recovered in the  $n_b^{reco}$  signal region  
2203 (3-4).

2204 The fits are performed independently within each of the defined analysis bins to reduce the  
2205 dependence of the shapes of these distributions on simulation. The half of the simulation  
2206 sample for which the templates are fitted too, are taken directly from simulation, extending  
2207 this procedure to also be a validation of the formula method to accurately estimate  
2208 the  $n_b^{reco}$  distribution. Additionally as this test is performed in simulation, the relevant  
2209 corrections of the b-tagging rates between data and simulation are *not* applied.

2210 Within Figure 6.2, the results of this fitting procedure is shown for each **CSV** working  
2211 point. Results are presented for the  $n_{jet} \geq 5$  category, using the  $\mu +$  jets control sample

<sup>2212</sup> selection in the inclusive  $H_T > 375$  GeV analysis bin. The grey bands represent the  
<sup>2213</sup> statistical uncertainty on the template shapes. Additional fits are shown for other  $n_{jet}$   
<sup>2214</sup> category within Appendix D.1.

<sup>2215</sup> Furthermore the extrapolated fit predictions within the high  $n_b^{reco}$  signal region, are  
<sup>2216</sup> summarised for all  $H_T$  bins and working points in Table 6.2.

$H_T$	275-325	325-375	>375
Loose working point			
Simulation $n_b = 3$	$793.0 \pm 14.8$	$387.9 \pm 10.2$	$794.1 \pm 14.34$
Template $n_b = 3$	$820.4 \pm 26.7$	$376.3 \pm 11.9$	$780.1 \pm 15.1$
Simulation $n_b = 4$	$68.2 \pm 3.9$	$27.6 \pm 2.7$	$91.28 \pm 4.9$
Template $n_b = 4$	$72.5 \pm 4.7$	$28.25 \pm 2.34$	$84.4 \pm 3.8$
Medium working point			
Simulation $n_b = 3$	$133.7 \pm 5.7$	$74.5 \pm 4.5$	$164.2 \pm 6.4$
Template $n_b = 3$	$132.8 \pm 4.8$	$74.5 \pm 3.9$	$159.9 \pm 5.7$
Simulation $n_b = 4$	$1.6 \pm 0.6$	$0.6 \pm 0.4$	$3.4 \pm 0.9$
Template $n_b = 4$	$1.8 \pm 0.2$	$1.1 \pm 0.2$	$4.1 \pm 0.4$
Tight working point			
Simulation $n_b = 3$	$26.9 \pm 2.6$	$13.9 \pm 1.9$	$31.8 \pm 2.9$
Template $n_b = 3$	$24.7 \pm 1.5$	$13.8 \pm 1.2$	$28.1 \pm 1.5$
Simulation $n_b = 4$	$0.5 \pm 0.4$	-	-
Template $n_b = 4$	$0.1 \pm 0.1$	$0.1 \pm 0.1$	$0.2 \pm 0.1$

**Table 6.2.:** Summary of the fit predictions in the  $n_b^{reco}$  signal region for  $n_{jet} = 3, = 4, \geq 5$ . The fit region is  $n_b^{reco} = 0, 1, 2$  and simulation yields are normalised to an integrated luminosity of  $10 \text{ fb}^{-1}$ . The uncertainties quoted on the template yields are purely statistical.

<sup>2217</sup> The pull distributions for all the fits performed can be found in Appendix D.2, and  
<sup>2218</sup> are compatible with a mean of zero and standard deviation of one. The good overall  
<sup>2219</sup> agreement summarised in the table validates both the formula method used to generate  
<sup>2220</sup> the templates as well as the fitting procedure itself. The application of this method to  
<sup>2221</sup> the same selection in a data control sample, is now used to demonstrate necessary control  
<sup>2222</sup> over the efficiency and mis-tagging rates when b-tagging scale factors are applied.

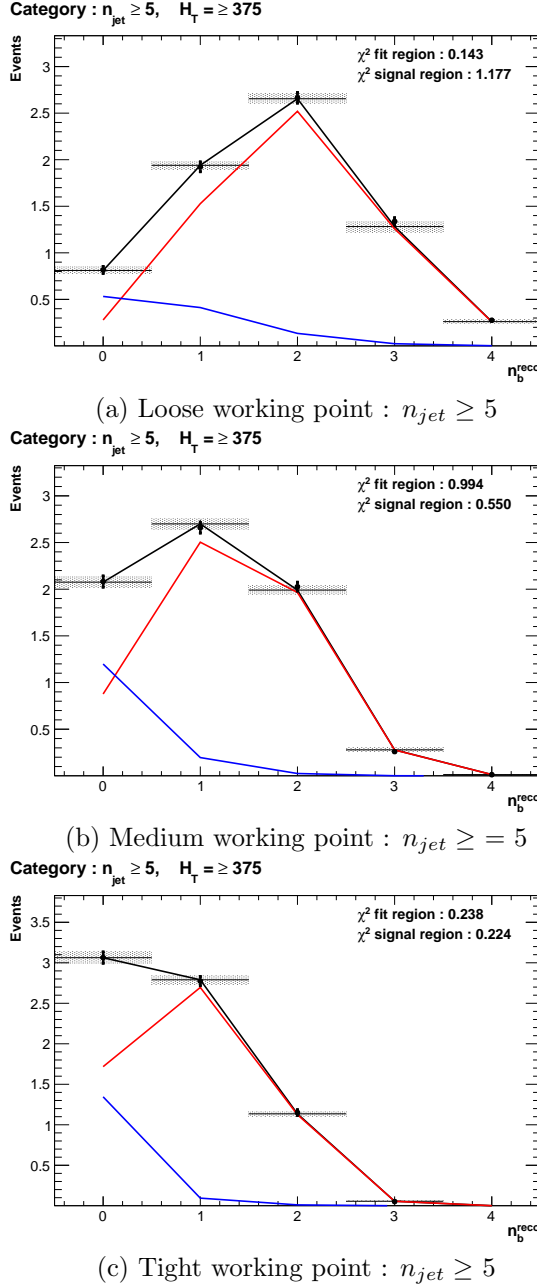


**Figure 6.2.:** The results of fitting the  $Z = 0$  and  $Z = 2$  templates to the  $n_b^{reco} = 0, 1, 2$  bins taken directly from simulation in the region  $H_T > 375$  GeV, for the  $n_{jet} \geq 5$  category. The blue template represents  $Z = 0$ , while the red template represents  $Z = 2$ . Grey bands represent the statistical uncertainty of the fit. The  $\chi^2$  parameter displayed represents the goodness of fit to the low  $n_b^{reco}$  (0-2) control region.

---

### 6.2.2. Results in a data control sample

- The method above is now applied to the 2012 8 TeV dataset in the  $\mu +$  jets control sample, to establish the validity of this method in data. The relevant data to simulation scale factors are applied to get corrected values of the efficiency and mis-tagging rates measured in data [64] [87].
- Figure 6.3 show the the results of the templates derived from simulation to each of the three defined  $H_T$  bins, in the  $n_{jet} \geq 5$  category for the medium working point CSV tagger (the same working point used within the  $\alpha_T$  analysis). Grey bands represent the statistical uncertainty of the fit combined in quadrature with the systematic uncertainties of varying the data to simulation scale factors up and down by their measured systematic uncertainties. Additional fit results for other jet multiplicities are found in Appendix D.3
- The numerical results and extrapolation to the  $n_b^{reco} = 3, 4$  bins for all  $H_T$  and working points is shown in Table 6.3.

$H_T$	275-325	325-375	>375
Loose working point			
Data $n_b = 3$	838	394	717
Template $n_b = 3$	$861.8 \pm 16.7$	$372.1 \pm 10.1$	$673.2 \pm 14.1$
Data $n_b = 4$	81	43	81
Template $n_b = 4$	$74.5 \pm 2.3$	$27.6 \pm 1.2$	$71.6 \pm 2.6$
Medium working point			
Data $n_b = 3$	137	79	152
Template $n_b = 3$	$131.2 \pm 2.3$	$65.1 \pm 1.7$	$127.8 \pm 2.4$
Data $n_b = 4$	1	1	3
Template $n_b = 4$	$1.8 \pm 0.1$	$0.9 \pm 0.1$	$3.1 \pm 0.1$
Tight working point			
Data $n_b = 3$	24	15	25
Template $n_b = 3$	$23.0 \pm 0.4$	$10.9 \pm 0.3$	$20.3 \pm 0.5$
Data $n_b = 4$	0	0	1
Template $n_b = 4$	$0.1 \pm 0.1$	$0.1 \pm 0.1$	$0.2 \pm 0.1$

**Table 6.3.:** Summary of the fit predictions in the  $n_b^{reco}$  signal region of the  $\mu +$  jets control sample, for  $n_{jet} = 3, = 4, \geq 5$ . The fit region is  $n_b^{reco} = 0, 1, 2$  using  $11.4 \text{ fb}^{-1}$  of data at  $\sqrt{s} = 8\text{TeV}$ . The uncertainties quoted on the template yields are purely statistical.

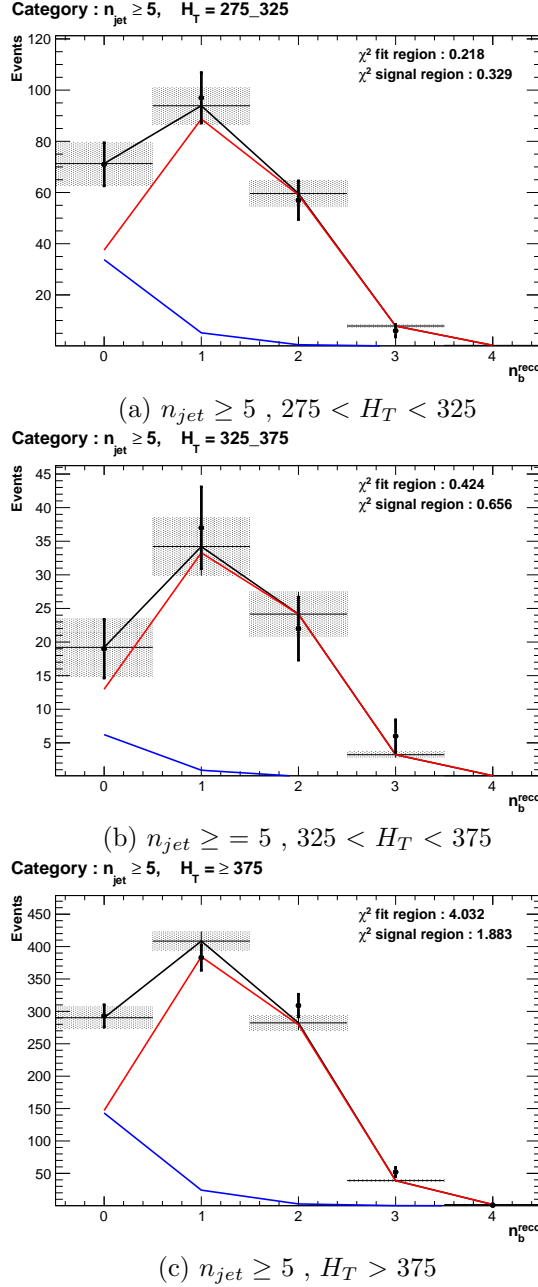


**Figure 6.3.:** The results of fitting the  $Z = 0$  and  $Z = 2$  templates to the  $n_b^{reco} = 0, 1, 2$  bins taken directly from data, for the  $n_{jet} \geq 5$  category and medium CSV working point. The blue template represents  $Z = 0$ , while the red template represents  $Z = 2$ . The  $\chi^2$  parameter displayed represents the goodness of fit to the low  $n_b^{reco}$  (0-2) control region.

2236 The agreement for all working points demonstrates a good control of the b-tagging  
 2237 efficiency and mis-tagging rates and gives confidence in the method outlined.

---

### 2238 6.2.3. Application to the $\alpha_T$ hadronic search region

- 2239 As an accompaniment to the background estimation methods outlined by the  $\alpha_T$  search.  
 2240 The b-tag template method offers a complimentary way of testing the SM only background  
 2241 of the hadronic signal region of the search. In the absence presence of a natural SUSY  
 2242 signature, containing four underlying b or t quarks, the number of reconstructed three/four  
 2243 b-tagged events will be enhanced.
- 2244 Figure 6.4 show the the results of the templates derived from simulation to each of  
 2245 the three CSV working points, in the  $n_{jet} \geq 5$ ,  $H_T > 375$  GeV category. Grey bands  
 2246 represent the statistical uncertainty of the fit combined in quadrature with the systematic  
 2247 uncertainties of varying the data to simulation scale factors up and down by their  
 2248 measured systematic uncertainties. Additional fit results for other jet multiplicities are  
 2249 found in Appendix D.4
- 2250 The numerical results and extrapolation to the  $n_b^{reco} = 3, 4$  bins for all  $H_T$  and working  
 2251 points is shown in Table 6.4. No excess of data is found and predictions from this method  
 2252 are found to be compatible with the  $\alpha_T$  maximum likelihood fit results from Table 5.2.

$H_T$	275-325	325-375	>375
Loose working point			
Data $n_b = 3$	198	85	126
Template $n_b = 3$	$207.1 \pm 9.0$	$103.4 \pm 5.9$	$124.98 \pm 7.4$
Data $n_b = 4$	15	9	16
Template $n_b = 4$	$15.9 \pm 1.2$	$8.05 \pm 0.9$	$13.1 \pm 1.3$
Medium working point			
Data $n_b = 3$	28	15	12
Template $n_b = 3$	$24.4 \pm 0.9$	$12.7 \pm 0.8$	$19.9 \pm 2.4$
Data $n_b = 4$	1	0	2
Template $n_b = 4$	$0.3 \pm 0.2$	$0.3 \pm 0.1$	$0.5 \pm 0.1$
Tight working point			
Data $n_b = 3$	5	2	0
Template $n_b = 3$	$4.03 \pm 0.2$	$2.4 \pm 0.2$	$3.1 \pm 0.2$
Data $n_b = 4$	1	0	0
Template $n_b = 4$	$0.1 \pm 0.1$	$0.1 \pm 0.1$	$0.0 \pm 0.1$

**Table 6.4.:** Summary of the fit predictions in the  $n_b^{reco}$  signal region of the  $\mu +$  jets control sample, for  $n_{jet} = 3, = 4, \geq 5$ . The fit region is  $n_b^{reco} = 0, 1, 2$  using  $11.7 \text{ fb}^{-1}$  of data at  $\sqrt{s} = 8\text{TeV}$ . The uncertainties quoted on the template yields are purely statistical.

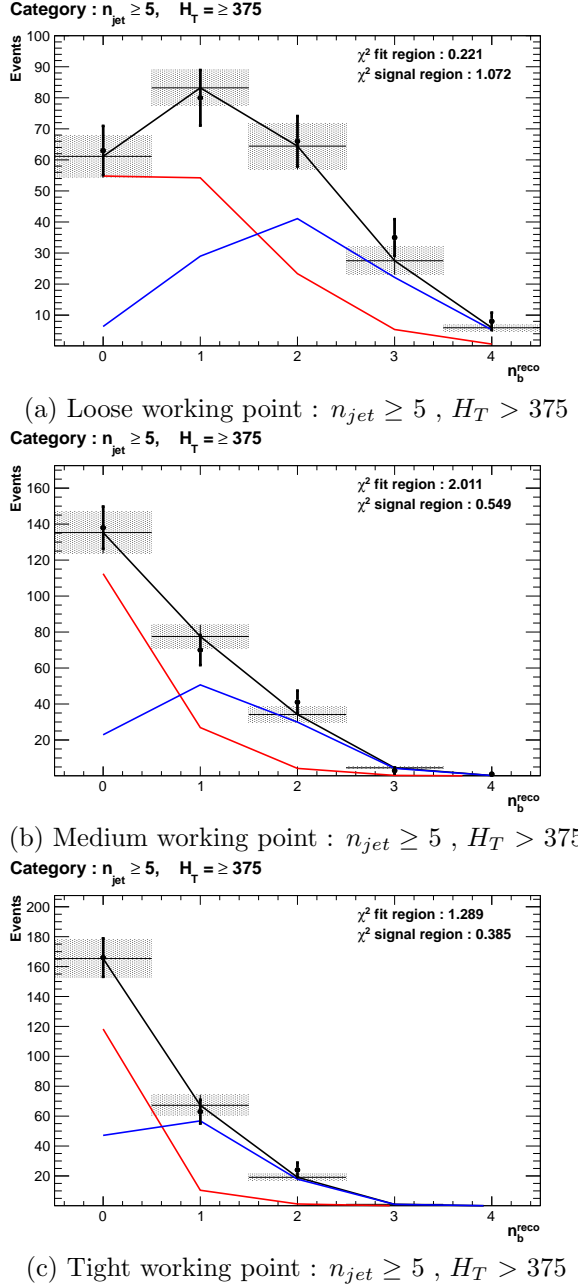


**Figure 6.4.:** The results of fitting the  $Z = 0$  and  $Z = 2$  templates to the  $n_b^{reco} = 0, 1, 2$  bins taken from data, in the  $n_{jet} \geq 5$  and  $H_T > 375$  category for all CSV working points. The blue template represents  $Z = 0$ , while the red template represents  $Z = 2$ . The  $\chi^2$  parameter displayed represents the goodness of fit to the low  $n_b^{reco}$  (0-2) control region.

2253 **6.3. Summary**

2254 A **SUSY** signature such as one from gluino-induced third-generation squark production,  
2255 would result in a final state with an underlying b-quark content greater than two. In  
2256 order to be able to discriminate such signatures from the **SM** background, templates are  
2257 generated based on a parameterisation of the number of the **SM** processes, where the  
2258 underlying b-quarks per event is typically zero or two. These templates are then fit to  
2259 data in a low  $n_b^{reco}$  (0-2) control region in order to extrapolate a prediction in a high  
2260  $n_b^{reco}$  (3-4) signal region.

2261 The method was demonstrated both in simulation and also in data, using the **SM** enriched  
2262  $\mu + \text{jets}$  selection from the  $\alpha_T$  search, to prove conceptually and experimentally that the  
2263 method works and there is adequate control over the efficiency and mis-tagging rates in  
2264 data for all working points of the **CSV** tagger. Additionally this method was also applied  
2265 to the  $\alpha_T$  analysis signal region where good agreement is observed between data and the  
2266 background estimation method of the  $\alpha_T$  analysis.

# Chapter 7.

## <sup>2267</sup> Conclusions

<sup>2268</sup> A search for supersymmetry is presented based on a data sample of pp collisions collected  
<sup>2269</sup> at  $\sqrt{s} = 8$  TeV, corresponding to an integrated luminosity of  $11.7 \pm 0.5$  fb<sup>-1</sup>. Final  
<sup>2270</sup> states with two or more jets and significant  $\cancel{E}_T$ , a typical final state topology of R-parity  
<sup>2271</sup> conserving SUSY models have been analysed. The sum of standard model backgrounds  
<sup>2272</sup> per bin are estimated from a simultaneous binned likelihood fit to hadronic,  $\mu +$  jets,  
<sup>2273</sup>  $\mu\mu +$  jets, and  $\gamma +$  jets samples. Systematic errors due to theory, detector effects and  
<sup>2274</sup> analysis choices are quantified through the use of data driven closure tests and accounted  
<sup>2275</sup> for in the final interpretation.

<sup>2276</sup> No excess of events is observed over the expected SM background. The analysis is  
<sup>2277</sup> further interpreted in a set of SMS models, with a special emphasis on third generation  
<sup>2278</sup> squarks and compressed spectra scenarios. In the considered models with gluino pair  
<sup>2279</sup> production and for small LSP masses, exclusion limits of the gluino mass are in the range  
<sup>2280</sup> 950-1125 GeV. For SMS with squark pair production, first or second generation squarks  
<sup>2281</sup> are excluded up to around 775 GeV and bottom squarks are excluded up to 600 GeV,  
<sup>2282</sup> again for small LSP masses.

<sup>2283</sup> A complementary approach using a templated method to estimate the b-tag jet distribu-  
<sup>2284</sup> tion of SM processes, is used to search for gluino induced third generation squark SUSY  
<sup>2285</sup> production. The  $\alpha_T$  analysis is used to demonstrate conceptually and experimentally  
<sup>2286</sup> this technique in the  $\mu +$  jets control sample. This method is further applied to the  
<sup>2287</sup>  $\alpha_T$  hadronic search region where good agreement is observed between the data and the  
<sup>2288</sup> background estimation procedure of the  $\alpha_T$  analysis.

<sup>2289</sup> The performance of the Level-1 trigger for jets and energy sum quantities is also presented.  
<sup>2290</sup> These studies quantify any change in level-1 performance after the introduction of a 5

<sub>2291</sub> GeV jet seed threshold into the jet algorithm configuration. No significant change in  
<sub>2292</sub> single jet trigger efficiencies is observed and good performance is observed for a range of  
<sub>2293</sub> level-1 quantities.

<sub>2294</sub>

# Appendix A.

## <sup>2295</sup> **Miscellaneous**

### <sup>2296</sup> **A.1. Jet Identification Criteria**

<sup>2297</sup> For Calo jets the following criteria were applied:

Loose CaloJet Id	
Variable	Definition
$f_{HPD} < 0.98$	Fraction of jet energy contributed from “hottest” <b>HPD</b> , which rejects <b>HCAL</b> noise.
$f_{EM} > 0.01$	Noise from the <b>HCAL</b> is further suppressed by requiring a minimal electromagnetic component to the jet $f_{EM}$ .
$N_{hits}^{90} \geq 2$	Jets that have $> 90\%$ of its energy from a single channel are rejected, to serve as a safety net that catches jets arising from undiagnosed noisy channels.

**Table A.1.:** Criteria for a reconstructed jet to pass the loose calorimeter jet id.

<sup>2298</sup> For PF jets the following criteria were applied:

---

Loose PF jet Id	
Variable	Definition
<code>nfhJet &lt; 0.99</code>	Fraction of jet composed of neutral hadrons. <b>HCAL</b> noise tends to populate high values of neutral hadron fraction.
<code>nemfJet &lt; 0.99</code>	Fraction of jet composed of neutral electromagnetic energy. <b>ECAL</b> noise tends to populate high values of neutral EM fraction.
<code>nmultiJet &gt; 1</code>	Number of constituents that jet is composed from.
<code>chfJet &gt; 0</code>	Fraction of jet composed of charged hadrons.
<code>cmultiJet &gt; 0</code>	Number of charged particles that compose jet.
<code>cemfJet &lt; 0.99</code>	Fraction of jet composed of charged electromagnetic energy.

---

**Table A.2.:** Criteria for a reconstructed jet to pass the loose PF jet id.

## 2299 A.2. Primary Vertices

2300 The pileup per event is defined by the number of 'good' reconstructed primary vertices  
2301 in the event, with each vertex satisfying the following requirements

---

Good primary vertex requirement	
Variable	Definition
$N_{dof} > 4$	The number of degree of freedom, from the vertex fit to compute the best estimate of the vertex parameters.
$ \Delta z_{vtx}  < 24\text{cm}$	The distance, $ \Delta z_{vtx} $ , to the position of the closest <b>HLT</b> primary vertex.
$\rho < 2\text{cm}$	The perpendicular distance of track position to the beam spot.

---

**Table A.3.:** Criteria for a vertex in an event to be classified as a 'good' reconstructed primary vertex.

# Appendix B.

## 2302 L1 Jets

### 2303 B.1. Jet matching efficiencies

2304 The single jet turn-on curves are derived from events independent of whether the leading  
2305 jet in an event is matched to a Level 1 jet using  $\Delta R$  matching detailed in Section (3.4.3)  
2306 or not. These turn-ons are produced from events which are not triggered on jet quantities  
2307 and therefore it is not guaranteed that the lead jet of an event will be seeded by a Level  
2308 1 jet. Figure B.1 shows the particular matching efficiency of a lead jet to a L1 jet.

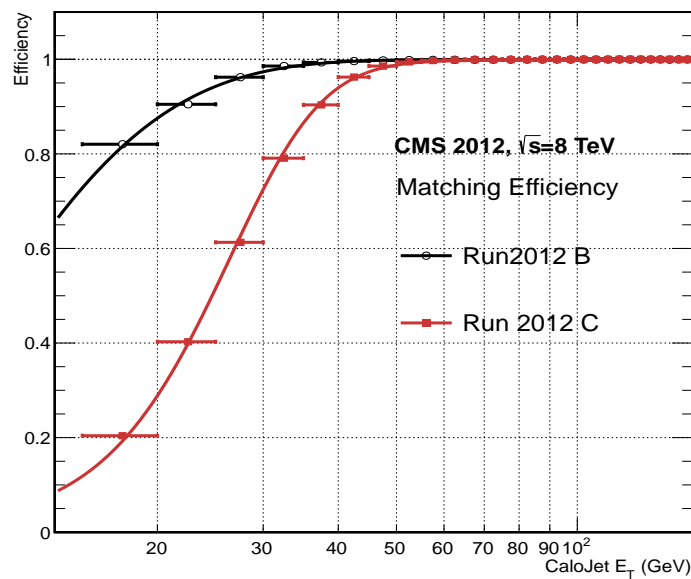


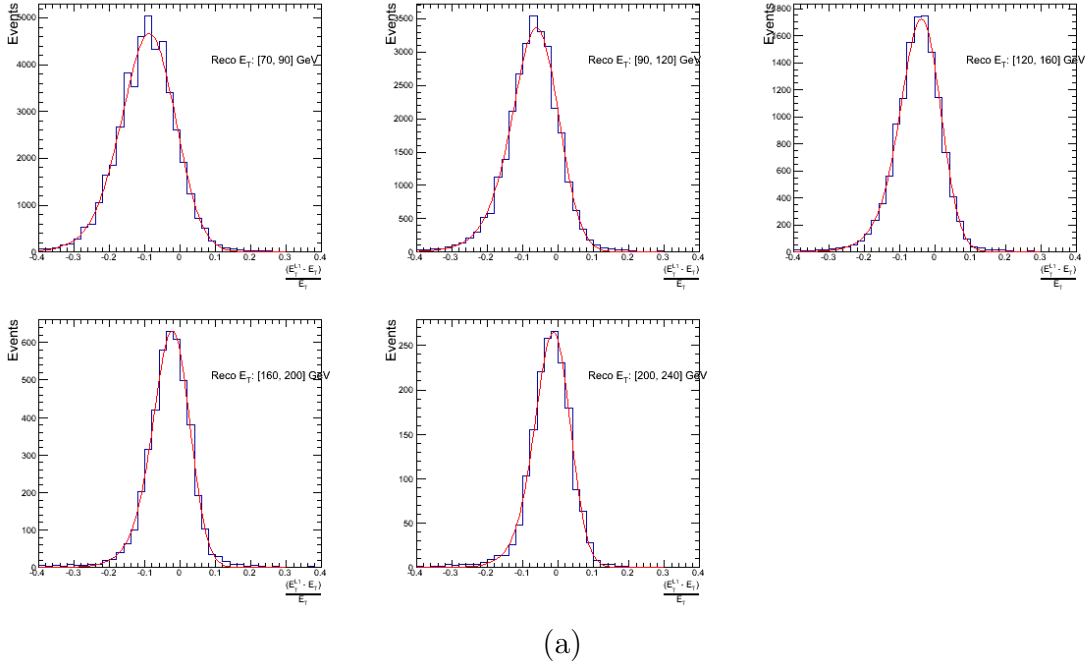
**Figure B.1.:** Leading jet matching efficiency as a function of the offline CaloJet  $E_T$ , measured in an isolated muon triggered dataset in the 2012B and 2012C run periods.

Run Period	$\mu$	$\sigma$
2012B	$6.62 \pm 0.01$	$0.79 \pm 0.03$
2012C	$19.51 \pm 0.03$	$7.14 \pm 0.02$

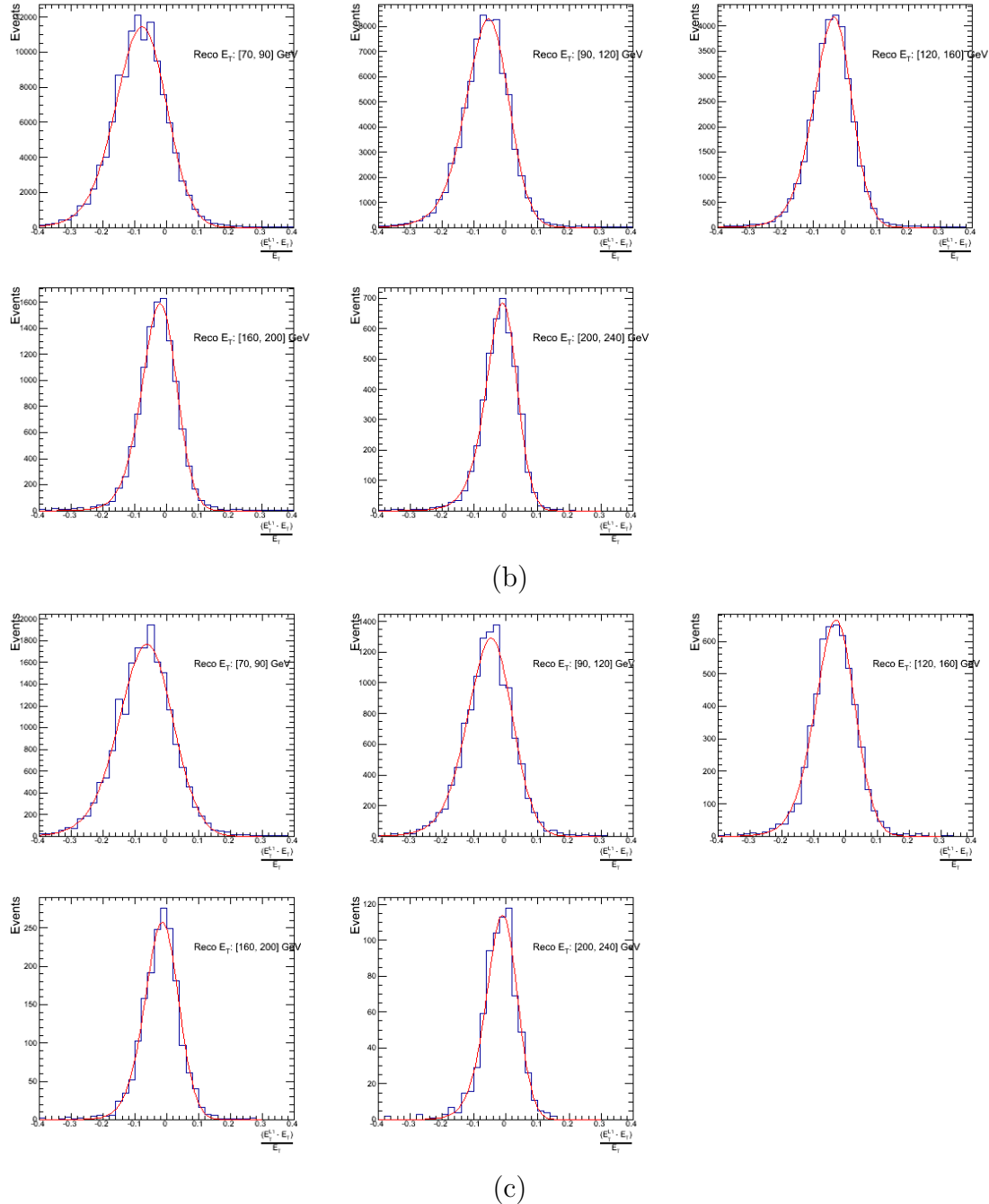
**Table B.1.:** Results of a cumulative EMG function fit to the turn-on curves for the matching efficiency of the leading jet in an event to a Level-1 jet in run 2012C and 2012B data, measured in an isolated muon triggered sample. The turn-on point,  $\mu$ , and resolution,  $\sigma$ , are measured with respect to offline Calo Jet  $E_T$ .

- 2309 It can be seen that the turn on is sharper during the 2012B run period. The seed  
 2310 threshold requirement of a 5 GeV jet seed in run 2012C results in more events in which  
 2311 even the lead offline jet does not have an associated L1 jet. For larger jet  $E_T$  thresholds,  
 2312 typical of thresholds used in physics analyses, 100% efficiency is observed.  
 2313 The matching efficiencies have a  $\mu$  values of 6.62 GeV and 19.51 GeV for Run 2012B  
 2314 and 2012C respectively and is shown in Table B.1.

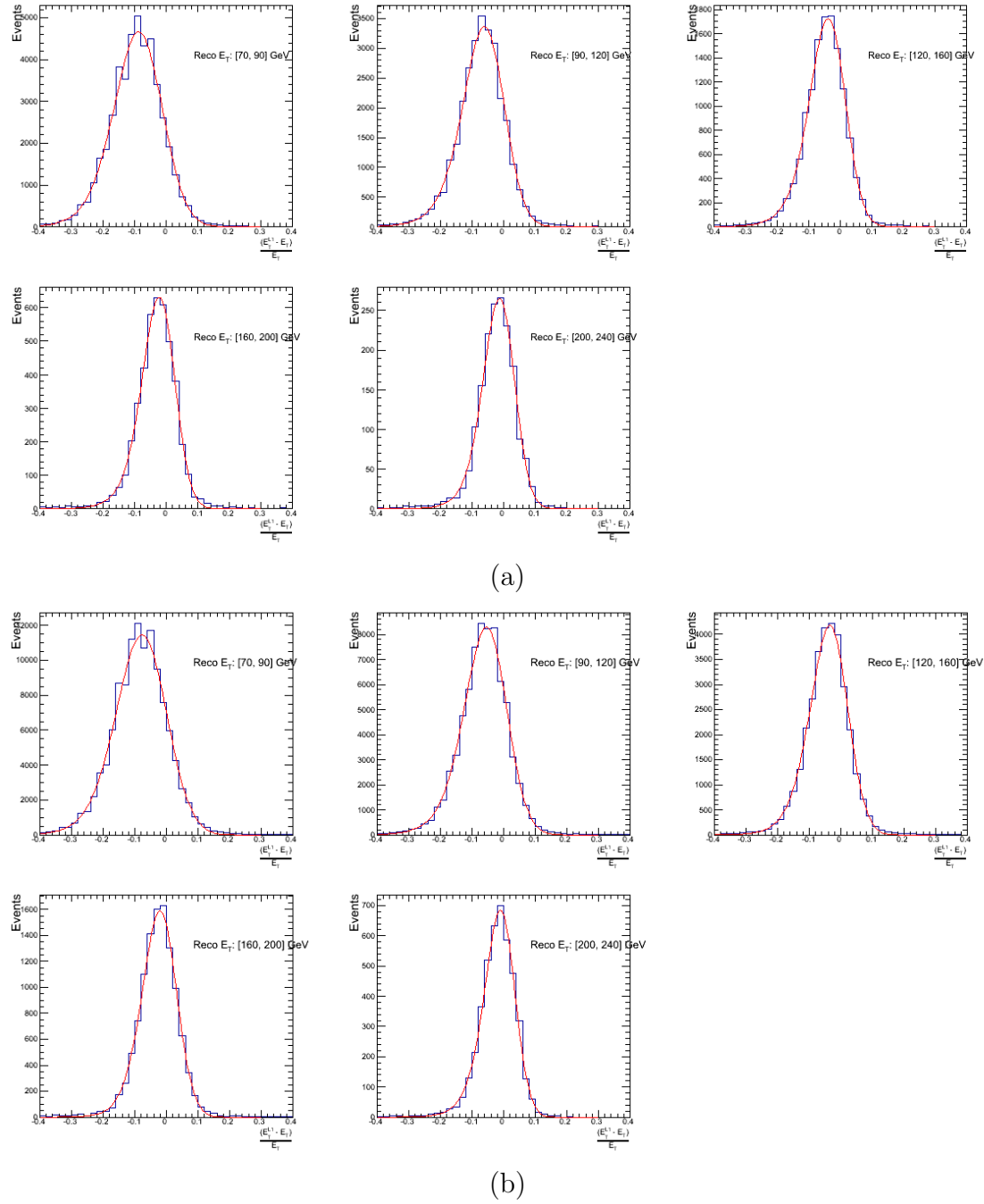
## 2315 B.2. Leading Jet Energy Resolution

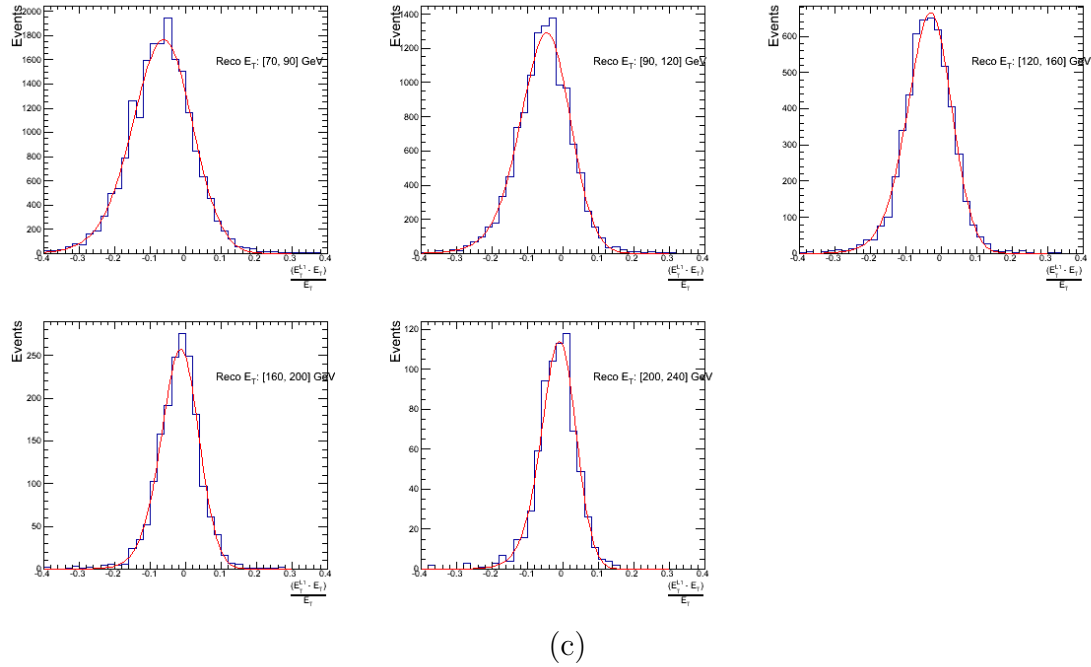


(a)



**Figure B.2.:** Resolution plots of the leading offline jet Calo  $E_T$  measured as a function of  $\frac{(L1\ E_T - \text{Offline}\ E_T)}{\text{Offline}\ E_T}$  for low (a), medium (b) and high (c) pile-up conditions.





(c)

**Figure B.3.:** Resolution plots of the leading offline jet PF  $E_T$  measured as a function of  $\frac{(\text{L1 } E_T - \text{Offline } E_T)}{\text{Offline } E_T}$  for low (a), medium (b) and high (c) pile-up conditions.

### 2316 B.3. Resolution for Energy Sum Quantities

2317 The following plots show the resolution parameters for the four energy sum quantities as  
 2318 a function of the quantity ( $q$ ) itself. In this case, The mean and RMS of the individual  
 2319  $\frac{(\text{L1 } q - \text{Offline } q)}{\text{Offline } q}$  distributions, in bins of the quantity  $q$  is displayed.

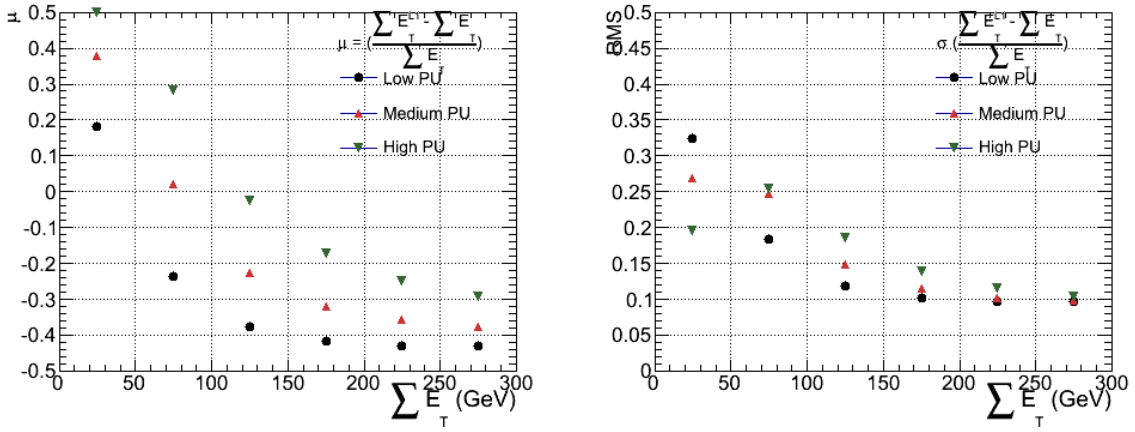


**Figure B.4.:**  $\sum E_T$  resolution parameters in bins of Calo  $\sum E_T$  measured for the defined low, medium and high pile up conditions. The plots show the mean  $\mu$  (left), resolution  $\sigma$  (RMS) of the  $\frac{\Delta q}{q}$  distributions.

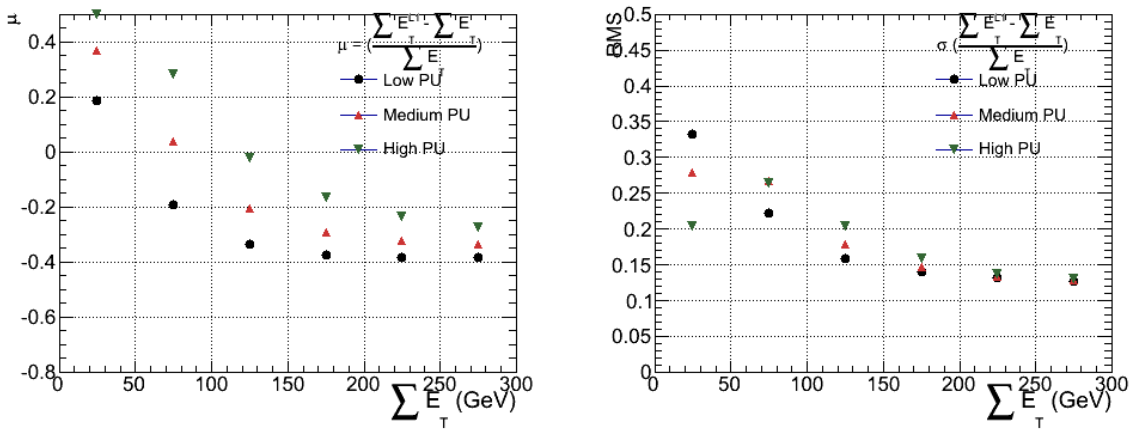


**Figure B.5.:**  $\sum E_T$  resolution parameters in bins of PF  $\sum E_T$  measured for the defined low, medium and high pile up conditions. The plots show the mean  $\mu$  (left), resolution  $\sigma$  (RMS) of the  $\frac{\Delta q}{q}$  distributions.

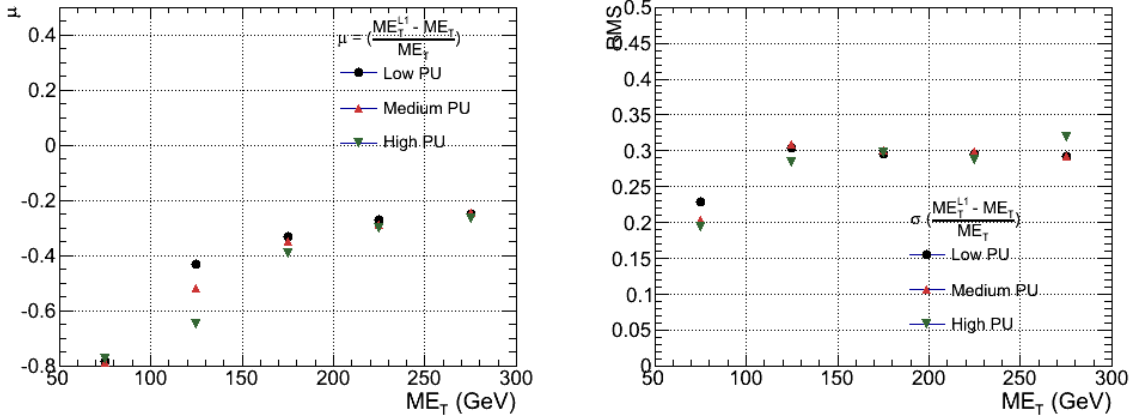


**Figure B.6.:**  $\mathcal{E}_T$  resolution parameters in bins of Calo  $\mathcal{E}_T$  measured for the defined low, medium and high pile up conditions. The plots show the mean  $\mu$  (left), resolution  $\sigma$  (RMS) of the  $\frac{\Delta q}{q}$  distributions.

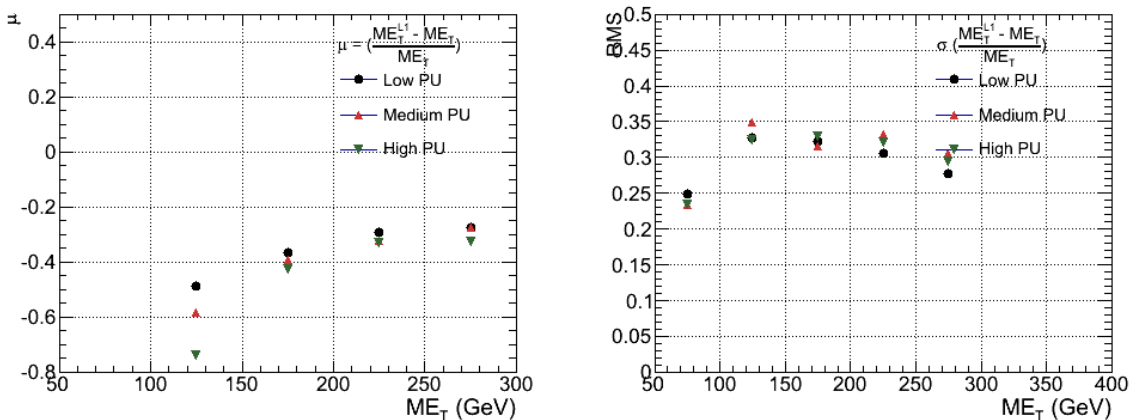


**Figure B.7.:**  $\mathcal{E}_T$  resolution parameters in bins of PF  $\mathcal{E}_T$  measured for the defined low, medium and high pile up conditions. The plots show the mean  $\mu$  (left), resolution  $\sigma$  (RMS) of the  $\frac{\Delta q}{q}$  distributions.

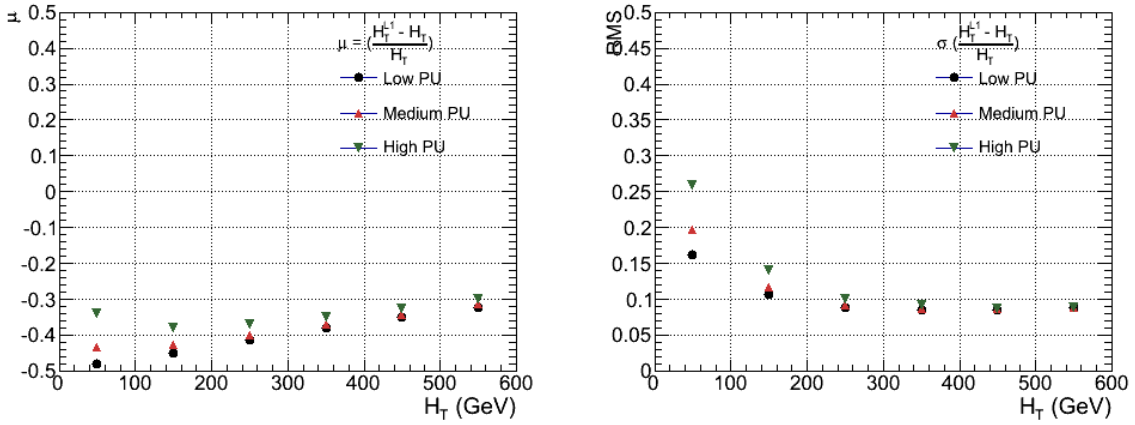


**Figure B.8.:**  $H_T$  resolution parameters in bins of Calo  $H_T$  measured for the defined low, medium and high pile up conditions. The plots show the mean  $\mu$  (left), resolution  $\sigma$  (RMS) of the  $\frac{\Delta q}{q}$  distributions.

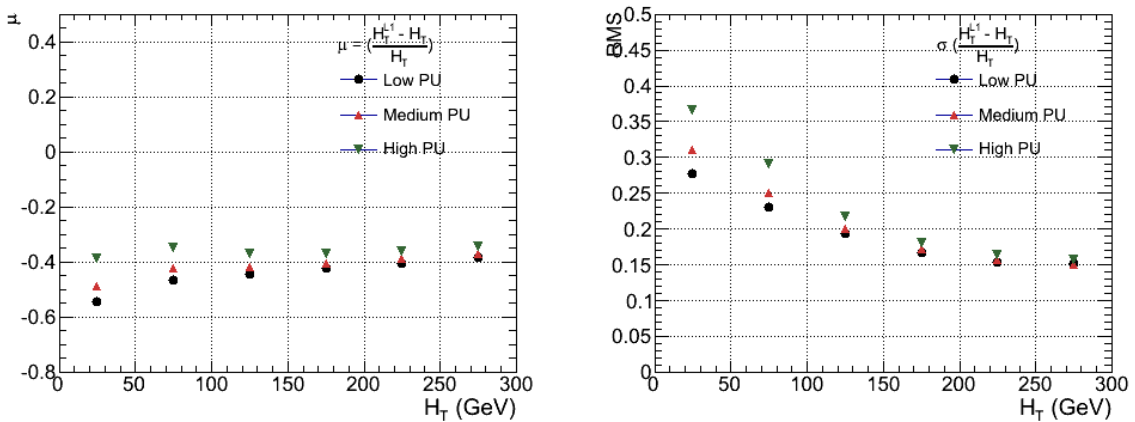


**Figure B.9.:**  $H_T$  resolution parameters in bins of PF  $H_T$  measured for the defined low, medium and high pile up conditions. The plots show the mean  $\mu$  (left), resolution  $\sigma$  (RMS) of the  $\frac{\Delta q}{q}$  distributions.

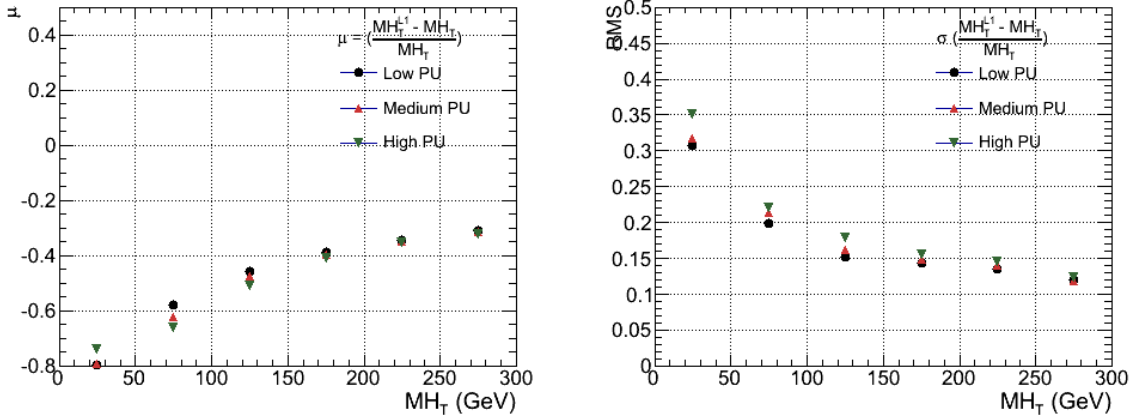


**Figure B.10.:**  $H_T$  resolution parameters in bins of  $H_T$  measured for the defined low, medium and high pile up conditions. The plots show the mean  $\mu$  (left), resolution  $\sigma$  (RMS) of the  $\frac{\Delta q}{q}$  distributions.

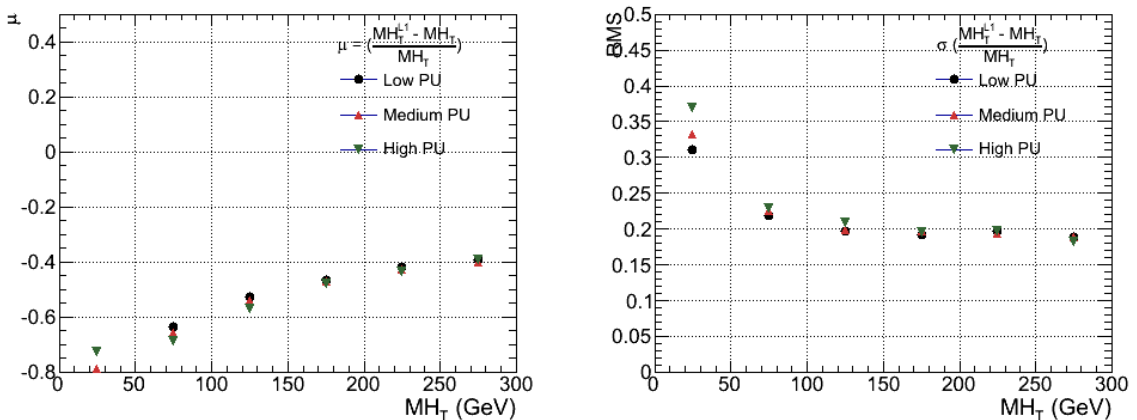


**Figure B.11.:**  $H_T$  resolution parameters in bins of PF  $H_T$  measured for the defined low, medium and high pile up conditions. The plots show the mean  $\mu$  (left), resolution  $\sigma$  (RMS) of the  $\frac{\Delta q}{q}$  distributions.

# Appendix C.

## <sup>2320</sup> Additional material on background <sup>2321</sup> estimation methods

### <sup>2322</sup> C.1. Determination of $k_{QCD}$

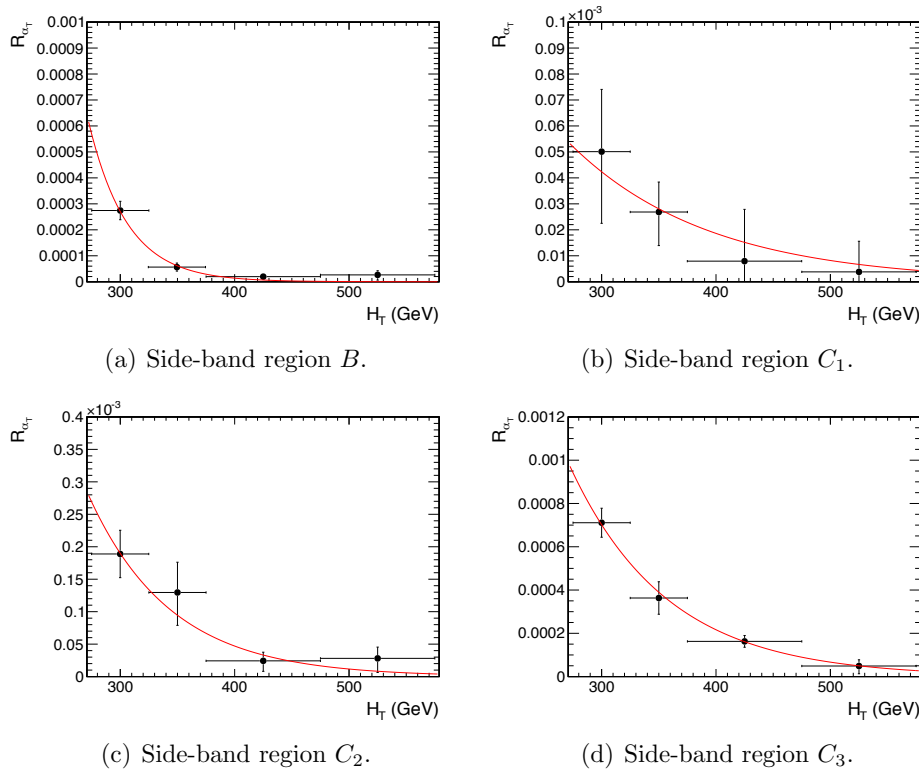


**Figure C.1.:**  $R_{\alpha_T}(H_T)$  and exponential fits for each of the data sideband regions. Fit is conducted between the  $H_T$  region  $275 < H_T < 575$ .

2324 **C.2. Effect of varying background cross sections on**  
2325 **closure tests**

2326 Closure tests with cross section variations of +20% and -20% applied to  $W + \text{jets}$  and  $t\bar{t}$   
2327 processes respectively.

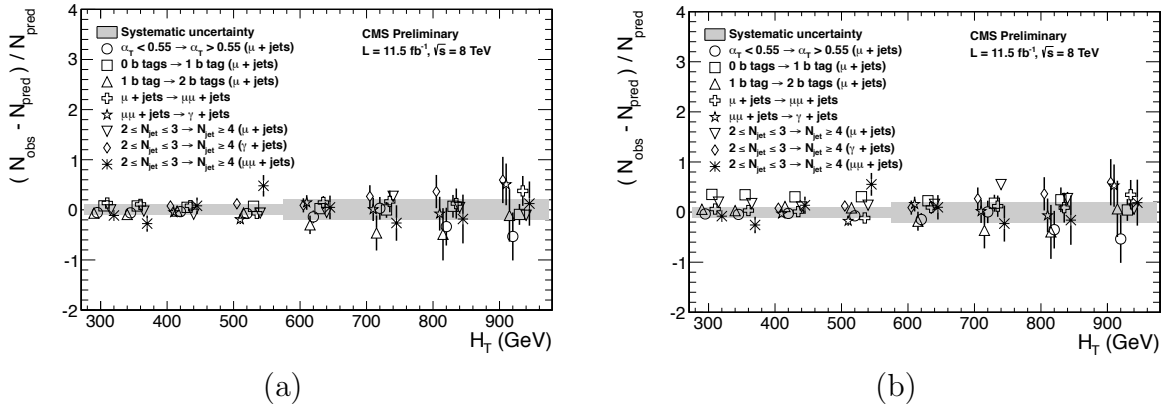


**Figure C.2.:** Sets of closure tests (open symbols) overlaid on top of the systematic uncertainty used for each of the five  $H_T$  regions (shaded bands) and for the two different jet multiplicity bins: (a)  $2 \leq n_{jet} \leq 3$  and (b)  $n_{jet} \geq 4$ .

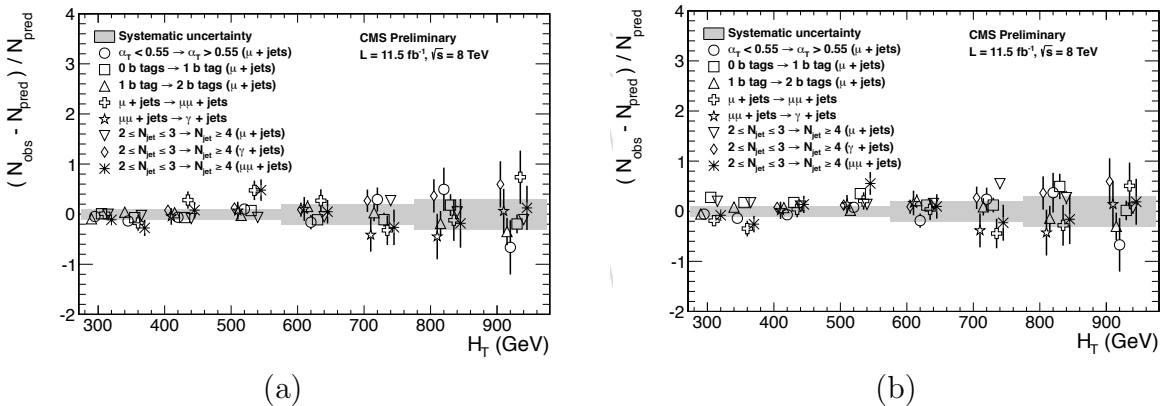


**Figure C.3.:** Sets of closure tests (open symbols) overlaid on top of the systematic uncertainty used for each of the five  $H_T$  regions (shaded bands) and for the two different jet multiplicity bins: (a)  $2 \leq n_{jet} \leq 3$  and (b)  $n_{jet} \geq 4$ .

		$H_T$ (GeV)			
$n_b^{reco}$	Cross Section	275–325	325–375	375–475	475–575
0	Nominal	$0.303 \pm 0.010$	$0.258 \pm 0.007$	$0.192 \pm 0.003$	$0.148 \pm 0.004$
	Varied	$0.300 \pm 0.010$	$0.256 \pm 0.007$	$0.191 \pm 0.003$	$0.147 \pm 0.004$
1	Nominal	$0.294 \pm 0.005$	$0.246 \pm 0.004$	$0.189 \pm 0.003$	$0.139 \pm 0.003$
	Varied	$0.295 \pm 0.006$	$0.248 \pm 0.004$	$0.191 \pm 0.003$	$0.140 \pm 0.003$
2	Nominal	$0.208 \pm 0.003$	$0.183 \pm 0.004$	$0.145 \pm 0.003$	$0.123 \pm 0.004$
	Varied	$0.211 \pm 0.004$	$0.185 \pm 0.004$	$0.147 \pm 0.003$	$0.124 \pm 0.004$
3	Nominal	$0.214 \pm 0.005$	$0.202 \pm 0.007$	$0.159 \pm 0.006$	$0.140 \pm 0.007$
	Varied	$0.215 \pm 0.005$	$0.203 \pm 0.007$	$0.159 \pm 0.006$	$0.140 \pm 0.007$
$\geq 4$	Nominal	$0.220 \pm 0.015$	$0.245 \pm 0.035$	$0.119 \pm 0.009$	-
	Varied	$0.220 \pm 0.015$	$0.245 \pm 0.035$	$0.119 \pm 0.009$	-
$n_b^{reco}$	Cross Section	575–675	675–775	775–875	875– $\infty$
0	Nominal	$0.119 \pm 0.004$	$0.098 \pm 0.005$	$0.077 \pm 0.006$	$0.049 \pm 0.005$
	Varied	$0.120 \pm 0.005$	$0.098 \pm 0.006$	$0.077 \pm 0.007$	$0.049 \pm 0.005$
1	Nominal	$0.115 \pm 0.004$	$0.093 \pm 0.005$	$0.075 \pm 0.007$	$0.063 \pm 0.006$
	Varied	$0.116 \pm 0.004$	$0.098 \pm 0.005$	$0.081 \pm 0.007$	$0.065 \pm 0.006$
2	Nominal	$0.096 \pm 0.005$	$0.070 \pm 0.006$	$0.051 \pm 0.007$	$0.063 \pm 0.008$
	Varied	$0.098 \pm 0.005$	$0.073 \pm 0.006$	$0.053 \pm 0.007$	$0.064 \pm 0.008$
3	Nominal	$0.114 \pm 0.009$	$0.065 \pm 0.007$	$0.070 \pm 0.017$	$0.092 \pm 0.020$
	Varied	$0.114 \pm 0.009$	$0.066 \pm 0.007$	$0.070 \pm 0.016$	$0.093 \pm 0.020$

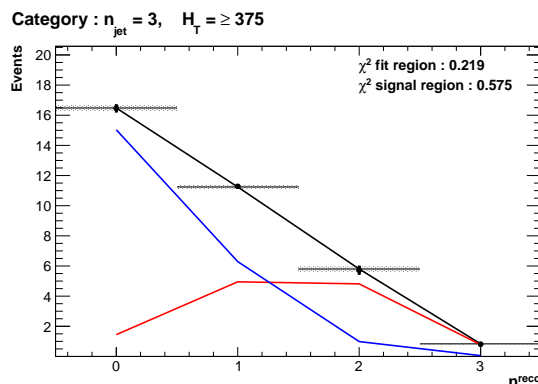
**Table C.1.:** Translation factors constructed from the  $\mu +$  jets control sample and signal selection MC, to predict yields for the  $W +$  jets and  $t\bar{t}$  back-grounds in the signal region with (a) NNLO cross sections corrected by k-factors determined from a data sideband see Section (4.4), marked as Nominal, and (b) the same cross sections but with those for  $W +$  jets and  $t\bar{t}$  varied up and down by 20%, respectively, marked as Varied. No requirement is placed on the jet multiplicity of events within this table.

## Appendix D.

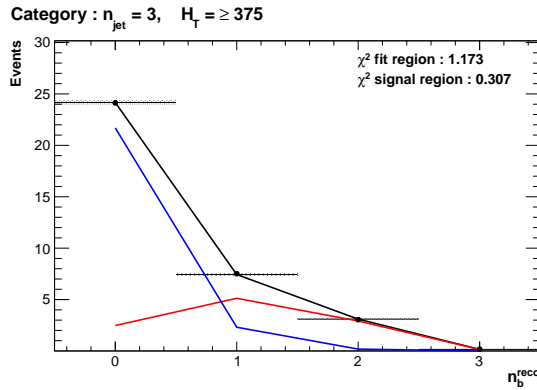
### <sup>2328</sup> Additional Material For B-tag <sup>2329</sup> Template Method

#### <sup>2330</sup> D.1. Templates Fits in Simulation

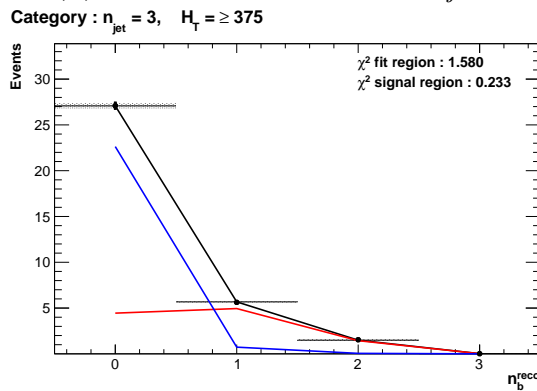
<sup>2331</sup> Template fits for the three **CSV** working points in the  $n_{jet} = 3, H_T > 375$  category :



(a) Loose working point  $n_{jet} = 3$



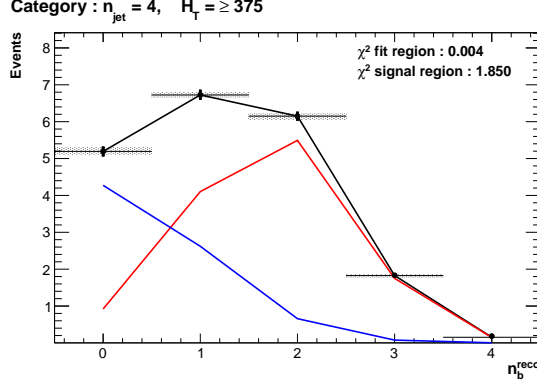
(b) Medium working point  $n_{jet} = 3$



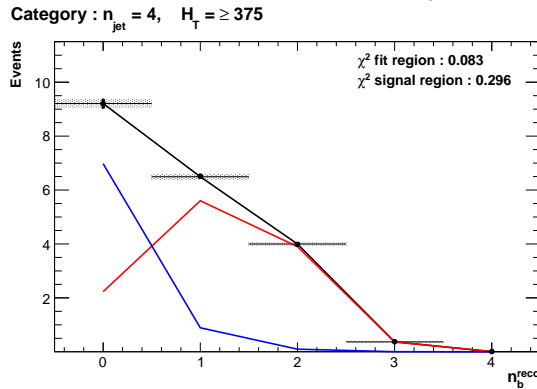
(c) Tight working point  $n_{jet} = 3$

**Figure D.1.:** The results of fitting the  $Z = 0$  and  $Z = 2$  templates to the  $n_b^{reco} = 0, 1, 2$  bins taken directly from simulation in the region  $H_T > 375$  GeV, for the  $n_{jet} = 3$  category. The blue template represents  $Z = 0$ , while the red template represents  $Z = 2$ . Grey bands represent the statistical uncertainty of the fit. The  $\chi^2$  parameter displayed represents the goodness of fit to the low  $n_b^{reco}$  (0-2) control region.

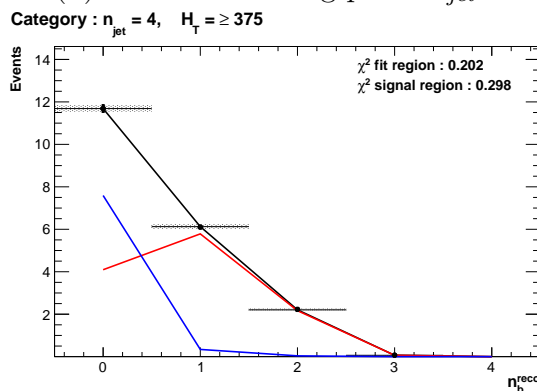
2332 Template fits for the three **CSV** working points in the  $n_{jet} = 4$ ,  $H_T > 375$  category :



(a) Loose working point  $n_{jet} = 4$



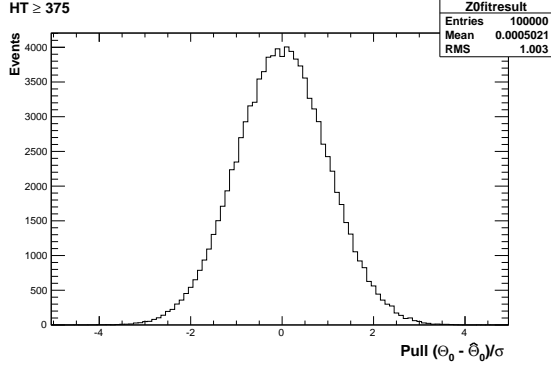
(b) Medium working point  $n_{jet} = 4$



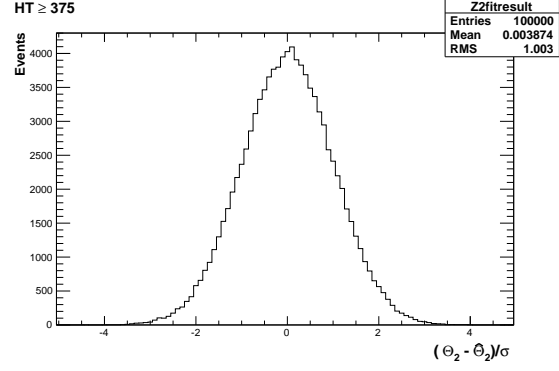
(c) Tight working point  $n_{jet} = 4$

**Figure D.2.:** The results of fitting the  $Z = 0$  and  $Z = 2$  templates to the  $n_b^{reco} = 0, 1, 2$  bins taken directly from simulation in the region  $H_T > 375$  GeV, for the  $n_{jet} = 4$  category. The blue template represents  $Z = 0$ , while the red template represents  $Z = 2$ . Grey bands represent the statistical uncertainty of the fit. The  $\chi^2$  parameter displayed represents the goodness of fit to the low  $n_b^{reco}$  (0-2) control region.

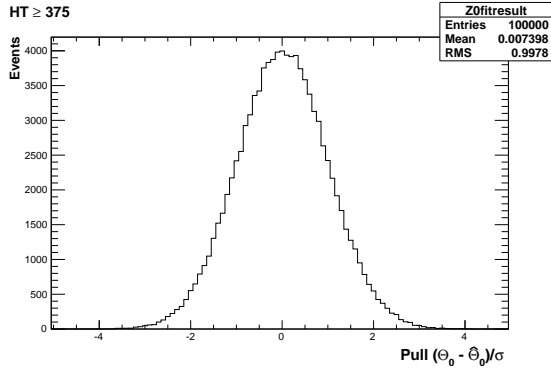
2333 D.2. Pull Distributions for Template Fits



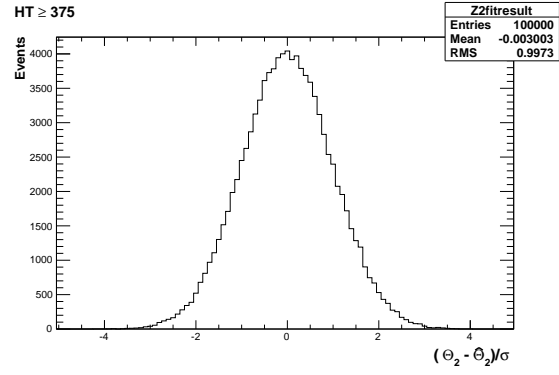
(a) Z0 Template,  $H_T > 375$ ,  $n_{jet} = 3$



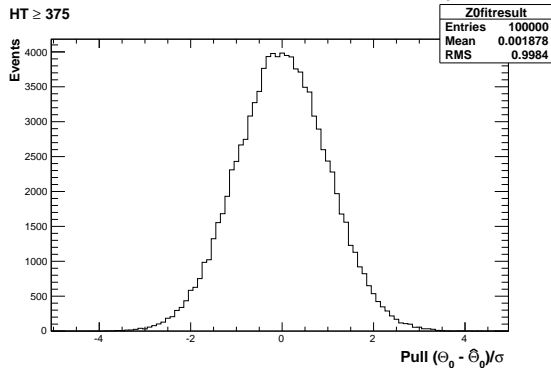
(b) Z2 Template,  $H_T > 375$ ,  $n_{jet} = 3$



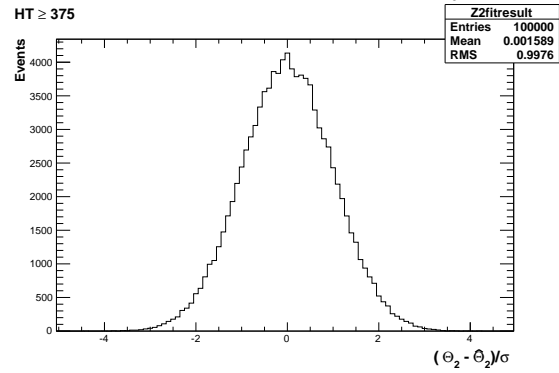
(a) Z0 Template,  $H_T > 375$ ,  $n_{jet} = 4$



(b) Z2 Template,  $H_T > 375$ ,  $n_{jet} = 4$



(a) Z0 Template,  $H_T > 375$ ,  $n_{jet} \geq 5$



(b) Z2 Template,  $H_T > 375$ ,  $n_{jet} \geq 5$

**Figure D.3.:** Pull distributions of  $\frac{(\theta - \hat{\theta})}{\sigma}$  for  $10^4$  pseudo-experiments generated from a gaussian distribution centred on the  $n_b^{reco}$  template values from simulation with width  $\sigma$ . Distributions are shown for both Z0 and Z2 templates for the medium CSV working point.

<sup>2334</sup> **D.3. Templates Fits in Data Control Sample**

<sup>2335</sup> Template fits for the three  $H_T$  bins, in the  $n_{jet} = 3$ , medium **CSV** working point:

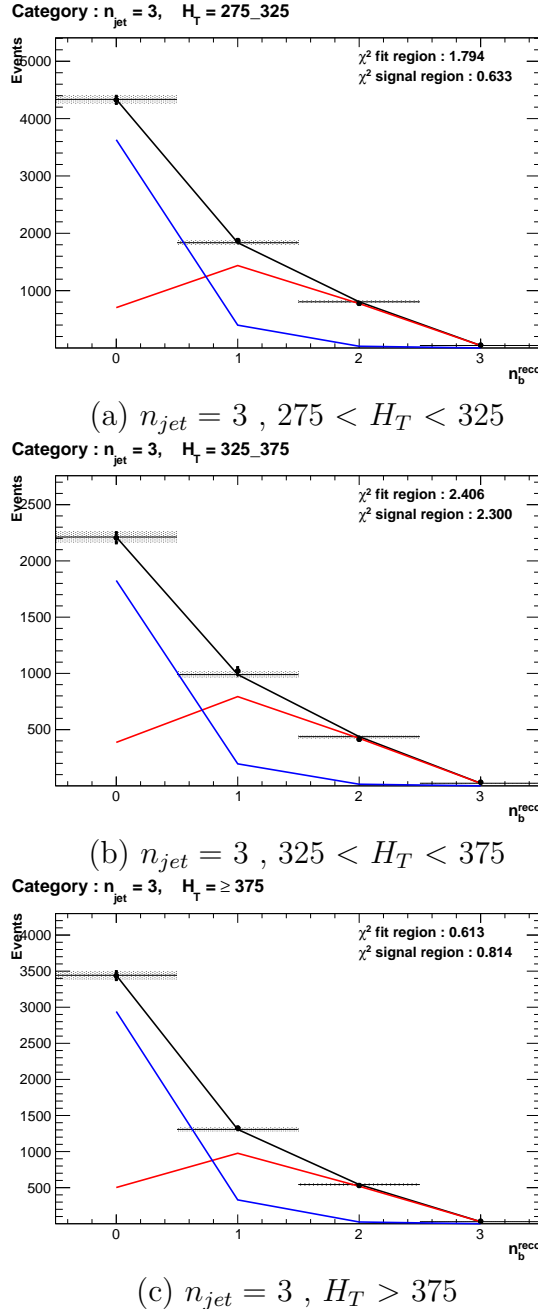


**Figure D.4.:** The results of fitting the  $Z = 0$  and  $Z = 2$  templates to the  $n_b^{reco} = 0, 1, 2$  bins taken from data, for the  $n_{jet} = 3$  category and medium **CSV** working point. The blue template represents  $Z = 0$ , while the red template represents  $Z = 2$ . The  $\chi^2$  parameter displayed represents the goodness of fit to the low  $n_b^{reco}$  (0-2) control region.

2336 Template fits for the three  $H_T$  bins, in the  $n_{jet} = 4$ , medium CSV working point:

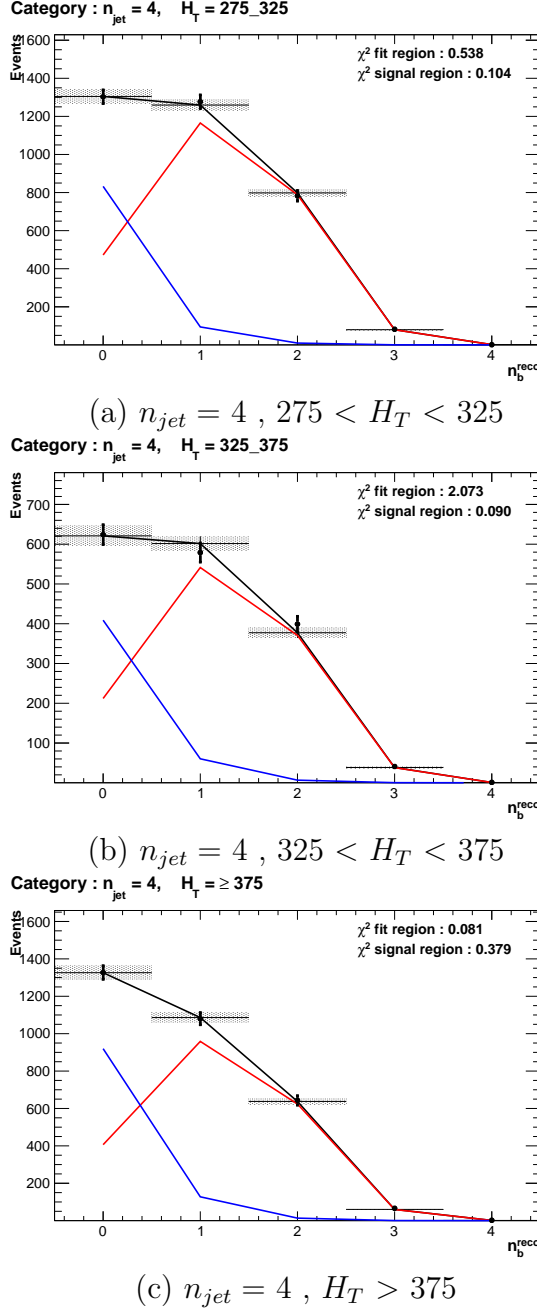
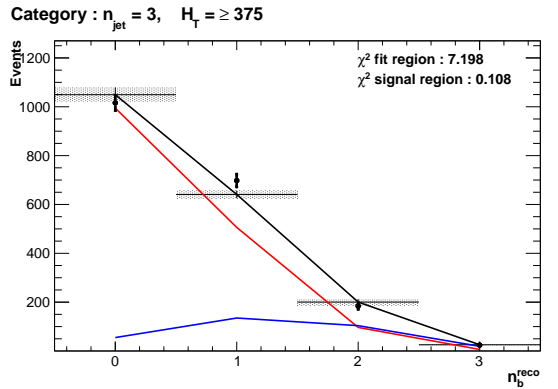


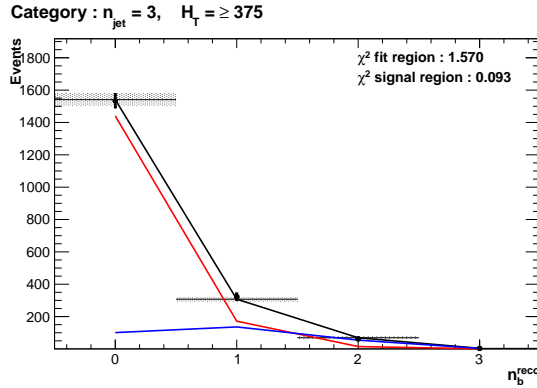
**Figure D.5.:** The results of fitting the  $Z = 0$  and  $Z = 2$  templates to the  $n_b^{reco} = 0, 1, 2$  bins taken from data, for the  $n_{jet} = 4$  category and medium CSV working point. The blue template represents  $Z = 0$ , while the red template represents  $Z = 2$ . The  $\chi^2$  parameter displayed represents the goodness of fit to the low  $n_b^{reco}$  (0-2) control region.

<sup>2337</sup> **D.4. Templates Fits in Data Signal Region**

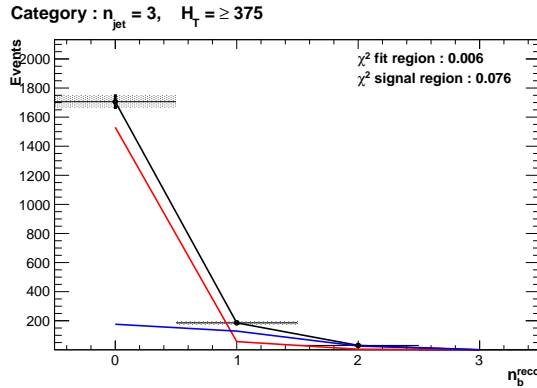
<sup>2338</sup> Template fits for the three **CSV** working points, in the  $n_{jet} = 3, H_T > 375$  category :



(a) Loose working point :  $n_{jet} = 3, H_T > 375$



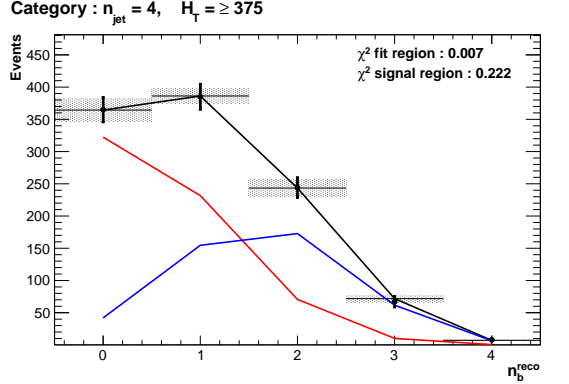
(b) Medium working point :  $n_{jet} = 3, H_T > 375$



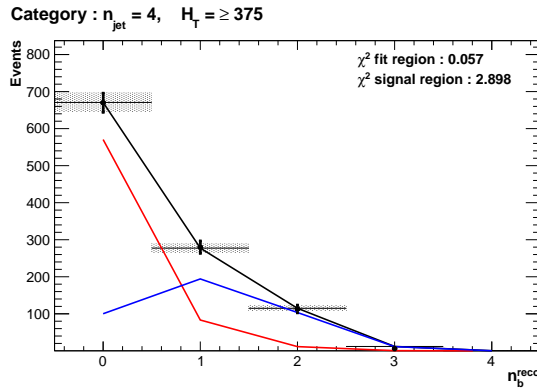
(c) Tight working point :  $n_{jet} = 3, H_T > 375$

**Figure D.6.:** The results of fitting the  $Z = 0$  and  $Z = 2$  templates to the  $n_b^{reco} = 0, 1, 2$  bins taken from data, in the  $n_{jet} = 3$  and  $H_T > 375$  category for all **CSV** working points. The blue template represents  $Z = 0$ , while the red template represents  $Z = 2$ . The  $\chi^2$  parameter displayed represents the goodness of fit to the low  $n_b^{reco}$  (0-2) control region.

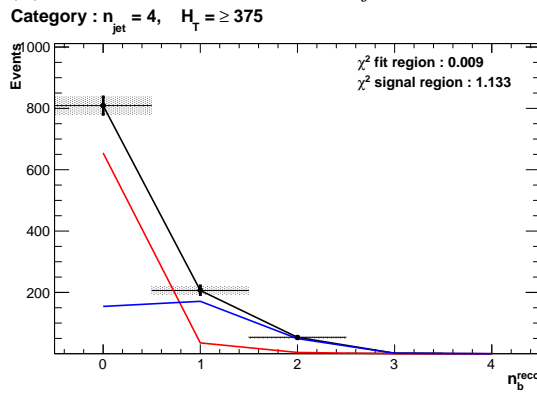
2339 Template fits for the three **CSV** working points, in the  $n_{jet} = 4$ ,  $H_T > 375$  category :



(a) Loose working point :  $n_{jet} = 4$  ,  $H_T > 375$



(b) Medium working point :  $n_{jet} = 4$  ,  $H_T > 375$



(c) Tight working point :  $n_{jet} = 4$  ,  $H_T > 375$

**Figure D.7.:** The results of fitting the  $Z = 0$  and  $Z = 2$  templates to the  $n_b^{reco} = 0, 1, 2$  bins taken from data, in the  $n_{jet} = 4$  and  $H_T > 375$  category for all **CSV** working points. The blue template represents  $Z = 0$ , while the red template represents  $Z = 2$ . The  $\chi^2$  parameter displayed represents the goodness of fit to the low  $n_b^{reco}$  ( $0-2$ ) control region.



# <sup>2341</sup> Bibliography

- <sup>2342</sup> [1] Particle Data Group Collaboration, “Review of Particle Physics (RPP)”, *Phys.Rev.*  
<sup>2343</sup> **D86** (2012) 010001, [doi:10.1103/PhysRevD.86.010001](https://doi.org/10.1103/PhysRevD.86.010001).
- <sup>2344</sup> [2] G. H. et al., “Nine-year Wilkinson Microwave Anisotropy Probe (WMAP)  
<sup>2345</sup> Observations: Cosmological Parameter Results”, *The Astrophysical Journal*  
<sup>2346</sup> *Supplement Series* **208** (2013), no. 2, 19.
- <sup>2347</sup> [3] ATLAS Collaboration Collaboration, “Observation of a new particle in the search  
<sup>2348</sup> for the Standard Model Higgs boson with the ATLAS detector at the LHC”,  
<sup>2349</sup> *Phys.Lett.* **B716** (2012) 1–29, [doi:10.1016/j.physletb.2012.08.020](https://doi.org/10.1016/j.physletb.2012.08.020),  
<sup>2350</sup> [arXiv:1207.7214](https://arxiv.org/abs/1207.7214).
- <sup>2351</sup> [4] CMS Collaboration Collaboration, “Observation of a new boson at a mass of 125  
<sup>2352</sup> GeV with the CMS experiment at the LHC”, *Phys.Lett.* **B716** (2012) 30–61,  
<sup>2353</sup> [doi:10.1016/j.physletb.2012.08.021](https://doi.org/10.1016/j.physletb.2012.08.021), [arXiv:1207.7235](https://arxiv.org/abs/1207.7235).
- <sup>2354</sup> [5] CMS Collaboration Collaboration, “Search for supersymmetry in hadronic final  
<sup>2355</sup> states with missing transverse energy using the variables AlphaT and b-quark  
<sup>2356</sup> multiplicity in pp collisions at 8 TeV”, *Eur.Phys.J.* **C73** (2013) 2568,  
<sup>2357</sup> [doi:10.1140/epjc/s10052-013-2568-6](https://doi.org/10.1140/epjc/s10052-013-2568-6), [arXiv:1303.2985](https://arxiv.org/abs/1303.2985).
- <sup>2358</sup> [6] S. Weinberg, “A Model of Leptons”, *Phys. Rev. Lett.* **19** (Nov, 1967) 1264–1266,  
<sup>2359</sup> [doi:10.1103/PhysRevLett.19.1264](https://doi.org/10.1103/PhysRevLett.19.1264).
- <sup>2360</sup> [7] S. Glashow, “Partial Symmetries of Weak Interactions”, *Nucl.Phys.* **22** (1961)  
<sup>2361</sup> 579–588, [doi:10.1016/0029-5582\(61\)90469-2](https://doi.org/10.1016/0029-5582(61)90469-2).
- <sup>2362</sup> [8] A. Salam, “Weak and Electromagnetic Interactions”, *Conf.Proc.* **C680519** (1968)  
<sup>2363</sup> 367–377.
- <sup>2364</sup> [9] G. Hooft, “Renormalizable Lagrangians for massive Yang-Mills fields”, *Nuclear*  
<sup>2365</sup> *Physics B* **35** (1971), no. 1, 167 – 188,

- 2366        [doi:  
http://dx.doi.org/10.1016/0550-3213\(71\)90139-8](http://dx.doi.org/10.1016/0550-3213(71)90139-8).
- 2367 [10] Gargamelle Neutrino Collaboration Collaboration, “Observation of Neutrino Like  
2368        Interactions Without Muon Or Electron in the Gargamelle Neutrino Experiment”,  
2369        *Phys.Lett.* **B46** (1973) 138–140, [doi:  
10.1016/0370-2693\(73\)90499-1](http://dx.doi.org/10.1016/0370-2693(73)90499-1).
- 2370 [11] UA1 Collaboration Collaboration, “Experimental Observation of Lepton Pairs of  
2371        Invariant Mass Around 95-GeV/c\*\*2 at the CERN SPS Collider”, *Phys.Lett.*  
2372        **B126** (1983) 398–410, [doi:  
10.1016/0370-2693\(83\)90188-0](http://dx.doi.org/10.1016/0370-2693(83)90188-0).
- 2373 [12] UA2 Collaboration Collaboration, “Observation of Single Isolated Electrons of High  
2374        Transverse Momentum in Events with Missing Transverse Energy at the CERN  
2375        anti-p p Collider”, *Phys.Lett.* **B122** (1983) 476–485,  
2376        [doi:  
10.1016/0370-2693\(83\)91605-2](http://dx.doi.org/10.1016/0370-2693(83)91605-2).
- 2377 [13] E. Noether, “Invariante Variationsprobleme”, *Nachrichten von der Gesellschaft der  
2378        Wissenschaften zu Gttingen, Mathematisch-Physikalische Klasse* **1918** (1918)  
2379        235–257.
- 2380 [14] F. Halzen and A. D. Martin, “Quarks and Leptons”. Wiley, 1985.
- 2381 [15] “Introduction to Elementary Particles”. Wiley-VCH, 2nd edition, October, 2008.
- 2382 [16] C. S. Wu et al., “Experimental Test of Parity Conservation in Beta Decay”,  
2383        *Physical Review* **105** (February, 1957) 1413–1415,  
2384        [doi:  
10.1103/PhysRev.105.1413](http://dx.doi.org/10.1103/PhysRev.105.1413).
- 2385 [17] P. Higgs, “Broken symmetries, massless particles and gauge fields”, *Physics Letters*  
2386        **12** (1964), no. 2, 132 – 133,  
2387        [doi:  
http://dx.doi.org/10.1016/0031-9163\(64\)91136-9](http://dx.doi.org/10.1016/0031-9163(64)91136-9).
- 2388 [18] F. Englert and R. Brout, “Broken Symmetry and the Mass of Gauge Vector  
2389        Mesons”, *Phys. Rev. Lett.* **13** (Aug, 1964) 321–323,  
2390        [doi:  
10.1103/PhysRevLett.13.321](http://dx.doi.org/10.1103/PhysRevLett.13.321).
- 2391 [19] P. W. Higgs, “Broken Symmetries and the Masses of Gauge Bosons”, *Phys. Rev.  
2392        Lett.* **13** (Oct, 1964) 508–509, [doi:  
10.1103/PhysRevLett.13.508](http://dx.doi.org/10.1103/PhysRevLett.13.508).
- 2393 [20] G. S. Guralnik, C. R. Hagen, and T. W. B. Kibble, “Global Conservation Laws and  
2394        Massless Particles”, *Phys. Rev. Lett.* **13** (Nov, 1964) 585–587,  
2395        [doi:  
10.1103/PhysRevLett.13.585](http://dx.doi.org/10.1103/PhysRevLett.13.585).

- 2396 [21] S. Weinberg, “A Model of Leptons”, *Phys. Rev. Lett.* **19** (Nov, 1967) 1264–1266,  
2397 [doi:10.1103/PhysRevLett.19.1264](https://doi.org/10.1103/PhysRevLett.19.1264).
- 2398 [22] H. Yukawa, “On the Interaction of Elementary Particles. I”, *Progress of  
2399 Theoretical Physics Supplement* **1** (1955) 1–10, [doi:10.1143/PTPS.1.1](https://doi.org/10.1143/PTPS.1.1),  
2400 [arXiv:<http://ptps.oxfordjournals.org/content/1/1.1.full.pdf+html>](http://ptps.oxfordjournals.org/content/1/1.1.full.pdf+html).
- 2401 [23] (Super-Kamiokande Collaboration) Collaboration, “Evidence for Oscillation of  
2402 Atmospheric Neutrinos”, *Phys. Rev. Lett.* **81** (Aug, 1998) 1562–1567,  
2403 [doi:10.1103/PhysRevLett.81.1562](https://doi.org/10.1103/PhysRevLett.81.1562).
- 2404 [24] R. Becker-Szendy et al., “A Search for muon-neutrino oscillations with the IMB  
2405 detector”, *Phys.Rev.Lett.* **69** (1992) 1010–1013,  
2406 [doi:10.1103/PhysRevLett.69.1010](https://doi.org/10.1103/PhysRevLett.69.1010).
- 2407 [25] S. P. Martin, “A Supersymmetry primer”, [arXiv:hep-ph/9709356](https://arxiv.org/abs/hep-ph/9709356).
- 2408 [26] H. Nilles, “Supersymmetry, Supergravity and Particle Physics”. Physics reports.  
2409 North-Holland Physics Publ., 1984.
- 2410 [27] H. E. Haber and G. L. Kane, “The Search for Supersymmetry: Probing Physics  
2411 Beyond the Standard Model”, *Phys.Rept.* **117** (1985) 75–263,  
2412 [doi:10.1016/0370-1573\(85\)90051-1](https://doi.org/10.1016/0370-1573(85)90051-1).
- 2413 [28] E. Witten, “Dynamical Breaking of Supersymmetry”, *Nucl.Phys.* **B188** (1981)  
2414 513, [doi:10.1016/0550-3213\(81\)90006-7](https://doi.org/10.1016/0550-3213(81)90006-7).
- 2415 [29] J. Wess and B. Zumino, “Supergauge transformations in four dimensions”, *Nuclear  
2416 Physics B* **70** (1974), no. 1, 39 – 50,  
2417 [doi:\[http://dx.doi.org/10.1016/0550-3213\\(74\\)90355-1\]\(http://dx.doi.org/10.1016/0550-3213\(74\)90355-1\)](http://dx.doi.org/10.1016/0550-3213(74)90355-1).
- 2418 [30] H. Muller-Kirsten and A. Wiedemann, “Introduction to Supersymmetry”. World  
2419 Scientific lecture notes in physics. World Scientific, 2010.
- 2420 [31] I. Aitchison, “Supersymmetry in Particle Physics: An Elementary Introduction”.  
2421 Cambridge University Press, 2007.
- 2422 [32] K. A. Intriligator and N. Seiberg, “Lectures on Supersymmetry Breaking”,  
2423 *Class.Quant.Grav.* **24** (2007) S741–S772,  
2424 [doi:10.1088/0264-9381/24/21/S02](https://doi.org/10.1088/0264-9381/24/21/S02), [10.1016/S0924-8099\(08\)80020-0](https://doi.org/10.1016/S0924-8099(08)80020-0),  
2425 [arXiv:hep-ph/0702069](https://arxiv.org/abs/hep-ph/0702069).

- [33] Y. Shadmi, “Supersymmetry breaking”, [arXiv:hep-th/0601076](https://arxiv.org/abs/hep-th/0601076).
- [34] C. Burgess et al., “Warped Supersymmetry Breaking”, *JHEP* **0804** (2008) 053, [doi:10.1088/1126-6708/2008/04/053](https://doi.org/10.1088/1126-6708/2008/04/053), [arXiv:hep-th/0610255](https://arxiv.org/abs/hep-th/0610255).
- [35] H. Murayama, “Supersymmetry breaking made easy, viable, and generic”, [arXiv:0709.3041](https://arxiv.org/abs/0709.3041).
- [36] H. Baer and X. Tata, “Weak Scale Supersymmetry: From Superfields to Scattering Events”. Cambridge University Press, 2006.
- [37] S. P. Martin, “Implications of supersymmetric models with natural R-parity conservation”, [doi:10.1103/PhysRevD.54.2340](https://doi.org/10.1103/PhysRevD.54.2340), [arXiv:hep-ph/9602349](https://arxiv.org/abs/hep-ph/9602349).
- [38] G. L. Kane, C. F. Kolda, L. Roszkowski, and J. D. Wells, “Study of constrained minimal supersymmetry”, *Phys.Rev.* **D49** (1994) 6173–6210, [doi:10.1103/PhysRevD.49.6173](https://doi.org/10.1103/PhysRevD.49.6173), [arXiv:hep-ph/9312272](https://arxiv.org/abs/hep-ph/9312272).
- [39] C. Stuge et al., “Updated global fits of the cMSSM including the latest LHC SUSY and Higgs searches and XENON100 data”, *JCAP* **1203** (2012) 030, [doi:10.1088/1475-7516/2012/03/030](https://doi.org/10.1088/1475-7516/2012/03/030), [arXiv:1112.4192](https://arxiv.org/abs/1112.4192).
- [40] M. Citron et al., “The End of the CMSSM Coannihilation Strip is Nigh”, *Phys.Rev.* **D87** (2013) 036012, [doi:10.1103/PhysRevD.87.036012](https://doi.org/10.1103/PhysRevD.87.036012), [arXiv:1212.2886](https://arxiv.org/abs/1212.2886).
- [41] D. Ghosh, M. Guchait, S. Raychaudhuri, and D. Sengupta, “How Constrained is the cMSSM?”, *Phys.Rev.* **D86** (2012) 055007, [doi:10.1103/PhysRevD.86.055007](https://doi.org/10.1103/PhysRevD.86.055007), [arXiv:1205.2283](https://arxiv.org/abs/1205.2283).
- [42] LHC New Physics Working Group Collaboration, “Simplified Models for LHC New Physics Searches”, *J.Phys.* **G39** (2012) 105005, [doi:10.1088/0954-3899/39/10/105005](https://doi.org/10.1088/0954-3899/39/10/105005), [arXiv:1105.2838](https://arxiv.org/abs/1105.2838).
- [43] J. Alwall, P. Schuster, and N. Toro, “Simplified Models for a First Characterization of New Physics at the LHC”, *Phys.Rev.* **D79** (2009) 075020, [doi:10.1103/PhysRevD.79.075020](https://doi.org/10.1103/PhysRevD.79.075020), [arXiv:0810.3921](https://arxiv.org/abs/0810.3921).
- [44] CMS Collaboration Collaboration, “Interpretation of Searches for Supersymmetry with simplified Models”, *Phys.Rev.* **D88** (2013) 052017, [doi:10.1103/PhysRevD.88.052017](https://doi.org/10.1103/PhysRevD.88.052017), [arXiv:1301.2175](https://arxiv.org/abs/1301.2175).
- [45] J. Hisano, K. Kurosawa, and Y. Nomura, “Natural effective supersymmetry”, [arXiv:1406.2502](https://arxiv.org/abs/1406.2502).

- 2456        *Nucl.Phys.* **B584** (2000) 3–45, [doi:10.1016/S0550-3213\(00\)00343-6](https://doi.org/10.1016/S0550-3213(00)00343-6),  
2457        [arXiv:hep-ph/0002286](https://arxiv.org/abs/hep-ph/0002286).
- 2458 [46] M. Papucci, J. T. Ruderman, and A. Weiler, “Natural SUSY Endures”, *JHEP*  
2459        **1209** (2012) 035, [doi:10.1007/JHEP09\(2012\)035](https://doi.org/10.1007/JHEP09(2012)035), [arXiv:1110.6926](https://arxiv.org/abs/1110.6926).
- 2460 [47] B. Allanach and B. Gripaios, “Hide and Seek With Natural Supersymmetry at the  
2461        LHC”, *JHEP* **1205** (2012) 062, [doi:10.1007/JHEP05\(2012\)062](https://doi.org/10.1007/JHEP05(2012)062),  
2462        [arXiv:1202.6616](https://arxiv.org/abs/1202.6616).
- 2463 [48] ALICE Collaboration, “The ALICE experiment at the CERN LHC”, *JINST* **3**  
2464        (2008) S08002, [doi:10.1088/1748-0221/3/08/S08002](https://doi.org/10.1088/1748-0221/3/08/S08002).
- 2465 [49] ATLAS Collaboration, “The ATLAS Experiment at the CERN Large Hadron  
2466        Collider”, *JINST* **3** (2008) [doi:10.1088/1748-0221/3/08/S08003](https://doi.org/10.1088/1748-0221/3/08/S08003).
- 2467 [50] CMS Collaboration, “The CMS experiment at the CERN LHC”, *JINST* **0803**  
2468        (2008) S08004,  
2469        [doi:10.1088/1748-0221/3/08/S08004](https://doi.org/10.1088/1748-0221/3/08/S08004), [10.1088/1748-0221/3/08/S08004](https://doi.org/10.1088/1748-0221/3/08/S08004).
- 2470 [51] LHCb Collaboration, “The LHCb Detector at the LHC”, *JINST* **3** (2008) S08005,  
2471        [doi:10.1088/1748-0221/3/08/S08005](https://doi.org/10.1088/1748-0221/3/08/S08005).
- 2472 [52] J.-L. Caron, “LHC Layout.. Schema general du LHC.”, (Sep, 1997).
- 2473 [53] C. Collaboration, “CMS Luminosity - Public Results”, (2011).  
2474        [twiki.cern.ch/twiki/bin/view/CMSPublic/LumiPublicResults](http://twiki.cern.ch/twiki/bin/view/CMSPublic/LumiPublicResults).
- 2475 [54] CERN, “CMS Compact Muon Solenoid.”, (Feb, 2010).  
2476        <http://public.web.cern.ch/public/Objects/LHC/CMSnc.jpg>.
- 2477 [55] “The CMS electromagnetic calorimeter project: Technical Design Report”.  
2478        Technical Design Report CMS. CERN, Geneva, 1997.
- 2479 [56] “The CMS muon project: Technical Design Report”. Technical Design Report  
2480        CMS. CERN, Geneva, 1997.
- 2481 [57] CMS Collaboration, “The CMS Physics Technical Design Report, Volume 1”,  
2482        *CERN/LHCC* **2006-001** (2006).
- 2483 [58] M. Cacciari, G. P. Salam, and G. Soyez, “The anti-  $k_t$  jet clustering algorithm”,  
2484        *Journal of High Energy Physics* **2008** (2008), no. 04, 063.

- 2485 [59] “Jet Performance in pp Collisions at 7 TeV”, Technical Report  
2486 CMS-PAS-JME-10-003, CERN, Geneva, (2010).
- 2487 [60] X. Janssen, “Underlying event and jet reconstruction in CMS”, Technical Report  
2488 CMS-CR-2011-012, CERN, Geneva, (Jan, 2011).
- 2489 [61] T. C. collaboration, “Determination of jet energy calibration and transverse  
2490 momentum resolution in CMS”, *Journal of Instrumentation* **6** (2011), no. 11,  
2491 P11002.
- 2492 [62] R. Eusebi and on behalf of the CMS collaboration), “Jet energy corrections and  
2493 uncertainties in CMS: reducing their impact on physics measurements”, *Journal of  
2494 Physics: Conference Series* **404** (2012), no. 1, 012014.
- 2495 [63] CMS Collaboration Collaboration, “Algorithms for b Jet identification in CMS”,  
2496 Technical Report CMS-PAS-BTV-09-001, CERN, 2009. Geneva, (Jul, 2009).
- 2497 [64] “Performance of b tagging at  $\sqrt{s}=8$  TeV in multijet, ttbar and boosted topology  
2498 events”,.
- 2499 [65] T. C. collaboration, “Identification of b-quark jets with the CMS experiment”,  
2500 *Journal of Instrumentation* **8** (2013), no. 04, P04013.
- 2501 [66] CMS Collaboration Collaboration, “CMS. The TriDAS project. Technical design  
2502 report, vol. 1: The trigger systems”,.
- 2503 [67] CMS Collaboration Collaboration, “CMS: The TriDAS project. Technical design  
2504 report, Vol. 2: Data acquisition and high-level trigger”,.
- 2505 [68] J. B. et al., “Calibration and Performance of the Jets and Energy Sums in the  
2506 Level-1 Trigger”,.
- 2507 [69] B. et al., “Study of Level-1 Trigger Jet Performance in High Pile-up Running  
2508 Conditions”,.
- 2509 [70] J. J. Brooke, “Performance of the CMS Level-1 Trigger”, Technical Report  
2510 CMS-CR-2012-322. CERN-CMS-CR-2012-322, CERN, Geneva, (Nov, 2012).
- 2511 [71] CMS Collaboration Collaboration, “Search for supersymmetry in final states with  
2512 missing transverse energy and 0, 1, 2, or at least 3 b-quark jets in 7 TeV pp  
2513 collisions using the variable alphaT”, *JHEP* **1301** (2013) 077,  
2514 [doi:10.1007/JHEP01\(2013\)077](https://doi.org/10.1007/JHEP01(2013)077), [arXiv:1210.8115](https://arxiv.org/abs/1210.8115).

- 2515 [72] CMS Collaboration Collaboration, “SUSY searches with dijet events”,.
- 2516 [73] L. Randall and D. Tucker-Smith, “Dijet Searches for Supersymmetry at the Large  
2517 Hadron Collider”, *Phys. Rev. Lett.* **101** (Nov, 2008) 221803,  
2518 [doi:10.1103/PhysRevLett.101.221803](https://doi.org/10.1103/PhysRevLett.101.221803).
- 2519 [74] CMS Collaboration Collaboration, “Search strategy for exclusive multi-jet events  
2520 from supersymmetry at CMS”, Technical Report CMS-PAS-SUS-09-001, CERN,  
2521 2009. Geneva, (Jul, 2009).
- 2522 [75] CMS Collaboration Collaboration, “Calorimeter Jet Quality Criteria for the First  
2523 CMS Collision Data”, Technical Report CMS-PAS-JME-09-008, CERN, 2010.  
2524 Geneva, (Apr, 2010).
- 2525 [76] T. C. collaboration, “Performance of CMS muon reconstruction in pp collision  
2526 events at  $\sqrt{s} = 7$  TeV”, *Journal of Instrumentation* **7** (2012), no. 10, P10002.
- 2527 [77] The CMS Collaboration, “Performance of CMS muon reconstruction in pp collision  
2528 events at 7 TeV”, *Journal of Instrumentation* **7** (October, 2012) 2P,  
2529 [doi:10.1088/1748-0221/7/10/P10002](https://doi.org/10.1088/1748-0221/7/10/P10002), [arXiv:1206.4071](https://arxiv.org/abs/1206.4071).
- 2530 [78] CMS Collaboration Collaboration, “Search for supersymmetry in events with  
2531 photons and missing energy”, Technical Report CMS-PAS-SUS-12-018, CERN,  
2532 Geneva, (2012).
- 2533 [79] M. Cacciari and G. P. Salam, “Pileup subtraction using jet areas”, *Phys.Lett.*  
2534 **B659** (2008) 119–126, [doi:10.1016/j.physletb.2007.09.077](https://doi.org/10.1016/j.physletb.2007.09.077),  
2535 [arXiv:0707.1378](https://arxiv.org/abs/0707.1378).
- 2536 [80] Z. Bern et al., “Driving missing data at next-to-leading order”, *Phys. Rev. D* **84**  
2537 (Dec, 2011) 114002, [doi:10.1103/PhysRevD.84.114002](https://doi.org/10.1103/PhysRevD.84.114002).
- 2538 [81] Z. Bern et al., “Driving Missing Data at Next-to-Leading Order”, *Phys.Rev.* **D84**  
2539 (2011) 114002, [doi:10.1103/PhysRevD.84.114002](https://doi.org/10.1103/PhysRevD.84.114002), [arXiv:1106.1423](https://arxiv.org/abs/1106.1423).
- 2540 [82] CMS Collaboration Collaboration, “Data-Driven Estimation of the Invisible Z  
2541 Background to the SUSY MET Plus Jets Search”, Technical Report  
2542 CMS-PAS-SUS-08-002, CERN, 2009. Geneva, (Jan, 2009).
- 2543 [83] T. Sjostrand, S. Mrenna, and P. Z. Skands, “PYTHIA 6.4 Physics and Manual”,  
2544 *JHEP* **0605** (2006) 026, [doi:10.1088/1126-6708/2006/05/026](https://doi.org/10.1088/1126-6708/2006/05/026),  
2545 [arXiv:hep-ph/0603175](https://arxiv.org/abs/hep-ph/0603175).

- 2546 [84] W. Beenakker, R. Hopker, M. Spira, and P. Zerwas, “Squark and gluino production  
2547 at hadron colliders”, *Nucl.Phys.* **B492** (1997) 51–103,  
2548 [doi:10.1016/S0550-3213\(97\)80027-2](https://doi.org/10.1016/S0550-3213(97)80027-2), [arXiv:hep-ph/9610490](https://arxiv.org/abs/hep-ph/9610490).
- 2549 [85] S. Abdullin *et al.*, “The Fast Simulation of the CMS Detector at LHC”, *Journal of*  
2550 *Physics: Conference Series* **331** (2011), no. 3, 032049.
- 2551 [86] S. Banerjee, M. D. Hildreth, and the CMS Collaboration, “Validation and Tuning  
2552 of the CMS Full Simulation”, *Journal of Physics: Conference Series* **331** (2011),  
2553 no. 3, 032015.
- 2554 [87] C. Collaboration, “CMS Btag POG : CMS b-tagging performance database”,  
2555 (2013). <https://twiki.cern.ch/twiki/bin/viewauth/CMS/BtagPOG>.
- 2556 [88] CMS Collaboration Collaboration, “CMS Luminosity Based on Pixel Cluster  
2557 Counting - Summer 2012 Update”, Technical Report CMS-PAS-LUM-12-001,  
2558 CERN, Geneva, (2012).
- 2559 [89] E. M. Laird, “A Search for Squarks and Gluinos with the CMS Detector”,.
- 2560 [90] R. Cousins, “Probability Density Functions for Positive Nuisance Parameters”,  
2561 (2012). <http://www.physics.ucla.edu/cousins/stats/cousinslognormalprior.pdf>.
- 2562 [91] L. Moneta, K. Cranmer, G. Schott, and W. Verkerke, “The RooStats project”,  
2563 2010. [arXiv:1009.1003](https://arxiv.org/abs/1009.1003).
- 2564 [92] F. James and M. Roos, “Minuit: A System for Function Minimization and Analysis  
2565 of the Parameter Errors and Correlations”, *Comput.Phys.Commun.* **10** (1975)  
2566 343–367, [doi:10.1016/0010-4655\(75\)90039-9](https://doi.org/10.1016/0010-4655(75)90039-9).
- 2567 [93] A. L. Read, “Presentation of search results: the  $CL_s$  technique”, *Journal of*  
2568 *Physics G: Nuclear and Particle Physics* **28** (2002), no. 10, 2693.
- 2569 [94] T. Junk, “Confidence level computation for combining searches with small  
2570 statistics”, *Nuclear Instruments and Methods in Physics Research Section A:*  
2571 *Accelerators, Spectrometers, Detectors and Associated Equipment* **434** (1999),  
2572 no. 23, 435 – 443, [doi:\[http://dx.doi.org/10.1016/S0168-9002\\(99\\)00498-2\]\(http://dx.doi.org/10.1016/S0168-9002\(99\)00498-2\)](https://doi.org/10.1016/S0168-9002(99)00498-2).
- 2573 [95] A. L. Read, “Modified frequentist analysis of search results (the  $CL_s$  method)”,.
- 2574 [96] G. Cowan, K. Cranmer, E. Gross, and O. Vitells, “Asymptotic formulae for  
2575 likelihood-based tests of new physics”, *The European Physical Journal C* **71**

- 2576 (2011), no. 2, 1–19, [doi:10.1140/epjc/s10052-011-1554-0](https://doi.org/10.1140/epjc/s10052-011-1554-0).
- 2577 [97] G. Cowan, K. Cranmer, E. Gross, and O. Vitells, “Asymptotic formulae for  
2578 likelihood-based tests of new physics”, *European Physical Journal C* **71** (February,  
2579 2011) 1554, [doi:10.1140/epjc/s10052-011-1554-0](https://doi.org/10.1140/epjc/s10052-011-1554-0), [arXiv:1007.1727](https://arxiv.org/abs/1007.1727).

2580 **Acronyms**

- 2581 **ALICE** A Large Ion Collider Experiment
- 2582 **ATLAS** A Toroidal LHC ApparatuS
- 2583 **APD** Avalanche Photo-Diodes
- 2584 **BSM** Beyond Standard Model
- 2585 **CERN** European Organization for Nuclear Research
- 2586 **CMS** Compact Muon Solenoid
- 2587 **CMSSM** Compressed Minimal SuperSymmetric Model
- 2588 **CSC** Cathode Stripe Chamber
- 2589 **CSV** Combined Secondary Vertex
- 2590 **CSVM** Combined Secondary Vertex Medium Working Point
- 2591 **DT** Drift Tube
- 2592 **ECAL** Electromagnetic CALorimeter
- 2593 **EB** Electromagnetic CALorimeter Barrel
- 2594 **EE** Electromagnetic CALorimeter Endcap
- 2595 **ES** Electromagnetic CALorimeter pre-Shower
- 2596 **EMG** Exponentially Modified Gaussian
- 2597 **EPJC** European Physical Journal C
- 2598 **EWK** Electroweak Sector
- 2599 **GCT** Global Calorimeter Trigger

2600	<b>GMT</b>	Global MuonTrigger
2601	<b>GT</b>	Global Trigger
2602	<b>HB</b>	Hadron Barrel
2603	<b>HCAL</b>	Hadronic CALorimeter
2604	<b>HE</b>	Hadron Endcaps
2605	<b>HF</b>	Hadron Forward
2606	<b>HLT</b>	Higher Level Trigger
2607	<b>HO</b>	Hadron Outer
2608	<b>HPD</b>	Hybrid Photo Diode
2609	<b>ISR</b>	Initial State Radiation
2610	<b>LUT</b>	Look Up Table
2611	<b>L1</b>	Level 1 Trigger
2612	<b>LEP</b>	Large Electron-Positron Collidor
2613	<b>LHC</b>	Large Hadron Collider
2614	<b>LHCb</b>	Large Hadron Collider Beauty
2615	<b>LO</b>	Leading Order
2616	<b>LSP</b>	Lightest Supersymmetric Partner
2617	<b>NLL</b>	Next to Leading Logarithmic Order
2618	<b>NLO</b>	Next to Leading Order
2619	<b>NNLO</b>	Next to Next Leading Order
2620	<b>POGs</b>	Physics Object Groups
2621	<b>PS</b>	Proton Synchrotron
2622	<b>QED</b>	Quantum Electro-Dynamics
2623	<b>QCD</b>	Quantum Chromo-Dynamics
2624	<b>QFT</b>	Quantum Field Theory

2625	<b>RBXs</b>	Readout Boxes
2626	<b>RPC</b>	Resistive Plate Chamber
2627	<b>RCT</b>	Regional Calorimeter Trigger
2628	<b>RMT</b>	Regional Muon Trigger
2629	<b>SUSY</b>	SUperSYmmetry
2630	<b>SM</b>	Standard Model
2631	<b>SMS</b>	Simplified Model Spectra
2632	<b>SPS</b>	Super Proton Synchrotron
2633	<b>TF</b>	Transfer Factor
2634	<b>TP</b>	Trigger Primate
2635	<b>VEV</b>	Vacuum Expectation Value
2636	<b>VPT</b>	Vacuum Photo-Triodes
2637	<b>WIMP</b>	Weakly Interacting Massive Particle